DENSITY, MAGNETIC PROPERTIES AND SOUND VELOCITIES OF IRON-RICH MATERIALS AT HIGH TEMPERATURE AND HIGH PRESSURE

BY

LILI GAO

DISSERTATION

Submitted in partial fulfillment of the requirements
for the degree of Doctor of Philosophy in Geology
in the Graduate College of the
University of Illinois at Urbana-Champaign, 2010

Urbana, Illinois

Doctoral Committee:

Professor Jie Li, Chair
Wolfgang Sturhahn, Ph.D, Argonne National Laboratory, Co-Director of Research
Esen Ercan Alp, Ph.D, Argonne National Laboratory, Co-Director of Research
Professor Jay Bass
Professor Craig Lundstrom

Abstract

Understanding the composition of Earth's inner core is crucial for revealing the mechanisms of core formation and the evolution of Earth. The presence of light elements in the Earth's inner core has been indicated in recent studies, based on the mismatch between the observed density of the inner core and the density of pure iron at relevant conditions. The nature and abundance of light element(s) are under debate, yet they are fundamental in understanding the formation and evolution of the Earth's core. Carbon has been considered a possible major light element candidate, besides hydrogen, oxygen, silicon and sulphur. In particular, Fe_3C has been proposed to be the major component in the Earth's inner core in a previous thermodynamics study. However, the possibility of Fe_3C being a major inner core component has been under debate in recent studies, largely due to our limited knowledge of the properties of Fe_3C at extreme pressure and temperature (*P*-*T*) conditions.

In this thesis work, I investigated the possibility of carbon as a principal light element in the inner core in the form of Fe_3C. Considering the lack of direct accessibility to the inner core, the only way to test a carbon-rich inner core model is to compare the properties of iron-carbon compounds, including the density and sound velocities, with the observed values of inner core, e.g., the values in preliminary reference Earth model (PREM) determined using normal mode data and seismic travel time data. In this work, I studied the density, elasticity, sound velocity and magnetism of Fe_3C using a series of experimental methods, including X-ray diffraction (XRD), nuclear resonant inelastic X-ray scattering (NRIXS), synchrotron Mössbauer spectroscopy (SMS) and conventional Mössbauer spectroscopy (CMS). The starting materials of (^{57}Fe-enriched) Fe_3C samples were synthesized using large-volume presses. The composition and purity of the samples were confirmed using high-resolution XRD and CMS methods.

A magnetic transition in Fe_3C from the low-pressure ferromagnetic phase to a high-pressure non-magnetic phase was reported in literature; however, the transition pressure has been controversial, ranging from 9 GPa to 25 GPa. The effect of this transition on compressibility is not well understood. In this study, I carried out SMS and CMS experiments in an attempt to resolve the controversy. The results from both methods show that the transition pressure is ~ 6

GPa (Chapter 5). A discontinuity around this pressure was also observed in sound velocity versus density data (Chapter 4), as well as the compression curves from the XRD data (Chapter 8). In addition, the SMS data in this work indicate an electronic transition between 50 GPa and 73 GPa (Chapter 8). The nature of this electronic transition remains to be further investigated. The compression curves from the XRD data also indicate a discontinuity around this pressure (Chapter 8).

To study the sound velocities of Fe_3C, I performed NRIXS experiments on a few-crystal sample (composed of one or a few single crystals) up to 50 GPa at 300 K (Chapter 4) and on powder Fe_3C samples up to 45 GPa and 1450 K (Chapter 7). Compressional velocities V_P and shear velocities V_S were derived combining an existing equation of state, estimated thermal expansion parameters and the phonon (vibration) densities of state extracted from NRIXS spectra. The derived V_P and V_S follow Birch's law - a linear relationship between sound velocity and density. The extrapolated values of V_P and V_S at the inner core *P-T* conditions are higher than those of the inner core. This is consistent with one of the criteria for a light element candidate – the light element should raise the V_P of iron, as the sound velocities of pure iron are suggested to be too low for the inner core from previous studies (e.g., Mao *et al*., 2005a).

The effect of temperature on sound velocity is not well understood, partially due to a lack of data. Among the existing data, it has been controversial whether or not the high-temperature sound velocities deviate from Birch's law. To shed light on the temperature effect on sound velocities, I carried out NRIXS experiments on powder Fe_3C samples up to 45 GPa and 1450 K (Chapter 7). The results at high temperatures suggest temperature induced shear velocity decrease, and also indicate that the temperature effect increases as temperature increases and decreases as pressure increases. The temperature needed to reconcile the sound velocity mismatch between Fe_3C and the inner core at 300 K is within the expected values for the inner core, supporting Fe_3C as a possible candidate material for the inner core.

In Chapter 7, a recent experimental capability of simultaneous nuclear resonant scattering and XRD measurements using synchrotron radiation at beamline 3-ID of the Advanced Photon Source is discussed. Here the application of this method to determine the sound velocities of compressed Fe_3C is shown. The XRD measurements allow detection of microscale impurities, phase transitions and chemical reactions upon compression or heating. They also provide

information on sample pressure, grain size distribution and unit cell volume. By combining the Debye velocity extracted from the NRIXS measurements and the structure, density and elasticity data from the XRD measurements simultaneously obtained, more accurate sound velocity data can be derived. In this chapter, I also reported the anisotropy in Fe_3C at ambient conditions, inferred from the difference in sound velocities between the few-crystal sample and a powder sample (Chapter 6, 7; Gao *et al*., 2009).

To study the density and elastic properties of Fe_3C, I carried out single crystal XRD measurements to 200 GPa at 300 K (Chapter 8). Elastic constants of bulk modulus and pressure derivative of bulk modulus are derived through equation-of-state fitting to these density versus pressure data. The extrapolated densities of Fe_3C at inner core *P*-*T* conditions are close to PREM values. These results suggest that pure Fe_3C or Fe_3C mixed with a small amount of iron can match the density of the inner core, supporting carbon as a major light element candidate in the Earth's inner core.

Dedicated to my loving and supporting

husband Joseph E. Bullock

and parents Litang Gao, Lanzhi Wang

Acknowledgement

I am deeply in debt to my advisors Prof. Jie Li, Dr. E. Ercan Alp, Dr. Wolfgang Sturhahn and Prof. Jay Bass. Jie introduced me to the field of high pressure geophysics. Throughout the years of my graduate study, her advising, guidance, encouragement and support have also enlightened me. One person I can't thank enough is Ercan. During the time I have been at Argonne, he interacted with me on a daily basis. He is always patient and has taught me a great amount of knowledge in science and techniques I would not have gained from elsewhere. I am also very grateful to Wolfgang for offering me the opportunity to work at Argonne, and for his guidance and help throughout my thesis research. Jay's assistance in the past year has been a great help to me.

Thanks also go to Dr. Holger Hellwig, who taught me Raman spectroscopy, and offered me valuable advice in my research. I also thank Dr. Bin Chen for his help in experiments at the University of Illinois and Argonne National Laboratory and for synthesizing the Fe_3C sample in run 092, Dr. Jingyun Wang for teaching me diamond anvil cell techniques and helping with my beamline experiments and Dr. Fang Huang for his help in my sample synthesis and sample characterization with SEM instrument, and Mr. Xing Ding for his assistance in Fe_3C synthesis in run PC04. I am also grateful to Prof. Jay Bass, Profs. Craig Lundstrom, Stephen Marshak and Susan W. Kieffer for offering me valuable advice in my exams towards my doctoral degree.

I am also thankful for Dr. Jiyong Zhao and Dr. Michael Lerche for their help in my nuclear resonant scattering experiments, Dr. Barbara Lavina and Dr. Przemyslaw C. Dera for teaching me single crystal X-ray diffraction technique and how to use the gas loading system, Dr. Vitali B. Prakapenka for his help in my single crystal X-ray diffraction project, Dr. Yuming Xiao for his help with the synchrotron Mössbauer experiments at beamline 16-ID-D of the APS, and Dr. Inno Kantor for teaching me how to use the laser gasket drilling system. I thank Dr. Brian Toby, Dr. Jun Wang, Dr. Lynn Ribaud and Dr. Sytle Antao for their help with Fe_3C sample characterization using the high-resolution X-ray diffraction method at beamline 11-BM of the APS. Dr. Brian Toby also offered me great help in formulating least squares fitting method for the program *FitEoS*. I also thank Prof. Henry Scott for his help and advice on my sound velocity project, Prof.

Jung-Fu (Afu) Lin for lending me cubic boron nitride seats for experiments and his advice on Be gasket preparation with cBN insert, Dr. Jay Bass for lending me a diamond anvil cell, Dr. Wenge Yang, Dr. Stas Sinogeikin, Dr. Yue Meng and Dr. Yang Ding for their help with X-ray diffraction setup in Fe_3C sample selections. I also thank Dr. David (Ho-Kwang) Mao, Prof. Henry Scott, Prof. Jung-Fu (Afu) Lin and my advisors for providing me recommendation letters for Argonne guest student application, postdoctoral positions applications and other conference traveling scholarship applications.

I would like to recognize all the people who have made my years in graduate school at Urbana-Champaign and Argonne enjoyable and productive, namely Jingyun Wang, Fang Huang, Xinlei Sun, Zhaofeng Zhang, Yingchun Li, Bin Chen, Jie Zheng, Lanfang Li, Weiwei Xie, Zhaohui Yang, Tai-Ling Tseng, Meijuan Jiang, Wei Dai, Zhen Xu, Jennifer Jackson, Emily Wisseman, Shane Butler, Tom Schickel, Theodore Flynn, James Klauss, Barb Elmore, Marilyn Whalen, Michael Sczerba, Julie Dyar, Scott Morris, Jennifer Drennan, Lori Baker … at UIUC, and Lifen Yan, Thomas Toellner, Hasan Yavas, Ahmet Alatas, Bogdan Leu, Becky Forsythe, Jun-Dar Su and Norman Mashalls, …. at Argonne National Laboratory. I also thank all the people who have affected me personally and contributed to my successes in career and life.

Last but not least, I would like to thank my husband Dr. Joseph Bullock, my parents, brother and sister, my parents-in-law, and my friends for their support and love during the long process of my Ph.D degree study. My husband Joseph has also helped me with keeping the X-ray intensity optimized during the days of sleepless beamlime work, X-ray diffraction data fittings as well as proof-readings of this thesis.

I also would like to acknowledge the funding support from sector 3 of the Advanced Photon Source at Argonne National Laboratory since January 2008, teaching assistantship from the department of Geology, predoctoral fellowship from the University of Illinois and department of Geology in the year 2004, and research assistantship from Prof. Jie Li. I also appreciate the traveling scholarship from the Department of Geology at University of Illinois and COMPRES - Consortium for Materials Properties Research in Earth Sciences. Use of the APS in this thesis work is supported by DOE under DEAC0206CH11357. This work was supported by National Science Foundation Grants EAR0609639 and EAR0738973.

Table of Contents

LIST OF FIGURES xii

LIST OF TABLES xv

LIST OF ABBREVIATIONS xvi

LIST OF UNITS AND CONSTANTS xviii

LIST OF SELECTED NOTATIONS xx

CHAPTER 1: INTRODUCTION 1

CHAPTER 2: METHODOLOGY 8

2.1 Introduction 8

2.2 High Pressure Devices for Static Compression 8

2.2.1 Diamond Anvil Cell 9

2.2.2 Multi-anvil Press 12

2.2.3 Piston-cylinder Press 14

2.3 X-ray Diffraction 14

2.4 Nuclear Resonant Scattering 16

2.4.1 Theoretical Aspects of Nuclear Resonance Scattering 16

2.4.2 Mössbauer Spectroscopy 17

2.4.3 Nuclear Resonant Inelastic X-ray Scattering 21

CHAPTER 3: SYNTHESIS AND CHARACTERIZATION OF FE_3C SAMPLES 24

3.1 Introduction 24

3.2 Sample Synthesis 26

3.3 Sample Characterization 27

3.3.1 Conventional Mössbauer Spectroscopy 28

3.3.2 Synchrotron Mössbauer Spectroscopy 31

3.3.3 High-resolution X-ray Diffraction 33

3.4 Concluding Remarks 43

CHAPTER 4: MAGNETIC TRANSITION AND SOUND VELOCITY OF FE_3C AT HIGH PRESSURE 45

4 Abstract 45

4.1 Introduction 45

4.2 Experimental Procedure 46

4.3 Results and Discussion 47

4.3.1 Magnetic Transition and Core Density Deficit 47

4.3.2 Sound Velocities, Poisson's Ratio and Birch's Law 49

4.Appendix. Converted Sound Velocities for Fe_3C with Natural Iron 54

CHAPTER 5: MAGNETIC TRANSITION AT ~ 5 GPA AND MÖSSBAUER SPECTROSCOPY 56

5.1 Experimental Procedure 56

5.2 Results and Discussion 57

CHAPTER 6: SOUND VELOCITIES AT SIMULTANEOUS HIGH PRESSURE AND HIGH TEMPERATURE 60

6 Abstract 60

6.1 Introduction 60

6.2 Experimental Procedure 62

6.3 Results 64

6.3.1 Phonon Density of States and Sound Velocities 64

6.3.2 ^{57}Fe Correction for V_P and V_S 66

6.3.3 Uncertainty Analysis 69

6.3.4 Sound Velocities and Thermal Effect 72

6.4 Conclusions 74

CHAPTER 7: EXPERIMENTAL ASPECTS ON SIMULTANEOUS X-RAY DIFFRACTION AND NUCLEAR RESONANT SCATTERING 75

7 Abstract 75

7.1 Introduction 75

7.2 Experiments 76

7.2.1 Nuclear Resonant Scattering 77

7.2.2 X-ray Diffraction 79

7.2.3 Sample Preparation 81

7.2.4 NRIXS, SMS, CMS and XRD Data Evaluation 83

7.3 Results and Discussion 83

7.3.1 Effect of Impurity on Sound Velocity Measurements 84

7.3.2 Sound Velocities from Simultaneous PDoS and EoS Measurements 87

7.3.3 Grain Size Distribution and Anisotropy 92

7.4 Conclusions 94

CHAPTER 8: DENSITY OF Fe_3C AT MULTI-MEGABAR PRESSURES FROM SINGLE CRYSTAL X-RAY DIFFRACTION 95

8 Abstract 95

8.1 Introduction 95

8.2 Experimental Method 98

8.3 Results 100

8.3.1 Lattice Parameters and Equation of State 101

8.3.2 Pressure Medium and Pressure Calibration 111

8.3.3 Uncertainty Analysis 113

8.4 Implications for Carbon in the Earth's Inner Core 114

CHAPTER 9: SUMMARY AND FUTURE PERSPECTIVE 117

9.1 Summary and Discussion 117

9.2 Future Perspective 121

APPENDIX A: *FITEOS* - A JAVA GRAPHICAL USER INTERFACE FOR HIGH PRESSURE AND HIGH TEMPERATURE EQUATION OF STATE FITTING 124

A.1 Introduction 124

A.2 Isothermal EoS 126
A.2.1 Murnaghan's Integrated Linear EoS 126
A.2.2 Birch-Murnaghan EoS 126
A.2.3 The Hencky(Natural)-Strain (Logarithmic) EoS 127
A.2.4 The Vinet EoS 127
A.3 High-temperature EoS 127
A.3.1 High-temperature Birch-Murnaghan EoS 128
A.3.2 Mie-Grüneisen-Debye EoS 128
A.3.3 Modified Mie-Grüneisen-Debye EoS 129
A.4 Weighted Least Squares Fitting Method 130
A.5 Graphical User Interface 131
APPENDIX B: *PRESSURE SCALE* - A JAVA PROGRAM FOR PRESSURE CALIBRATION 133
B.1 Input 133
B.1.1 Equation of State Input 133
B.1.2 Temperature and Volume Input 133
B.2 Output 136
B.3 Graphical User Interface 137
REFERENCES 139
AUTHOR'S BIOGRAPHY 146

List of Figures

1.1 The structure of Earth's interior 2

1.2 Cores of planets and a few other terrestrial bodies 6

2.1 Approximate pressure and temperature ranges that can be achieved using current static compression techniques 9

2.2 A schematic of the cross section of a symmetrical diamond anvil cell 10

2.3 A symmetrical diamond anvil cell and the accessories 11

2.4 A panoramic diamond anvil cell 11

2.5 Sample assembly in a multi-anvil press. 13

2.6 Cross section of a multi-anvil sample assembly 13

2.7 Cross section of a piston-cylinder sample assembly 14

2.8 Illustration of ^{57}Fe nuclear energy levels and simulated conventional and synchrotron Mössbauer spectra with presence of isomer shift, quadrupole splitting and magnetic hyperfine field 19

3.1 Structure of Fe_3C 24

3.2 Simplified phase diagrams of iron-carbon binary system at ambient pressure, 5 GPa and 10 GPa. 25

3.3 Conventional Mössbauer spectra of synthesized Fe_3C samples at ambient conditions 28

3.4 Ambient-condition synchrotron Mössbauer spectra of synthesized Fe_3C samples collected at beamline 16-ID-D of the APS 32

3.5 Sample assembly in X-ray diffraction measurements at beamline 11-BM-B of the APS 33

3.6 X-ray diffraction data collected at beamline 11-BM-B of the APS on synthetic Fe_3C samples plotted in log scale 34

3.7 X-ray diffraction data collected at beamline 11-BM-B of the APS on synthetic Fe_3C samples plotted in linear scale 35

3.8 X-ray diffraction data with only the diffraction peaks from Fe_3C marked 36

3.9 X-ray diffraction data with only the diffraction peaks from α-Fe (metallic iron) marked 37

3.10 X-ray diffraction data with only the diffraction peaks from calcite marked 38

3.11 X-ray diffraction data with only the diffraction peaks from FeO marked 39

3.12 X-ray diffraction data with only the diffraction peaks from MgO marked 40

3.13 Comparison of the X-ray diffraction line widths between samples PC03 and 090 41

3.14 Lattice parameters and unit cell volume of synthetic Fe_3C 42

4.1 Synchrotron Mössbauer spectra of synthesized Fe_3C and fitting results for the 1-bar data 48

4.2 Fe partial phonon density of states of Fe_3C extracted from NRIXS spectra between 1 bar and 50 GPa at 300 K 50

4.3 Comparison of V_P and V_s versus density between Fe_3C and other Fe-rich alloys 53

4.4 V_P and V_s for Fe_3C converted from those for $^{57}Fe_3C$ 55

5.1 Synchrotron Mössbauer spectra of compressed Fe_3C collected at beamline 16-ID-D of the APS 57

5.2 Conventional Mössbauer spectra of compressed Fe_3C collected at sector 3 of the APS 58

6.1 NRIXS spectra and derived partial phonon density of states of Fe in Fe_3C 66

6.2 High-temperature high-pressure sound velocities of Fe_3C with comparison to other Fe-bearing materials 68

6.3 Propagated uncertainty for the data point at 1450 K in run 090-DAC-III 72

7.1 Experimental set-up at beamline 3-ID of the Advanced Photon Source at Argonne National Laboratory 77

7.2 Schematic view of the DAC configuration, showing its effective opening angle and the range of 2θ accessible to the XRD measurements 80

7.3 X-ray diffraction spectrum of Fe_3C from synthesis run 093 (λ = 0.41416 Å) 82

7.4 Typical sample configuration in the DAC 82

7.5 Synchrotron Mössbauer data and fit spectra of almost pure Fe_3C at ambient conditions and an Fe_3C sample containing iron impurity at high pressures 84

7.6 XRD data of a powder Fe_3C sample at 48 GPa and 300 K, after being heated at ~ 1400 K for about three days (run 090-DAC-III) 85

7.7 The effect of iron impurity on the measured Debye sound velocity of Fe_3C for a conceivable range of η between 0.6 and 1.7 87

7.8 XRD data of a few-crystal Fe_3C sample in a panoramic DAC, under ambient conditions before compression (run 090-DAC-I) 88

7.9 (a) NRIXS spectra of $^{57}Fe_3C$ (b) Corresponding partial phonon density of state of Fe in Fe_3C. 89

7.10 (a) Compressional wave velocity (V_P) and shear wave velocity (V_S) of Fe_3C at 300 K as a function of density (b) Poisson's ratio of Fe_3C as a function of density 90

7.11 XRD spectra of Fe_3C at 17 GPa and 1000 K and 300 K (λ = 0.8603 Å). 91

8.1 Microscopic images, X-ray diffraction patterns of Fe_3C and predicted diffraction spot positions... 100

8.2 Compression curve and *f-F* relationship of Fe_3C. 102

8.3 Axial and volumetric compression curves of Fe_3C in the 300-μm run 107

8.4 Axial and volumetric compression curves of Fe_3C in the 100-μm run 108

8.5 Mössbauer spectroscopy results indicating a transition between 50 GPa and 73 GPa. 109

8.6 The differences in pressures determined using various equations of state 113

8.7 Estimated densities of Fe_3C to the inner core pressures and 5000 K, with comparisons to Fe the inner core 116

A.1 A screenshot of the *FitEoS* program (version 1.0)..... 132

B.1 A screenshot of the *Pressure Scale* program (version 1.3) 138

List of Tables

3.1 Summary of Fe_3C sample synthesis conditions and run products 26

3.2 Magnetic hyperfine fitting parameters used in Fig. 3.2 29

3.3 Magnetic hyperfine fitting parameters used in Fig. 3.3 32

4.1 EoS Parameters and Densities of HCP-Fe and Fe_3C 49

4.2 Compressional Wave Velocity V_P, Shear Wave Velocity V_s, Isothermal Bulk Modulus K_T, Shear Modulus G and Poisson's Ratio v of Fe_3C at 300 K 51

4.3 Compressional Wave Velocity V_P, Shear Wave Velocity V_s, Isothermal Bulk Modulus K_T, Shear Modulus G and Poisson's Ratio v of Fe_3C at 300 K converted from those for $^{57}Fe_3C$ 54

6.1 Sound velocity of Fe_3C at high pressures and high temperatures 69

7.1 Magnetic hyperfine field parameters of Fe_3C and Fe 85

7.2 Lattice parameters of NaCl and Fe_3C at high pressures 92

8.1 Unit cell parameters of Fe_3C from the 100-μm run 103

8.2 Unit cell parameters of Fe_3C from the 300-μm run 105

8.3 Equation of state parameters of Fe_3C 110

List of Abbreviations

ANL	Argonne National Laboratory
APS	Advanced Photon Source
BM	Birch-Murnaghan
CMB	Core Mantle Boundary
CMS	Conventional Mössbauer Spectroscopy (Spectra)
DAC	Diamond Anvil Cell
EOS	Equation of State
FWHM	Full width at Half Maximum
GPa	Giga-Pascal
HF	Hyperfine Filed
IC	Inner Core
ICB	Inner(-outer) Core Boundary
IS	Isomer Shift
LS	Least Squares (Fitting)
MA	Multi-anvil Apparatus
Mbar	Megabar
NRIXS	Nuclear Resonant Inelastic X-ray Scattering
NRS	Nuclear Resonant Scattering
P-V-T	Pressure-Volume-Temperature
P-T	Pressure-Temperature
OC	Outer Core
PREM	Preliminary Reference Earth Model

QS	Quadrupole splitting
SMS	Synchrotron Mössbauer Spectroscopy (spectra)
WC	Tungsten carbide
WLS	Weighted Least Squares (Fitting)
XES	X-ray Emission Spectroscopy
XMCD	X-ray Magnetic Circular Dichroism
XRD	X-Ray Diffraction

List of Units and Constants

Avogadro number, N_A	6.022142×10^{23} mol^{-1}
Gravitational constant, G	6.67×10^{-11} N(m/kg)$^{-2}$
Ideal gas constant, R	8.314472 J/K/mol
Planck constant, h	6.626068×10^{-34} J/s (or m^2 kg / s)
	4.135667×10^{-15} eV/s
Dirac constant, reduced Planck constant, $\hbar$	$1.0545716 \times 10^{-34}$ J/s (or m^2 kg / s)
	$6.5821190 \times 10^{-16}$ eV/s
Speed of light, c	2.99792458×10^{8} m/s
Boltzmann constant, k_B	$1.3806504 \times 10^{-23}$ J/K
	8.617343×10^{-5} eV/K
Mass of electron	9.109382×10^{-31} kg
Mass of proton	1.672622×10^{-27} kg
Curie, a unit of radioactivity	3.7×10^{10} decays/s
Energy units	1 eV = $1.60217653 \times 10^{-19}$ J
	1 Calorie = 4.184 J
Unit of cross section	1 b (barn) = 10^{-24} cm^2
Relationship between energy and wavelength for photon	$E\lambda = hc$ = 12.39842 keV·Å
Exponential decay	$N = N_0 \exp(-t/\tau)$
Relationship between mean life τ and half life $t_{1/2}$	$t_{1/2} = \ln 2\ \tau$

CONSTANTS FOR ^{57}FE

Nuclear transition energy from 1st excited state to ground state	E_R = 14.1425 keV

Absorption cross section	$\sigma = 2.56$ Mb $= 2.56 \times 10^{-18}$ cm^2
Natural line width	$\Gamma = 4.665$ neV
Mean life time of the 1st excited state	$\tau = 141$ ns
^{57}Co source velocity and energy shift relationship	1 mm/s ~ 48.07 neV
^{57}Co source velocity and natural line width relationship	1 mm/s = 0.097 Γ

List of Selected Notations

P	Pressure
T	Temperature
F	Force
A	Area
K_S	Adiabatic bulk modulus
K_T	Isothermal bulk modulus
K	Bulk modulus
	Or, deflection parameter of undulator
K'	Pressure derivative of the bulk modulus
G	Shear modulus
ρ	Density
V_P	Compressional wave velocity
V_S	Shear wave velocity
V_D	Debye sound velocity
v	Poisson's ratio
α	Thermal expansion coefficient
	Or, concentration of impurity
γ	Mie-Grüneisen parameter
Θ	Debye temperature
n	Number of ^{57}Fe atoms per cm^2
	Or, number of atoms in a formula
Z	Number of chemical formulas in a unit cell

$\tilde{M}$	Atomic mass of ^{57}Fe
d	d-spacing, the distance between adjacent atomic planes in a crystal
θ	Incident X-ray angle
λ	Wavelength
E_{R}	Nuclear resonant energy
E_{recoil}	Recoil energy
E	Energy
ΔE	Energy shift due to Doppler effect
$S(E)$ (NRIXS spectrum)	Phonon excitation and annihilation probability as a function of energy
E_{kinetic}	Kinetic energy
Γ	Natural line width
τ	Mean life time
t	Effective thickness
	Or, time
$g(E)$	Phonon density of state (PDoS)
σ_{N}	Cross sections of nuclear resonance
σ_{T}	Cross sections of Thomson scattering on electrons
σ_{pe}	Cross sections of photoelectric processes
D	Mean force constant
M	Mass
f	Lamb-Mössbauer factor
$\langle \Delta x^2 \rangle$	Mean-square deviation of the vibrating atom from its equilibrium position
h	Planck's constant
c	Speed of light

u	Speed
|e>	Nuclear excited state
|g>	Nuclear ground state
$\|I, m\rangle$	A nuclear level with a spin quantum number I and a magnetic quantum number m
M_n	n-th order centered moment of a spectrum

Chapter 1

Introduction

With a radius of about 3480 km (Fig. 1.1), the core comprises about one eighth of the Earth by volume, and one third by mass. The density contrast at the core-mantle boundary (CMB), 4.3 g/cm^3, is even larger than that at the boundary between the atmosphere and the solid Earth. The density jump at the inner-core boundary (ICB) is around 0.5-0.6 g/cm^3 based on seismic travel time observations and normal mode data (e.g., Morelli and Dziewonski, 1993; Masters and Shearer, 1990). Although it is not, or not yet, possible to directly obtain a sample from the core, seismic wave travel time observations, normal mode data as well as the observed mass and moment of inertia of the Earth can be used to construct models about the density and sound velocity profiles of the Earth's interior. An often-used model is the preliminary reference Earth model (PREM) (Dziewonski and Anderson, 1981). Later models have also been developed to refine the sound velocity and density. These velocity models include, but are not limited to, iasp91 (Kennett and Engdahl, 1991), sp6 (Morelli and Dziewonski, 1993) and AK135 (Kennett *et al*., 1995). Density has also been refined, e.g., by Shearer and Masters (1990). In the core regime, these models provide similar sound velocity and density profiles.

Combining the density and sound velocity profiles, compositional systematics of meteorites and solar photosphere, and the chemical and petrological models of peridotite-basalt melting relations (i.e. the pyrolite model), a compositional model of the Earth's core and mantle was derived (McDonough and Sun, 1995). The major element in the core is widely accepted to be iron (e.g., McDonough and Sun, 1995; Li and Fei, 2007, and references therein). Iron is an abundant element in the solar system. Iron has maximal nuclear stability and is the end product of stellar nucleosynthesis (e.g., Prantzos, 2007). The densities and bulk sound velocities of iron at the pressure and temperature (*P*-*T*) conditions of the Earth's core are similar to the observed values for the core (e.g., Dziewonski and Anderson, 1981). Existence of iron meteorites, which are believed to be the core fragments of ancient asteroids, provides additional evidence of an iron-rich Earth core. Nickel is believed to be another major element in the core (Ni:Fe ~ 5:95)

due to its affinity with iron. This is also supported by the common presence of iron-nickel alloys in iron meteorites.

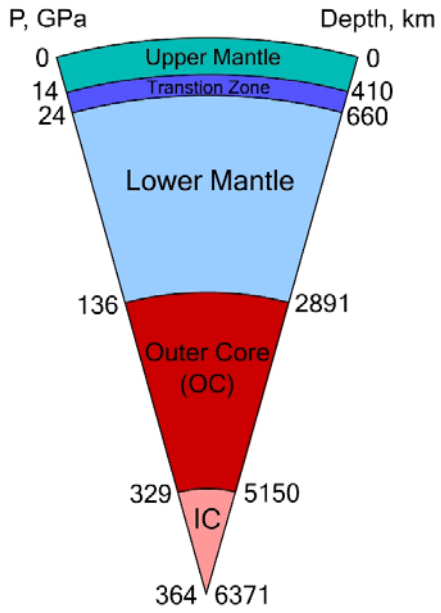

Fig. 1.1. The structure of Earth's interior. Pressure and depth of the upper and lower bounds of the transition zone are from a recent article by Frost (2008). Other numbers are from the preliminary reference Earth model (Dziewonski and Anderson, 1981).

Besides iron and nickel, light elements (lighter than iron or nickel) are also believed to exist in the Earth's core (e.g., Birch, 1952). This is inferred from the mismatch between the observed density and sound velocity values of the core and the estimated values of iron-nickel alloy at core *P-T* conditions based on experimental measurements. The current existence of a liquid outer core also indicates the presence of lighter element(s), since the estimated core temperature is lower than the estimated melting temperature of pure iron at core pressures (e.g., Stevenson, 1981). The amount of density deficit is estimated to be ~ 10 % in the outer core (e.g., Li and Fei, 2007; and references therein) and 1.4-9.1 % in the inner core (e.g., Dewaele *et al*., 2006).

While a wealth of knowledge about the core has been obtained over the last century, many mysteries still remain to be unraveled. One of the long-standing issues is the nature and amount of the light elements. Understanding the detailed composition of the Earth's core is fundamental in understanding the formation of the core and the evolution of Earth and the solar system, as well as the core convection mechanism, which is believed to be the driving force of the Earth's

magnetic field (e.g., Stevenson, 2003). Over the last century, our understandings of the core formation have been drastically improved (e.g., Rubie *et al*., 2007, and references therein), yet many questions remain unanswered. In the modern era, it is believed that Earth is the end product of multiple collisions between kilometer-sized planetesimals, which are suggested to already possess metallic cores by recent scientific findings (ibid). Collisions between moon-sized or Mars-sized terrestrial protoplanets also contributed to the growth of the Earth. The collisions between the protoplanets inevitably led to a molten magma ocean near the surface of the Earth. Once the melting starts, segregation and differentiation are unavoidable. The density difference between the iron metal phase and the silicate phase naturally led to the segregation between these two phases. The nature of the segregation mechanism is not yet clear. Possible sinking motions of iron metal phase through the silicate mantle include percolation (through a partially molten mantle), diapirism (through a viscously deformable mantle) and dyking (through brittle fractures) (ibid). These three mechanisms have different time scales, and lead to drastically different chemical consequences, one of which is the nature and amount of light elements in the Earth's core. Understanding the core formation mechanism hence in turn requires accurate knowledge about the detailed composition of the Earth's core. Light elements also play important roles in the dynamics of planetary cores. The exclusion of light elements at the ICB and the released latent heat during cooling of the core over time could contribute to the convection in the liquid outer core and the maintenance of the Earth's magnetic field (Stevenson, 2003). Various amounts of light elements may also lead to various convection models in planetary cores (e.g., Hauck *et al*., 2006; Chen *et al*., 2008).

Among all light elements, hydrogen, carbon, oxygen, silicon and sulfur have been considered the most likely major ones in the Earth's core (e.g., Poirier 1994, and references therein; Li and Fei, 2007, and references therein). To test whether a certain element could be the major light element in the core, a crucial way is to compare the densities, elastic parameters and sound velocities of iron-light element(s) compounds against the reference model values of the inner core (e.g., Dziewonski and Anderson, 1981). In this work, I investigated the possibility of carbon as a major light element in the inner core, in the form of Fe_3C. The methods used in this study can be applied to other iron-light element(s) systems as well.

Fe_3C, known as cementite, or cohenite when a small fraction of iron is replaced with nickel,

contains the least amount of carbon (6.7 wt.%) among all stable forms of iron-carbon compounds at ambient conditions. $(Fe,Ni)_3C$ has been observed in meteorites (e.g., Goodrich, 1992), as well as in inclusions of polycrystalline diamond aggregates from the Venetia kimberlite (Limpopo central belt, South Africa) (Jacob *et al*., 2004). It was proposed to be the major component in the Earth's inner core instead of iron-nickel alloy in a thermodynamics calculation study (Wood, 1993), although this view has been under debate (e.g., Scott *et al*., 2001; Vočadlo *et al*., 2002; Lin *et al*., 2004a; Gao *et al*., 2008; Fiquet *et al*., 2009; Nakajima *et al*., 2009; Lord *et al*., 2009; Ono and Mibe, 2010), partially due to the limited knowledge on the densities and phase stabilities of Fe_3C at high pressures and high temperatures.

This dissertation reports my experimental results on the elasticity, density and sound velocity of Fe_3C in a previously unexplored *P-T* region, and addresses how these results impact our understanding about the inner core. To generate high pressure, I used a piston-cylinder apparatus, multi-anvil press and diamond anvil cell. To study the different aspects of Fe_3C, a combination of various techniques were used, including X-ray diffraction (XRD) and nuclear resonant scattering (NRS). NRS further includes nuclear resonant inelastic X-ray scattering (NRIXS), synchrotron Mössbauer spectroscopy (SMS), and conventional Mössbauer spectroscopy (CMS). These methods are introduced in chapter 2.

In chapter 3, I discuss the Fe_3C sample synthesis procedures and sample characterizations. Fe_3C samples with both natural iron and ^{57}Fe-enriched iron were synthesized. As NRIXS is a low count-rate method, usage of ^{57}Fe-enriched sample is beneficial, and even necessary at high pressures. To characterize the purity and structure of the synthesis run products, I used the classic XRD method and the well-established CMS method. High-resolution XRD measurements were conducted at beamline 11-BM-B of the APS; and CMS measurements were carried out at sector 3 of the APS. XRD probes the long-range order of a material. As most materials have distinct structures (different lattice structures and/or different lattice parameters), XRD spectrum for each material is unique. CMS method probes the hyperfine field around the ^{57}Fe nuclei, and provides information on the surrounding electronic environments, which is unique for each material.

Chapters 4 to 7 are about the nuclear resonant scattering experimental results on Fe_3C. A magnetic transition of Fe_3C at high pressure had been previously observed in an X-ray emission

spectroscopy (XES) study (Lin *et al*., 2004a) and an X-ray magnetic circular dichroism (XMCD) study (Duman *et al*., 2005). The transition pressure is, however, controversial, i.e., ~ 25 GPa inferred from the XES study and ~ 9 GPa from the XMCD study, yet it is an important parameter since the transition is expected to affect the sound velocity and density. In this thesis work, I utilized SMS and CMS methods to study the magnetic transition in an attempt to resolve the controversy on the transition pressure. These SMS and CMS data both confirm this magnetic transition, and indicate that this transition from a low-pressure ferromagnetic phase to a high-pressure non-magnetic phase completes at ~ 6 GPa. These results are shown in chapters 4 and 5. The sound velocities measured using NRS method at the beamline 3-ID of the APS and their implications for the Earth's inner core are presented in chapters 4 and 6. In chapter 7, I address a few experimental issues, including the experimental setup at beamline 3-ID, effect of impurity on sound velocity determination and improved accuracy of sound velocity with simultaneous XRD measurements. I also report the preliminary results on elastic anisotropy in Fe_3C at ambient conditions, as indicated by the differences of sound velocities between a powder sample and a few-crystal sample (composed of one or a few crystals).

Chapter 8 is on the density and elasticity of Fe_3C at high pressures. Accurate knowledge on the density of iron-carbon compounds is critical in evaluating the role and amount of carbon in the inner core. Previous measurements on the density of Fe_3C were conducted to 30 GPa by Li *et al.* (2002), 73 GPa by Scott *et al.* (2001) and 67 GPa by Ono and Mibe (2010) at 300 K. In this work, I explored the density of Fe_3C using XRD method on a single crystal Fe_3C sample to 200 GPa. Equations of state (EoS) of Fe_3C were derived from these data. The extrapolated densities of Fe_3C at the inner core *P-T* conditions based on the EoS are compared with the values of PREM (Dziewonski and Anderson, 1981). These results indicate that pure Fe_3C or Fe_3C mixed with a small amount of iron could match the density of the inner core.

The last chapter summarizes the findings in this thesis study and points out future directions extended from this work. Appendixes A and B describe the two java programs I developed - *Pressure Scale* and *FitEoS*. *Pressure Scale* program calculates pressure from known temperature and lattice parameters. *FitEoS* program performs sophisticated mathematical calculations and converts experimental data to EoS parameters, which are necessary in comparing densities of a material with those of the Earth's interior. Both of these programs are available online for public

use.

While this thesis is focused on the Earth's inner core, it should be pointed out that most of the terrestrial planets and terrestrial-like moons are also believed to possess iron-rich cores, inferred from observations of their magnetic fields, moments of inertia and spacecraft measurements of Love numbers (response to solar tide) (Fig. 1.2) (e.g., Rubie *et al*., 2007, and references therein). The results of this thesis work also benefit our understanding on the cores of other planets and terrestrial bodies.

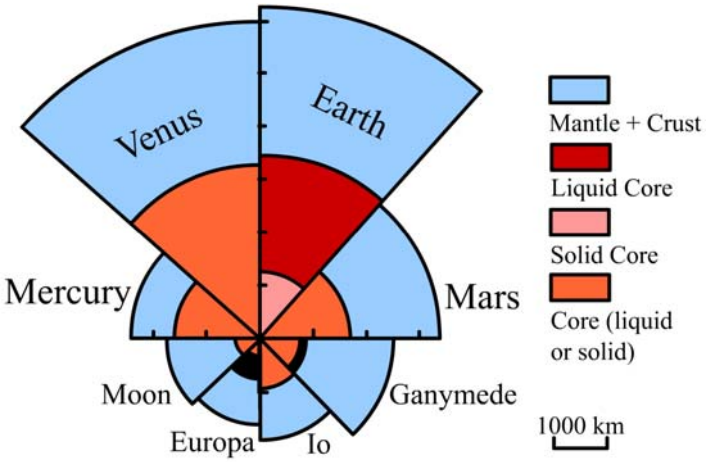

Fig. 1.2. Cores of planets and a few other terrestrial bodies. Data source: Rubie *et al*., 2007, and references therein. The thick dark bars for Jupiter's moons Io and Europa represent uncertainties on the core radii. The mechanical states (liquid or solid) of cores of these terrestrial bodies are still under debate except for Earth.

It is also worthy noting that the possibility of a carbon reservoir in the Earth's core also has potential implications for the Earth's carbon cycle. Typical forms of carbon in the solid Earth include graphite, diamond and carbonate. Carbon may subduct into the Earth's interior, as diamonds with subducting trace element signatures have been found (e.g., McCammon, 2001). Diamonds generally occur in kimberlites, which have been indicated to be correlated to plume generation zones (Torsvik *et al*., 2010) that originate from as deep as the CMB. It is possible that some carbon could be delivered to the bottom of the lower mantle through subducting slabs and eventually enter the core, even though evidence lacks for this scenario up to date. On the other hand, a possible leaky carbon-rich core may provide carbon flux to the mantle and affect the

mantle electrical conductivity (Hayden and Watson, 2008).

Chapter 2

Methodology

2.1 INTRODUCTION

The techniques used in this thesis work are introduced in this chapter. I will first outline the high pressure devices used in this work, namely piston-cylinder press, multi-anvil press, and diamond anvil cell (DAC). Piston-cylinder and multi-anvil presses were mainly used in Fe_3C sample synthesis. DAC was used in most synchrotron experiments performed at the advanced photon source (APS) of Argonne National Laboratory (ANL). To measure magnetic, elastic and acoustic properties of Fe_3C, I used X-ray diffraction (XRD), conventional Mössbauer spectroscopy (CMS), synchrotron Mössbauer spectroscopy (SMS), and nuclear resonant X-ray inelastic scattering (NRIXS) methods. The principles of these methods will be outlined below.

2.2 HIGH-PRESSURE DEVICES FOR STATIC COMPRESSION

To achieve high pressure, both static and dynamic methods are currently used in research. In dynamics method, high pressure is generated when a shock wave passes though the sample (e.g., Mao and Hemley, 1998, and references therein). Simultaneous high pressure and high temperature are generated in this process. The peak pressure can be very high (tens of megabars); however, the time duration at the peak pressure is only in the order of microsecond. Up to date, shock wave instruments are only available in selected few places in the world. On the other hand, static compression instruments are readily available in a great number of labs around the world. Although the achievable pressure and temperature (*P*-*T*) range from the static compression method is lower, static methods offer much longer duration of time (hours to months) and allow long-duration measurements. With long measurement time, accuracy is also enhanced. A schematic of the approximate *P*-*T* ranges that can be achieved using current static compression techniques is shown in Fig. 2.1.

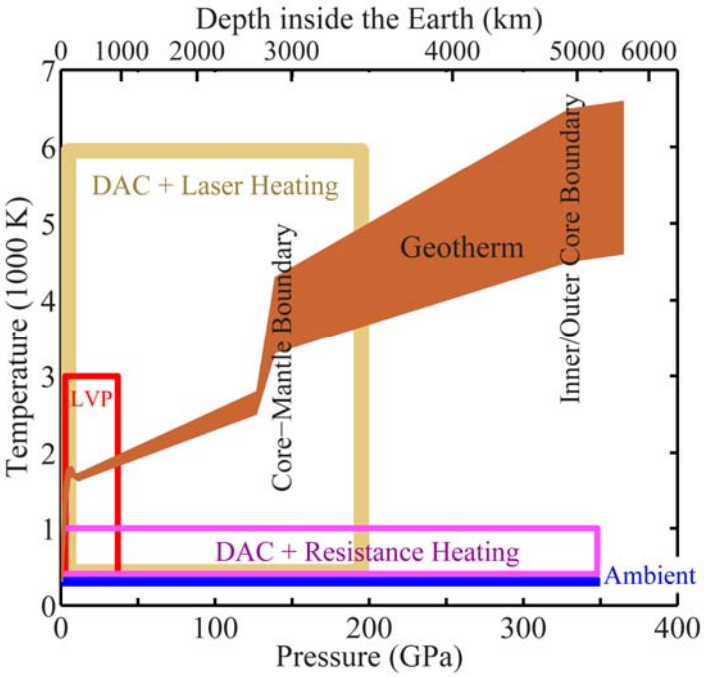

Fig. 2.1. Approximate pressure and temperature ranges that can be achieved using current static compression techniques. Actual experiments at simultaneous high temperature and high pressure are very challenging, and the ranges in this plot are close to the limits of current techniques. LVP-large volume pressure, including multi-anvil and piston-cylinder presses; DAC-diamond anvil cell; Geotherm-temperature profile inside the Earth. Data source for Geotherm: Upper mantle (3 ~ 13 GPa) – Anderson *et al*., 1980; Core-mantle boundary (D'' region, 127 ~ 139 GPa) – Lay *et al*., 2008; Inner core (329 ~ 365 GPa) – Mao and Hemley, 1998, and references therein.

2.2.1 Diamond Anvil Cell

From the definition of pressure - force derived by surface area ($P = F/A$), it is evident that applying large force to a small area results in high pressure. In a DAC (Figs. 2.2, 2.3, 2.4), high pressure is generated by turning screws, either manually or remotely. A diamond anvil is gem-shaped, with a small culet (ranging from a few microns to hundreds of microns in diameter) and a large base (~ 4 mm in diameter). Two diamond anvils are placed with the small culets facing each other in a DAC. A gasket is placed between the two diamond anvils. A hole drilled in the gasket serves as the sample chamber. The gasket should be prepared in a way that it is thick (hundreds of microns) in the rim to support high pressure and thin (tens of microns) in the center

(between the two culets) so the sample chamber does not collapse at high pressure (Fig. 2.2). This is achieved by indenting a gasket with a homogeneous initial thickness of hundreds of microns using diamond anvils to the desired thickness. When force is applied to the screws, it is transferred through the cell and seats to the diamond anvils and eventually to the sample chamber with a small size of ~ 10^{-4} mm^3 or even smaller. Generally, diamond anvils with smaller culet sizes can reach higher pressures. Diamond anvils with a culet size of 300 μm in diameter can reach a maximum pressure of 70 GPa approximately. To reach Mbar pressures (1 Mbar = 100 GPa) and beyond, beveled diamonds are often used. Conducting experiments at Mbar pressure range is not uncommon, but still challenging as diamonds break at extreme pressures. Careful preparation of the DAC assembly is necessary. Mishandling and improper alignment of diamonds can easily lead to breakage of diamond anvils. In this thesis work, 300/100-μm beveled diamonds have been used to generate pressure of 200 GPa.

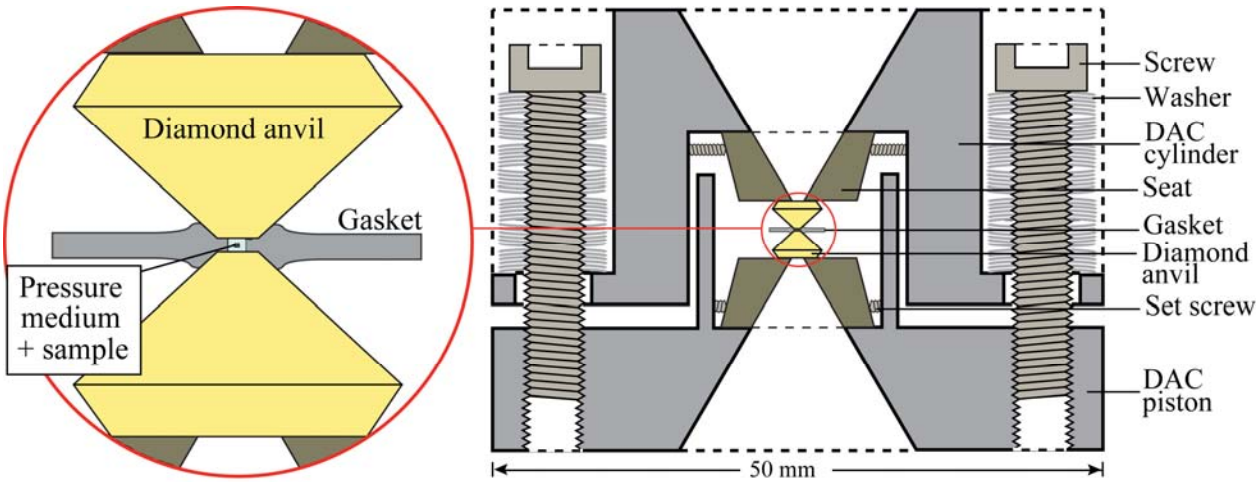

Fig. 2.2. A schematic of the cross section of a symmetrical diamond anvil cell.

Two types of DACs were used in this thesis work: symmetrical DACs (Figs. 2.2, 2.3) and panoramic DACs (Fig. 2.4). A panoramic DAC has three side openings, allowing detection of inelastic signals. To take advantage of this feature, gaskets with low X-ray absorption are needed. An often-used gasket is Be metal. Be metal is soft and brittle, and becomes very thin at high pressures. To enhance the gasket thickness, cubic boron nitride insert has been used in previous studies (e.g., Lin *et al*., 2004b; Gao *et al*., 2009). If one is only interested in the signal along the DAC axis, a symmetrical DAC can be used instead of panoramic DAC. In symmetrical DACs, Re and steel gaskets are widely used.

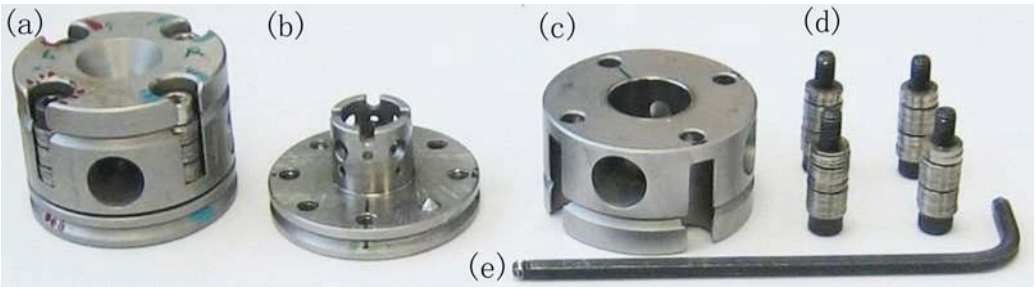

Fig. 2.3. A symmetrical diamond anvil cell and the accessories. (a) Assembled DAC. (b) Piston part of the DAC. (c) Cylinder part of the DAC. (d) Screws and washers. (e) Allen wrench used for applying pressure.

Fig. 2.4. A panoramic diamond anvil cell. Compared to symmetrical DACs, panoramic DACs have more side openings hence allowing detection of inelastic signals.

The choice of pressure medium is greatly related to how hydrostatic the pressure is inside the sample chamber. Commonly used pressure mediums include, but are not limited to, helium, neon, methanol-ethanol(-water) mixture, silicon oil and NaCl. Methanol-ethanol-water (16:3:1 by volume) pressure medium has been shown to maintain hydrostaticity up to 14.4 GPa (Fujishiro *et al*., 1982). Helium and neon have been shown to maintain better hydrostaticity compared to methanol-ethanol(-water) mixture or NaCl (e.g., Bell and Mao, 1981; Klotz *et al*., 2009). NaCl has a structural transition from the face-center cubic (FCC) with space group of Fm3m (#225) to another cubic phase with space group of Pm3m (#221) at ~ 30 GPa. To better maintain hydrostatic condition, the geometry of the sample should also be carefully chosen so that the sample does not bridge the two diamond anvils or the gasket at high pressures.

In a DAC, high temperature can be reached from resistive heating using wires or from laser heating. The temperature can be estimated based on grey-body radiation or XRD measurement of

pressure calibrants such as MgO and NaCl. In NRIXS experiments, temperatures can also be derived from NRIXS spectra based on the relationship of detailed balance (e.g., Shen *et al*., 2004) using *PHOENIX* software (Sturhahn, 2000).

2.2.2 Multi-anvil Press

While a DAC is light and small, multi-anvil and piston-cylinder presses are heavy and massive. In a multi-anvil press, large force produced using an electrically-controlled hydraulic pump is applied to a ram with a large surface area. In the Kawai-type two-stage multi-anvil press that is widely used today and also used in this thesis work, the force applied to the ram with a surface area of ~ 0.5 m^2 is transferred to the sample with a volume of ~ 10^{-7} m^3 or less through typically two stages. These two stages include a stage of six steel wedges and a stage of eight tungsten carbide (WC) cubes with truncated edges (Fig. 2.5). The six steel wedges form a cubic cavity, and the eight WC cubes nest in this cavity. Inside the octahedron space formed from the truncated edges of the eight WC cubes, an MgO octahedron with sample enclosed resides. In a multi-anvil press, high temperature is generated using resistive heating. Typical heaters include rhenium, graphite and $LaCrO_3$. Temperature is measured using thermocouples. A thermocouple consists of two metal wires. The junction of these two wires is placed close to the sample chamber in an experiment. The voltage difference of the two wires depends on the temperature at the junction. The relationship between the temperature and the voltage difference have been well calibrated for various types of thermocouples, and these thermocouples are commercially available (e.g., from Alfa-Aesar). A detailed description of a multi-anvil press can be found in a previous article (Liebermann and Wang, 1992). The maximum pressure that can be reached using a multi-anvil press is ~ 30 GPa with WC cubes, and ~ 60 GPa when sintered diamond cubes are used (e.g., Li and Fei, 2007). High temperature of ~ 2000 K can be kept under high pressure stably for a long duration of days.

To achieve the required *P-T* conditions in the sample synthesis in this thesis work, we used a 21/16 sample assembly following the design in a previous study (Bertka and Fei, 1997). A cross section of the assembly is shown in Fig. 2.6. The number 21 in '21/16' refers to the octahedron edge length, and the number 16 refers to the truncated edge length of WC cubes.

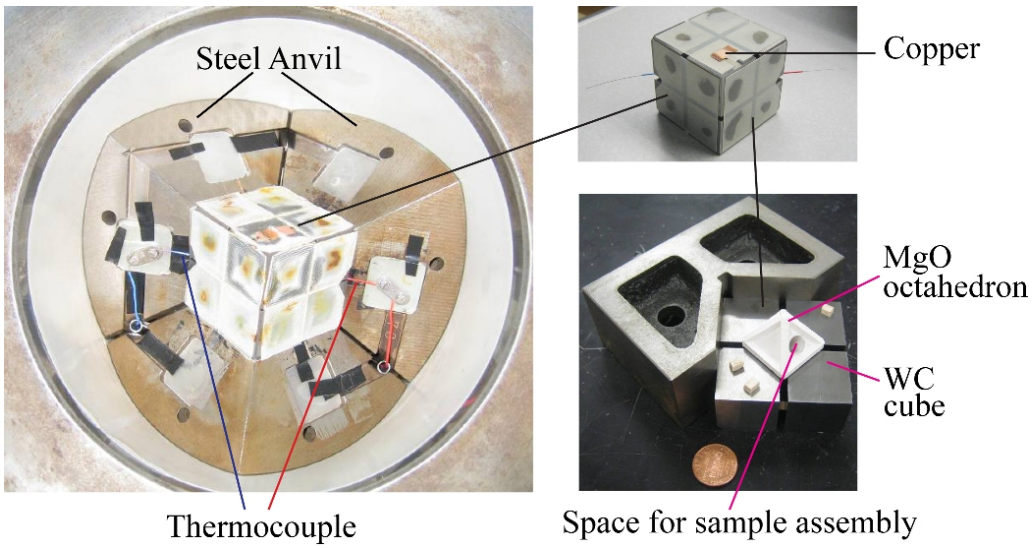

Fig. 2.5. Sample assembly in a multi-anvil press. The left figure is a top view, showing the bottom three steel wedges and a cube formed from eight tungsten carbide (WC) edge-truncated cubes. MgO octahedron with the sample assembly (Fig. 2.6) is enclosed inside the octahedron cavity formed by the eight WC cubes (the right bottom figure). Copper is used to conduct electricity for resistive heating.

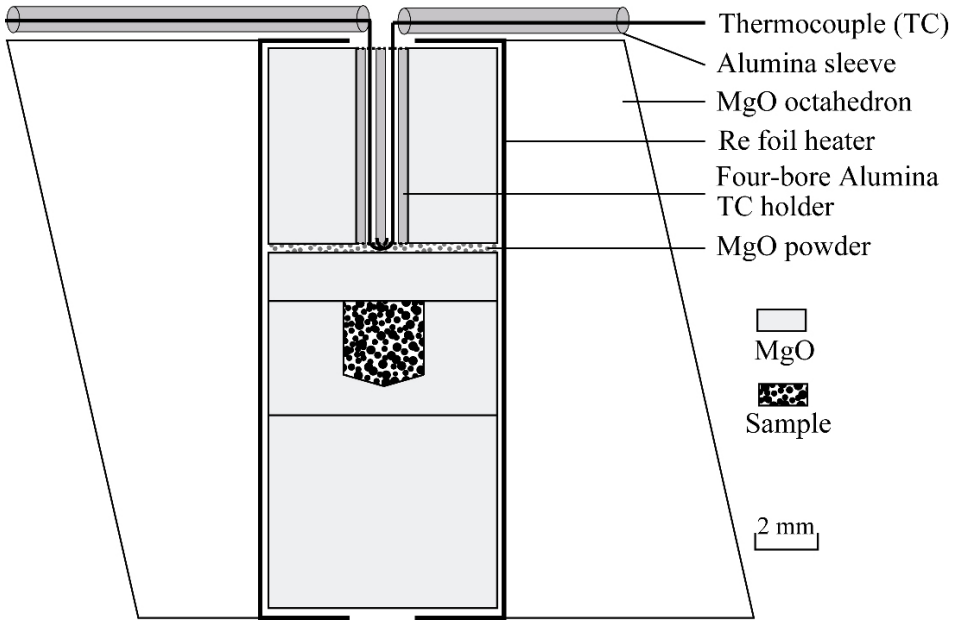

Fig. 2.6. Cross section of a multi-anvil sample assembly. MgO powder was used to fill the space between the MgO spacers to prevent thermocouple junction from intruding into the sample chamber. Thermocouple wires are used for measuring temperature, and are placed in a four-bore alumina tube.

2.2.3 Piston-cylinder Press

The principle of a piston-cylinder press is similar to that of a multi-anvil press. In a piston-cylinder press, a large force is applied to a ram with a large surface area, and transmitted through a WC piston with a smaller area to the sample. The surface area of the WC piston matches that of the sample assembly, and both are only ~ 0.1 % of the surface area of the ram. The large contrast of the surface areas gives rise to high pressure. In Fig 2.7, the cross section of a piston-cylinder sample assembly used in this work is shown. High temperature in a piston-cylinder is generated using the resistive heating method. Typically, the maximum pressure that can be reached using a piston-cylinder press is less than 6 GPa (e.g., Li and Fei, 2007). High temperature of ~ 2000 K can be stabilized at high pressure in a piston-cylinder press for a duration of days to weeks.

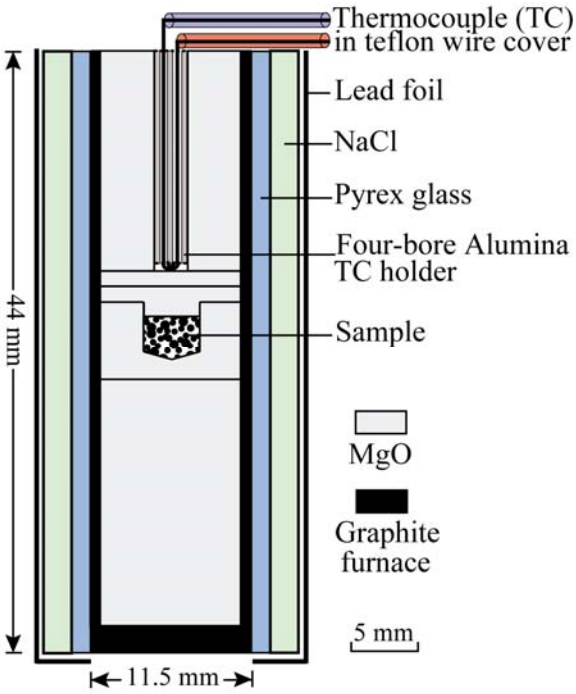

Fig. 2.7. Cross section of a piston-cylinder sample assembly. Graphite serves as a heater. Lead foil serves as a lubricant, and can be replaced with Teflon foil.

2.3 X-RAY DIFFRACTION

X-ray diffraction (XRD) is an elastic X-ray scattering technique that probes the long-range ordering of a crysstal. A description of the theory can be found in numerous books (e.g., Warren, 1969; Kittel, 2005). When X-rays strike a crystal, the incident photons interact with the electron

clouds in the material. The diffraction condition can be conveniently described in the reciprocal lattice space, which is the Fourier transformation of the real lattice space. The axis vectors of the reciprocal space can be defined as:

$$\mathbf{b}_1 = 2\pi \frac{\mathbf{a}_2 \times \mathbf{a}_3}{\mathbf{a}_1 \cdot (\mathbf{a}_2 \times \mathbf{a}_3)}; \quad \mathbf{b}_2 = 2\pi \frac{\mathbf{a}_3 \times \mathbf{a}_1}{\mathbf{a}_1 \cdot (\mathbf{a}_2 \times \mathbf{a}_3)}; \quad \mathbf{b}_3 = 2\pi \frac{\mathbf{a}_1 \times \mathbf{a}_2}{\mathbf{a}_1 \cdot (\mathbf{a}_2 \times \mathbf{a}_3)} \tag{2.1}$$

where $\mathbf{a}_1$, $\mathbf{a}_2$ and $\mathbf{a}_3$ are the lattice vectors in the real space. A point in the reciprocal lattice space therefore is described as $\boldsymbol{G} = v_1\mathbf{b}_1 + v_2\mathbf{b}_2 + v_3\mathbf{b}_3$. The diffraction condition is $\boldsymbol{k}' - \boldsymbol{k} = \boldsymbol{G}$, where $\boldsymbol{k}'$ and $\boldsymbol{k}$ are the vectors of the emitted X-ray and the incident X-ray, respectively. This description of the diffraction condition is equivalent to the Bragg's law:

$$2d\sin\theta = n\lambda, \; n \text{ is an integer} \tag{2.2}$$

where d is the distance between adjacent planes in the crystal, θ is the incident angle, and λ is the wavelength of the incident X-ray beam.

XRD patterns can be collected with either varying X-ray incident angle θ or varying wavelength λ. The former approach is known as angular-dispersive XRD and the latter is energy-dispersive XRD. From an XRD pattern, information about the crystal structure can be derived. As most crystals have distinct unit cell parameters and/or structures, XRD patterns can be used for identifying crystalline materials. In this thesis work, XRD is mainly used for three purposes: 1. to characterize the structure and purity of synthetic Fe_3C samples; 2. to measure the unit cell parameters of Fe_3C at high pressures for equation-of-state study; 3. to measure unit cell parameters of neon and NaCl for pressure calibration.

A great number of programs are available for deriving unit cell parameters from XRD data. *GSE-ADA* program (Dera, 2007) is a widely-used program for processing single crystal XRD data. To convert the XRD patterns collected on an image plate (or other types of detectors) in angular-dispersive XRD experiments to one-dimensional intensity versus 2θ data, *Fit2d* (Hammersley, 2004) has been commonly used. *GSAS* package (Larson and Von Dreele, 2004) and a graphical useful interface *EXPGUI* (Toby, 2001) based on *GSAS* are powerful programs in fitting XRD patterns. To derive unit cell parameters, one can use *CMPR* program (Toby, 2005) to fit the positions of individual peaks and use *UnitCell* program (Holland and Redfern, 1997) to

calculate unit cell parameters from the peak positions. To calculate pressures and derive equation of state parameters based on the XRD results of lattice parameters, I developed programs *Pressure Scale* (Appendix B) and *FitEoS* (Appendix A).

2.4 NUCLEAR RESONANT SCATTERING

Nuclear resonant scattering (NRS) probes the energy levels of the nuclear resonant nuclei, such as ^{57}Fe. Owing to the interaction between electrons, phonons and the nuclei, information about the electrons and phonons can be obtained by studying the properties of nuclei using NRS method. NRS method includes NRIXS and Mössbauer spectroscopy. Conventional Mössbauer experiments are performed in the energy domain (equivalent to velocity) with a radioactive γ-ray source. Synchrotron Mössbauer experiments are carried out in the time domain.

2.4.1 Theoretical Aspects of Nuclear Resonance Scattering

This section describes the theoretical background of nuclear resonance scattering. The experimental aspects and setup are described in chapter 7. Resonance refers to the phenomenon of a large magnitude of oscillation around a certain frequency or energy compared to others in a system. Nuclear resonance occurs when the incident photons have comparable energy to the nuclear transition energy E_R – the energy difference between an excited nuclear state and the ground state. At the resonant energy E_R, absorption of the incident photons by the absorber (sample) is anomalously larger compared to at other energies. In a process involving interactions between the incident particles and a certain type of particle in the studied material, the probability of interaction is described by cross section, which has a unit of barn (1 barn = 10^{-28} m^2). For ^{57}Fe, the cross section at resonance σ_N is 2.56 Mb (e.g., Sturhahn, 2004). Compared to Thomson scattering on electrons (interaction between incident photons and electrons) and photoelectric processes (emission of electrons from matter upon incident photons), the absorption cross section of NRS is large: $\sigma_N / \sigma_T \approx 5700$ and $\sigma_N / \sigma_{pe} \approx 450$ (ibid). Here, σ_T and σ_{pe} refer to the cross sections of Thomson scattering on electrons and the photoelectric process, respectively.

Despite the large cross section of NRS, it is difficult to observe NRS signals experimentally due to the small energy range involved in the NRS process. For ^{57}Fe, the first excited nuclear

state of ^{57}Fe has a very small line width of only Γ = 4.665 neV. Such small energy range of ~ 4.665 neV can not be easily detected by X-ray detectors. On the other hand, as the natural line width of a nuclear transition Γ is inversely related to the mean life time, a narrow line width of Γ = 4.665 neV leads to a relatively long mean life time of τ = 141 ns, which is much longer than the time scale of < 10^{-12} s for electronic scattering. This time difference permits discrimination between the electronic scattering signals and the NRS signals. In experiments, this is realized using time-differentiation electronics. The relatively long life time of the excited state is one of the reasons that make ^{57}Fe a suitable isotope for NRS studies.

2.4.2 Mössbauer Spectroscopy

The related theory of Mössbauer spectroscopy can be found in numerous books and articles (e.g., Frauenfelder, 1962; Bancroft, 1973; McCammon, 2004; Dyer *et al*., 2006). Consider a free nucleus (isolated from other nuclei) with mass M and nuclear transition energy of E_R between an excited state |e> and the ground state |g>. Upon decay from |e> to |g>, a photon is emitted, and the nucleus experiences a recoil with an energy E_{recoil}. E_{recoil} is confined by the energy and momentum conservations and has the following form:

$$E_{recoil} = \frac{E_R^{\,2}}{2Mc^2} \tag{2.3}$$

For ^{57}Fe, E_{recoil} = 1.95 meV, much larger than the natural line width of the nuclear transition energy Γ = 4.665 neV. For resonance to occur, $2E_{recoil}$ needs to be comparable to or smaller than Γ (one E_{recoil} for the energy loss in the source, and another E_{recoil} for the energy loss in the sample). In gas or liquid, the binding between nuclei is weak, and each individual nucleus can be considered as a free nucleus approximately. It is evident that $2E_{recoil}$ is much larger than Γ in gas or liquid hence preventing resonance from happening. In a solid, however, nuclei are bound together and each individual nucleus can no longer be considered as a free nucleus. To calculate the recoil energy in a solid using equation (2.3), the mass of the whole solid, instead of the mass of an individual nucleus, should be used. This leads to a recoil energy that is very small, close to zero. This phenomenon is known as Mössbauer effect.

The probability of recoilless fraction is described by the Lamb-Mössbauer factor f, which is

related to the mean-square deviation of the vibrating atom from its equilibrium position $<\Delta x^2>$ by the following relationship:

$$f = \exp(-<(\Delta x)^2>2\pi/\lambda) = \exp(-<(\Delta x)^2>2\pi E_R/hc) \qquad (2.4)$$

where h is the Planck constant and c is the speed of light. The nuclear absorption cross section σ is related to the intrinsic cross section at resonance σ_N via the Lamb-Mössbauer factor f according to $\sigma \approx \pi/2\, f\, \sigma_N$ (Sturhahn, 2004). For liquid or gas, f is close to 0, and therefore the nuclear absorption cross section at resonance is 0. In other words, nuclear resonance scattering can not be observed in liquid or gas. On other hand, f is a number between 0 and 1 for solid, and the absorption cross section at resonance can be appreciable. From equation (2.4), it is also evident that small nuclear transition energy of E_R is necessary to obtain large Lamb-Mössbauer factor f. The small nuclear transition energy of 14.4 keV for ^{57}Fe also makes ^{57}Fe a suitable isotope for Mössbauer studies.

In CMS method, a spectrum of transmission intensity is recorded with energy as the x axis. A Mössbauer setup includes a radioactive γ–ray source, a Mössbauer drive that moves the source back and forth, the sample (also referred as the absorber) and data processing system. The radioactive source emits γ–rays with energies similar to the nuclear transition energy (energies). The motion of the source modifies the emitted γ–ray according to Doppler shift. The energy shift ΔE is related to the moving speed of the source u by $\Delta E = (u/c)\, E_R$, where c is the speed of light. For ^{57}Fe, 1 mm/s corresponds to 48.07 neV. When the energy of γ-rays matches the nuclear transition energy E_R, resonant absorption occurs and an absorption line is observed at this energy in the Mössbauer spectrum.

When both the excited nuclear level and ground level are degenerate, there is only one transition energy E_R hence only one absorption line is observed (Fig. 2.8). With the presence of hyperfine interaction, which is the interaction between nucleus and the electronic environment, energies of the ground level and the excited level are modified and the degeneracy of these levels may be removed. The hyperfine interactions can be characterized using mainly three parameters: the isomer shift (I.S.) with unit of mm/s, the quadrupole splitting (Q.S.) with unit of mm/s and the magnetic hyperfine field (H.F.) with unit of Tesla (or equivalent units such as Gauss).

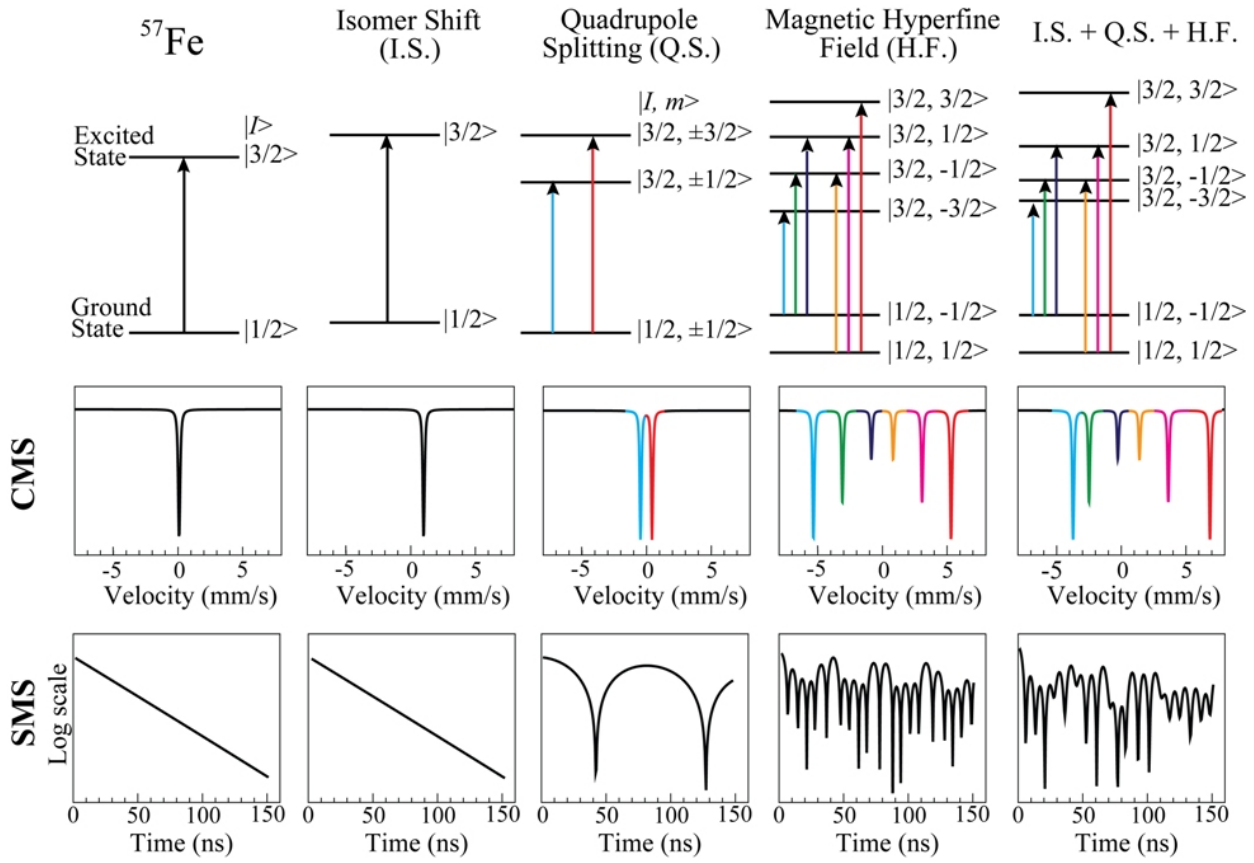

Fig. 2.8. Illustration of ^{57}Fe nuclear energy levels and simulated conventional and synchrotron Mössbauer spectra with presence of isomer shift, quadrupole splitting and magnetic hyperfine field. Values used in simulations are: I.S. = 1.0 mm/s, Q.S. = 1.0 mm/s; H.F. = 33.0 Tesla; effective thickness of sample = 1.

Electric monopole interaction between the nuclear charge and the finite density of s-electrons at the nucleus causes a shift in the nuclear transition energy E_R (Fig. 2.8). This shift is called the isomer shift. Isomer shift is a relative value. For Fe-bearing materials, the isomer shift of α-Fe under ambient conditions is conventionally chosen to be the reference zero point. The isomer shift of ^{57}Fe increases when the s-electron density at the nucleus decreases since the excited ^{57}Fe nucleus has a smaller radius compared to the ground state (e.g., Bancroft, 1973).

For a nucleus with spin quantum number of > 1/2, the nuclear charge distribution is not spherical. The magnitude of the charge deformation is described by quadrupole moment. The interaction between the quadrupole moment and the electric field gradient at the nucleus created by the surrounding electrons give rise to quadrupole splitting. For ^{57}Fe, the excited level |e> splits into two levels with the presence of quadrupole splitting while the ground state |g> remains

degenerate (Fig. 2.8). The corresponding Mössbauer spectrum therefore has two absorption lines.

With a magnetic hyperfine field at the nucleus, the degeneracy of nuclear levels is fully removed. For ^{57}Fe, the excited level |e> with a spin of 3/2 splits into four sublevels and the ground level |g> with a spin of 1/2 splits into two sublevels (Fig. 2.8). Here, the four sublevels of the excited state are denoted as $|I, m>$, $I = 3/2$, $m = -3/2, -1/2, 1/2, 3/2$, and the two sublevels of the ground state are denoted as $|I, m>$, $I = 1/2$, $m = -1/2, 1/2$. The transition between the ground state and the first excited state generally follows the magnetic dipole selection rule, i.e., transition only occurs between two levels with $\Delta m = \pm 1, 0$. Therefore, typically only six different transitions are allowed and the Mössbauer spectrum consists of six absorption lines (Fig. 2.8). In rare occasions, when the orientations of nuclear magnetic moment and the nuclear magnetic field are not parallel, $\Delta m = \pm 2$ transitions are no longer forbidden and eight-line Mössbauer spectra can be observed (Dyar *et al*., 2006, and references therein).

By measuring the nuclear transition energy (energies), CMS method can obtain information about the surrounding electronic environments. The same information can be acquired from a different approach – the synchrotron Mössbauer spectroscopy (SMS). SMS is also known as nuclear forward scattering, since only the photons in the forward direction (along X-ray direction, opposite side of the sample compared to the source) are measured. SMS measures the intensity of delayed photons as a function of time following a nuclear excitement and de-excitement process. With sufficient bandwidth for the incident X-ray photons, different nuclear transitions can be excited simultaneously. For ^{57}Fe, the 1 meV energy bandwidth at beamline 3-ID of the APS is sufficient for SMS measurement since the difference between the maximum and minimum nuclear transition energies is usually less than 0.5 μeV. Upon excitation using a short-pulsed X-ray, all nuclear transitions are excited in phase. Shortly afterwards, de-excitation begins. As different nuclear transitions have different energies (equivalent to frequencies), their phases change over time at slightly different rates. The differences in phase lead to interference in the time domain.

Interpretation of SMS data is less straightforward compared to CMS data. However, SMS data collection time is usually much shorter than CMS data collection time, owing to the high flux of X-rays at synchrotron facilities. SMS also enables Mössbauer studies on parentless

isotopes. Moreover, SMS has the advantage of being able to probe small samples in a DAC, as X-rays in synchrotron facilities can be focused to a small size of a few microns. On the other hand, the signal to noise ratio in CMS measurements decreases significantly with decreased diamond culet sizes in a DAC experiment. This poses a limit on the achievable pressure range in CMS method.

As both SMS and CMS methods have pros and cons and they probe the same physics from different aspects, they are complimentary to each other. A combination of both methods is powerful in placing stringent constraints on the fitted hyperfine parameters. In this thesis work, both SMS and CMS data were fitted using the commonly-used program *CONUSS* (Sturhahn, 2000).

2.4.3 Nuclear Resonant Inelastic X-ray Scattering

During the interaction between a solid material (with a nuclear resonant energy E_R) and incident photons with energies close to E_R, some of the photons are absorbed and reemitted in the forward direction. These phonons are measured in SMS method introduced in the previous section. The rest photons interact with the phonons (lattice vibrations) of the material, and the reemitted photons from this process are along all directions. This is an inelastic process as the energies of the photons are modified in this process. By measuring the phonon excitation and annihilation probability at various energies, the information of phonon density of state projected along the X-ray direction can be extracted. This method is known as the nuclear resonant inelastic X-ray scattering (NRIXS). Description on this technique can be found in a previous article by Sturhahn (2004).

From an NRIXS spectrum $S(E)$, which is the phonon excitation and annihilation probability as a function of energy, several parameters can be derived by simply calculating the moments of the NRIXS spectrum. The first moment gives the nuclear recoil energy (Sturhahn, 2004, and references therein):

$$E_{\text{recoil}} = M_1 = \int_{-\infty}^{+\infty} ES(E)\mathrm{d}E \tag{2.5}$$

The n-th order centered moment of a spectrum $S(E)$ is defined as:

$$M_n = \int_{-\infty}^{+\infty} (E - E_{\text{recoil}})^n S(E) \mathrm{d}E \tag{2.6}$$

2nd-order centered moment is related to kinetic energy E_{kinetic} along the X-ray beam via the following relationship (ibid):

$$E_{\text{kinetic}} = \frac{M_2}{4E_{\text{recoil}}} \tag{2.7}$$

From the 3rd-order centered moment, mean force constant D, which is a measure of the binding strength between atoms in a crystal, can be estimated according to the following relationship (ibid):

$$D = 2\hbar^2 c^2 \frac{{E_{\text{R}}}^2}{{E_{\text{recoil}}}^2} \frac{1}{M_3} \tag{2.8}$$

where is the $\hbar$ is the reduced Planck constant (Dirac constant).

It should be pointed out that these parameters only represent the contributions from the resonant isotope and projected along the incident X-ray direction. It should also be noted that the calculation of these parameters does not depend on the vibration model of the material. With assumption of a vibration model, phonon density of states (PDoS) can be extracted. In this study, PDoS is extracted using the *PHOENIX* program (Sturhahn, 2000), in which a quasi-harmonic vibration model is used.

From the PDoS, Debye sound velocity (V_{D}) can be derived from parabolic fittings of the low-frequency PDoS on a basis of Debye-like low-frequency dynamics, following the relation

$$\rho {V_{\text{D}}}^3 = \frac{3\tilde{M}}{2\pi^2\hbar^3} \frac{E^2}{g(E)} \tag{2.9}$$

where ρ is density, $g(E)$ is the PDoS, $\hbar$ is the reduced Planck constant and $\tilde{M}$ is the atomic mass of ^{57}Fe, equivalent to equation (3.25) in a book by Poirier (2000) (see also Kieffer, 1979). The term '3' in the numerator arises from the existence of three acoustic modes: the longitudinal mode and the two shear modes. This parabolic relationship, the central feature of Debye model,

is valid for any crystal while frequency reaches the limit of zero ($\omega \rightarrow 0$) (Kieffer, 1979). Combining V_D and elastic parameters, compressional sound velocities V_P and shear sound velocities V_S can be derived (e.g., Mao *et al*., 2001). More information on this procedure will be introduced in chapter 4.

Chapter 3

Synthesis and Characterization of Fe_3C Samples

3.1 INTRODUCTION

In natural iron, the abundance of Mössbauer isotope ^{57}Fe is only ~ 2 %. As NRIXS is a low count rate method, usage of ^{57}Fe-enriched samples is beneficial, and even necessary at high pressures.

Fe_3C has orthorhombic structure (e.g., Fasiska and Jeffrey, 1965). Its structure can be approximately described as hexagonal close-packed arrangement of iron atoms with carbon atoms distributed in the largest interstitial sites (Fig. 3.1) (ibid). The hexagonal close-packed iron atoms are stacked along the *b* axis (the long axis) (e.g., Fasiska and Jeffrey, 1965; Jiang *et al*., 2008; Ono and Mibe, 2010).

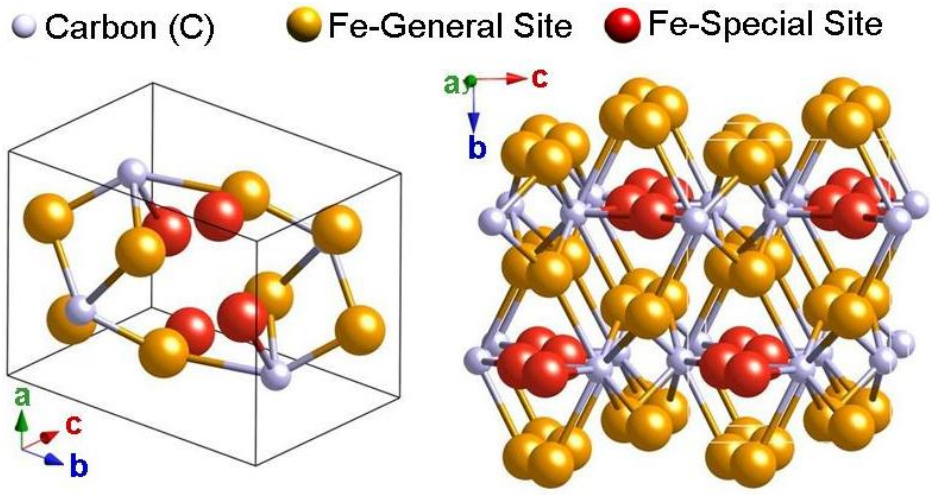

Fig. 3.1. Structure of Fe_3C. The left figure shows the atoms in a unit cell. The right figure shows the pleated structure along the *b* axis. Figures are generated using *CrystalMaker* software.

At ~ 5 GPa, experimental results (e.g., Chabot *et al*., 2008; Nakajima *et al*., 2009; Lord *et al*., 2009) and thermodynamics calculation results (e.g., Wood, 1993) suggest that Fe_3C is stable within a temperature range of 1400 K to 1600 K around a stoichiometric ratio of Fe:C = 3:1 (Fig. 3.2). At higher pressures, another iron-carbon compound, i.e., Fe_7C_3, has been observed in addition to Fe_3C (Fig. 3.2). At around 1 mega-bar (100 GPa), the phase diagrams of iron-carbon binary system were investigated using X-ray radiographic imaging method, in which the composition is inferred from the brightness contrast of X-ray radiographic images (Lord *et al*., 2009). Iron-carbon phase diagrams at this pressure range (~ 100 GPa) based on conventional methods, such as electron probe analysis, are not available yet.

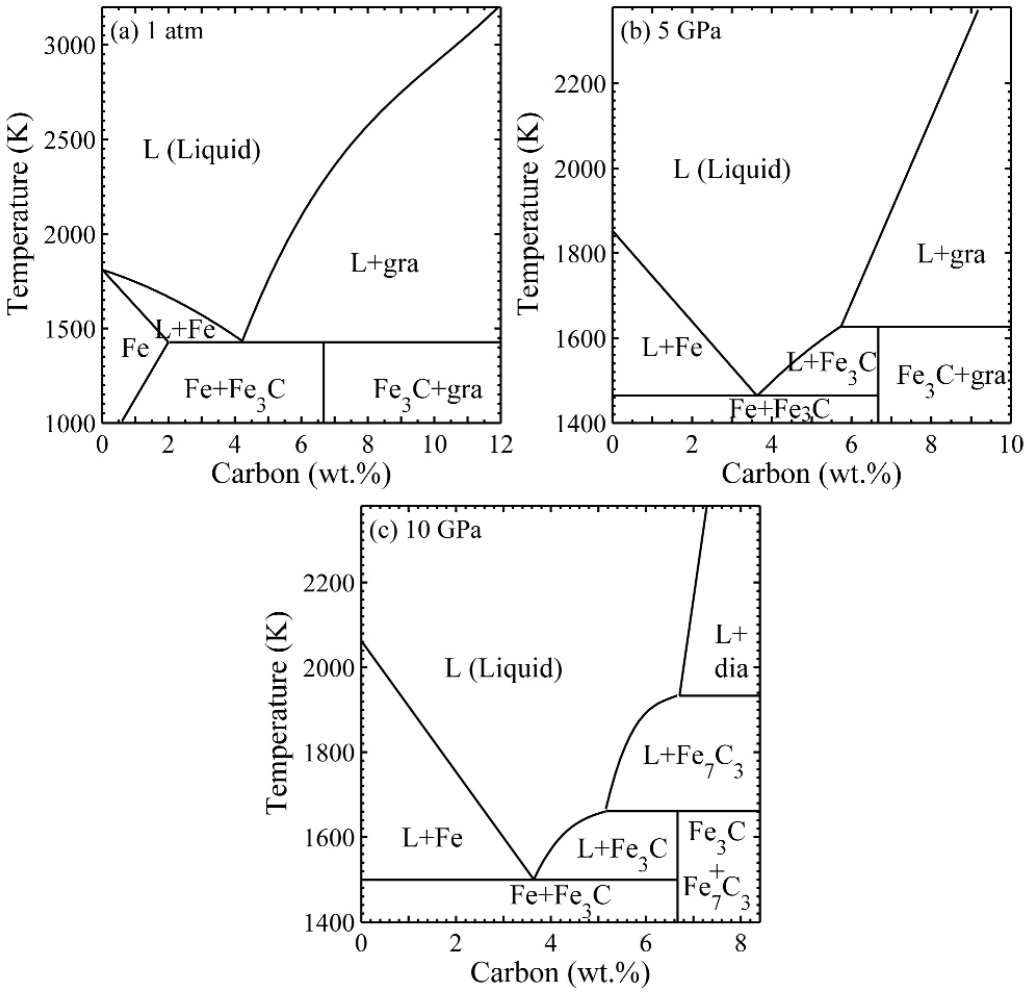

Fig. 3.2. Simplified phase diagrams of iron-carbon binary system at ambient pressure (1 atm) (modified after Chipman, 1972), 5 GPa (Nakajima *et al*., 2009, and references therein) and 10 GPa (ibid). Abbreviations: dia – diamond; gra – graphite.

3.2 SAMPLE SYNTHESIS

Table 3.1 Summary of Fe_3C sample synthesis conditions and run products.

Run	P (GPa)	T (K)	Duration (hours)	Starting material	Iron-carbon mixing method	[#]Run product
PC01	2	1273	72	Fe:C = 3.02:1	Ground in acetone for ~ 10 minutes	Fe_3C, FeO
PC02[$]	2	1273	72	Fe:C = 3.03:1	Ground in acetone for ~ 10 minutes	Fe_3C, Fe, FeO
PC03	2	1473	72	Fe:C = 2.83:1	Ground in air for 1 hour	Fe_3C
PC04	1.5	1423	1	Fe:C = 1.91:1	Ground in ethanol for 30 minutes, heated in vacuum at > 100 °C and then ground for 30 minutes in air	Fe_3C
085	5	1423	1	Fe:C = 3.02:1	Shaken and tumbled for 10 minutes	Fe_3C, FeO
086	5	1423	2	Fe:C = 3.00:1	Ground in carbon-coated mortar for 10 minutes	Fe_3C, FeO
087	5	1423	3	Fe:C = 3.02:1	Shaken and tumbled for 5 hours	Fe_3C , FeO
090[$]	3	1373	17	Fe:C = 2.92:1	Ground in carbon-coated mortar for 10 minutes	Fe_3C
091[$]	2	1373	0.5	Fe:C = 2.99:1	Shaken and tumbled for > 5 hours	Fe_3C, Fe, FeO
092[$!]	2	1373	48	Fe:C = 3.00:1	Ground	Fe_3C, Fe, FeO
093[†]	2	1373	4	Fe:C = 2.99:1	Shaken and tumbled for > 5 hours	Fe_3C, Fe, FeO
094[†]	2	1373	7	Fe:C ~ 2.76:1	Shaken and tumbled for > 5 hours	Fe_3C, Fe, FeO
095[†]	2	1373	6	Fe:C ~ 2.22:1	Shaken and tumbled for > 5 hours	Fe_3C, Fe, FeO

Shaded runs represent the usage of ^{57}Fe-enriched iron. 'PC' indicates a piston-cylinder run. Otherwise, a multi-anvil press was used. All runs are listed in temporal order.

[#] Only the iron-bearing phases are listed. Other possible components, such as graphite, may exist, especially when the starting material contained excess carbon (C:Fe > 1:3).

[$] Starting material of ~ 94.45 % ^{57}Fe-enriched iron purchased from Cambridge Isotope Laboratories Inc. (# FLM-1812-100) was used.

[!] Graphite capsule was used as the sample chamber in run 092 instead of MgO.

† Starting material of ^{57}Fe-enriched (> 90 % enrichment) iron fine powder was made from a piece of ^{57}Fe foil at Argonne National Laboratory by dissolving the foil into hydrochloric acid and nitric acid to form hydroxide, then oxidizing it to Fe_2O_3, and eventually reducing it in H_2 gas to powder with an average grain size of < 1 μm.

In this study, Fe_3C samples were synthesized from iron and graphite powders at high pressures and high temperatures, following the method by Li *et al.* (2002). MgO sample chambers were used in most runs, except in run 092 where graphite sample chamber was used instead. Two types of high pressure presses, piston-cylinder press and multi-anvil press, were used. Schematics of the sample assemblies are shown in Figs. 2.6 and 2.7 in the previous chapter. A total of thirteen runs were carried out. The run conditions and run products are listed in Table 3.1. Most of the runs were carried out at the University of Illinois, except run 092 which was performed at the Geophysical Laboratory at Carnegie institution of Washington, D.C.

In most of the early runs, natural iron in fine powder form (Alfa Aesar, #00170, 99.9 % purity metal basis) was used as one of the starting materials. In runs PC02, 090, 091 and 092, ^{57}Fe-enriched iron (~ 94.45 % enrichment) purchased from Cambridge Isotope Laboratories Inc. (# FLM-1812-100) was used. This starting material of ^{57}Fe-enriched iron was ground to thin flakes with a diameter of ~ 4 μm on average from an initial grain size of ~ 100 μm in diameter (grain size was estimated based on visual observation under microscope). In the rest of the runs where ^{57}Fe-enriched iron was used, i.e., #093, #094 and #095, fine powders of ^{57}Fe-enriched iron (> 90 % enrichment) were made from a piece of ^{57}Fe foil at Argonne National Laboratory by dissolving the foil into hydrochloric acid and nitric acid to form hydroxide, then oxidizing it to Fe_2O_3, and eventually reducing it in H_2 gas to powder with an average grain size of < 1 μm. The starting material of graphite powder with an average particle size of ~ 1 μm was ground from graphite rods in early runs. In later runs (run 087 and runs afterwards), graphite powder with average particle size of < 1 μm from Sigma-Aldrich (#282863) was used.

3.3 SAMPLE CHARACTERIZATION

To examine the purity and structure of synthesized Fe_3C samples, I conducted conventional Mössbauer spectroscopy (CMS) at Sector 3, synchrotron Mössbauer spectroscopy (SMS) at beamlines 16-ID-D and 3-ID-B at the APS, and high-resolution X-ray diffraction (XRD)

measurements at beamline 11-BM-B of the APS. For the SMS data, only the data collected at beamline 16-ID-D are shown in this chapter. The SMS data collected at beamline 3-ID-B are mainly at high pressures, and they will be shown in chapters 4 and 5. The samples were ground into small grains with an average particle size of ~ 2 μm in diameter for characterization measurements.

3.3.1. Conventional Mössbauer Spectroscopy

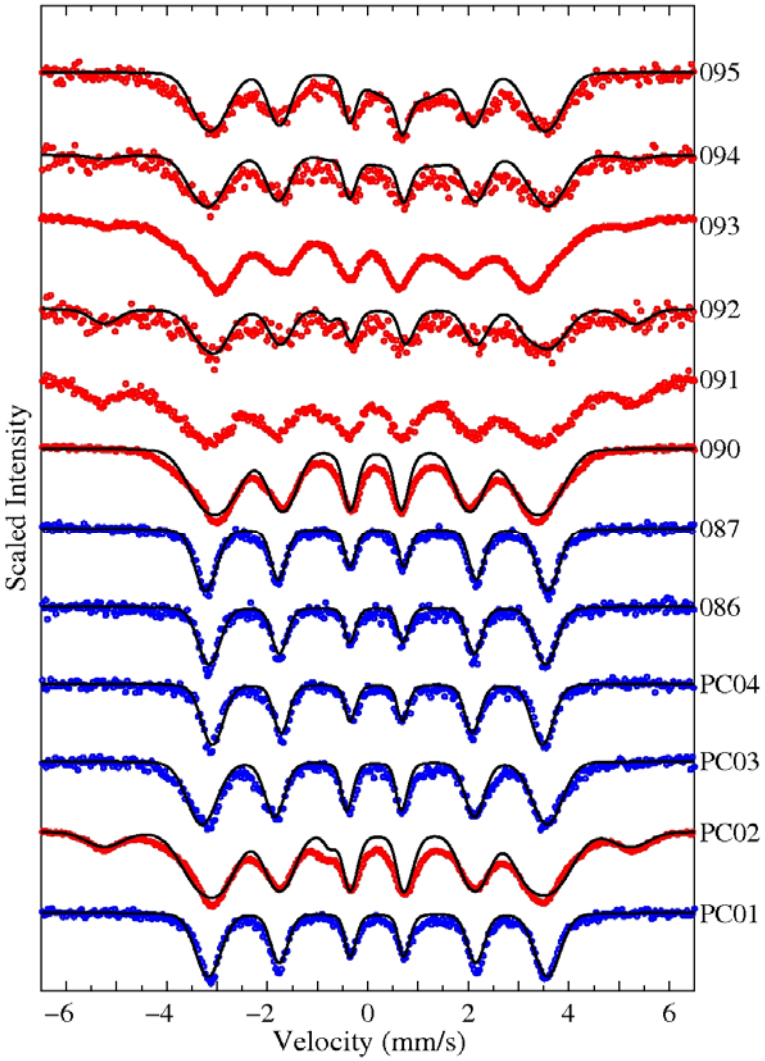

Fig. 3.3. Conventional Mössbauer spectra of synthesized Fe_3C samples at ambient conditions. The velocity scale is set in a conventional way that the isomer shift of α-iron is zero. Fe_3C samples with natural iron are shown in blue. ^{57}Fe-enriched Fe_3C samples are shown in red. The solid black lines represent fittings using program *CONUSS* (Sturhahn, 2000). The fitting parameters are in Table 3.2.

Table 3.2. Magnetic hyperfine filed fitting parameters used in Fig. 3.3.

	Site 1 (Fe_3C)				Site 2 (α-Fe)				Site 3 (FeO)		
Run	%	HF (Tesla)	FWHM (Tesla)	IS (mm/s)	%	HF (Tesla)	FWHM (Tesla)	%	IS (mm/s)	FWHM (mm/s)	QS (mm/s)
PC01	100	21.0	3	0.16	-	-	-	-	-	-	-
PC02	88	20.8	5	0.15	12	33	4	-	-	-	-
PC03	100	21.3	4	0.10	-	-	-	-	-	-	-
PC04	100	20.4	3	0.15	-	-	-	-	-	-	-
086	100	20.8	3	0.11	-	-	-	-	-	-	-
087	100	21.1	3	0.11	-	-	-	-	-	-	-
090	100	20.1	4	0.13	-	-	-	-	-	-	-
092	80	20.9	4	0.11	20	33	4	-	-	-	-
094	89	21.1	4	0.15	4	33	3	7	0.7	0.8	0.5
095	90	20.7	4	0.15	-	-	-	10	0.7	0.8	0.5

Isomer shift is relative to α-Fe. Shaded areas represent runs with ^{57}Fe-enriched iron. Abbreviations: HF – hyperfine filed; IS – isomer shift; QS – quadruple splitting; FWHM – full width at half maximum.

Conventional Mössbauer spectra of the synthesized Fe_3C samples (Fig. 3.3) were collected at sector 3 of the APS. ^{57}Co radioactive sources embedded in Rhodium matrixes were used. For the measurement on sample 093 (sample from run 093), I used a point source with a surface area of $\sim 0.5 \times 0.5$ mm^2. In measurements on other samples, I used an area source with a surface area of $\sim 5 \times 5$ mm^2.

Data collection time for a CMS spectrum in this study ranges from a few hours to one week, depending on the concentration of ^{57}Fe isotope in sample, the thickness of sample and the radiation strength of the source. The powder sample of Fe_3C from each run was spread out as evenly as possible on an area of $\sim 10 \times 10$ mm^2 on a tape. Compared to a thin sample, a thick sample shortens data collection times while increases line width in the Mössbauer spectrum. In this study, I kept the sample effective thickness to be in the range of 2 to 10. For ^{57}Fe-enriched samples, small quantities of Fe_3C samples were mixed with baking flour in order to maintain small effective thickness while keeping the sample thickness as even as possible. The effective thickness is a dimensionless parameter (e.g., McCammon, 2004, and references therein), defined as:

$$t = \sigma_N f n \quad (3.1)$$

where σ_N is the cross section at nuclear resonance for the Mössbauer transition, f is the Lamb-Mössbauer factor of the sample and n is the number of ^{57}Fe atoms per cm^2. For ~ 100 % ^{57}Fe-enriched Fe_3C, an effective thickness of 1 corresponds to an actual sample thickness of ~ 0.1 μm.

Compositions of the run products inferred from these CMS and XRD data (see section 3.3.3) are summarized in Table 3.1. These results confirm that the major phase in all run products is Fe_3C. The conventional Mössbauer spectrum of Fe_3C (Fig. 3.3) comprises of a characteristic sextet with outer lines at ~ + 3.6 mm/s and – 3.1 mm/s, corresponding to a magnetic hyperfine field of ~ 20.5 Tesla (205 Kilogauss) and an isomer shift (relative to α-Fe) of 0.1 to 0.2 mm/s (e.g., Ron and Mathalone, 1971; Bauer-Grosse *et al*., 1996; David *et al*., 2006).

These results indicate that the compositions of the run products may be related to the size of iron powder used in the starting material. In runs PC01, PC02, PC04, 086 and 087, where natural iron fine powders (< 1 μm in diameter) were used, Fe_3C is the only noticeable Fe-bearing phase in the run products based on the CMS results (Fig. 3.3). For runs PC02, 091 and 092, I used iron ^{57}Fe-enriched iron flakes with an average diameter of ~ 4 μm ground from iron particles with an initial diameter of ~ 100 μm. Thse CMS results reveal that the run products contain appreciable amounts of excess α-Fe, as shown by a sextet with outer lines at ~ +/- 4.5 mm/s (Fig. 3.3), corresponding to a magnetic hyperfine field of 33 Tesla matching that of iron (e.g., Dyer *et al*., 2006, and references therein). To overcome the problem of excess iron in the run product, I used more graphite in run 090 (Fe:C = 2.92:1). In the run product, only Fe_3C phase was detected. In later runs 093, 094 and 095, I used a fine powder of ^{57}Fe-enriched iron converted from an iron foil at Argonne National Laboratory (section 3.2). The amount of excess iron is reduced compared to runs PC02, 091 and 092, although it is still detectable.

I used *CONUSS* program (Sturhahn, 2000) to fit the CMS data. The fitting results that can reasonably represent the measured data are shown in Fig. 3.3. The fitting parameters are listed in Table 3.2. The spectra from runs PC01, PC03, PC04, 086, 087 and 090 were fitted using only one site with magnetic hyperfine field of ~ 20 Tesla and isomer shift of 0.10 mm/s to 0.16 mm/s, in accordance with the reported values of Fe_3C in previous studies (e.g., Ron and Mathalone, 1971; Bauer-Grosse *et al*., 1996; David *et al*., 2006). The spectra from runs PC02 and 092 were

fitted using two sites. The dominant site can be explained as Fe_3C. The minor site has a magnetic hyperfine field value of ~ 33 Tesla and an isomer shift value of 0, consistent with the known values of α-Fe (e.g., Dyar *et al*., 2006, and references therein). For the spectra on samples 094 and 095, another site with isomer shift of ~ 0.7 mm/s and quadruple splitting of ~ 0.5 mm/s was also included in the fitting. This site has similar values to those of FeO (wüstite) (e.g., Dyer *et al*., 2006, and references therein). The interpretation of this site as FeO is consistent with the XRD results (see section 3.3.3).

In a Mössbauer measurement with infinitely thin source and absorber (sample), the minimum line width is twice of the natural line width (e.g., McCammon, 2004). For ^{57}Fe, this is 0.194 mm/s. In practice, the line width may be larger due to finite sample thickness, instrumental broadening and distribution of hyperfine parameters. In this study, the Fe_3C samples with natural iron have line widths of 0.3 to 0.7 mm/s, small enough that the six absorption lines do not overlap. In ^{57}Fe-enriched samples, broader lines (> 1 mm/s FWHM) were observed. The instrumental broadening in this study is no more than 0.6 mm/s, based on measurements on α–Fe foil standards. By using various samples with different thicknesses, the possibility of thickness-induced broadening is ruled out. Therefore, the broad line widths from these Fe_3C samples is most likely due to distributions in hyperfine parameters. The nature and cause of the hyperfine parameter distributions are not clear yet.

3.3.2. Synchrotron Mössbauer Spectroscopy

SMS data collected at the undulator beamline 16-ID-D of the APS are shown in Fig. 3.4. In this experiment, samples were prepared the same way as in the CMS measurements (see the previous section). The incident X-ray beam was focused to a size of ~ 35 (vertical) × 50 (horizontal) μm^2 in this study. The energy resolution was ~ 2 meV (Shen *et al*., 2008). Data collection time for each spectrum ranged from ~ 0.5 to 2 hours.

Fitting results that can reasonably represent the data are shown in Fig. 3.4 and Table 3.3. The sample compositions deduced from the fittings are consistent with the CMS results. The fitting results show good match to the measured SMS data in terms of quantum beat frequencies, and small mismatches in terms of intensity. The intensity mismatches are mostly like due to the unaccounted distributions in isomer shift, quadruple splitting, thickness and possible preferred

orientation in the samples.

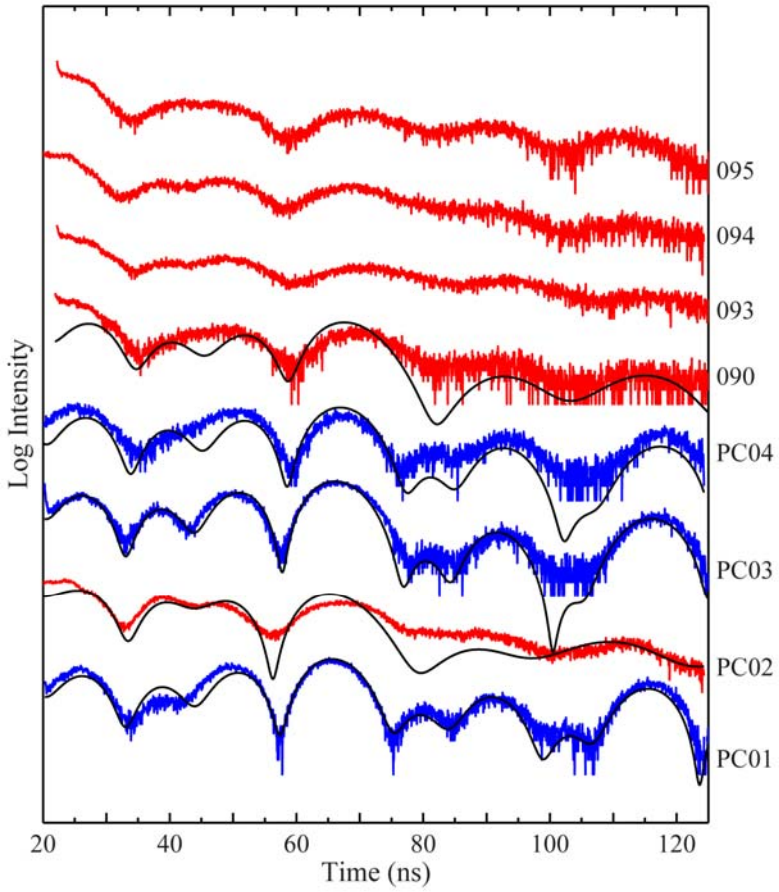

Fig. 3.4. Ambient-condition synchrotron Mössbauer spectra of synthesized Fe_3C samples collected at beamline 16-ID-D of the APS. SMS data of ^{57}Fe-enriched Fe_3C samples are shown in red. The solid black lines represent fittings using *CONUSS* program (Sturhahn, 2000). The fitting parameters are listed in Table 3.3.

Table 3.3. Magnetic hyperfine fitting parameters used in Fig. 3.4.

Run	Site 1 (Fe_3C)				Site 2 (Fe)				
	%	HF (Tesla)	FWHM (Tesla)	QS (mm/s)	%	HF (Tesla)	FWHM (Tesla)	IS[#] (mm/s)	QS (mm/s)
PC01	100	20.6	2	0	-	-	-	-	-
PC02[$]	87	20.6	4	0	13	33	7	-0.1	0
PC03	100	20.3	2	0	-	-	-	-	-
PC04	100	20.1	3	0	-	-	-	-	-
090	100	20.1	4	0	-	-	-	-	-

[$] Isomer shift is relative to site 1.

3.3.3 High-resolution X-ray Diffraction

High-resolution XRD measurements were carried out at beamline 11-BM-B of the APS (http://11bm.xor.aps.anl.gov/). X-ray beams with wavelength (λ) of 0.4011 Å was used in the measurements in March 2008 and X-ray beam with λ=0.4142 Å was used in July 2008. The beam size was 1.5 mm (horizontal) × 0.5 mm (vertical). Twelve independent analyzers were used to collect high resolution data. Each sample was placed inside a Kapton capillary tube which was mounted onto a base (Fig. 3.5). With an incident X-ray wavelength of ~ 0.4 Å, the major XRD peak from Kapton is at $2\theta \sim 5°$ ($d \sim 5$ Å), far away from the XRD signals from the samples in this study. The sample assembly, including the base, the Kapton capillary and sample, can be easily mounted onto and removed from the sample holding tray through magnetic forces. A robotic arm was used to pick up the sample, mount the sample along the X-ray beam and change samples automatically. With large beam size and high speed sample rotation, effect of sample preferred orientation on the XRD patterns is effectively removed. The data collection time was typically one hour for each sample.

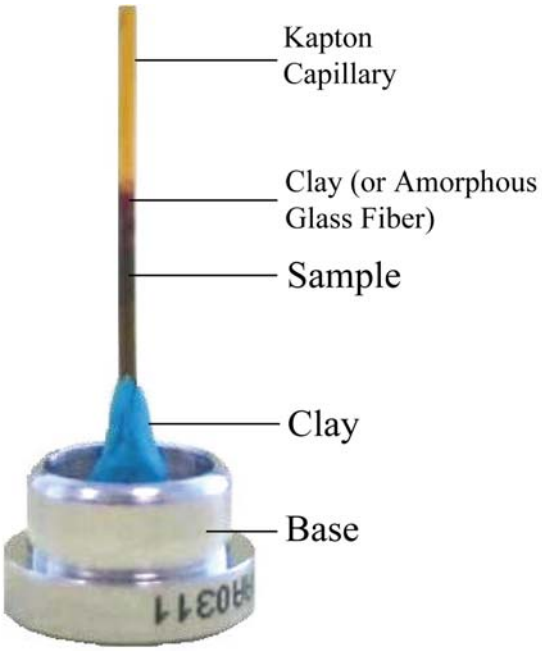

Fig. 3.5. Sample assembly in X-ray diffraction measurements at beamline 11-BM-B of the APS.

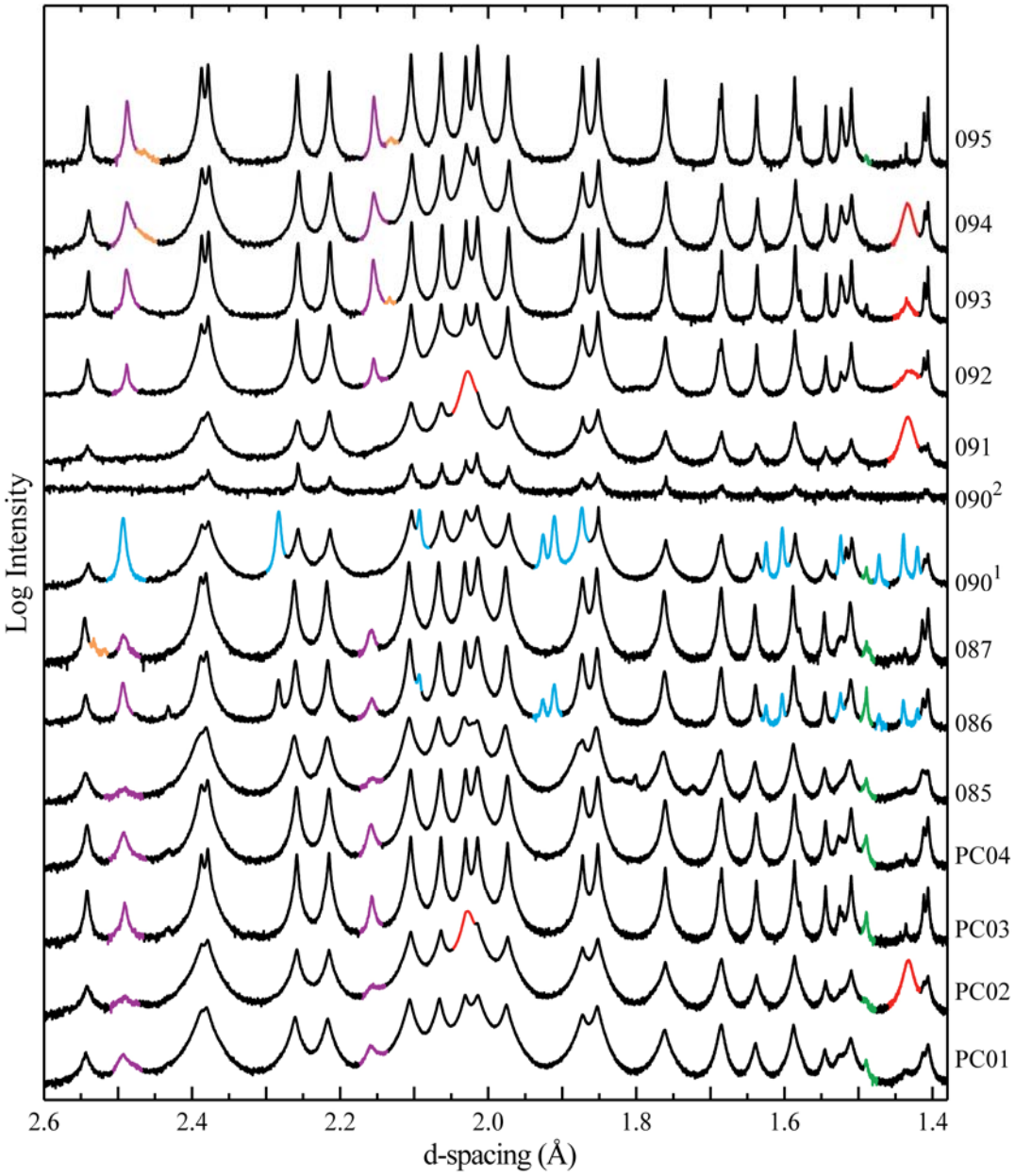

Fig. 3.6. X-ray diffraction data collected at beamline 11-BM-B of the APS on synthetic Fe_3C samples plotted in log scale. The superscript '[1]' in 090^1 denotes that clay was used to seal the capillary in which sample was contained; the superscript '[2]' denotes that amorphous glass fiber was used instead of clay. The high background in 090^2 is due to the small quantity of sample (sample area < X-ray beam size). Color notations of impurity phases: red – metallic iron; purple – FeO; blue – calcite (in clay); green – MgO (sample chamber); orange – unidentified peaks. When diffraction peaks from various phases overlap, only the dominant phase is marked. See Figs. 3.8 – 3.12 for the diffraction peaks from individual phases.

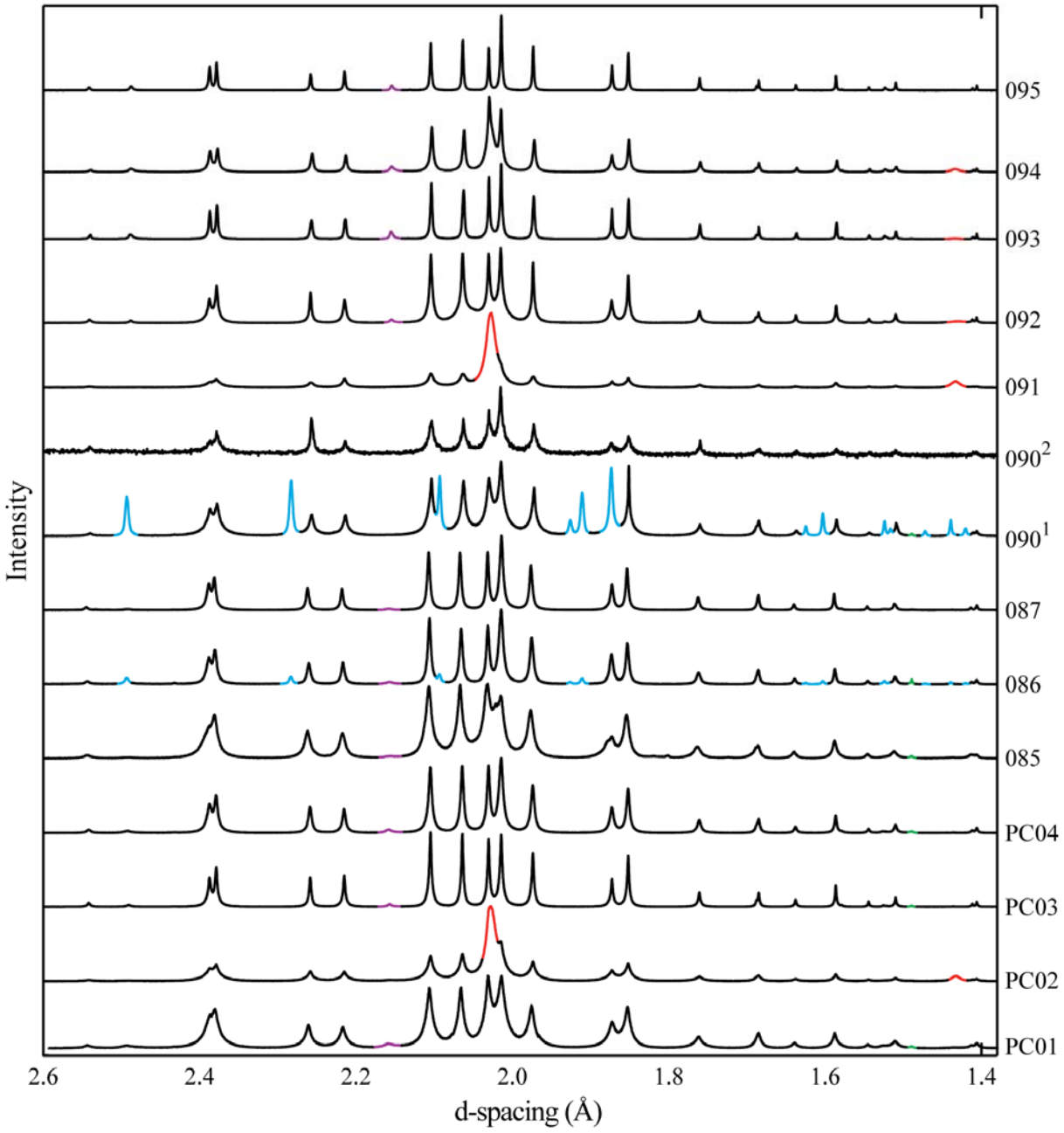

Fig. 3.7. X-ray diffraction data collected at beamline 11-BM-B of the APS on synthetic Fe_3C samples plotted in linear scale. The color notations are the same as in the previous figure.

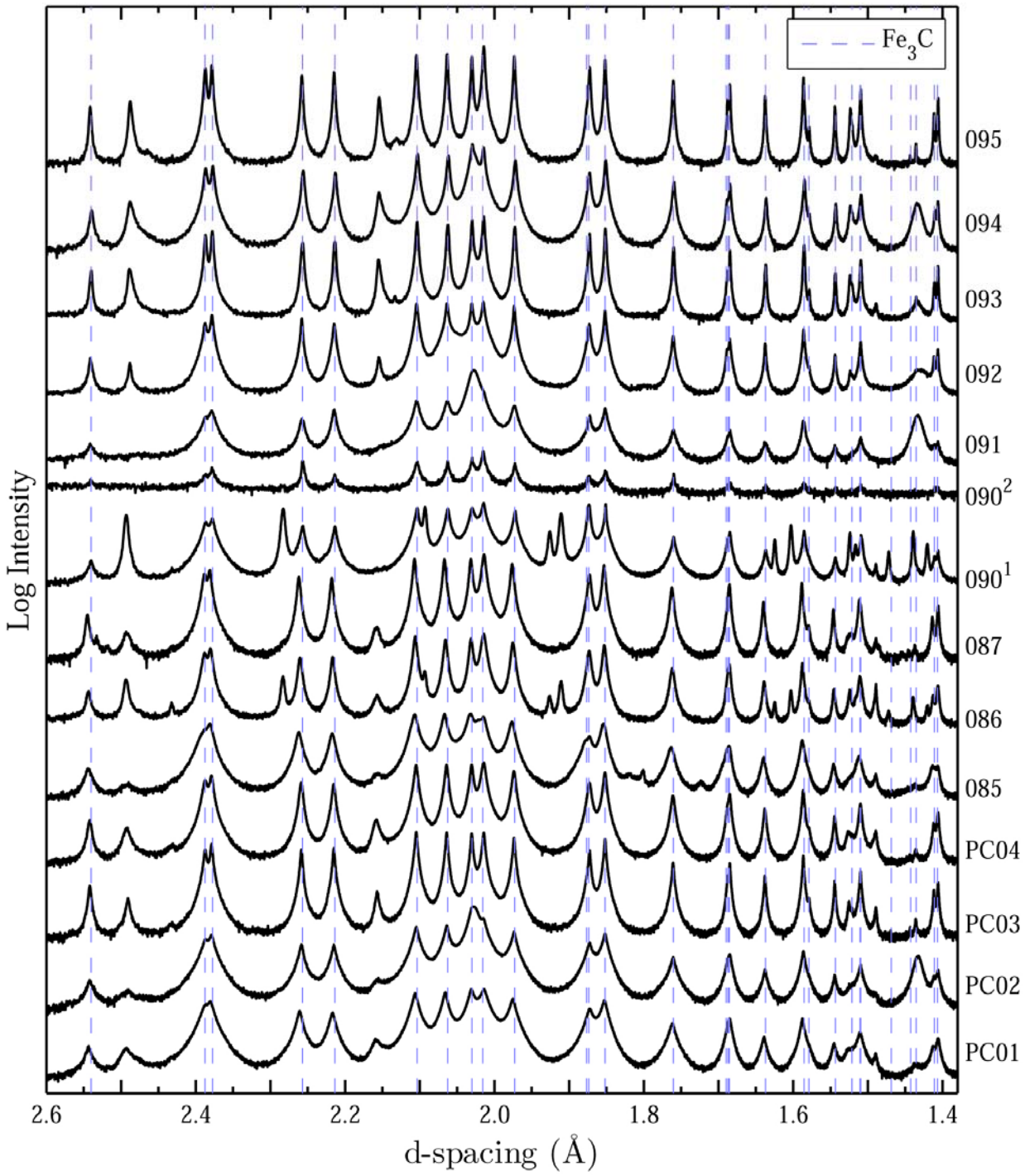

Fig. 3.8. X-ray diffraction data with only the diffraction peaks from Fe_3C marked.

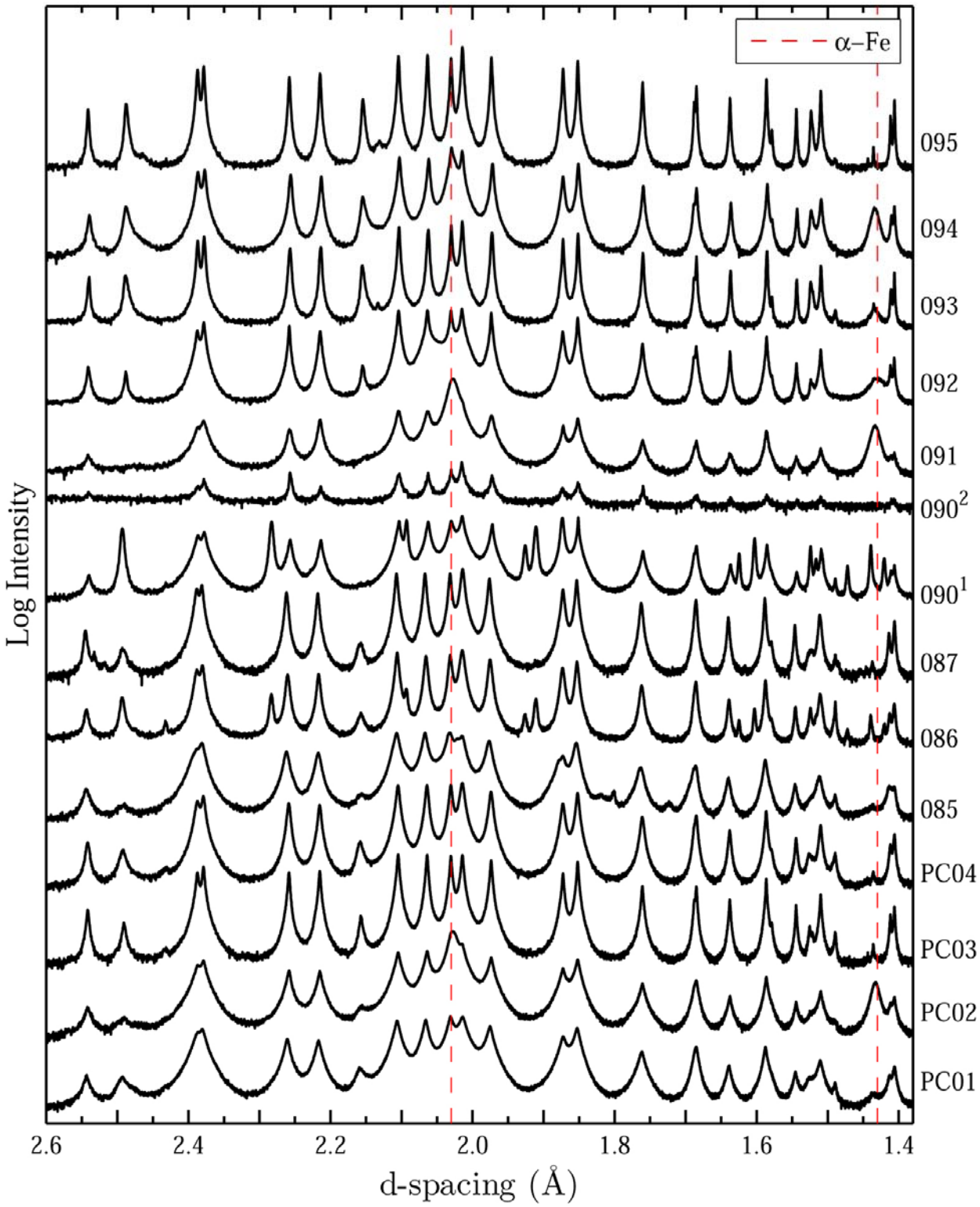

Fig. 3.9. X-ray diffraction data with only the diffraction peaks from α-Fe (metallic iron) marked.

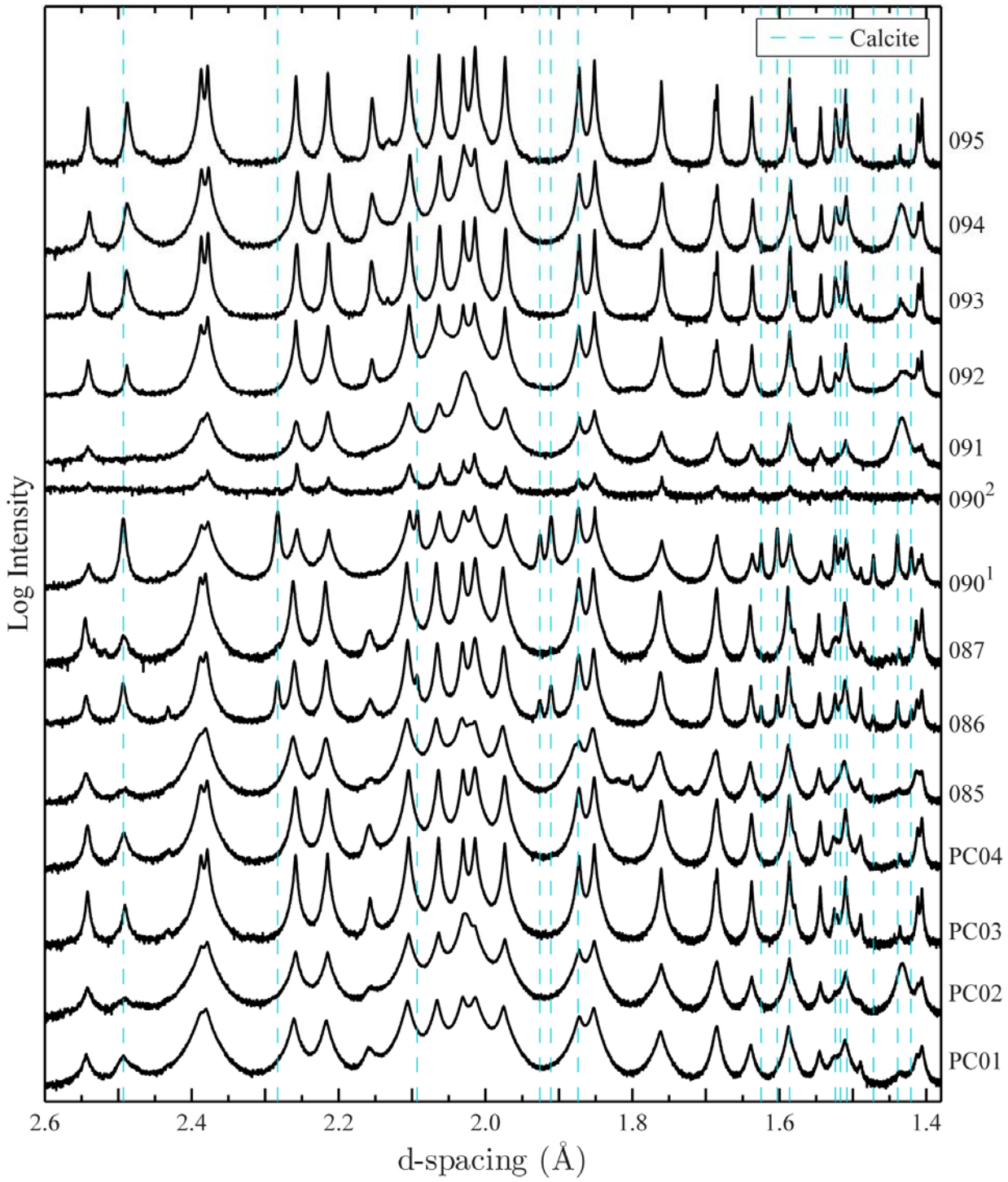

Fig. 3.10. X-ray diffraction data with only the diffraction peaks from calcite marked. The calcite phase is introduced during the diffraction measurement from the capillary sealing material clay.

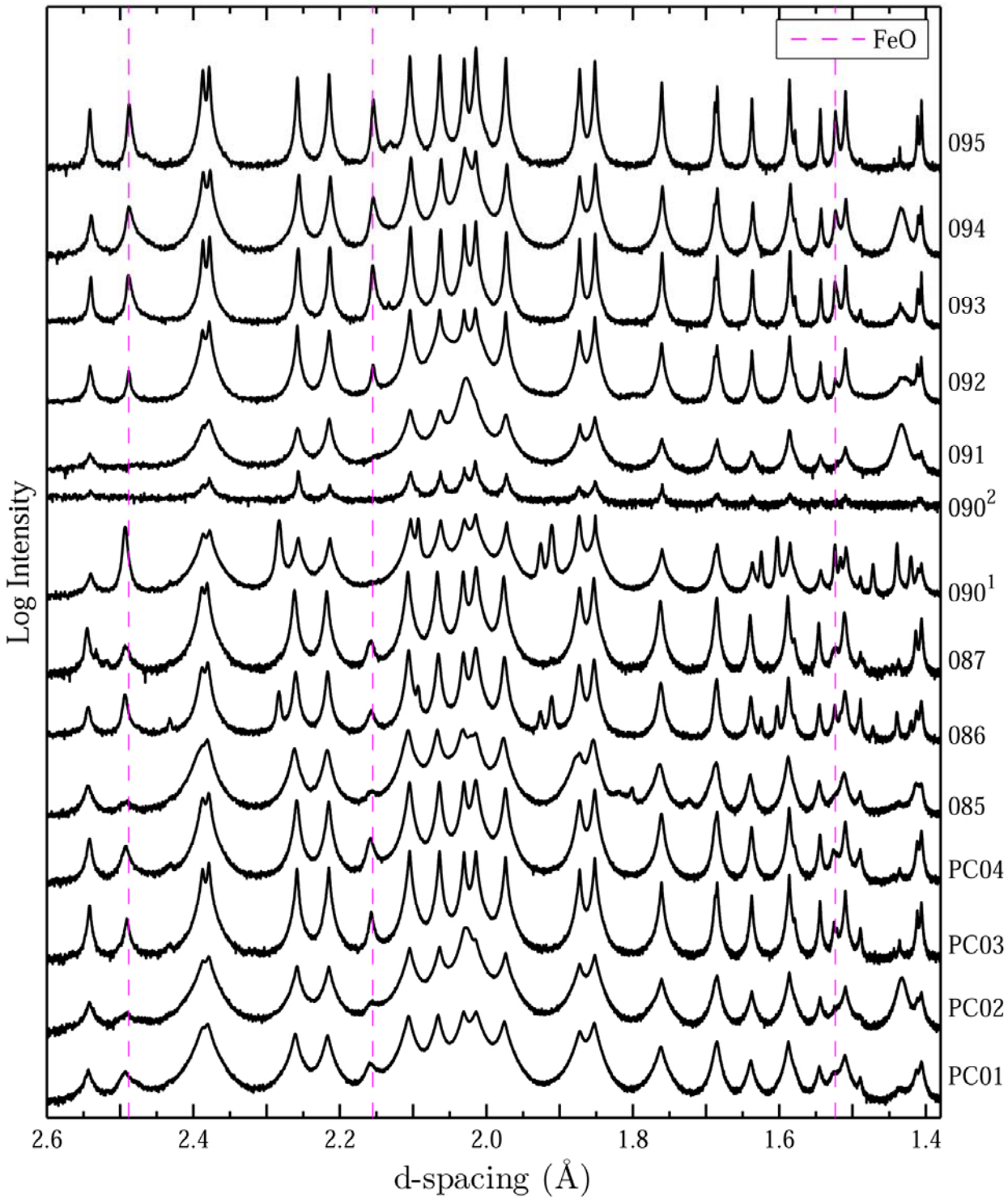

Fig. 3.11. X-ray diffraction data with only the diffraction peaks from FeO marked.

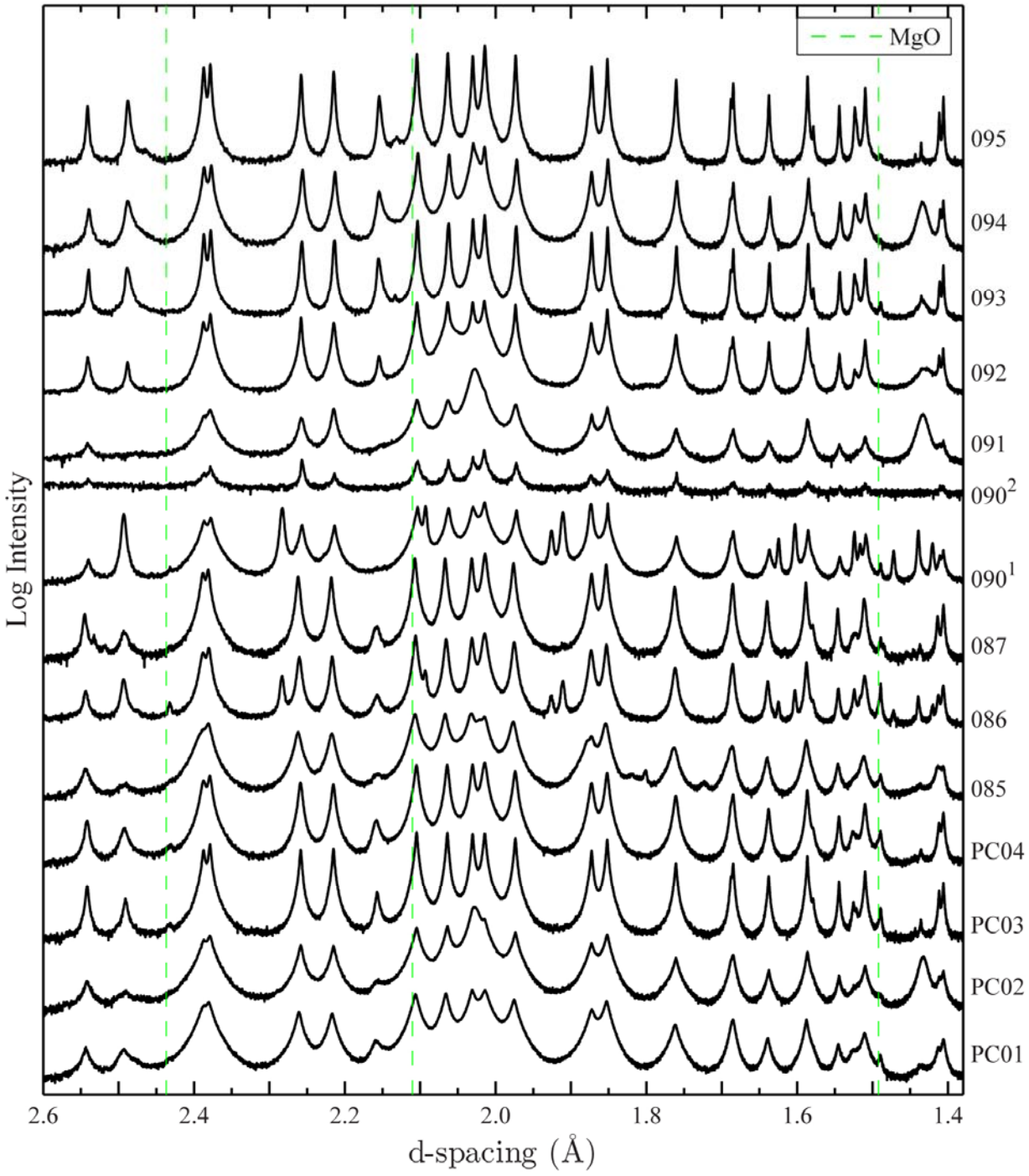

Fig. 3.12. X-ray diffraction data with only the diffraction peaks from MgO marked. MgO was used as the sample chamber in sample synthesis.

In the early run (in March 2008), I used clay to seal the sample into the Kapton capillary. When clay was accidentally exposed along the X-ray beam, undesired signals from calcite – the

main ingredient of clay – were observed in the XRD patterns. To avoid signals from the clay, I used amorphous glass fibers to seal the Kapton capillaries in the later run (in July 2008). It should be noted that the clay contamination does not affect the later measurements of nuclear resonant scattering (NRS) and XRD. NRS measurement with energy of 14.4 keV is only sensitive to the ^{57}Fe atoms and their bonding atoms. Moreover, clay is not expected to react with Fe_3C within the pressure and temperature conditions in the experiments in this thesis work. Furthermore, an XRD measurement with a DAC only requires very small amount of sample, and the small amount of leftover sample that was not contaminated by clay was sufficient enough.

The high-resolution XRD data are shown in Figs. 3.6 to 3.12. These results confirm that the major components in the samples from all the runs are Fe_3C with orthorhombic structure (#62, space group - Pnma), consistent with the reported structure in previous studies (e.g., Scott *et al*., 2001; Li *et al*., 2002). An appreciable amount of metallic iron is observed in the run products from runs PC02 and 091. A small amount of FeO is observed in most runs except runs 090 and 091. These results are consistent with the results from Mössbauer measurements.

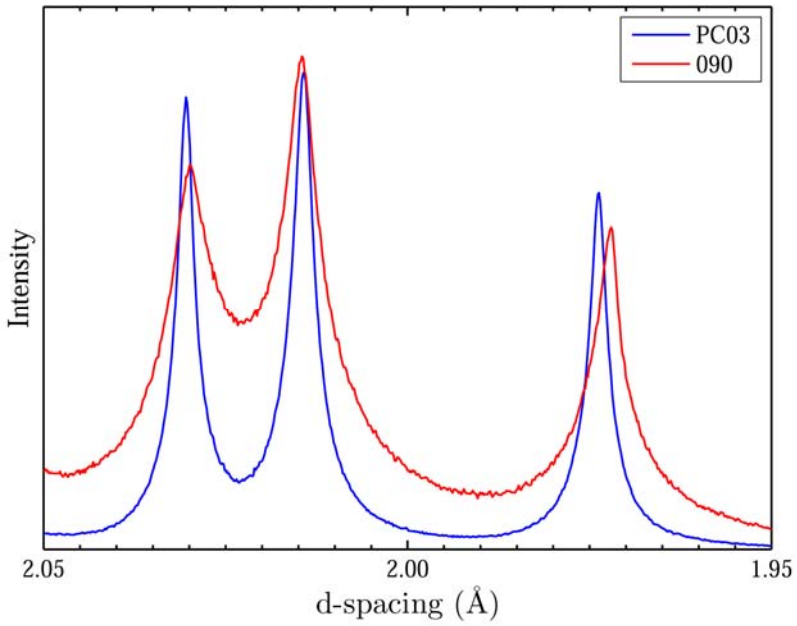

Fig. 3.13. Comparison of the X-ray diffraction line widths between samples PC03 and 090.

Compared to the XRD spectrum from sample PC03, the XRD spectrum on sample 090

exhibits much broader (more than twice) diffraction lines (Fig. 3.13). This is consistent with the larger hyperfine parameter distribution in the sample 090 compared to the sample PC03 as indicated by the CMS data.

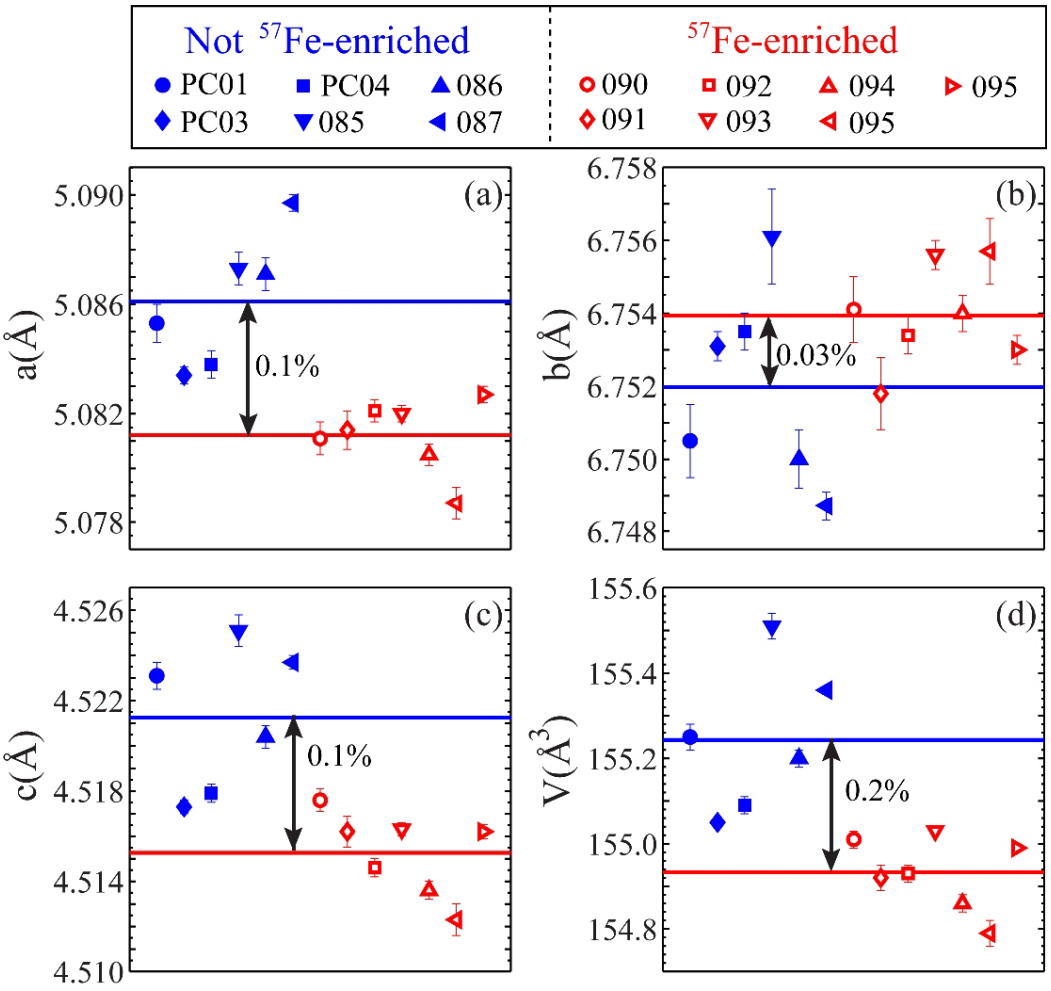

Fig. 3.14. Lattice parameters and unit cell volume of synthetic Fe_3C samples at ambient conditions derived from the high-resolution X-ray diffraction data collected at beamline 11-BM-B of the APS. Red open symbols represent ^{57}Fe-enriched Fe_3C (> 90 % enrichment). Blue solid symbols represent Fe_3C with natural iron. The red and blue lines represent the average lattice parameters of ^{57}Fe-enriched Fe_3C and Fe_3C with natural iron, respectively.

Lattice parameters of Fe_3C were derived from these high-resolution XRD data (Fig. 3.14, Table 3.4). The diffraction peak positions were fitted using the *CMPR* program (Toby, 2005). The lattice parameters were derived by fitting them to the peak positions using weighted least

squares method integrated in the *UnitCell* program (Holland and Redfern, 1997).

The lattice parameters of each synthetic Fe_3C sample differ from the rest samples, indicating variations in the sample structure. For lattice parameters *a* and *c*, and the unit cell volume, those of the seven ^{57}Fe-enriched Fe_3C samples are systematically smaller than those of the six Fe_3C samples with natural iron. The average of the former is lower than the average of the latter by 0.1 % for *a* axis, 0.1 % for *c* axis and 0.2 % for the unit cell volume. For *b* axis, the difference between the samples with and without ^{57}Fe enrichment is smaller (0.03 %). The average lattice parameter for the ^{57}Fe-enriched samples is larger than that for the non-enriched samples, contrary to the cases for *a* and *c* axes. The different behavior between *b* axis and the other two axes is probably because the hexagonal close-packed iron atoms in Fe_3C are stacked along the *b* axis (e.g., Fasiska and Jeffrey, 1965; Jiang *et al*., 2008; Ono and Mibe, 2010).

Table 3.4. Lattice parameters and unit cell volume of synthetic Fe_3C.

Run#	*a* (Å)	*b* (Å)	*c* (Å)	*V* (Å^3)
PC01	5.0853(7)	6.750(1)	4.5231(6)	155.25(3)
PC02	5.0811(6)	6.7531(9)	4.5176(5)	155.01(2)
PC03	5.0834(3)	6.7521(4)	4.5173(3)	155.05(1)
PC04	5.0838(5)	6.7525(5)	4.5179(4)	155.09(2)
085	5.0873(6)	6.755(1)	4.5251(7)	155.51(3)
086	5.0871(6)	6.7490(8)	4.5204(5)	155.20(2)
087	5.0897(3)	6.7477(4)	4.5237(3)	155.36(1)
090	5.0814(7)	6.751(1)	4.5162(7)	154.92(3)
091	5.0821(4)	6.7524(5)	4.5146(4)	154.93(2)
092	5.0820(3)	6.7546(4)	4.5163(3)	155.03(1)
093	5.0805(4)	6.7530(5)	4.5136(4)	154.86(2)
094	5.0787(6)	6.7547(9)	4.5123(7)	154.79(3)
095	5.0827(3)	6.7520(4)	4.5162(3)	154.99(1)

Numbers in the parentheses are the uncertainties in the last digit, which represent the standard derivations in the lattice parameter fittings to the diffraction peak positions using the weighted least square fitting method integrated in the *UnitCell* program (Holland and Redfern, 1997).

3.4 CONCLUDING REMARKS

Fe_3C samples with natural iron as well as ^{57}Fe-enriched iron were synthesized. I used

Mössbauer measurements and XRD methods to characterize the compositions and structures of the run products. The major components in all samples are confirmed to be Fe_3C with orthorhombic structure (#62, space group - Pnma). In sample 090, which is used in later high-pressure NRS and XRD studies, Fe_3C is the only observed phase. In several other runs excess iron and FeO are observed in run products.

The results from this work indicate that the run products are related to the particle size of Fe in the starting materials; large grain size of iron in the starting material is likely to result in excess iron in the run product. This is demonstrated in runs PC02, 091 and 092. With reduced particle size of iron powders in a later run, i.e., run 093, where iron and graphite powders were also mixed in a stoichiometric ratio, the amount of excess iron was reduced.

In all ^{57}Fe-enriched Fe_3C samples, broad absorption lines are observed in CMS results, indicating distributions in magnetic hyperfine parameters. XRD diffraction data also exhibit broad diffraction lines for the ^{57}Fe-enriched Fe_3C samples. The cause and nature of the hyperfine parameter distributions and diffraction line broadening remain to be further investigated.

Systematic differences in lattice parameters and unit cell volumes between the seven ^{57}Fe-enriched Fe_3C samples and six Fe_3C sample with natural iron. Average lattice parameters *a* and *c* and the unit cell volumes of the ^{57}Fe-enriched samples are smaller than those of the non-enriched samples by 0.1 %, 0.1 % and 0.2 %, respectively, while the average lattice parameter *b* (the long axis) of the ^{57}Fe-enriched samples is larger than that of the non-enriched samples by 0.03 %.

Chapter 4[1]

Magnetic Transition and Sound Velocity of Fe_3C at High Pressure

4 ABSTRACT

We have carried out nuclear resonant scattering measurements on ^{57}Fe-enriched Fe_3C between 1 bar and 50 GPa at 300 K. Synchrotron Mössbauer spectra reveal a pressure-induced magnetic transition in Fe_3C between 4.3 and 6.5 GPa. On the basis of our nuclear resonant inelastic X-ray scattering spectra and existing equation-of-state data, we have derived the compressional wave velocity V_P and shear wave velocity V_S for the high-pressure nonmagnetic phase. Our results suggest that the addition of carbon to iron-nickel alloy brings density, V_P and V_S closer to seismic observations, supporting carbon as a principal light element in the Earth's inner core.

4.1 INTRODUCTION

Carbon is one of the candidate light elements for the Earth's core (Li and Fei, 2007, and references therein). Wood (1993) proposed that for most conceivable sulfur to carbon ratios, Fe_3C could be the major inner core component rather than iron-nickel alloy, and may account for the density deficit in the inner core. A critical test for this hypothesis is to compare the density and sound velocities of Fe_3C with those of the inner core under corresponding pressure and temperature conditions.

Upon compression, Fe_3C transforms into a non-magnetic phase. The effects of the pressure-induced magnetic transition on the density and the compressibility of Fe_3C remain controversial.

[1] This chapter is based on the published article: Gao, L., Chen, B., Wang, J., Alp, E.E., Zhao, J., Lerche, M., Sturhahn, W., Scott, H.P., Huang, F., Ding, Y., Sinogeikin, S.V., Lundstrom, C.C., Bass, J.D. and Li, J. (2008) Pressure-induced magnetic transition and sound velocities of Fe_3C: implications for carbon in the Earth's inner core. *Geophys. Res. Lett.*, 35, L17306, doi:10.1029/2008GL034817. In addition to the published article, I added a figure (Fig. 4.4) and a table (Table 4.3) in this chapter, which are similar to Fig. 4.3 and Table 4.2, but with sound velocities converted to those of natural Fe_3C, following the method in chapter 6. This change does not affect the applications for the Earth's core inferred from this work.

Within experimental uncertainties, X-ray diffraction measurements at 300 K do not show any discontinuity in the compression curve of Fe_3C up to 73 GPa (Scott *et al*., 2001; Li *et al*., 2002). On the other hand, an *ab initio* study predicted a pressure-induced magnetic transition at 60 GPa and 0 K and found the high-pressure nonmagnetic phase less compressible than the low-pressure magnetic counterpart (Vočadlo *et al*., 2002). Experimental measurements at 300 K confirmed the occurrence of a magnetic transition under high pressure, but indicated different transition pressures for X-ray emission spectroscopy (XES) (25 GPa) (Lin *et al*., 2004a) versus for X-ray magnetic circular dichroism (XMCD) (9 GPa) (Duman *et al*., 2005) measurements. Synchrotron Mössbauer spectroscopy (SMS) is an established technique to investigate the electronic configuration and magnetic ordering of iron in iron-bearing phases (e.g., Alp *et al*., 1995; Sturhahn and Jackson, 2007, and references therein). SMS measurements can provide an independent constraint on the pressure of the magnetic transition, and allow a reassessment of the compressibility of Fe_3C.

On the V_P versus density plot, the inner core has a different slope from pure iron at 300 K, although the two linear trends overlap within the inner core density range (Lin *et al.,* 2003a; Mao *et al*., 2004). In contrast, the linear trends of V_S versus density of the inner core and pure iron at 300 K are nearly parallel, but with a considerable offset of ~ 2 km/s. The mismatch in density and velocities can not be explained by the addition of nickel but may reflect the effect of temperature and/or the presence of light elements such as carbon. To date, the only velocity data on Fe_3C have been calculated from ultrasonic measurements on porous samples at 1 bar and 300 K (Dodd *et al*., 2003). Nuclear resonant inelastic X-ray scattering (NRIXS) is a newly developed technique for measuring the partial phonon density of state (PDoS) of iron in iron-rich alloys (e.g., Sturhahn and Jackson, 2007). Combining high-pressure PDoS with equation of state (EoS) data, compressional and shear velocities of compressed Fe_3C can be derived.

4.2 EXPERIMENTAL PROCEDURE

An Fe_3C sample (sample 090) was synthesized from a mixture of 94.45 % ^{57}Fe-enriched iron (Cambridge Isotope Laboratories Inc., # FLM-1812-100) and graphite powder (Sigma-Aldrich, # 282863) at an atomic ratio of Fe:C = 2.922:1 (see chapter 3 for details on sample synthesis and characterization). The mixture was packed in a MgO capsule and equilibrated at 3 GPa and 1373

K for 19 hours, using the multi-anvil apparatus at the University of Illinois. Conventional Mössbauer measurements at ambient conditions confirmed that the run product is pure Fe_3C, with a magnetic hyperfine field of 21.8 (±2.7) Tesla, in accordance with previous results (e.g., Ron and Mathalone, 1971). The lattice parameters of the orthorhombic Fe_3C phase (space group Pnma, #62) are a = 5.080 Å, b = 6.758 Å, c = 4.514 Å, based on a high-resolution X-ray diffraction pattern collected at 11-BM-B of the Advanced Photon Source (APS), Argonne National Laboratory.

SMS and NRIXS experiments were performed at the undulator beamline 3-ID-B of the APS. The focused X-ray beam was less than 10 mm in diameter and has an energy resolution of 1.0 meV. SMS measurements were conducted in a symmetrical diamond-anvil cell (DAC) with a Re gasket and methanol-ethanol-water (16:3:1 by volume) pressure medium, which has been shown to maintain hydrostaticity up to 14.4 GPa (Fujishiro *et al*., 1982). An avalanche photodiode detector (APD) was placed along the X-ray beam path to collect SMS signals. Typical collection time for each SMS spectrum was 30 minutes. The *CONUSS* program package (Sturhahn, 2000) was used to extract magnetic hyperfine field parameters from synchrotron Mössbauer spectra.

NRIXS measurements were carried out on a piece of polycrystalline Fe_3C sample in a panoramic DAC using flat diamonds with 300-mm culet size, a Be gasket, NaCl pressure medium and ruby balls as the pressure marker (Mao *et al*., 1978). Three APDs were used to collect the delayed fluorescence radiation from three directions perpendicular to the X-ray beam. The diameter of the sample chamber was kept within 50–70 mm to limit pressure gradients and self-absorption of the inelastic scattering signals by the sample. Each NRIXS spectrum was collected over an energy range of ~ 70 to +90 meV around the ^{57}Fe nuclear resonance energy of 14.4125 keV in steps of 0.2 meV. The collection time was typically 4 hours for each pressure. Partial PDoS was derived from NRIXS data using the program *PHOENIX* (Sturhahn, 2000).

4.3 RESULTS AND DISCUSSION

4.3.1 Magnetic Transition and Core Density Deficit

At 1 bar and 300 K, Fe_3C is ferromagnetic. The SMS spectrum at 1 bar can be fitted assuming one iron site with a hyperfine field of 20.0 (± 2.4) T (Fig. 4.1), consistent with the

known value of ~ 20.5 T (e.g., Ron and Mathalone, 1971), and with the conventional Mössbauer measurements on the same sample. A loss of magnetism was observed between 4.3 and 6.5 GPa, as indicated by the disappearance of fast oscillations in the SMS spectra (Fig. 4.1).

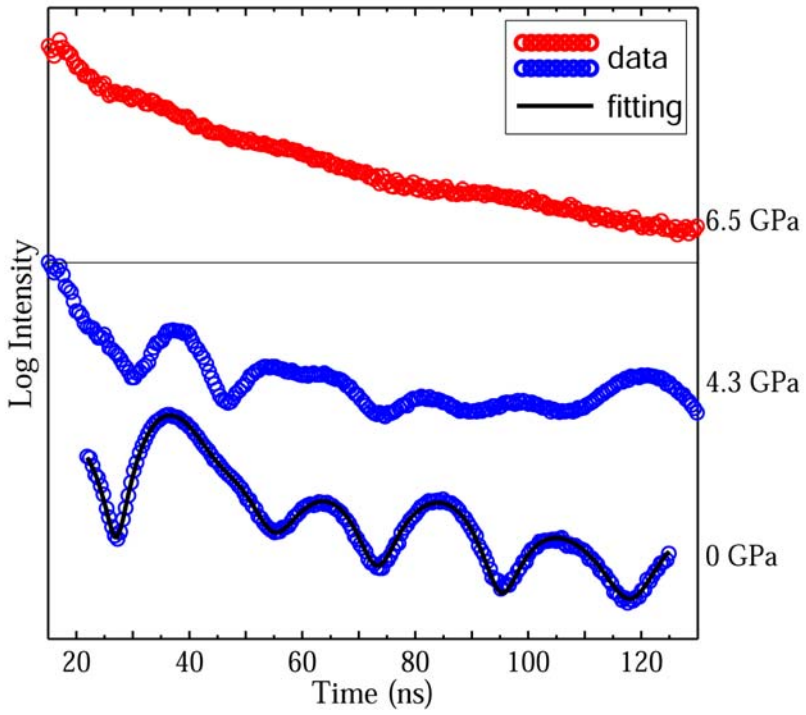

Fig. 4.1. Synchrotron Mössbauer spectra of synthesized Fe_3C (open circles) and fitting results for the 1-bar data (solid curve). The loss of the quantum beats (fast oscillations) between 4.3 and 6.5 GPa indicates the occurrence of a pressure-induced magnetic transition.

This magnetic transition pressure is lower than the XES results showing a gradual reduction in the satellite intensity between 1 bar and ~ 25 GPa (Lin *et al*., 2004a), and the XMCD results showing a continuous decrease of integrated intensity between ~ 6 and ~ 15 GPa (Duman *et al*., 2005). The discrepancy in transition pressure may reflect the uncertainties introduced in data evaluation and pressure calibration. Within the experimental uncertainties, the magnetic transition between 4.3 GPa and 6.5 GPa appears invisible in the compression curve of Fe_3C in previous studies (Scott *et al*., 2001; Li *et al*., 2002), therefore we use the set of V_0, K_0 and K' values from Scott *et al.* (2001) to estimate the density of Fe_3C at core pressures. For direct comparison with previous studies, we calculated the density of Fe_3C at an average inner core

pressure of 338 GPa and a likely inner core temperature of 5300 K, using the third-order Birch-Murnaghan EoS and estimated thermal expansion coefficients at 338 GPa following the method described by Wood (1993) and Vočadlo *et al.* (2002). Our calculated results suggest that Fe_3C is 2.4 % lighter than the inner core at these pressure and temperature conditions, similar to the previous result of 2.6 % (Lin *et al*., 2004a), but less than 3.8 % (Vočadlo *et al*., 2002) and more than 0.9 % (Wood *et al*., 2004) (Table 4.1). The density of Fe at 338 GPa and 5300 K is 2.9 % higher than that of the inner core (Table 4.1). Indeed, Fe_3C alone cannot reproduce the inner core density. To account for the density deficit in the inner core, ~ 3 wt. % carbon (equivalent to about 50 % Fe_3C) is needed. This estimate is sensitive to the EoS parameters and the core temperature and needs to be revised when more accurate data become available. In chapter 7, density of Fe_3C at inner core conditions will be reassessed using our recently acquired multi-megabar (1 megabar = 100 GPa) X-ray diffraction data.

Table 4.1 EoS Parameters and Densities of HCP-Fe and Fe_3C.

Reference	V_0 (Å^3)	K (GPa)	K'	α ($\times 10^{-5}$ K^{-1}) [a]	ρ (g/cm^3) [b]
		Fe_3C			
Scott *et al.* (2001)	155.26	175	5.2	0.385	12.54
Lin *et al.* (2004a)	148	288	4.0	0.448	12.52
Vočadlo *et al.* (2002)[c]	143.40	316.62	4.3	0.542	12.35
Wood (1993)	154.82	174	5.1	0.335	12.74
		HCP-Fe			
Mao *et al.* (1990) Issak and Anderson (2003)	22.36	165	5.33	0.69-1.25	13.22

[a] Thermal expansion coefficient a of Fe_3C at 338 GPa is estimated based on $\alpha_0 = 4.1 \times 10^{-5}$ K^{-1} for the high-temperature paramagnetic phase at 1 bar and 480– 600 K (Wood *et al*., 2004) following the method described by Wood (1993) and Vočadlo *et al.* (2002). Thermal effect on α is ignored.

[b] Calculated values at 338 GPa and 5300 K; see text for details.

[c] The reference temperature of V_0, K, K' is 0 K as given by Vočadlo *et al.* (2002) and 300 K in other EoS.

4.3.2 Sound Velocities, Poisson's Ratio and Birch's Law

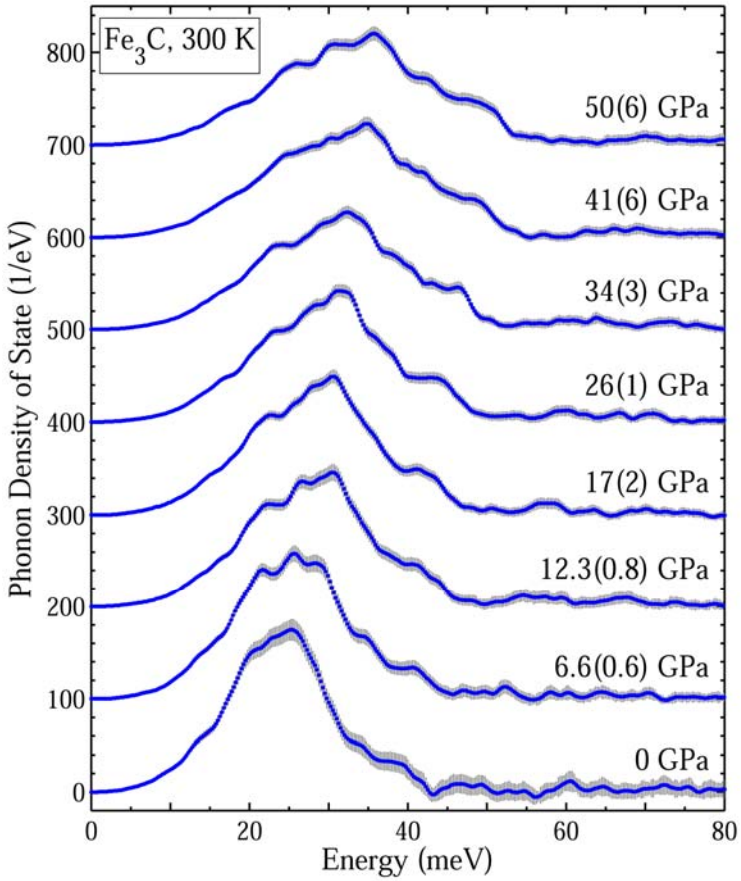

Fig. 4.2. Fe partial phonon density of states (PDoS) of Fe_3C extracted from NRIXS spectra between 1 bar and 50 GPa at 300 K. High-pressure spectra are shifted vertically for clarity.

From the NRIXS spectra collected at 300 K and up to 50 GPa, we derived the partial PDoS of Fe in Fe_3C (Fig. 4.2). At each pressure, the Debye velocity (V_D) of Fe_3C is extracted from a parabolic fitting of the low-energy portion of the PDoS between 3.0 and 12.0 meV. The following relations allow us to calculate aggregate compressional velocities V_P, shear wave velocity V_S, shear modulus G and Poisson's ratio v from V_D and EoS parameters (Table 4.2):

$$\frac{3}{V_D^3} = \frac{1}{V_P^3} + \frac{2}{V_S^3} \tag{4.1}$$

$$\frac{K_S}{\rho} = V_P^2 - \frac{4}{3}V_S^2 \tag{4.2}$$

$$\frac{G}{\rho} = V_S^2 \tag{4.3}$$

$$\upsilon = \frac{3K_S - 2G}{2(3K_S + G)} = \frac{\left(V_P / V_S\right)^2 - 2}{2\left(\left(V_P / V_S\right)^2 - 1\right)} \tag{4.4}$$

V_P, V_S and v of Fe_3C are calculated using the EoS parameters of Fe_3C at 300 K (Scott *et al*., 2001). The difference between the adiabatic bulk modulus K_S and the isothermal bulk modulus K_T at 300 K (< 2 %, corresponding to < 1 % difference in V_P) is within experimental uncertainties, hence ignored in the calculation.

Table 4.2 Compressional Wave Velocity V_P, Shear Wave Velocity V_s, Isothermal Bulk Modulus K_T, Shear Modulus G and Poisson's Ratio v of Fe_3C at 300 K.

P (GPa)	ρ (g/cm^3) [a]	V_P (km/s)	V_S (km/s)	K_T (GPa)	G (GPa)	v
			Fe_3C (Dodd *et al*., 2003)			
0	7.68(0)	5.33-5.14	3.01-3.08	105-125	69-72	0.22-0.27
			$^{57}Fe_3C$ (this study)			
0	7.83(0)	5.89(5)	3.05(7)	175(4)	73(3)	0.32(1)
6.6(6)	8.10(4)	6.43(9)	3.4(1)	209(9)	95(6)	0.30(1)
12.3(8)	8.31(5)	6.7(1)	3.48(6)	239(12)	101(2)	0.32(1)
17(2)	8.47(9)	6.9(2)	3.50(6)	263(20)	104(3)	0.33(2)
26(1)	8.75(7)	7.3(1)	3.60(6)	310(17)	113(3)	0.34(2)
34(3)	9.0(1)	7.6(2)	3.66(6)	352(30)	120(2)	0.35(1)
41(6)	9.2(2)	7.7(3)	3.60(6)	388(48)	119(3)	0.36(2)
50(6)	9.4(2)	8.1(3)	3.77(6)	435(50)	133(3)	0.36(2)

[a] The density of $^{57}Fe_3C$ is higher than that of natural Fe_3C used by Dodd *et al.*'s (2003) study. Numbers in the parentheses are uncertainties in the last digit(s). Contributions to uncertainties include: pressure - the pressure differences between different rubies and before and after NRIXS measurements; density - pressure and EoS parameters; V_P, V_S and G - pressure, EoS, and PDoS parabolic fitting parameters; K_T - pressure and EoS parameters; v - V_P and V_S.

Compared with porosity-corrected values from ultrasonic measurements (Dodd *et al*., 2003), our V_P at ambient condition is 11–15 % higher. The ultrasonic results appear questionable, as the same study also gives a much smaller bulk modulus K_0 (105–125 GPa) than determined by X-ray

diffraction measurements (Scott *et al*., 2001; Li *et al*., 2002), and a Poisson's ratio of 0.22–0.27, smaller than the known values of various Fe-rich alloys (0.27–0.37) (Mao *et al*., 2001; Lin *et al*., 2003a, 2004b, 2005a; Mao *et al*., 2004). V_P and V_S of Fe_3C do not increase smoothly with density (Fig. 4.3). The V_P of the low-pressure magnetic phase plots slightly below the linear trend of the high-pressure non-magnetic phase, whereas the V_S of the magnetic phase plots well below the linear trend of the non-magnetic phase, reflecting a significant increase in shear modulus across the magnetic transition boundary. The effects of the magnetic transition on the sound velocities of Fe_3C are similar to FeH_x, but different from pure iron, Fe-Ni, Fe_3S, and $Fe_{0.85}Si_{0.15}$, of which the V_P and V_S decrease upon magnetic transition, due to an increase in density and/or decrease in shear modulus.

For the non-magnetic phase of Fe_3C, V_P increases linearly with density (ρ): V_P (km/s) = -3.99 + 1.29ρ (g/cm^3) (Fig. 4.3). Birch (1961) found that at pressures above a few kilobars (when most cracks are closed), the principal factors determining V_P are the density and the mean atomic mass M: V_P (km/s) = a + b·ρ(g/cm3), where the constant a (km/s) generally decreases with increasing M, and b = 3.05 ((km·cm^3)/ (s·g)) for a large number of mantle minerals. Like other iron-rich alloys at 300 K, the linear relation between the V_P and ρ of Fe_3C is consistent with Birch's law. The mean atomic mass of Fe_3C (44.9) is smaller than that of Fe_3S (49.9) and $Fe_{0.85}Si_{0.15}$ (51.7), yet at a given ρ, V_P of Fe_3C is similar to or lower than that of Fe_3S and $Fe_{0.85}Si_{0.15}$, contrary to what is expected from Birch's law. At 300 K, the Birch's law slope of the non-magnetic Fe_3C is similar to that of pure iron, but significantly steeper than PREM (Fig. 4.3). Extrapolated to the inner core pressures, V_P of Fe_3C is ~ 10 % higher than the PREM value. The presence of carbon can counter the effect of nickel to bring a closer match between the V_P of Fe-Ni alloy and the inner core.

V_S of the non-magnetic phase of Fe_3C also increases linearly with density: V_S (km/s) = 1.45 + 0.24 ρ (g/cm^3). Interestingly, the slope is smaller than that of pure iron at 300 K. As a result, the extrapolated V_S of Fe_3C at inner core pressure is 1.5 km/s lower than that of pure iron, and considerably closer to the PREM value (Fig. 4.3). Although the presence of other light elements can not be ruled out, carbon may hold the key to explaining the low shear velocity of the inner core.

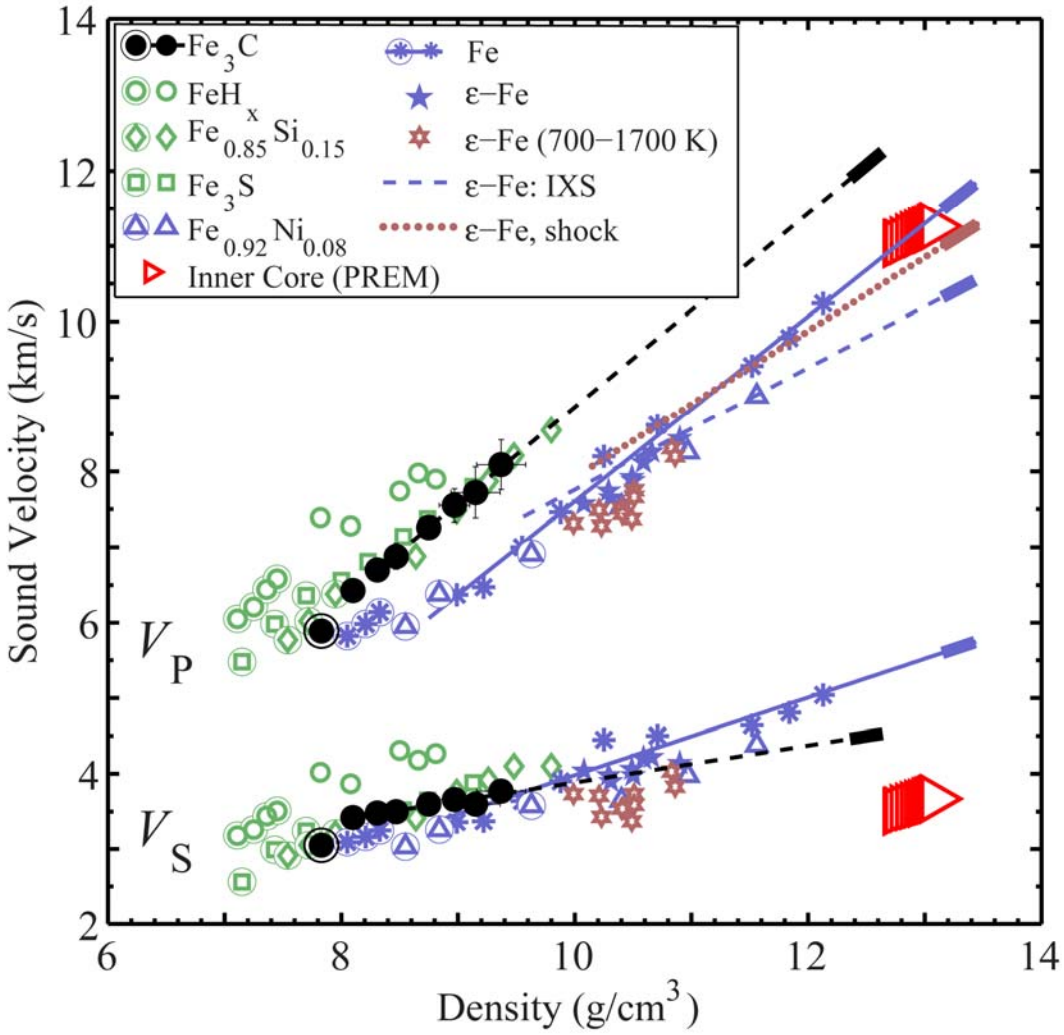

Fig. 4.3. Comparison of V_P and V_s versus density between Fe_3C and other Fe-rich alloys. Density of $^{57}Fe_3C$ is used for all NRIXS data. All data are at 300 K unless otherwise indicated. Magnetic phases are marked by outer circles. Long lines are linear fits to the data of the nonmagnetic phases of Fe_3C (black, dashed) and ε-Fe (blue, solid). Short solid bars mark the density of Fe_3C (black) and ε-Fe (blue) at inner core pressures and 5300 K (see text and Table 4.1 for details). Data sources: Fe_3C (this study); FeH_x (Mao *et al*., 2004); $Fe_{0.85}Si_{0.15}$ (Lin *et al*., 2003a); Fe_3S (Lin *et al*., 2004b); $Fe_{0.92}Ni_{0.08}$ (Lin *et al*., 2003a); ε-Fe (asterisk) (Mao *et al*., 2001); ε-Fe (star) and ε-Fe (700–1700 K) (Lin *et al*., 2005a); ε-Fe, shock (Brown and McQueen, 1986); ε-Fe, IXS (Fiquet *et al*., 2001).

Poisson's ratio is an important seismic observation that provides an additional constraint on models of core composition. The observed value of the inner core is 0.44 (Dziewonski and Anderson, 1981). At 300 K, the measured Poisson's ratios of iron, Fe-Ni alloys, FeH_x, Fe_3S and $Fe_{0.85}Si_{0.15}$ are smaller than 0.35 and show little pressure dependence (Mao *et al*., 2001; Lin *et al*.,

2003a, 2004b, 2005a; Mao *et al*., 2004). The Poisson's ratio of the nonmagnetic Fe_3C at 300 K falls into a comparable range to other iron-rich alloys, but gradually increases from 0.30 at 6.6 GPa to 0.36 at 50 GPa (Table 4.2), approaching the PREM value.

Recent NRIXS measurements on iron revealed a significant reduction of V_P and V_S at high temperature, and a deviation of the V_P - density relation from Birch's law (Lin *et al*., 2005a). In order to provide a stringent test for the hypothesis of a carbon-rich inner core, the effects of temperature on the sound velocities of Fe_3C need to be investigated.

4.Appendix. Converted Sound Velocities for Fe_3C with Natural Iron

The sound velocities of ^{57}Fe-enriched Fe_3C in this work are converted to those for Fe_3C with natural iron (Table 4.3, Fig. 4.4), following the method in chapter 6. The compressional wave velocity V_P and shear wave velocity V_S for the high-pressure nonmagnetic phase, which can be expressed as functions of density (ρ): V_P (km/s) = - 4.20 + 1.35 ρ(g/cm^3) and V_S (km/s) = - 1.42 + 0.26 ρ(g/cm^3).

Table 4.3 Compressional Wave Velocity V_P, Shear Wave Velocity V_s, Isothermal Bulk Modulus K_T, Shear Modulus G and Poisson's Ratio v of Fe_3C at 300 K converted from those for $^{57}Fe_3C$ in Table 4.2.

P (GPa)	ρ (g/cm^3) [a]	V_P (km/s)	V_S (km/s)	K_T (GPa)	G (GPa)	v
0	7.68(0)	6.00(5)	3.11(7)	178(5)	73(1)	0.320(5)
6.6(6)	7.95(2)	6.55(9)	3.5(1)	213(6)	93(2)	0.309(5)
12.3(8)	8.16(3)	6.89(1)	3.55(6)	243(8)	101(2)	0.318(5)
17(2)	8.31(6)	7.0(2)	3.57(6)	268(13)	100(1)	0.334(6)
26(1)	8.59(3)	7.4(1)	3.6796)	315(11)	114(3)	0.338(5)
34(3)	8.80(8)	7.8(2)	3.73(6)	358(20)	118(2)	0.351(7)
41(6)	9.0(1)	7.9(3)	3.67(6)	395(35)	118(2)	0.36(1)
50(6)	9.2(1)	8.3(3)	3.84(6)	442(36)	136(3)	0.36(1)

[a] Numbers in the parentheses are uncertainties in the last digit(s). Contributions to uncertainties include: pressure - the pressure differences between different rubies and before and after NRIXS measurements; density - pressure and EoS parameters; V_P, V_S and G - pressure, EoS, and PDoS parabolic fitting parameters; K_T - pressure and EoS parameters; v - V_P and V_S.

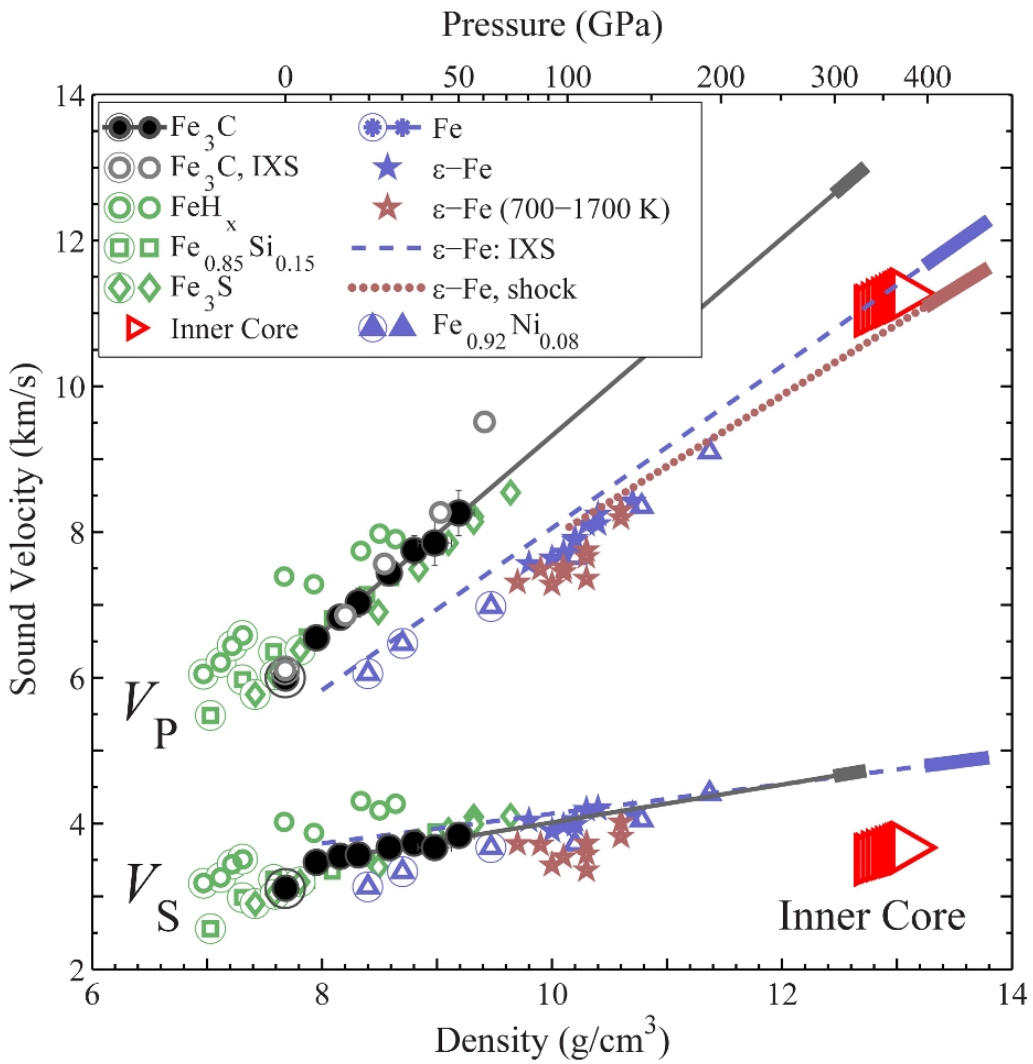

Fig. 4.4. V_P and V_s for Fe_3C converted from those for $^{57}Fe_3C$, compared to those for other Fe-rich alloys. All data are at 300 K unless otherwise indicated. Magnetic phases are marked by outer circles. Long lines are linear fits to the data of the nonmagnetic phases of Fe_3C (black, dashed) and ε-Fe (blue, solid). Short solid bars mark the density of Fe_3C (black) and ε-Fe (blue) at inner core pressures and 5300 K (see text and Table 4.1 for details). Data sources: Fe_3C (this study); Fe_3C, IXS (Fiquet *et al*., 2009); FeH_x (Mao *et al*., 2004); $Fe_{0.85}Si_{0.15}$ (Lin *et al*., 2003a); Fe_3S (Lin *et al*., 2004b); $Fe_{0.92}Ni_{0.08}$ (Lin *et al*., 2003a); ε-Fe (asterisk) (Mao *et al*., 2001); ε-Fe (star) and ε-Fe (700–1700 K) (Lin *et al*., 2005a); ε-Fe, shock (Brown and McQueen, 1986); ε-Fe, IXS (Antonangeli *et al*., 2004).

Chapter 5

Magnetic Transition at ~ 5 GPa and Mössbauer Spectroscopy

The magnetic transition between 4.3 and 6.5 GPa was further investigated using synchrotron Mössbauer spectroscopy (SMS) and conventional Mössbauer spectroscopy (CMS). These results confirm the magnetic transition and place further constraints on the pressure and nature of the transition.

5.1 EXPERIMENTAL PROCEDURE

SMS measurements were performed at the beamline 16-ID-D of the APS, with the incident X-ray beam focused to a size of ~ 35 (vertical) × 50 (horizontal) μm^2. High pressure was achieved using a symmetrical diamond anvil cell (DAC) with diamond anvils that have a culet size of 600 μm. With a pressure interval of ~ 1.5 GPa, we collected SMS data between 0.6 and 12 GPa at ambient temperature. The data collection time for each spectrum was 1 to 3 hour(s). The ^{57}Fe-enriched Fe_3C sample was synthesized in run 090 and its purity and structure was confirmed using CMS at sector 3 of the APS and high-resolution X-ray diffraction measurements at the beamline 11-BM-B of APS (Chapter 2).

A Re gasket was used in this experiment. It was indented to a thickness of 70 μm, and a hole with a diameter of 300 μm was drilled on the Re gasket as the sample chamber. A piece of $^{57}Fe_3C$ powder flake was loaded in a sample chamber, together with the pressure transmitting medium of methanol–ethanol-water (MEW) (volume ratio 16:3:1), which has been indicated to maintain hydrostaticity up to 14.4 GPa (Fujishiro *et al*., 1982), covering the pressure range of this study. For pressure measurement, we loaded two ruby balls into the sample chamber, one at the center and one at the rim of the sample chamber. The two ruby balls provide a way to estimate the pressure gradient across the sample chamber.

In the CMS run carried out at sector 3 of the APS, a piece of $^{57}Fe_3C$ powder flake from the

synthesis run 090 was also used in a symmetrical DAC. In this loading, we used neon as the pressure medium. An initial pressure of 3.1 GPa was achieved after the neon gas loading procedure. The incident γ-ray was produced using a ^{57}Co radioactive point source. The data collection time at each pressure point was ~ 3 days.

5.2 RESULTS AND DISCUSSION

The SMS data (Fig. 5.1) show a loss of fast quantum beats at ~ 5.5 GPa, confirming the magnetic transition from a low-pressure magnetic phase to a high-pressure non-magnetic phase (Gao *et al*., 2008).

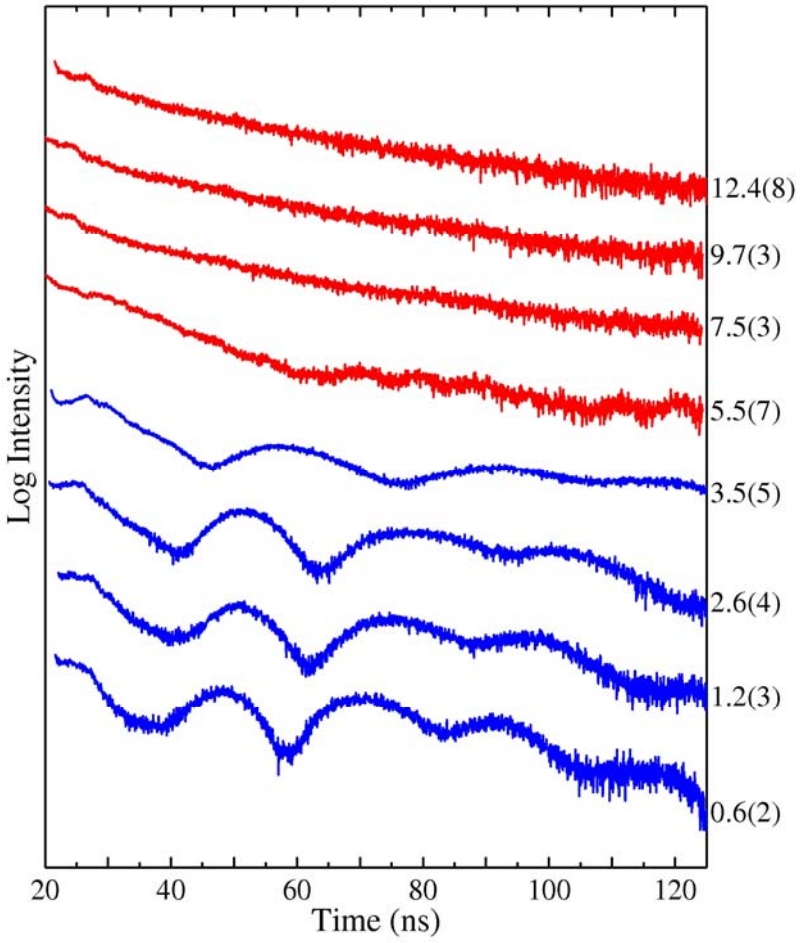

Fig. 5.1. Synchrotron Mössbauer spectra of compressed Fe_3C collected at beamline 16-ID-D of the APS. The magnetic loss of the quantum beats (fast oscillations) at ~ 5.5 GPa confirms the magnetic transition from a low-pressure magnetic phase to a high-pressure non-magnetic phase (Gao *et al*., 2008).

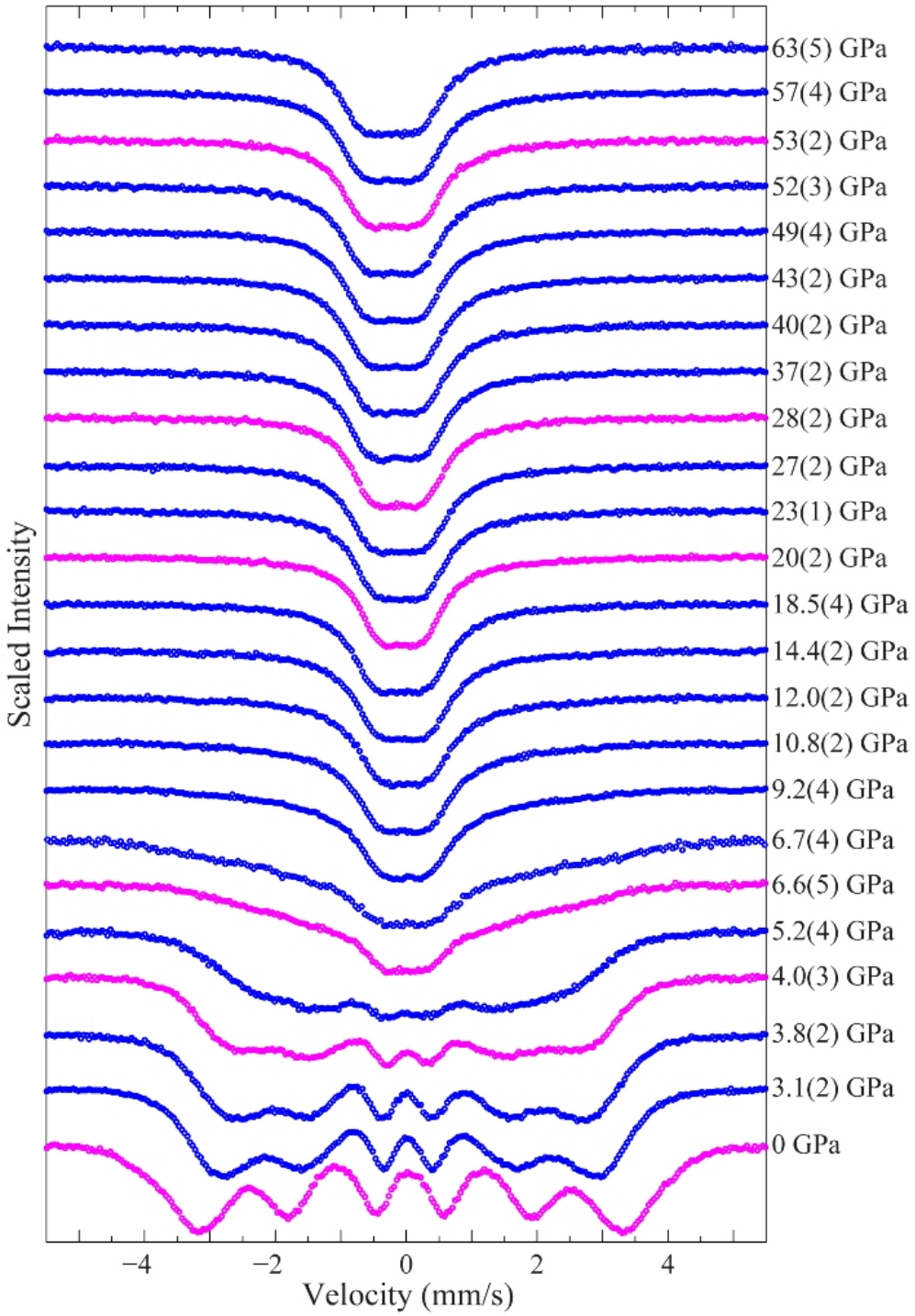

Fig. 5.2. Conventional Mössbauer spectra of compressed Fe_3C collected at sector 3 of the APS. The gradual change from a sextet to a doublet in the CMS spectra indicates a magnetic transition at ~ 6 GPa, consistent with the results from our SMS study (Gao *et al*., 2008). Blue color represents data upon compression and magenta color represents data upon decompression.

This experiment also provides additional data on evaluating the pressure gradient sustained with a pressure medium of MEW mixture. We observed that up to 9.7 GPa, the pressure difference between the two ruby balls, one in the center and the other in the rim of the sample chamber, is no more than 0.1 GPa. At the last pressure point of 12.4 GPa, this difference increased to 0.8 GPa.

The CMS data (Fig. 5.2) show a gradual change from a sextet to a doublet, confirming the magnetic transition. This transition completes at ~ 6 GPa, consistent with the results from our SMS study.

Chapter 6[2]

Sound Velocities at Simultaneous High Pressure and High Temperature

6 ABSTRACT

To test whether carbon is a major light element in the inner core, it is necessary to compare the sound velocity of iron-carbon compounds with the observed values of the inner core. To date, most sound velocity measurements on compressed core candidate materials were performed at ambient temperature. The temperature effect on sound velocity is not well understood, and there has been controversy on whether high temperature causes reduction in sound velocities (Lin *et al*., 2005a; Kantor *et al*., 2007). In this study, we carried out nuclear resonant inelastic X-ray scattering (NRIXS) measurements on polycrystalline samples of Fe_3C up to 45 GPa and 1450 K. Compressional sound velocities V_P and shear sound velocities V_S were derived from the NRIXS results combined with previously determined ambient-temperature equations of state and typical thermal expansion parameters. The V_P and V_S at 300 K follow Birch's law – the linear dependence of sound velocity on density. The linearly extrapolated V_S to the inner core pressures based on the ambient-temperature data is higher than that of the inner core by ~ 60 %. Our results at high temperatures suggest temperature induced shear velocity decrease, and also indicate that the temperature effect increases as temperature increases and decreases as pressure increases. The temperature needed to reconcile the sound velocity mismatch between Fe_3C and the inner core at 300 K is within the expected values of the inner core, thus supporting Fe_3C as a possible candidate material for the inner core and carbon as a possible candidate light element.

6.1 INTRODUCTION

Recent studies suggest that the inner core is composed of mainly iron-nickel alloy and a small fraction of lighter element (e.g., Li and Fei, 2007, and references therein; Dewaele *et al.*,

[2] This chapter will be submitted to a journal. Collaborators in this work include: Bin Chen, Jiyong Zhao, Esen E. Alp, Wolfgang Sturhahn and Jie Li.

2006). Fe_3C was proposed to be the major inner core component based on a thermodynamic calculation study (Wood, 1993), although this view has been under debate recently (Vočadlo *et al*., 2002; Lin *et al*., 2004a). Using the nuclear resonant inelastic X-ray scattering (NRIXS) method, sound velocities of Fe_3C have been investigated up to 50 GPa at 300 K on a sample composed of one or a few crystals (Gao *et al*., 2008). The compressional sound velocity of Fe_3C has also been determined using inelastic X-ray scattering (IXS) method to 68 GPa at 300 K (Fiquet *et al*., 2009). At simultaneous high temperature and high pressure, the sound velocities of Fe_3C have not yet been measured.

Fe_3C, also known as cementite, or cohenite when a small amount of iron is substituted with nickel, has an orthorhombic structure (Jiang *et al*., 2008, and references therein). No structural change has been observed in X-ray diffraction (XRD) studies up to 30 GPa (Li *et al*., 2002) or up to ~ 70 GPa (Scott *et al*., 2001; Ono and Mibe, 2010) at ambient temperature. Quenched samples from > 1500 K at 16-25 GPa could also be indexed with this structure (Scott *et al*., 2001). On the other hand, a pressure-induced magnetic transition from the ferromagnetic state to a non-magnetic state at ~ 6 GPa was observed in a synchrotron Mössbauer study (Gao *et al*., 2008). Around this pressure, a magnetic transition has also been observed in an X-ray emission spectroscopy study (Lin *et al*., 2004a) and an X-ray magnetic circular dichroism study (Duman *et al*., 2005). Within the pressure and temperature (*P*-*T*) range explored in this study, i.e., from 17 GPa and 300 K to 1450 K and 45 GPa, Fe_3C is expected to be in orthorhombic structure and in non-magnetic state.

To extrapolate the experimentally measured sound velocities to the *P*-*T* conditions of Earth's inner core, Birch's law has been widely used. Birch's law is an empirical relationship, stating the linear dependence of compressional sound velocity on density (Birch, 1961). Although Birch's law was originally referred to only compressional sound velocities, the linear dependence of shear sound velocity and bulk sound velocity on density has also been referred as Birch's law in literature. At ambient temperature and high pressures, most single-phase Fe-enriched materials were found to follow this linear sound velocity-density relationship, including Fe (e.g., Antonangeli *et al*., 2004), Fe_3C (Gao *et al*., 2008; Fiquet *et al*., 2009), Fe-Ni alloys (e.g., Lin *et al*., 2003a; Kantor *et al*., 2007), Fe-Si alloys (Lin *et al*., 2003a) and Fe_3S (Lin *et al*., 2004b). At high temperature, whether or not sound velocities still follow Birch's law is controversial. An

IXS study on $Fe_{0.78}Ni_{0.22}$ up to 72 GPa and 715 K (Kantor *et al*., 2007) showed that high-temperature (715-K) data plot both above and below the ambient-temperature sound velocity data, whereas an NRIXS study on Fe up to 73 GPa and 1700 K (Lin *et al*., 2005a) revealed that sound velocities of iron at high temperatures are well below the ambient-temperature data on a sound velocity versus density plot.

In this study, we investigated the compressional and shear sound velocities of powder Fe_3C using the recently-established NRIXS method (e.g., Sturhahn *et al*., 1995; Sturhahn and Jackson, 2007) in a hitherto unexplored *P-T* range, i.e., to 1450 GPa at 45 GPa. NRIXS method is unique in determining the shear sound velocity V_S, as will be discussed later in this article. This method has also been used in sound velocity studies on FeH_x (Mao *et al*., 2004), Fe-Ni (Lin *et al*., 2003a), Fe_3S (Lin *et al*., 2004b), and $Fe_{0.85}Si_{0.15}$ (Lin *et al*., 2003a) at high pressures, and on iron at high pressures (Mao *et al*., 2001) and high temperatures (Lin *et al*., 2005a). The validity of NRIXS method in measuring sound velocities has been demonstrated at ambient conditions (e.g., Hu *et al*., 2003). The simultaneous high-temperature and high-pressure data on Fe_3C in this study will shed light on the controversial issue of temperature effect on Birch's law. The comparison of sound velocities of Fe_3C against those of the inner core (Dziewonski and Anderson, 1981) will place constraint on the role of carbon in the Earth's inner core.

6.2 EXPERIMENTAL PROCEDURE

The starting materials of ^{57}Fe-enriched Fe_3C (from synthesis run #090) were synthesized using a large-volume press at University of Illinois. Details of the synthesis have been described previously (Gao *et al*., 2008). The run products were confirmed to be pure Fe_3C with orthorhombic structure using the XRD setup at beamline 11-BM-B of the Advanced Photon Source (APS) (λ = 0.4142 Å and λ = 0.3344 Å) and conventional Mössbauer method with a ^{57}Co radioactive source at sector 3 of the APS, although α-iron pieces or Fe_3C pieces with α-iron inclusions were occasionally observed among individual pieces with a diameter in the order of 10 μm (Gao *et al*., 2009).

In this study, we conducted two NRIXS runs (Table 6.1), run 090-DAC-II and run 090-DAC-III, at beamline 3-ID-B of the APS at Argonne National Laboratory. The setup of this beamline has been described previously (e.g., Gao *et al*., 2009, and references therein). To calibrate

pressure and confirm sample composition, XRD spectra were collected on the sample in run 090-DAC-II at 300 K and 17 GPa as well as at ~ 1000 K and ~ 15 GPa at beamline 3-ID-B of the APS (λ = 0.8603 Å) (Fig. 6.11 in Gao *et al*., 2009). Within the DAC opening (~ 26°), only one diffraction peak is expected for α-Fe (at 300 K) or γ-Fe (at ~ 1000 K). These peaks overlap with those of Fe_3C unfortunately, and therefore iron impurity can not be clearly distinguished from Fe_3C phase using this XRD setup at these *P-T* conditions even if it exists. For the sample in run 090-DAC-III, XRD patterns were collected at 16-BM-D of the APS (λ = 0.42348 Å) at 45 GPa and 300 K after NRIXS experiments were complete (Fig. 7.6). The sample was confirmed to be mainly Fe_3C with a detectable amount of Fe (integrated peak intensity of iron / iron + Fe_3C ~ 20 %).

NRIXS spectra were collected by tuning the X-ray energy within ± 70 or 90 meV around the ^{57}Fe nuclear transition energy of 14.4125 keV (corresponding to a wavelength of 0.8603 Å). The size of the X-ray beam was < 10 μm in diameter, and the energy resolution was ~ 1 meV. For each *P-T* point, multiple NRIXS spectra were collected until sufficient statistics were reached. These spectra were added together for further data analysis using *PHOENIX* program (Sturhahn, 2000). The data acquisition time at each pressure and temperature varied from 7 hours to 27 hours.

We used panoramic diamond anvil cells (DAC) with Be gaskets and boron nitride inserts to achieve high pressures. Boron nitride inserts were used to enhance the gasket thickness at high pressure (Lin *et al*., 2003b), since Be is soft and becomes thin at high pressure. Fe_3C was ground to powder in an agate mortar. The powder has an estimated average particle size of ~ 2 μm based on visual observations under microscope. In each run, a piece of Fe_3C powder flake was sandwiched between two layers of dried NaCl powder flakes. A microscopic image of DAC loading in run 090-DAC-III with BN insert in Be gasket has been shown in a previous study (Fig. 7.4). High temperatures were generated using double-sided laser heating technique with a Nd:YLF laser (e.g., Zhao *et al*., 2004; Lin *et al*., 2005a). The diameter of the donut-shaped laser beam was ~ 50 μm at the focus. Laser power of 44 to 70 Watt were used to reach the temperatures of 760 K to 1450 K in this study. We calculated temperatures from NRIXS spectra based on the relationship of detailed balance (e.g., Shen *et al*., 2004) using the *PHOENIX* software (Sturhahn, 2000). The uncertainty of temperature was propagated from the statistical

errors of NRIXS spectra following the method by Shen *et al*. (2004).

The starting pressure of run 090-DAC-III was 36 GPa, based on ruby R_1 fluorescence signals (Dewaele *et al*., 2004). A *P-T* path of this run is shown in Table 6.1. Run 090-DAC-II was conducted after run 090-DAC-III. In this run, we used a slot seat in the downstream side of the DAC. The large opening of the slot seat allowed collection of XRD spectrum that is sufficient for pressure calibration (Gao *et al*., 2009). XRD signals of NaCl (Fei *et al*., 2007) were used to estimate pressure in this run. The temperature in this run NRIXS was also estimated based on the relationship of detailed balance using the *PHOENIX* software (Sturhahn, 2000). Samples from both runs remained in polycrystalline forms after heating, as indicated by spotty rings in the XRD patterns on image plates.

6.3 RESULTS

6.3.1 Phonon Density of States and Sound Velocities

NRIXS technique probes the vibration modes (phonons) of Fe in ^{57}Fe-bearing materials and records the phonons projected to the direction of the X-ray beam (Gao *et al*., 2009, and references therein). From NRIXS spectra, phonon density of states (PDoS) of Fe in Fe_3C (Fig. 6.1) were extracted. Quasi-harmonic model is used in PDoS extraction using *PHOENIX* software (Sturhahn, 2000). From the PDoS, Debye sound velocities (V_D) were derived from parabolic fittings of the low-frequency PDoS's on a basis of Debye-like low-frequency dynamics according to the following relationship:

$$\rho V_D^{\,3} = \frac{3\tilde{M}}{2\pi^2\hbar^3}\frac{E^2}{g(E)} \qquad (6.1)$$

where ρ is density (density of the material with 100 % ^{57}Fe-enrichement), $g(E)$ is the PDoS, $\hbar$ is the reduced Planck constant and $\tilde{M}$ is the atomic mass of ^{57}Fe. This relationship is similar to equation (14) in an article by Hu *et al*. (2003), but with a correction term of '3' in the numerator, arising from the existence of three acoustic modes: the longitudinal mode and the two shear modes. This relationship is also equivalent to equation (3.25) in a book by Poirier (2000), but with an additional term $\tilde{M}/M$, considering the isotope selectivity in NRIXS method. This

parabolic relationship, the central feature of Debye model, is valid for any crystal while frequency reaches the limit of zero ($\omega \rightarrow 0$) (Kieffer *et al*., 1979). In this study, V_D is derived from PDoS in an energy range below 12 meV. To calculate compressional sound velocities V_P and shear sound velocities V_S (Table 6.1, Fig. 6.2), we used the following relationship between V_D, V_P, V_S and adiabatic bulk modulus K_S (e.g., Mao *et al*., 2001):

$$\frac{3}{V_D^3} = \frac{1}{V_P^3} + \frac{2}{V_S^3} \tag{6.2}$$

$$\frac{K_S}{\rho} = V_P^2 - \frac{4}{3} V_S^2 \tag{6.3}$$

where ρ is the density of the material with 100 % ^{57}Fe-enrichement. The derived V_P and V_S from this procedure represent those of a material with 100 % ^{57}Fe-enrichement. For comparison with the Earth's inner core, correction resulted from usage of ^{57}Fe should be applied to V_P and V_S. Details of the correction are discussed in the following section. The values in Table 6.1 and Fig. 6.2 are the corrected values.

K_S and thermal bulk modulus K_T can be calculated from EoS parameters according to the following relationships:

$$K_T = K_0 + K' \cdot P \tag{6.4}$$

$$K_S = K_T(1 + \alpha\gamma T) \tag{6.5}$$

Here, we used the bulk modulus at ambient conditions K_0 and the pressure derivative of bulk modulus K' from an XRD study (Scott *et al*., 2001). Using the EoS by Li *et al*. (2002) yields nearly indistinguishable results. For determination of K_S and density at high temperatures, we assumed a thermal expansion coefficient of 3 (± 2.5) $\times 10^{-5}$ K^{-1}, a Grüneisen parameter of 1.8 ± 0.6 and $\partial K/\partial P$ of - 0.3 ± 0.3, within a conceivable range of the values for Fe-rich materials (Chen *et al*., 2008, and references therein).

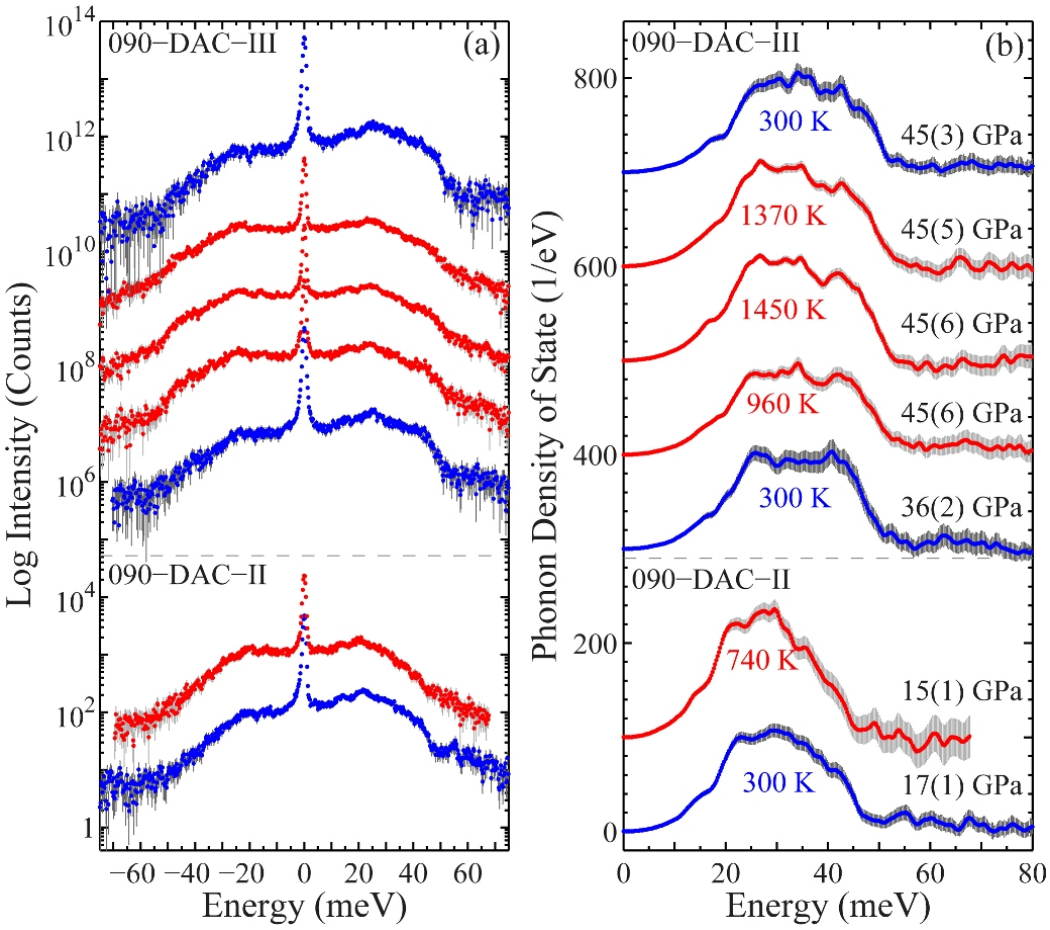

Fig. 6.1. (a) NRIXS spectra and (b) derived partial phonon density of states (PDoS) of Fe in Fe_3C, stacked in the same sequence. The gray margins represent statistical uncertainties. The spectra are shifted vertically for clarity.

6.3.2 ^{57}Fe Correction for V_P and V_S

NRIXS method measures only the partial PDoS of ^{57}Fe isotopes. For this reason, density (or equivalently, atomic mass) of the compound with 100 % ^{57}Fe-enrichment should be used when deriving the Debye velocity V_D following equation (6.1), even when natural Fe-compound was used in experiments. The sound velocities V_P and V_S derived subsequently following equations (6.2) and (6.3) are those for a 100 % ^{57}Fe-enriched compound. The density in equation (6.3) should also be the density of the compound with 100 % ^{57}Fe-enrichment. Since natural iron-bearing compounds instead of ^{57}Fe-enriched counterparts are expected to be in the Earth's core, when comparing experimentally measured V_P and V_S using NRIXS method with the observed values for the core, the experimental values of V_P and V_S should be corrected for the usage of

^{57}Fe.

As $V_P = \sqrt{(K_s + 4/3G)/\rho}$ and $V_s = \sqrt{G/\rho}$, and K_s and G are expected to be nearly the same for a compound with or without ^{57}Fe-enrichment, ^{57}Fe correction on V_P and V_S is simply a factor of $\sqrt{\rho^{57}/\rho^{N}}$, where ρ^{57} is the density of a 100 % ^{57}Fe-enriched compound, and ρ^{N} is the density of the compound with natural iron. In the table and figures in this study, ^{57}Fe correction on V_P and V_S is applied. On a sound velocity versus pressure plot, if no correction to V_P and V_S is applied, the resulted data points are expected to be lower than the data points for the compound with natural iron by a factor of $\sqrt{(\rho^{57}/\rho^{N})/\rho^{57}}$. For most core candidate materials, including Fe_3C, $\sqrt{(\rho^{57}/\rho^{N})/\rho^{57}}$ is ~ 2 %. If the sound velocity is plotted against the density of 100 % ^{57}Fe-enriched compound, the difference between the uncorrected data and the corrected data appear even larger, by a factor of $\sqrt{(\rho^{57}/\rho^{N})/\rho^{57}} + (dV/d\rho)\cdot(\rho^{57} - \rho^{N})/V$ (V stands for V_P or V_S), where the first term corresponds to the ^{57}Fe correction on sound velocity and the second term arises from the usage of density scale. This second term generally decreases as density (ore pressure) increases as V_P and V_S generally increase as density (ore pressure) increases. For most core candidate materials, including Fe_3C, the total difference, including the 2 % contribution from the first term, is in the range of 3-5 % for V_P (for $dV_P/d\rho$ ~ 1-1.5 (km/s)/(g·cm^3), V_P ~ 7-12 km/s), and 3-7 % for V_S (for $dV_S/d\rho$ ~ 0.2-1 (km/s)/(g·cm^3), V_S ~ 3-4 km/s). Using ρ^{N} incorrectly in equation (6.3) would result in a decrease of ~ 1 % in V_P, and a small increase of < 0.1 % in V_S.

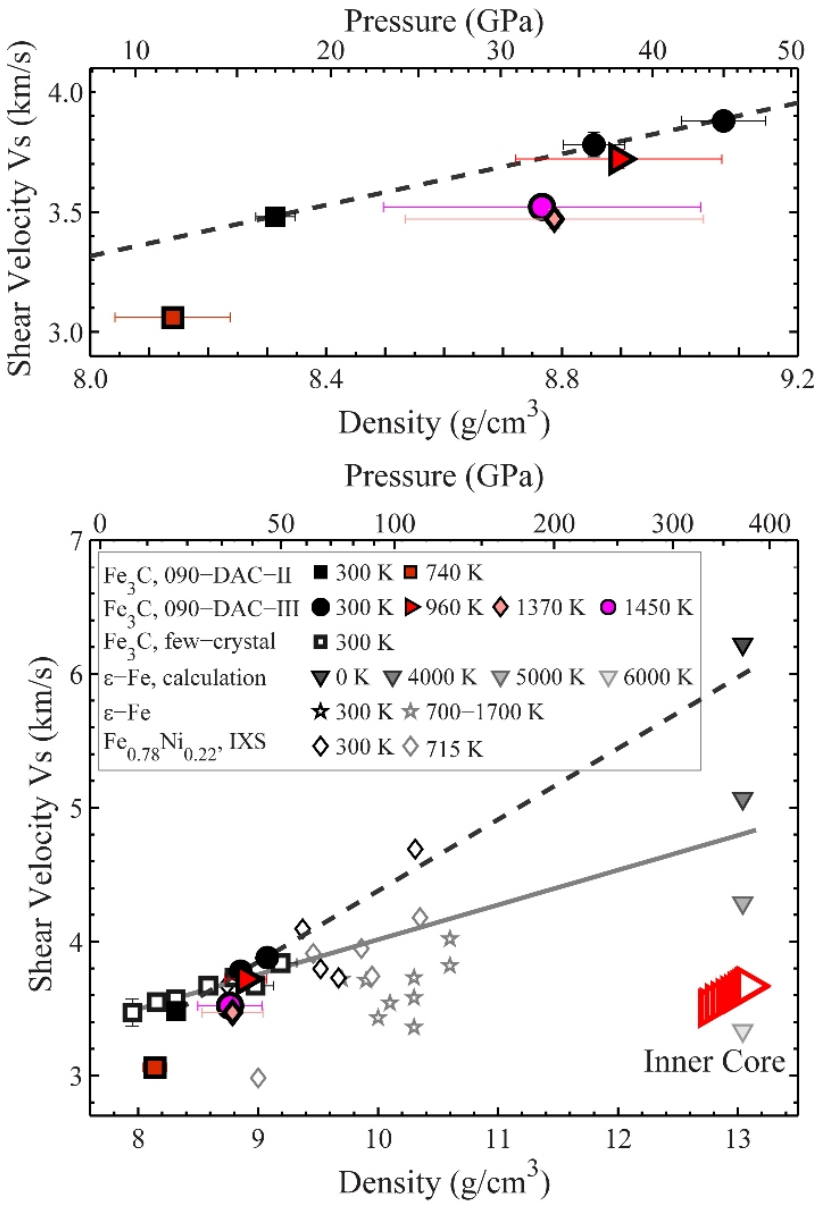

Fig. 6.2. (a) Shear velocity V_S of Fe_3C at high temperatures and high pressures from this study. The uncertainties in V_S (Table 6.1) are smaller than symbol sizes. (b) Shear velocity of Fe_3C in comparison with other Fe-bearing materials. The V_S of $^{57}Fe_3C$ derived from NRIXS data in this study and in Gao *et al*. (2008) are converted to that of natural Fe_3C (see section 6.3.2 for details). The dashed line in (a) represents a linear fit of V_S versus density ρ at ambient temperature. Data sources: Fe_3C (this study); Fe_3C, few-crystal (Gao *et al*., 2008); $Fe_{0.78}Ni_{0.22}$, IXS (Kantor *et al*., 2007); ε-Fe (Lin *et al*., 2005a); ε-Fe, calculation (Steinle-Neumann *et al*., 2001); inner core (large open triangles) (Dziewonski and Anderson, 1981).

Table 6.1. Sound velocity of Fe_3C at high pressures and high temperatures.

P (GPa)	T (K)	ρ (g/cm^3)	V_P (km/s)	V_S (km/s)	K_T (GPa)	G (GPa)	Poisson's Ratio
			Run 090-DAC-II				
17(1)[1]	300	8.31(3)	7.00(6)	3.48(3)	268(9)	99(2)	0.336(5)
15(1)[2]	740(80)	8.1(1)	6.6(2)	3.06(3)	249(18)	75(1)	0.364(9)
			Run 090-DAC-III				
36(2)[3]	300	8.85(5)	7.95(9)	3.78(5)	368(17)	120(3)	0.353(6)
45(6)[4]	960(100)	8.9(2)	8.1(3)	3.72(4)	409(45)	121(2)	0.37(2)
45(6)[4]	1450(80)	8.8(3)	8.0(4)	3.52(5)	404(59)	107(3)	0.38(2)
45(5)[4]	1370(100)	8.8(3)	7.9(4)	3.47(4)	405(53)	104(2)	0.38(1)
45(3)[5]	300	9.07(7)	8.2(1)	3.88(2)	416(22)	134(1)	0.355(6)

Data points in each run are listed in temporal order (following the P-T path). Density is that of natural Fe_3C (not ^{57}Fe-enriched). Numbers in parentheses are uncertainties in the last digit(s).

[1] Pressure is measured based on NaCl (Dorogokupets and Dewaele, 2007). Uncertainty in P is estimated as the pressure difference before and after NRIXS experiments, which is larger than the difference between ruby-based (Dewaele *et al*., 2004) and NaCl-based (Dorogokupets and Dewaele, 2007) pressures.

[2] Pressure is measured based on NaCl (Dorogokupets and Dewaele, 2007). Uncertainty in P is from the uncertainty in lattice parameter of NaCl, originating from the difference in lattice parameters based on (111) and (200) peaks.

[3] Pressure is based on ruby alone (Dewaele *et al*., 2004). The uncertainty was estimated from the difference between the two ruby balls.

[4] Pressure was measured after heating at ambient temperature, without correction for thermal pressure. The uncertainty includes the estimated thermal pressure (see text for details) and half of the pressure change before and after heating.

[5] Pressure is measured based on NaCl (Fei *et al*., 2007). Uncertainty in P is estimated as the pressure difference between ruby-based (Dewaele *et al*., 2004) and NaCl-based (Fei *et al*., 2007) pressures.

6.3.3 Uncertainty Analysis

Due to the lack of data, thermal expansion coefficient α, Grüneisen parameter γ, and the temperature dependence of bulk modulus $\partial K/\partial T$ of Fe_3C are allowed to vary over the entire range of the known values for Fe-rich materials (Chen *et al*., 2008, and references therein). This is one of the largest contributing factors for uncertainties in density and sound velocities in this study. Another major contributing factor of uncertainty is from the pressure determination in run

090-DAC-III. In this run, the pressure changed from 36 GPa at 300 K to 45 GPa at 300 K after NRIXS measurements at high temperatures as well as 300 K were completed (Table 6.1). The sample was quenched between the NRIXS data collections at ~ 960 K and at ~ 1450 K (Table 6.1). Since the pressures at high temperatures were not directly measured in this run, we used the pressure measured after heating without thermal correction and applied large uncertainty. The uncertainty is based on a combination of the isochoric thermal pressure and the pressure change over heating. The isochoric thermal pressure was estimated following the method by Audrault *et al*. (1998). Whether the pressure increases or decreases upon heating is unclear. It has been indicated that the *P*-*T* path in a laser-heated DAC may be dependent on gasket material, sample preparation and loading and the DAC itself (e.g., Kavner *et al*., 2001). Both temperature-induced pressure increase (e.g., Audrault *et al*., 1998; Kavner *et al*., 2001) and decrease (Kavner *et al*., 2001) have been observed in experiments with stainless-steel gaskets (Audrault *et al*., 1998; Kavner and Duffy, 2001) and Re gaskets (Kavner and Duffy, 2001). In run 090-DAC-II in this study where Be gasket with cBN insert was used, the pressure decreased from 17 GPa to 15 GPa (Table 6.1).

To acquire accurate information on pressures and densities of samples at high temperatures, *in situ* pressure measurement is needed. The XRD setup at sector 3 of the APS has been demonstrated to be useful in on-line pressure measurement. This setup has been used in this study in the 090-DAC-II run for pressure calibration. The density of Fe_3C acquired using X-ray diffraction method with this setup (Table 7.2) agrees with the values estimated based on the equation of state (Scott *et al*., 2001) within 0.3 %. To utilize this setup with an incident X-ray phonons energy of 14.4125 keV (^{57}Fe resonance energy, λ = 0.8603 Å), large opening in the diamond anvil cell is required to acquire sufficient signals (Gao *et al*., 2009).

We evaluated the propagated uncertainties from pressure P, temperature T, EoS parameters and statistical uncertainties in NRIXS spectra to density ρ, adiabatic bulk modulus K_S and sound velocities V_P and V_S. The results are shown in Fig. 6.3. The uncertainty term for density due to the correlation between K_0 and K' is estimated as following:

$$\sigma_{\rho}^{2} = \left(\frac{\partial\rho}{\partial K_0}\sigma_{K_0}\right)^2 + \left(\frac{\partial\rho}{\partial K'}\sigma_{K'}\right)^2 + \left(\frac{\partial\rho}{\partial V_0}\sigma_{V_0}\right)^2 + \ldots$$
$$+2Corr(K_0, K')\frac{\partial\rho}{\partial K_0}\frac{\partial\rho}{\partial K'}\sigma_{K_0}\sigma_{K'} \quad (6.6)$$

where σ is the uncertainty and $Corr(K_0, K')$ is the correlation coefficient between K_0 and K'. We applied $Corr(K_0, K')$ of -0.95, within the range of -0.90 to -0.95 reported by Angel (2000). The uncertainties for V_P and V_S originated from the correlation between K_0 and K' are estimated in the same method. In this study, the dominant sources for uncertainties in ρ, V_P and V_S are not from K_0 and K'. However, when K_0 and K' are the dominant sources for uncertainties, the correlation between K_0 and K' is not negligible. The propagated uncertainties from K_0 and K' alone without the correlation between K_0 and K' taken into account can be 3 times larger compared to when the correlation between K_0 and K' is considered.

For density ρ, the major contribution of uncertainty is from the thermal expansion coefficient (Fig. 6.3b). It is clear that V_S is mostly dependent on V_D, since the uncertainty of V_S is dominated by the uncertainty of V_D (Fig. 6.3d). Despite that we applied large uncertainties to the assumed thermal EoS parameters of α, γ and $\partial K/\partial T$ (Fig. 6.3a), the uncertainties propagated from these sources to V_S (Fig. 6.3d) are small. This allows us to acquire accurate knowledge of V_S from V_D, even when accurate knowledge on thermal EoS parameters is unavailable. On the other hand, the constraint on V_P from V_D is limited because uncertainty of V_P is dominated by the contributions from pressure P, ambient EoS parameters K_0 and K' and thermal EoS parameters (Fig. 6.3c). The strong constraint on V_S and weak constraint on V_P from V_D have also been pointed out previously (Mao *et al*., 2004; Sturhahn and Jackson, 2007). For this reason, we will focus our discussion on V_S in the following context.

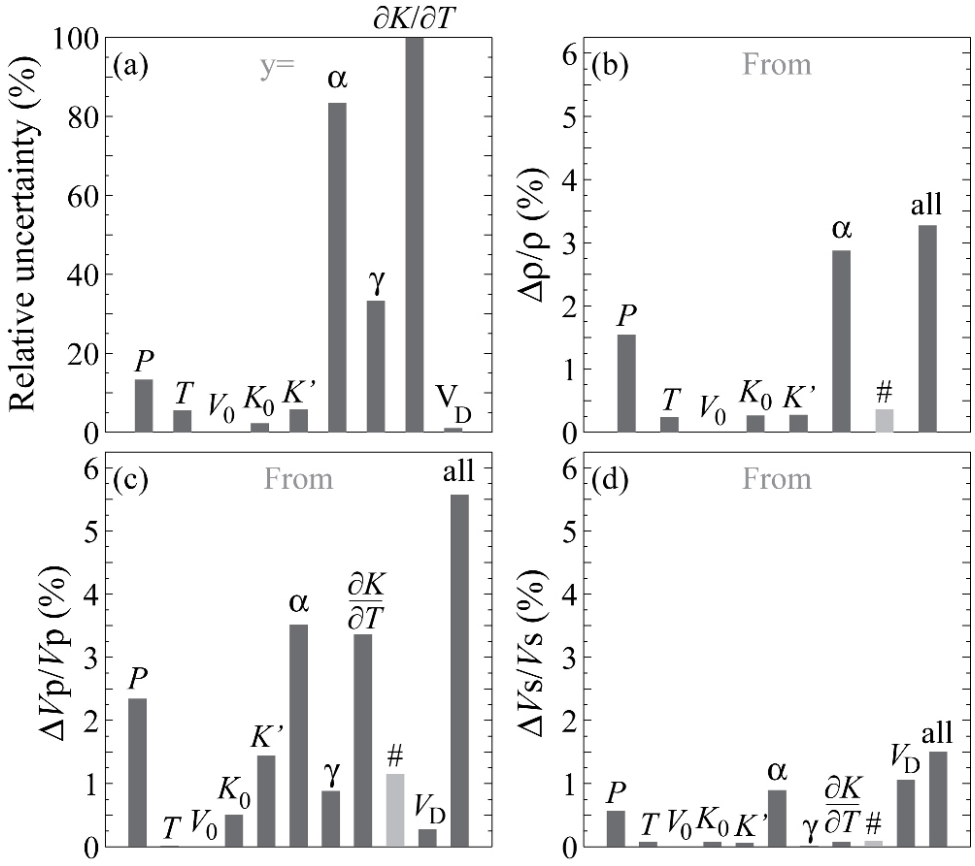

Fig. 6.3. Sources of uncertainty for the data point at 45 GPa and 1450 K in run 090-DAC-III. (a) Relative uncertainties of P, T and EoS parameters. Due to the lack of data, the thermal expansion coefficient α, Grüneisen parameter γ, and the temperature dependence of bulk modulus $\partial K/\partial T$ of Fe_3C are allowed to vary over the entire range of the known values for Fe-rich materials (Chen *et al*., 2008, and references therein). The uncertainty in V_D represents the uncertainty from PDoS alone. (b) (c) (d) Relative uncertainty in density ρ, V_P and V_S resulting from each source. 'all' represents the uncertainty with all sources considered. # represents the contribution from the correlation between K_0 and K' (see text for details).

6.3.4 Sound Velocities and Thermal Effect

Compared to the compressional velocities measured using inelastic scattering method (Fiquet *et al*., 2009), our results are consistent within 2 %. Compared to the ambient-temperature V_P and V_S on a Fe_3C sample reported in a previous NRIXS study on a sample composed of one or a few single crystal(s) (will be referred to as 'few-crystal' sample) (Gao *et al*., 2008), the values from

this study (Table 6.1, Fig. 6.2) are similar: V_P are consistent within ~ 2 %, and V_S are consistent within ~ 1 %. The strong anisotropy in sound velocities of Fe_3C observed at ambient conditions (Gao *et al*., 2009) is not observed at high pressures in this study. The shear sound velocities of the powder samples of Fe_3C at 300 K in this study can be described as a functions of density: V_S (km/s) = − 0.94 + 0.53ρ (g/cm^3). The extrapolated V_S to the inner core pressures at 300 K are higher than the seismically observed values in the PREM (PREM) by ~ 60 %. Compared to the V_S versus density slope of 0.24 (km/s)/(g/cm^3) in a previous NRIXS study on a few-crystal sample (Gao *et al*., 2008), the slope on the polycrystalline samples in this study is much higher. This discrepancy may be partially due to the limited amount of data points in this study (three data points) hence weak constraint on the slope. The extrapolated results may be revised when more data points at higher pressures are available in the future. This discrepancy may also be partially due to possible directional dependence of shear velocities of Fe_3C at high pressures.

Compared to the V_S at 300 K, the V_S at high temperature are lower by ~ 2 (±2) % at 960 K and 45 GPa, to ~ 7(±6) % at 1450 K and 1370 K at 45 GPa, and to ~ 10(±3) % at 740 K and 15 GPa. The temperature induced velocity decrease has been observed previously in an NRIXS study on ε-Fe (Lin *et al*., 2005a) to high temperatures of 1700 K. At the pressures of the Earth's inner core, a theoretical calculation study (Steinle-Neumann *et al*., 2001) also indicates significant thermal reduction on shear sound velocities. In an IXS study on $Fe_{0.78}Ni_{0.22}$ (Kantor *et al*., 2007) up to 715 K and 72 GPa, no systematic temperature induced sound velocity reduction was reported at pressures higher than 22 GPa although large sound velocity reduction was observed for both V_P and V_S at ~ 22 GPa (corresponding to a density of 9.0 g/cm^3 for $Fe_{0.78}Ni_{0.22}$) (Kantor *et al*., 2007).

The temperature effect in Fe_3C is observed to be larger at lower density (at lower pressure of ~ 15 GPa) and smaller at higher density (at higher pressure of ~ 45 GPa). This pressure dependence of temperature effect was also observed in a previous NRIXS study on Fe (Lin *et al*., 2005a). This can be partially explained by the density change: as $V_S^2 = G/\rho$, V_S decreases as the density ρ increases. This may also indicate that the temperature effect on G decreases as pressure increases. Our results also suggest that the temperature effect may increase as temperature increases, based on the data points at 940 K and 15 GPa versus the data points at 1450 K / 1370 K and 45 GPa. This is consistent with the results from a previous calculation study (Steinle-

Neumann *et al*., 2001) (Fig. 6.2). This indicates that the temperature effect on G increases as temperature increases. The average temperature induced shear velocity decrease in this study is ~ 1 % / 100 K. For this rate, an inner core temperature of ~ 6000 K can reconcile the ~ 60 % difference between the observed V_S of the inner core (Dziewonski and Anderson, 1981) and the estimated V_S of Fe_3C at relevant P-T conditions. This estimate depends on the investigated P-T range. To place more stringent constraints on the temperature effect at inner-core P-T conditions, measurements at more relevant P-T conditions are needed in future studies.

6.4 CONCLUSIONS

We have carried out NRIXS measurements on Fe_3C to high temperatures and high pressures of 1450 K and 45 GPa. Combining the partial phonon density of states of iron in Fe_3C derived from the NRIXS data with existing 300-K equation of state (Scott *et al*., 2001) and typical thermal expansion parameters, sound velocities of $^{57}Fe_3C$ were derived. To compare the measured sound velocity of $^{57}Fe_3C$ to the observed values in the Earth's interior, the sound velocity should be converted to those of natural Fe_3C (not ^{57}Fe-enriched). This procedure was discussed in section 6.3.2.

Within our investigated pressure and temperature range, the observed temperature induced shear velocity decrease is 2 - 10 %, with an average rate of ~ 1 % / 100 K. To reconcile the ~ 60 % difference between the observed V_S of the inner core (Dziewonski and Anderson, 1981) and the estimated V_S of Fe_3C at relevant P-T conditions based on the 300-K data in this study, an inner core temperature of ~ 6000 K is needed for a sound velocity decrease rate of 1 % / 100 K. This temperature is within the expected range (e.g., Li and Fei, 2007, and references therein), indicating that it is possible that Fe_3C may match the V_S of the inner core at inner-core pressure-temperature conditions. Our results also indicate that the temperature effect may increase as temperature increases and decrease as pressure increases. The temperature estimate of ~ 6000 K may be revised when more data become available in future.

Chapter 7[3]

Experimental Aspects on Simultaneous X-ray diffraction and Nuclear Resonant Scattering

7 ABSTRACT

The applications of nuclear resonant scattering in laser-heated diamond anvil cells have provided an important probe for the magnetic and vibrational properties of ^{57}Fe-bearing materials under high pressure and high temperature. Synchrotron X-ray diffraction is one of the most powerful tools for studying phase stability and equation of state over a wide range of pressure and temperature conditions. Recently an experimental capability has been developed for simultaneous nuclear resonant scattering and X-ray diffraction measurements using synchrotron radiation. Here the application of this method to determine the sound velocities of compressed Fe_3C is shown. The X-ray diffraction measurements allow detection of microscale impurities, phase transitions and chemical reactions upon compression or heating. They also provide information on sample pressure, grain size distribution and unit cell volume. By combining the Debye velocity extracted from the nuclear resonant inelastic X-ray scattering measurements and the structure, density and elasticity data from the X-ray diffraction measurements simultaneously obtained, more accurate sound velocity data can be derived. Our results on few-crystal and powder samples indicate strong anisotropy in the sound velocities of Fe_3C under ambient conditions.

7.1 INTRODUCTION

Nuclear resonant scattering (NRS) methods, including synchrotron Mössbauer spectroscopy (SMS) and nuclear resonant inelastic X-ray scattering (NRIXS), utilize synchrotron radiation with meV energy resolution to probe the magnetic structures and vibrational properties of

[3] This chapter is based on the published article: Gao, L., Chen, B., Lerche, M., Alp, E.E., Sturhahn, W., Zhao, J., Yavaş, H. and Li, J. (2009) Sound velocities of compressed Fe_3C from simultaneous synchrotron X-ray diffraction and nuclear resonant scattering measurements. *J. Synchrotron Rad.*, 16, 714722, doi:10.1107/S0909049509033731.

resonant isotopes (Sturhahn, 2004). A commonly used resonant isotope is ^{57}Fe. Combined with diamond anvil cells (DACs) and laser heating techniques, NRIXS and SMS have been widely used to probe the elastic, thermodynamic and magnetic properties of iron-bearing materials under high pressures (e.g., Mao *et al*., 2001; Lin *et al*., 2003a, 2004b; Mao *et al*., 2004; Sturhahn and Jackson, 2007; Gao *et al*., 2008) and at high temperatures (Shen *et al*., 2004; Lin *et al*., 2005a, b). In a recent review paper, Sturhahn and Jackson (2007) explained the basics of the NRS methods and summarized their geophysical applications in determining sound velocity, Grüneisen parameter, valence and spin state, and magnetic ordering of iron-bearing materials at high pressure.

An important application of the NRIXS technique is measuring the sound velocities of opaque samples under high pressure. From the NRIXS spectra, the partial phonon density of states (PDoS) of iron can be extracted. A parabolic fit to the PDoS at the low-energy region gives the Debye sound velocity V_D, which is related to the compressional wave velocity V_P and shear wave velocity V_S (Hu *et al*., 2003). X-ray diffraction (XRD) is a classical method for investigating the structures of crystalline solids. With brilliant and focused synchrotron X-ray sources, the XRD method has been widely used for equation-of-state (EoS) studies under high pressure. Combining V_D from NRIXS measurements and ρ and K_S from separate XRD experiments, the sound velocities of a number of iron-rich alloys have been derived (Mao *et al*., 2001; Mao *et al*., 2004; Lin *et al*., 2003a, 2004b, 2005a; Gao *et al*., 2008).

Recently, a new experimental capability has been established at beamline 3-ID-B of the Advanced Photon Source (APS), Argonne National Laboratory (ANL), allowing for simultaneous XRD and NRS measurements of compressed samples in the panoramic DAC. In this paper, we describe the new XRD set-up, focusing on the importance of simultaneous XRD and NRIXS measurements for determining sound velocities at high pressures and high temperatures.

7.2 EXPERIMENTS

The experimental set-up at beamline 3-ID-B consists of integrated NRS and XRD instruments that are compatible with the laser-heated DAC technique (Fig. 7.1).

7.2.1 Nuclear Resonant Scattering

The NRS techniques include SMS and NRIXS. Mössbauer experiments in the time domain have been reported as early as the 1960s (Lynch *et al*., 1960). More than 20 years later, the feasibility of Mössbauer experiments in the time domain using a synchrotron source was demonstrated (Gerdau *et al*., 1985). In the 1990s, the first NRIXS experiments were conducted (e.g., Seto *et al*., 1995; Sturhahn *et al*., 1995). Both SMS and NRIXS require a photon source with a defined time structure and high flux. With the advent of the third-generation synchrotron sources, these types of experiments are readily achievable.

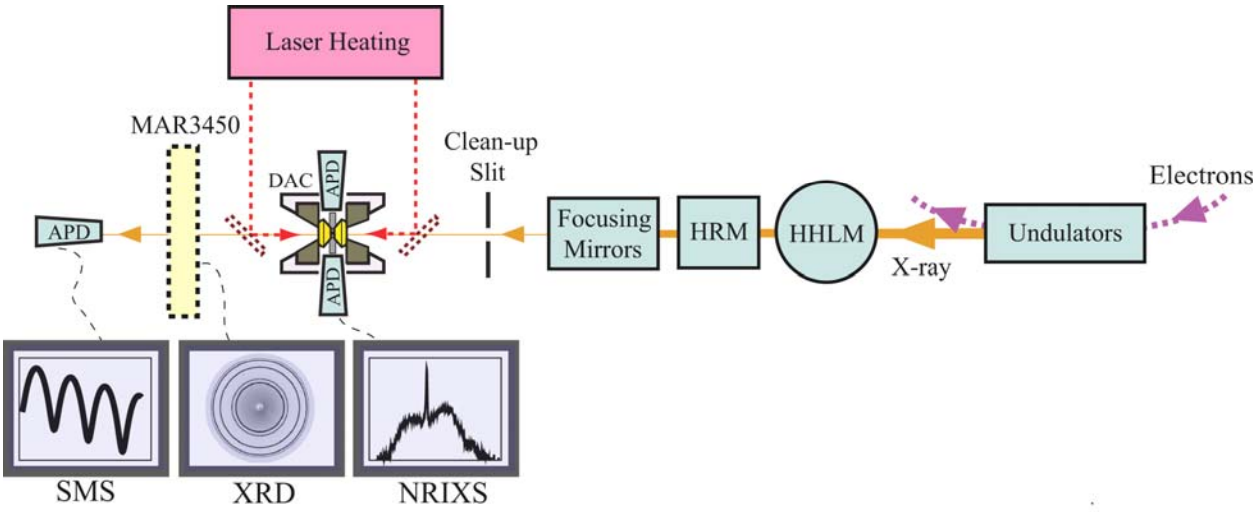

Fig. 7.1. Experimental set-up at beamline 3-ID of the Advanced Photon Source at Argonne National Laboratory, showing the optics including high-heat-load-monochromator (HHLM) and high-resolution monochromator (HRM), the instruments on the lower deck including those for nuclear resonant inelastic X-ray scattering (NRIXS), X-ray diffraction (XRD) and synchrotron Mössbauer spectroscopy (SMS), and the laser-heating system on the upper deck. The sample is mounted in a diamond anvil cell (DAC) for high-pressure experiments. Three avalanche photodiode (APD) detectors collect NRIXS signals within a plane that is perpendicular to the synchrotron radiation source, along the radial direction of the DAC. One APD detector records SMS signals in the forward direction, along the axial direction of the DAC. The MAR3450 image plate can be moved in for XRD measurements or out for SMS measurements.

The NRIXS and SMS set-ups in our measurements are similar to those described by Sturhahn and Jackson (2007). The laser-heating set-up is described by Zhao *et al*. (2004) and Lin *et al*. (2005b). NRS experiments at the undulator beamline 3-ID-B are carried out during standard

operating mode, with the 102 mA accelerator ring current evenly distributed over 24 electron bunches. The ring current is kept constant by a continuous 'top-up' at intervals of 2 min. The individual electron bunches are spaced 153 ns apart. Two undulators with a combined length of 4.8 m and a period of 27 mm are used. With a deflection parameter of $K = 0.65$, a photon beam at 14.41 keV can be generated at the first harmonic, providing a total flux of 10^{17} photons s^{-1} over a bandwidth of 500 eV.

NRS experiments require a small energy bandwidth in the incident X-ray beam (e.g., Sturhahn, 2004). This is achieved by two successive monochromators: a water-cooled high-heat-load monochromator (HHLM) and a high-resolution monochromator (HRM) (Toellner, 2000). The HHLM consists of two diamond (111) crystals of size ~ 4.5 mm × 8 mm. From the incident beam, it selects photons of ~ 14.41 keV with an energy bandwidth of ~ 1.1 eV. The X-ray beam coming out of the HHLM has a flux of 1.5×10^{13} photons s^{-1} eV^{-1}. The HRM, composed of four silicon crystals, further reduces the bandwidth to 1 meV (Toellner *et al*., 2006) and the X-ray flux to 4.5×10^{9} photons s^{-1} over the 1 meV bandwidth.

The X-ray beam needs to be focused to match the small sample size in high-pressure experiments utilizing DACs. A bimorph mirror with 16 electrode elements focuses the beam in the horizontal direction (Signorato *et al*., 1998). In the vertical direction, the beam is focused with an actively bent mirror in a Kirkpatrick–Baez arrangement (Eng *et al*., 1998). The focused beam is ~ 10 mm in both horizontal and vertical directions. To block unwanted background from small-angle scattering, a pair of clean-up slits is placed between the focusing mirrors and the sample.

The NRS scattering signals from the sample are collected using silicon avalanche photodiode (APD) detectors (e.g., Kishimoto, 1992; Toellner *et al*., 1994; Baron and Ruby, 1994; Sturhahn, 2004). In NRIXS experiments, three APD detectors are placed around the sample in a plane that is perpendicular to the X-ray beam. They collect delayed photons produced in the nuclear decay process, including the directly emitted nuclear fluorescence photons at 14.4 keV and the K_α fluorescence photons at 6.4 keV (e.g., Seto *et al*., 1995). One APD detector is placed along the beam to collect photons at 14.4 keV in the forward direction. Each APD detector has an area of 10 mm × 10 mm and a typical time resolution of ~ 1 ns (Sturhahn, 2004). The efficiency of the

APD detectors is ~ 80 % for the 6.4 keV photons and ~ 22 % for the 14.4 keV photons. The efficiency can be improved by tilting the detector to increase the X-ray path inside the detector.

A statistically meaningful NRIXS spectrum requires hours to days of data collection. Generally, a number of one-hour NRIXS spectra are collected and added together. The count rate depends on the sample size and geometry. With the incident beam along the axial direction of the DAC, a thick sample with a small diameter gives the highest count rate. The count rate usually decreases upon compression as the sample becomes thinner and larger, resulting in a smaller sample volume exposed to the X-ray and stronger self-absorption of the NRIXS signals. At high temperature, the count rate increases owing to enhanced phonon excitation.

7.2.2 X-ray Diffraction

Recently, an angular-dispersive XRD instrument was established and integrated with the NRIXS, SMS and laser heating set-ups at beamline 3-ID-B (Fig. 7.1). A MAR3450 image plate, placed between the downstream mirror of the laser-heating system and the APD for SMS measurements, records the XRD signals. It can be moved into or out of the X-ray path using computer-controlled motors. In this study, the XRD data collection time ranges from 50 s at ambient conditions to 10 min at 17 GPa and ~ 1000 K.

For measurements on iron-bearing materials, the incident X-rays are tuned to 14.4125 keV (λ = 0.86025 Å). This low energy limits the accessible range of 2θ. For high-pressure studies, the accessible range of 2θ depends on the configuration of the DAC and the size and position of the image plate. Our DACs have an opening angle of 60º. We used two types of tungsten carbide (WC) seats, one with a 1.0 mm circular opening and therefore a 30º opening angle, and the other with a 2.3 mm-long slot opening and therefore a 60º maximum opening angle (Fig. 7.2). With a typical diamond thickness of 2.2 mm, these seats allow ~ 26º and ~ 55º access to the sample inside the cell. We consider these angles as the effective opening angles of the cells. The image plate is 345 mm in diameter and located ~ 320 mm away from the sample, covering a ~ 60º angular range when centered with the sample. It can be moved off-center to cover as much as 120º opening angle. The accessible range of 2θ is, therefore, not limited by the image plate. To maximize the 2θ range, we use the slot WC seat on the downstream side of the cell. With the X-ray beam aligned with the axial direction of the cell, the maximum allowed 2θ is half of the

effective opening angle, i.e. 13º for the seat with 1.0 mm circular opening and 27.5º for the slot seat.

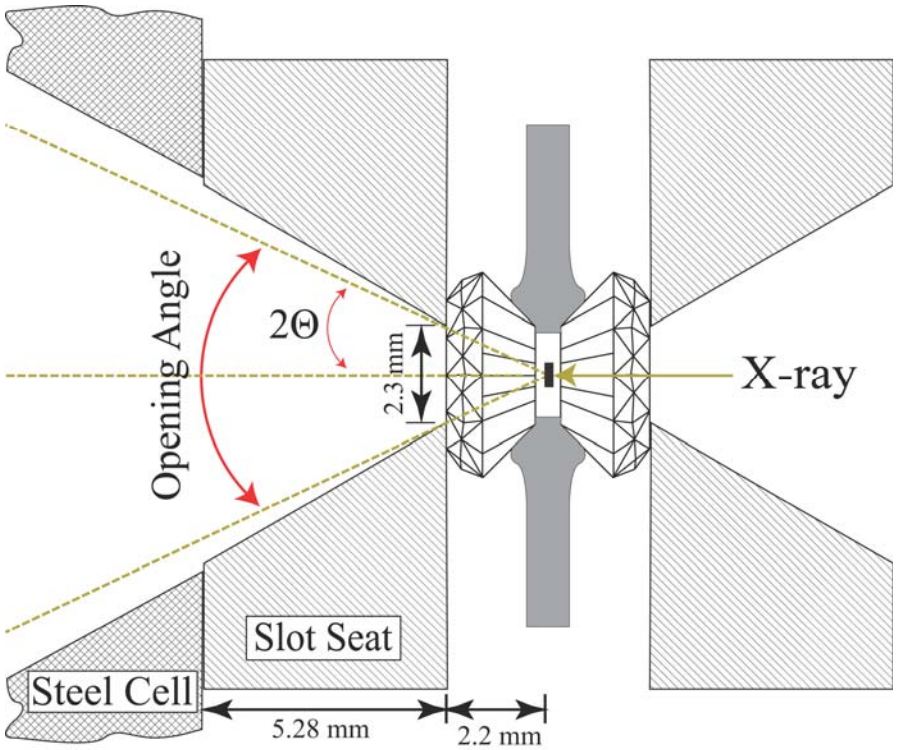

Fig. 7.2. Schematic view of the DAC configuration, showing its effective opening angle and the range of 2θ accessible to the XRD measurements. See text for details.

At 14.4125 keV, a maximum 2θ of 27.5º corresponds to a minimum d-spacing of 1.810 Å, according to Bragg's law, $2d\sin\theta = \lambda$. At ambient conditions, the major diffraction peaks of Fe_3C have d-spacings at 2.014 Å to 1.973 Å, and the major diffraction peak of NaCl has a d-spacing of 2.570 Å. With the current beam and cell configurations, we can observe most of the major peaks of Fe_3C and NaCl. As the d-spacing decreases with increasing pressure, however, the limited range of accessible d-spacing would hinder the use of the XRD set-up for measuring sample pressure, structure and lattice parameters.

To expand the accessible 2θ range, we could rotate the DAC so that the X-ray enters along the side of the seat opening, instead of through its center. This could potentially double the maximum 2θ if we use symmetrical DACs and slot seats on both sides of the cell. When panoramic DACs are used, the long cylinder would put a limit on the accessible 2θ range, and

alternative ways are needed to increase the range. One option is to change the energy of the incident X-ray beam from the undulator source from 14.4125 keV (the first harmonic) to 43.2375 keV (the third harmonic). Increasing the X-ray energy to 43.2375 keV does not increase the maximum 2θ, but would reduce the minimum d-spacing to 0.621 Å. Replacing the WC seats with X-ray-transparent cubic boron nitride (cBN) seats would expand the accessible 2θ range and hence reduce the minimum d-spacing.

7.2.3 Sample Preparation

A number of Fe_3C samples were synthesized from iron and graphite powders (Sigma-Aldrich, #282863) in an MgO capsule, using the piston-cylinder and multi-anvil large volume presses at the University of Illinois. In synthesis runs PC02 and 090, we used 94.45 % ^{57}Fe-enriched iron powder from Cambridge Isotope Laboratories (#FLM-1812-100). In run PC02, we followed the same procedure as described by Li *et al*. (2002). In run 090, a mixture with an atomic ratio of Fe:C = 2.922:1 was equilibrated at 3 GPa and 1373 K for 19 hours. In synthesis run 093, we made fine powder of ^{57}Fe from a piece of ^{57}Fe foil at Argonne National Laboratory by dissolving the foil into hydrochloric acid and nitric acid to form hydroxide, then oxidizing it to Fe_2O_3, and eventually reducing it in H_2 gas to powder with an average grain size of <1 mm. A stoichiometric mixture was equilibrated at 2 GPa and 1373 K for 4 hours.

To examine the purity of the synthesized Fe_3C, we measured their XRD patterns and conventional Mössbauer spectra (CMS) with a 5 mm × 5 mm-sized ^{57}Co γ-ray radioactive source at Sector 3 of the APS. The samples were ground into small grains with an average particle size of ~ 2 mm. We mixed 0.16 mg of the sample with flour to reduce the effective thickness of ^{57}Fe to ~ 3, equivalent to ~ 0.3 mm of $^{57}Fe_3C$. The XRD data (Fig. 7.3) were collected at beamline 11-BM-B of the APS, using a monochromatic X-ray beam that is at least 100 mm in diameter (λ = 0.41416 Å).

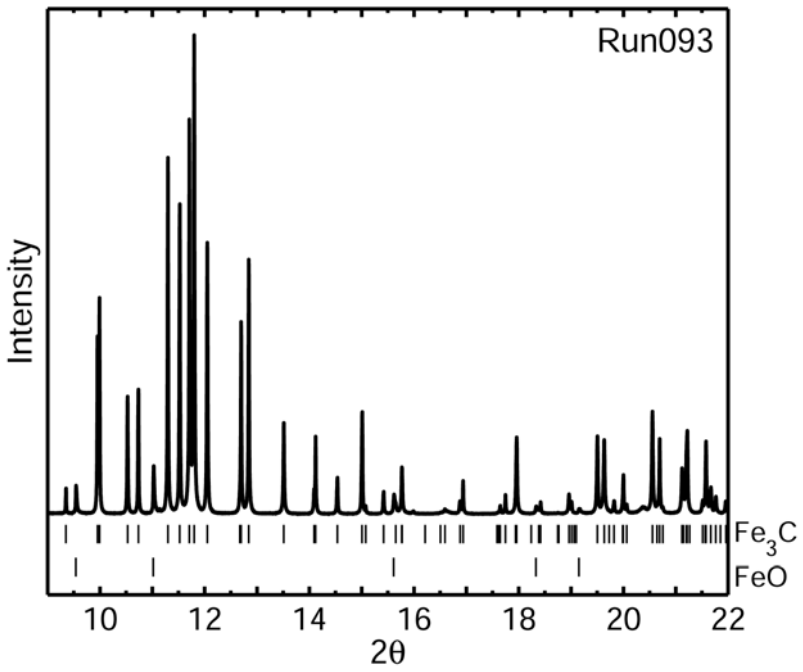

Fig. 7.3. X-ray diffraction spectrum of Fe_3C from synthesis run 093 (λ = 0.41416 Å). Tick marks indicate the expected peak positions of Fe_3C and an impurity phase, which can be indexed as FeO with f.c.c. structure. The integrated intensity of the FeO peaks accounts for < 3 % of the total intensity.

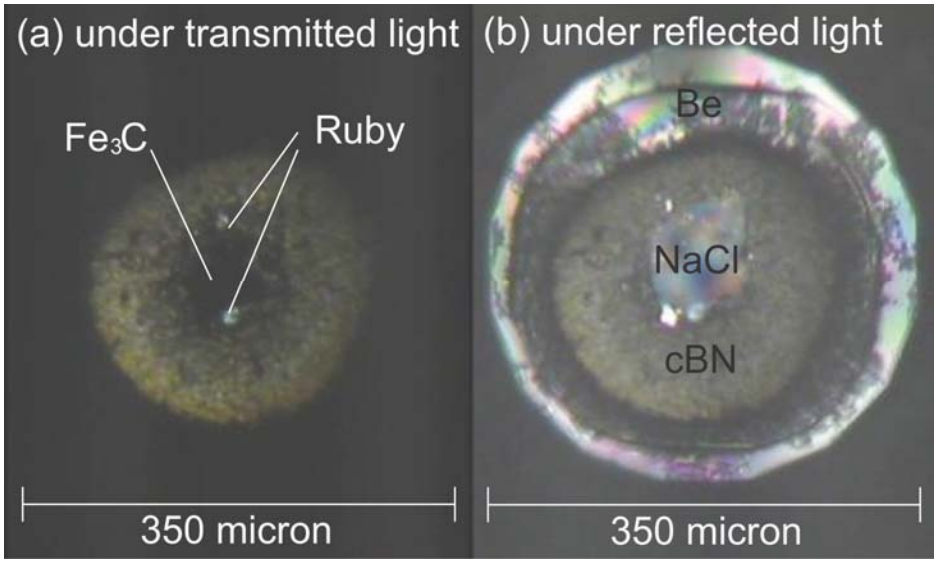

Fig. 7.4. Typical sample configuration in the DAC. The Fe_3C sample is sandwiched between NaCl layers and surrounded by cBN, which is packed inside a beryllium gasket.

Panoramic DACs with X-ray-transparent Be gaskets were used to generate high pressure. To minimize self-absorption of the NRIXS signals by the sample, the sample chamber was kept within a diameter of 70 mm. In some runs, a cBN insert, made from cBN powder (Alfa Aesar, 4-8 mm powder #40607) and epoxy (Versachem Clear Weld Epoxy System, #47609) at a ratio of 4:1 by weight, was used to reduce gasket shrinkage at high pressure (Lin *et al*., 2003b). The Fe_3C sample was sandwiched between two NaCl layers. Ruby balls were placed next to the sample as pressure markers (Fig. 7.4).

7.2.4 NRIXS, SMS, CMS and XRD Data Evaluation

From the NRIXS spectra, the PDoS of Fe in Fe_3C was extracted using the program *PHOENIX* (Sturhahn, 2000). A series of one-hour NRIXS spectra collected under the same pressure and temperature conditions were added together, to obtain sufficient statistics. The Debye sound velocity (V_D) was derived from a parabolic fitting to the low-energy portion of the PDoS, between 3 and 12 meV, following the relation

$$\rho {V_D}^3 = \frac{3\tilde{M}}{2\pi^2\hbar^3}\frac{E^2}{g(E)} \qquad (7.1)$$

where ρ is density, $g(E)$ is the PDoS, $\hbar$ is the reduced Planck's constant and $\tilde{M}$ is the atomic mass of ^{57}Fe.

The *CONUSS* program (Sturhahn, 2000) was used to fit the SMS and CMS spectra, in order to obtain magnetic hyperfine parameters, the percentage of each phase and the sample thickness. The magnetic hyperfine parameters include the magnetic hyperfine field strength (HF), quadrupole splitting (QS) and the isomer shift (IS) between different phases if multiple phases are present.

The image-plate XRD data were analyzed using the *FIT2D* program. We used the *CMPR* program (Toby, 2005) for peak fitting, and calculated the lattice parameters using the weighted least-squares fitting method implemented in the program *UnitCell* (Holland and Redfern, 1997).

7.3 RESULTS AND DISCUSSION

7.3.1 Effect of Impurity on Sound Velocity Measurements

Our SMS measurements of the $^{57}Fe_3C$ from run PC02 revealed iron impurity on the micrometer scale. The amount of excess iron varied from 0 to 90 %, indicating inhomogeneous distribution of the iron impurity in the sample (Fig. 7.5, Table 7.1). The presence of such impurity appears to be related to the large grain size of the ^{57}Fe starting material, as pure Fe_3C was produced when natural iron with smaller grain size was used. If large grains of iron metal in the starting mixture were preferentially loaded into the sample capsule, the actual Fe:C ratio would be higher than that of stoichiometric Fe_3C.

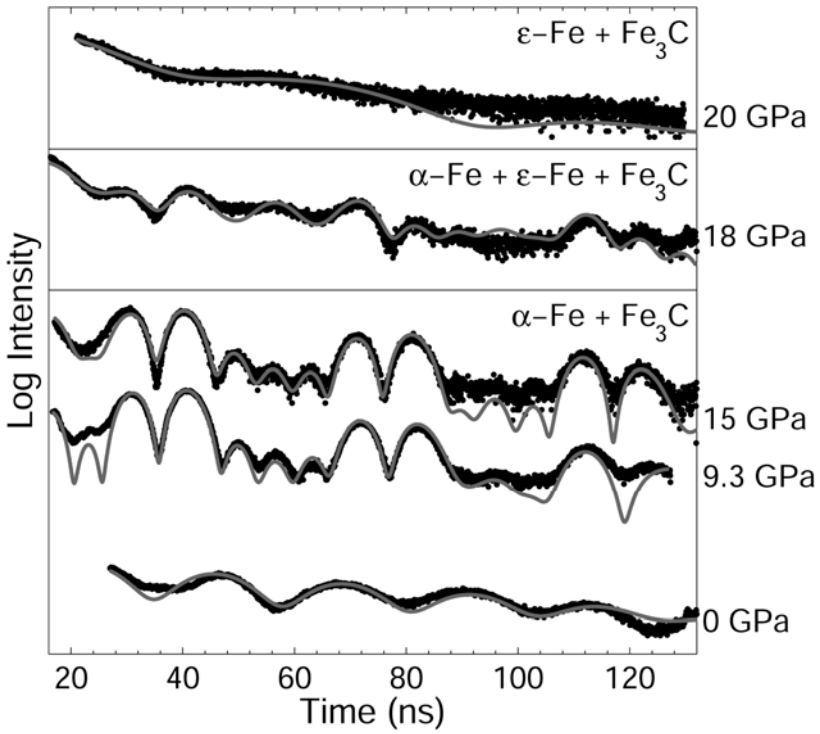

Fig. 7.5. Synchrotron Mössbauer data (black dots) and fit spectra (gray) of almost pure Fe_3C at ambient conditions and an Fe_3C sample containing iron impurity at high pressures (Table 7.1). The presence of iron is clearly indicated by the persistence of fast beats in the SMS spectra between 9.3 and 18 GPa, where Fe_3C is non-magnetic and b.c.c.-iron is magnetic. At 20 GPa, the b.c.c. (α) to h.c.p. (γ) transition and concurrent loss of magnetism in iron is complete, as indicated by the disappearance of fast beats in the SMS spectrum.

Table 7.1 Magnetic hyperfine field parameters of Fe_3C and Fe.

Run ID	*P* (GPa)	Fe_3C			Fe			
		HF (T)	%	QS (mm/s)	HF (T)	%	QS (mm/s)	IS (mm/s)
002-AIR-I	0	20.0(5)	100	0.1(1)	-	-	-	-
002-DAC-I	9.3(1)	0(1)	10(3)	0.1(2)	32.8(3)	90(5)	0.0(1)	0.3(1)
002-DAC-II	15(1)	0(1)	34(5)	0.1(2)	33.0(3)	66(5)	0.0(1)	0.5(1)
002-DAC-II	18(1)	0(1)	53(5)	0.1(2)	33.1(1)	18(5)	0.0(1)	0.5(1)
					1.5(3)	29(5)	1.2(1)	0.5(1)
002-DAC-III	20(1)	01(1)	64(5)	0.2(1)	1.5(5)	36(5)	1.2(1)	0.3(1)

Numbers in parentheses are uncertainties in the last digit(s), estimated from multiple fittings. HF, magnetic hyperfine field; QS, quadrupole splitting; IS, the isomer shift of Fe with respect to Fe_3C in the same loading. Run ID refers to the synthesis run number (002 – PC02) and the loading information (AIR for a free-standing sample and DAC for a sample in a diamond anvil cell).

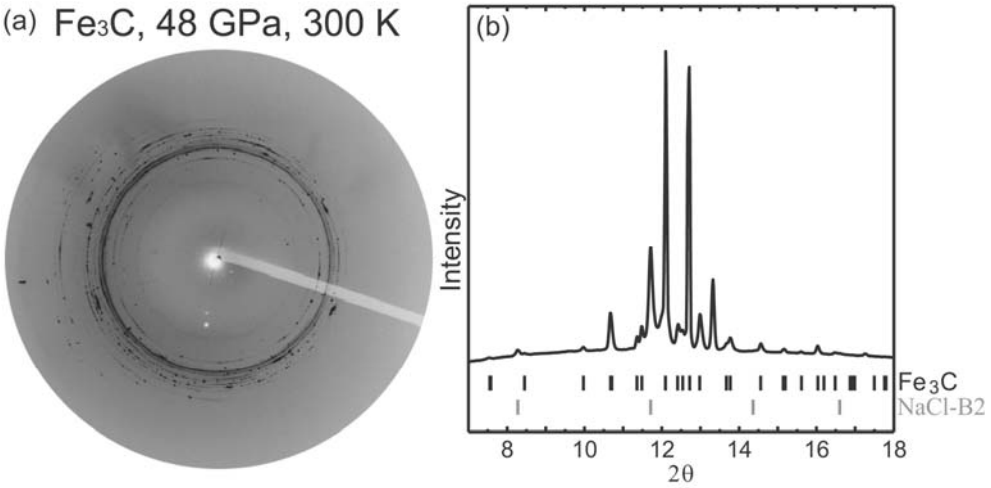

Fig. 7.6. XRD data of a powder Fe_3C sample at 48 GPa and 300 K, after being heated at ~ 1400 K for about three days (run 090-DAC-III). The data were collected at beamline 16-ID-B of the APS (λ = 0.42348 Å). (a) Debye-Scherrer patterns recorded on the image plate. (b) The corresponding spectrum and expected peak positions of Fe_3C and NaCl. The peaks at 13.32º and 17.26º do not belong to Fe_3C or NaCl, but can be matched by h.c.p.-Fe.

The XRD spectrum collected at beamline 11-BM-B of the APS indicates that the product from synthesis run 093 is almost pure Fe_3C at the > 100 mm scale (Fig. 7.3). The sextet in the Mössbauer spectrum also matches ferromagnetic Fe_3C with a hyperfine field of 20.4 (5) T, in

accordance with the known value (e.g., Ron and Mathalone, 1971). Some individual pieces from run 093, however, were found to contain Fe or FeO impurity based on XRD measurements in the DAC. These pieces were discarded. In a high-temperature experiment, iron impurity was not detected at 300 K but appeared after being heated at 1400 K and 48 GPa for three days (Fig. 7.6). Excess iron might have been present as nanometer particles in the synthesized Fe_3C and grew into micrometer-size grains upon heating. On the other hand, if excess carbon was present in the Fe_3C sample, it would react under high temperature to form Fe_7C_3 at pressures above 7 GPa (Bi *et al*., 1993). *In situ* detection of iron impurity is therefore important for measuring the sound velocity of Fe_3C under high pressure and high temperature.

The presence of impurity may be detected on the basis of *in situ* XRD or SMS measurements. The SMS approach works if the impurity has a distinct magnetic property from the sample. At pressures below ~ 14 GPa, iron impurity in Fe_3C can be detected from the Mössbauer spectrum. At high pressures, however, this approach does not work because both iron and Fe_3C are non-magnetic and have similar hyperfine parameters. Compared with XRD, analyzing SMS data is much more time-consuming. The XRD approach is preferred as long as the relevant 2θ range can be accessed.

The effect of the iron impurity on the measured sound velocity of Fe_3C can be evaluated following Sturhahn and Jackson (2007). Given that the Lamb-Mössbauer factors of iron and Fe_3C at 300 K are close to unity, the measured Debye sound velocity (V_D) of an Fe_3C sample containing an iron impurity with a concentration α can be approximated as

$$\frac{V_D}{V_{D,\,Fe_3C}} = \left\{ \frac{\left[(1-\alpha)+\alpha\xi\right]\left[(1-\alpha)+\alpha\rho_{ratio}\right]}{(1-\alpha)+\alpha\xi\eta} \right\}^{1/3} \qquad (7.2)$$

where $\xi = f_{Fe} / f_{Fe3C}$, $\eta = (\rho_{Fe} V^3_{D,Fe3C}) / (\rho_{Fe,Fe3} V^3_D)$, $\rho_{raito} = \rho_{Fe} / \rho_{Fe3C}$, f is the Lamb-Mössbauer factor, ρ is the density, V_D is the measured Debye sound velocity and $V_{D,Fe3C}$ is the actual Debye sound velocity of Fe_3C.

The value of ρ_{ratio} is ~ 1.05 between b.c.c.-Fe and Fe_3C, and ~ 1.09 between h.c.p.-iron and Fe_3C. For conceivable V_D, Fe_3C that is 15 % smaller or larger than that of the Fe (Mao *et al*., 2001), falls between ~ 0.6 and ~ 1.7. Assuming $\xi = 1$, which is reasonable for most iron-bearing

materials under high pressure, 10 % and 50 % iron impurity would introduce an error of ~ 2 % and ~ 9 % in the measured Debye sound velocity, respectively (Fig. 7.7). The measured V_D is larger than the actual value for $\eta < 1$, and smaller for $\eta > 1$. These results suggest that a small amount of iron impurity (> 10 %) has a negligible effect on the measured Debye sound velocity of Fe_3C at 300 K. The effect may be significant if the X-ray beam probes an iron-rich portion of the sample.

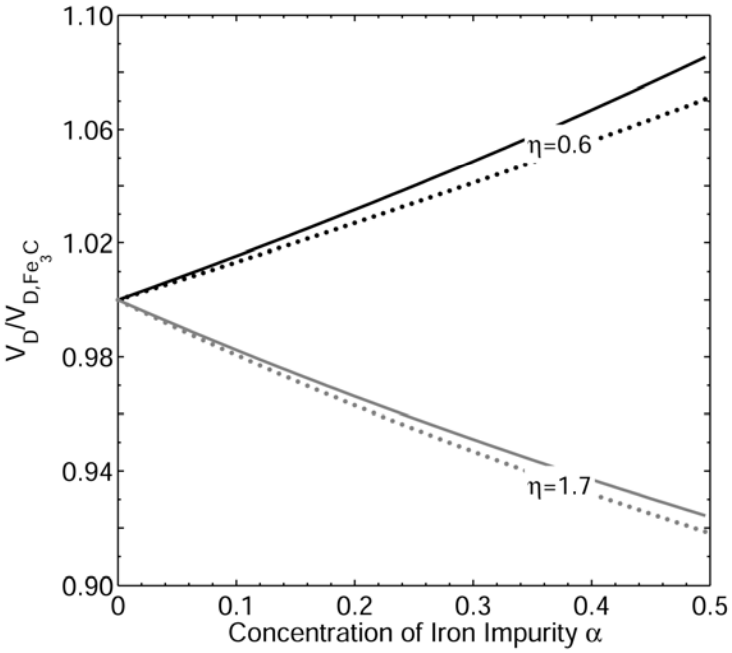

Fig. 7.7. The effect of iron impurity on the measured Debye sound velocity of Fe_3C for a conceivable range of η between 0.6 and 1.7. The ratio between measured and actual Debye sound velocity $V_D = V_{D,Fe3C}$ deviates from 1 as the concentration of iron impurity (α) increases. The density ratio between iron and Fe_3C (ρ_{ratio}) is ~ 1.05 for b.c.c.-iron (solid curves) and ~ 1.09 for h.c.p.-iron (dotted curves). The measured V_D is larger than the true value of $V_{D,Fe3C}$ for $\eta = 0.6$, and smaller for $\eta = 1.7$.

7.3.2 Sound Velocities from Simultaneous PDoS and EoS Measurements

The XRD spectra collected at ambient conditions and 48 GPa reveal that at the micrometer scale our Fe_3C sample consists of a few single crystals in some runs and behaves like powder in others (Fig. 7.6, Fig. 7.8). We measured NRIXS spectra and derived the PDoS of a few-crystal Fe_3C sample between ambient conditions and 50 GPa at 300 K, and that of a powder Fe_3C

sample at ambient conditions (Fig. 7.9).

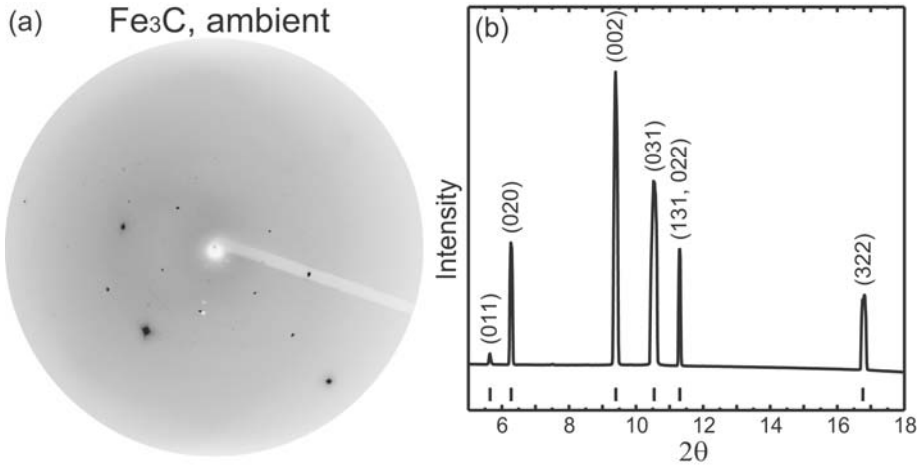

Fig. 7.8. XRD data of a few-crystal Fe_3C sample in a panoramic DAC, under ambient conditions before compression (run 090-DAC-I). The data were collected at beamline 16-ID-B of the APS (λ = 0.3694 Å). (a) Spotty X-ray diffraction pattern recorded on the image plate. (b) The corresponding spectrum and expected peak positions (tick marks).

Combining the PDoS and the existing EoS data (Scott *et al*., 2001; Li *et al*., 2002), we determined the compressional velocity V_P and shear wave velocity V_S (Fig. 7.10) using the following relations

$$\frac{3}{V_D^3} = \frac{1}{V_P^3} + \frac{2}{V_S^3} \tag{7.3}$$

$$\frac{K_S}{\rho} = V_P^2 - \frac{4}{3}V_S^2 \tag{7.4}$$

where V_D is the Debye sound velocity extracted from the PDoS, density ρ and adiabatic bulk modulus K_S are EoS parameters.

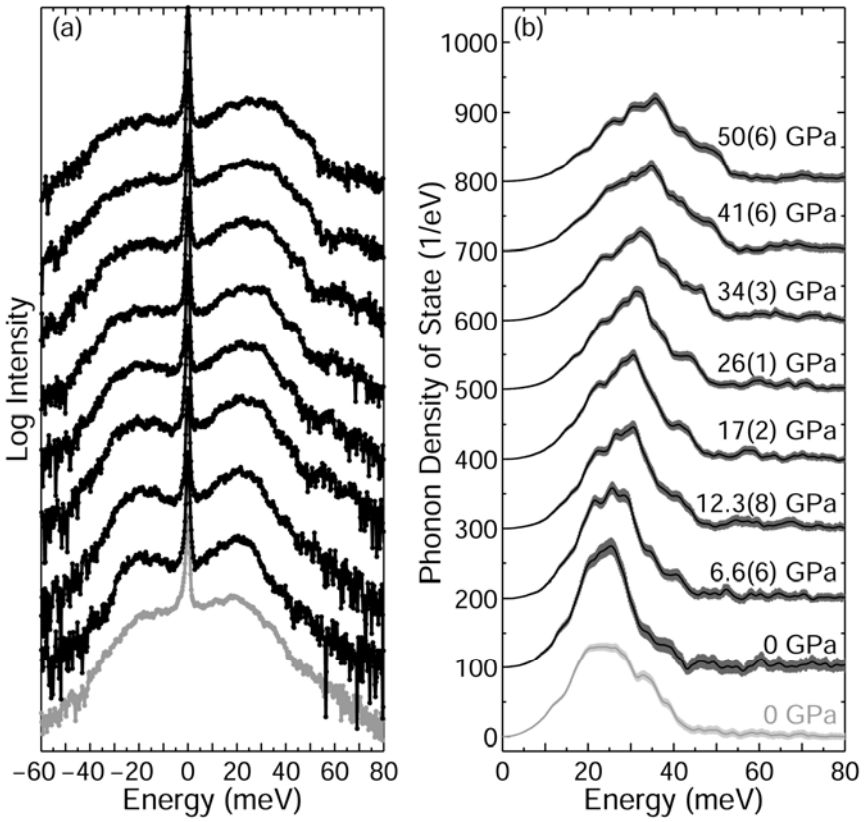

Fig. 7.9. (a) NRIXS spectra of $^{57}Fe_3C$. (b) Corresponding partial phonon density of state of Fe in Fe_3C. Spectra at high pressures are vertically shifted for clarity. All spectra were collected on the few-crystal sample (Gao *et al*., 2008) except for one measurement on a powder sample at ambient conditions (gray color).

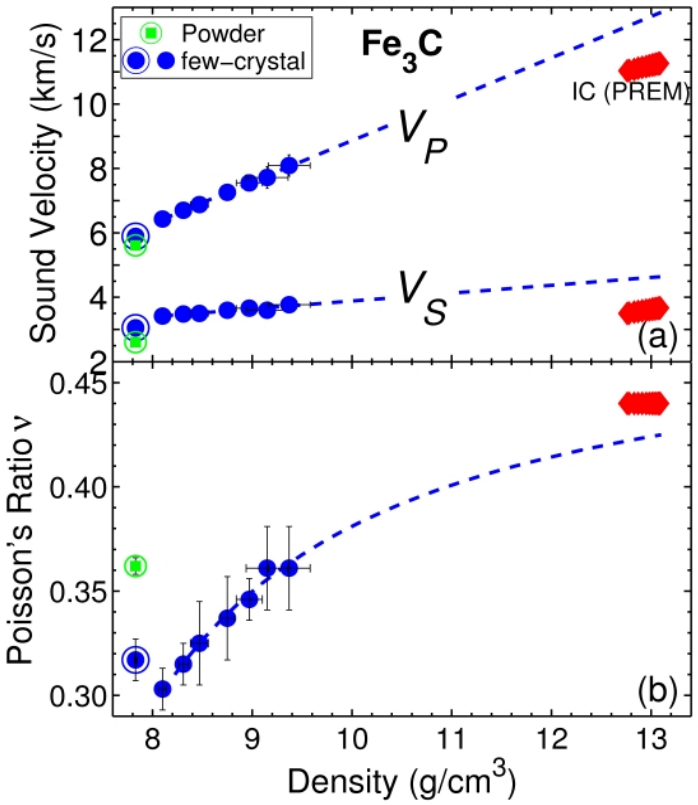

Fig. 7.10. (a) Compressional wave velocity (V_P) and shear wave velocity (V_S) of Fe_3C at 300 K as a function of density, which is corrected for ^{57}Fe enrichment. At pressures below 6 GPa, Fe_3C is magnetic (marked by outer circles). At ambient conditions, the V_P and V_S of the few-crystal sample are 5 % and 16 % larger than those of the powder sample, respectively, indicating strong anisotropy. (b) Poisson's ratio of Fe_3C as a function of density. At ambient conditions, Poisson's ratio of the powder sample is larger and closer to the limiting value of 0.5 for liquids.

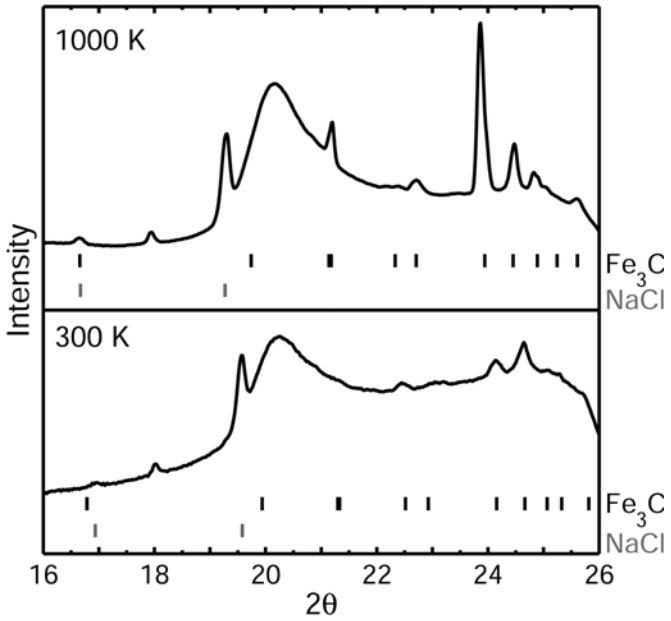

Fig. 7.11. XRD spectra of Fe_3C at 17 GPa and 1000 K and 300 K (λ = 0.8603 Å). The small peak at ~ 18º belongs to calcite, a minor contaminant which does not affect NRIXS measurements. The broad peak at 20.5º is the diffraction of the mirror in the laser-heating set-up.

Our in situ XRD spectra (Fig. 7.11) provide a direct measure of the sample pressure and the unit cell volume, from which the density of Fe_3C can be calculated (Table 7.2). The measured density at ambient conditions (Table 7.2) differs from the known values by ~ 0.2 % - 1 %, corresponding to ~ 0.1 % - 0.5 % difference in V_P and V_S. At 48 GPa, our measured density differs from the existing EoS (Scott *et al*., 2001) by ~ 2.5 %, corresponding to ~ 1 % difference in V_P and V_S. The discrepancy between the measured and calculated density at high pressure and 300 K can be attributed to a pressure gradient in the sample inside the DAC. Indeed, the NaCl pressure (Birch, 1986) differs from the ruby pressure by ~ 4 GPa at 48 GPa (Table 7.2). An error in the measured sample pressure (dP) leads to an error in density according to $\mathrm{d}\rho/\rho = \mathrm{d}P/K$. With a 10 % error in pressure, the resultant error in density is ~ 0.06 % at 1 GPa to ~ 6 % at 100 GPa. With the approximation of $V_P \approx 2\ V_S$ and ignoring dK/K, as K is less sensitive to errors in pressure, equation (7.4) implies that $\mathrm{d}V_P/V_P \approx \mathrm{d}V_S/V_S \approx \mathrm{d}\rho/\rho/2$. A 10 % error in pressure would therefore introduce a 0.03 % error in the measured V_P and V_S at 1 GPa, and a 3 % error at 100 GPa. The error is negligible at low pressure but significant at high pressure. The error can be eliminated through simultaneous PDoS and EoS measurements, which provide accurate sound

velocities at a given density.

Table 7.2 Lattice parameters of NaCl and Fe_3C at high pressures.

Run ID	P_{ruby} (GPa)	P_{NaCl} (GPa)	NaCl	Fe_3C			
			a (Å)	a (Å)	b (Å)	c (Å)	V (Å^3)
				300 K			
093-AIR-I	0	-	-	5.0813(6)	6.7537(8)	4.5139(6)	154.90(4)
090-DAC-I	0	-	-	5.158(3)	6.748(3)	4.510(3)	157.0(2)
090-DAC-II	17(1)	16.9(1)	5.065(3)	4.969(1)	6.574(3)	4.4060(7)	143.9(1)
090-DAC-III	48(3)	44.1(1)	2.934(1)	4.871(1)	6.407(3)	4.279(1)	133.5(1)
				750 K			
090-DAC-II	-	15(1)	6.139(7)	5.018(1)	6.587(5)	4.4424(8)	146.8(2)

P_{ruby}, pressure based on ruby R_1 fluorescence; P_{NaCl}, pressure based on EoS of NaCl. The unit cell volume of Fe_3C at ambient conditions and 300 K is 155.26 Å (Scott *et al*., 2001) and 155.28 Å^3 or 155.40 Å^3 (Li *et al*., 2002). The high temperature 750 K is estimated on the basis of detailed balance principle $I(E)/I(-E) = \exp(E/k_BT)$, where $I(E)/I(-E)$ is the probability ratio between phonon creation and annihilation, E is the nuclear resonant energy, k_B is Boltzmann's constant and T is the temperature. Numbers in parentheses are uncertainties in the last digit(s). The uncertainty in P_{ruby} is based on the pressure difference between different rubies and the pressure variation before and after the NRIXS measurements. Uncertainty in the lattice parameter is the error in least-square fitting of multiple peaks. Run ID refers to the synthesis run number (090 or 093) and the loading information (AIR for a free-standing sample and DAC for a sample in a DAC).

At high temperature, the presence of a temperature gradient could introduce additional errors in the measured velocities, if a separate EoS is used. The error in measured sample temperature (dT) leads to an error in density according to $d\rho/\rho = -\alpha dT$, where α is the thermal expansion coefficient. Assuming $\alpha = 10^{-5}$ K^{-1} , a temperature error of 200 K at 2000 K would introduce an error of 0.2 % in ρ and therefore a negligible error of 0.1 % in V_P and V_S.

7.3.3 Grain Size Distribution and Anisotropy

In NRIXS measurements, only the vibration modes projected in the direction of the incident X-ray beam contribute to the recorded signals. The PDoS spectrum of the sample, therefore, depends on the crystal orientation with respect to the incident X-ray beam (Chumakov *et al*.,

1997; Sturhahn and Kohn, 1999). Under ambient conditions, the NRIXS spectra and the corresponding PDoS of the few-crystal sample and powder sample are significantly different (Fig. 7.9). The derived V_P and V_S of the few-crystal Fe_3C are 5 and 16 %, respectively, higher than those of the powder Fe_3C (Fig. 7.10).

Poisson's ratio is an elastic parameter defined as the strain in the direction normal to a uniaxial stress divided by the strain along the stress direction (Poirier, 2000). Poisson's ratio can be derived from V_P and V_S based on the equation (4.4). We found that Poisson's ratio of the powder sample is 14 % larger than that of the few-crystal sample, and closer to the limiting value of 0.5 for liquids (Fig. 7.10). These results indicate that the sound velocity of Fe_3C is highly anisotropic, consistent with the recent report of extreme elastic anisotropy in cementite on the basis of first-principle calculations and XRD measurements (Nikolussi *et al*., 2008). Using the elastic tensor of Nikolussi *et al*. (2008), we calculated the Debye sound velocity of Fe_3C in different orientations. Following Sturhahn and Kohn (1999), the directional dependence of V_D is well approximated by

$$\frac{1}{V_D^3} = \frac{1}{\bar{V}_D^3} - \frac{1}{V_{D,\,mod}^3} P_2\left[\cos(\theta)\right] \qquad (7.5)$$

where $\bar{V}_D$ is the average of V_D, $V_{D,mod}$ is a term describing the modulation of V_D with the direction of the incident X-ray, θ is the angle between the a axis and the direction of the incident X-ray, and P_2 is the second-order Legendre polynomial, $P_2(x) = 0.5(3x^2-1)$.

We found that V_D = 3.245 km/s and $V_{D,mod}$ = 4.07 km/s. V_D is almost isotropic in the *bc* plane and more than 30 % larger along the *a* axis. The maximum value of V_D is 4.11 km/s for X-rays incident along the *a* axis. Smaller values of V_D, as low as 3.02 km/s, are expected if the incident X-rays are perpendicular to the *a* axis. Our measured V_D of the few-crystal sample is ~ 5 % larger than that of the powder sample, indicating that the few crystals are oriented with the average *a* axis neither parallel nor perpendicular but at an intermediate angle to the incident X-rays. Our experimental values of V_P and V_S for the powder sample extracted using equations (7.3) and (7.4) are both within 12 % of the calculated Voigt-Reuss-Hill average. With further development, the online XRD may allow quantitative determination of anisotropy in sound velocities of compressed and heated samples.

7.4 CONCLUSIONS

A new X-ray diffraction set-up at beamline 3-ID-B of the Advanced Photon Source, Argonne National Laboratory, is fully integrated with existing nuclear resonant scattering and laser-heating instrumentation, enabling on-line measurements of sample pressure and lattice parameters, as well as detection of impurity, phase transition and chemical reaction at the micrometer scale. The low energy of the incident X-rays (14.4125 keV, corresponding to 0.86025 Å) in ^{57}Fe NRS experiments limits the accessible range of the 2θ angle, but a number of options are available to expand the range.

Iron impurity was found in the Fe_3C synthesized from ^{57}Fe-enriched powder. In some cases the impurity may be present at the nanometer scale at ambient conditions and grow into micrometer-sized grains upon heating. The effect of Fe impurity on Debye sound velocity of Fe_3C ($V_{D,Fe3C}$) at 300 K is negligible if the concentration of the impurity is less than 10 %. The error introduced by Fe impurity could be as large as 9 % if the X-ray probes the Fe-rich portion of the sample. *In situ* detection of the impurity is critical to ensure data quality.

Previous measurements of sound velocities have combined PDoS and EoS data from separate measurements. This approach is reliable if the sample pressure is measured accurately. Under pressures near or above megabar, the pressure gradient in the DAC could lead to a significant error in the measured velocities. In situ measurement of sample pressure and density is therefore necessary for obtaining accurate sound velocities at a given density.

Our simultaneous XRD and NRIXS measurements under ambient conditions reveal considerable differences in the compressional wave velocity, shear wave velocity and Poisson's ratio between few-crystal and powder Fe_3C samples, indicating strong anisotropy in its sound velocities. This finding demonstrates a unique application of the integrated techniques, for investigating anisotropy in sound velocities at high pressures and high temperatures.

Chapter 8[4]

Density of Fe_3C at Multi-Megabar Pressures from Single Crystal X-ray Diffraction

8 ABSTRACT

Understanding the composition of Earth's inner core is crucial for revealing the mechanisms of core formation and evolution of the Earth. Carbon has been considered a principal light element candidate in the inner core. The possibility of Fe_3C being a major inner core component has been challenged in recent studies, partially due to our limited knowledge on its densities at relevant pressures and temperatures (e.g., Wood, 1993; Vočadlo *et al*., 2002; Lin *et al*., 2004a). Previously the density of Fe_3C at inner core conditions has been inferred from X-ray diffraction experimental data up to ~ 73 GPa as well as theoretical calculations. Here, we show X-ray diffraction experimental results on densities of Fe_3C to 200 GPa at 300 K. Equation of state parameters were derived from the X-ray diffraction data. Density of Fe_3C calculated based on the equations of state were compared with those of iron and the inner core. Our results indicate that pure Fe_3C or Fe_3C mixed with a small amount of iron could match the density of the inner core. Moreover, our data suggest a discontinuity in density and incompressibility at ~ 10 GPa, which might be related to a previously observed magnetic transition at similar pressures (e.g., Duman *et al*., 2005; Gao *et al*., 2008). Our synchrotron Mössbauer data also indicate another possible discontinuity at higher pressure between 50 and 73 GPa. This possible transition is also indicated in our X-ray diffraction data, although the exact pressure and nature of the transition are still uncertain.

8.1 INTRODUCTION

The presence of light elements in the Earth's core has been suggested early in 1950s by Birch

[4] This chapter will be submitted to a journal. Collaborators in this work are: Bin Chen, Przemyslaw K. Dera, Barbara Lavina, Vitali B. Prakapenka, Wolfgang Sturhahn, Esen E. Alp, Jiyong Zhao and Jie Li.

based on the density mismatch between iron and the core (Birch, 1952) and now is widely accepted (e.g., Li and Fei, 2007, and references therein). A recent study on the compressibility of pure iron under quasi-hydrostatic pressures to 2 Megabar (200 GPa) pressures constrained the core density deficit (difference in density between pure iron and the inner core) to 1.4 – 9.1 wt.% (Dewaele *et al*., 2006). The nature and abundance of light element(s) are under debate, yet they are fundamental issues in understanding the formation and evolution (e.g., Rubie, 2007, and references therein) of the Earth's core. Carbon as a possible major light element in the core has been mentioned by Birch (1952), though this possibility was not widely explored for decades, probably because carbon occupies the interstitial sites of iron and hence was thought to be unable to lower the density of iron (Ringwood, 1966). However, Ringwood (1977) later recognized that carbon could reduce the density of iron. In later studies, the density of an iron-carbon compound Fe_3C has been explored theoretically (Wood, 1993; Vočadlo *et al*., 2002; Huang *et al*., 2006; Ono and Mibe, 2010) and experimentally (Scott *et al*., 2001; Li *et al*., 2002; Ono and Mibe, 2010), and it has been under debate whether or not Fe_3C is too light for the inner core. Carbon was also thought to be too volatile to be retained in appreciable amounts during the early Earth accretion (Ringwood, 1966). However, quench experiments up to 12 GPa and ~ 1900 K (Hirayama *et al*., 1993) as well as to 14 GPa and ~ 2500 K (Nakajima *et al*., 2009) suggested that carbon forms eutectic melting system with iron at relatively low temperatures.

Carbon has a high cosmic abundance (10 times the abundance of silicon) resulted from the nucleosynthesis process (e.g., Prantzos, 2007, and references therein). In the bulk silicate Earth, the estimated average carbon content is in the order of 10^2 ppm (~ 0.01 % wt. %), much less than the measured value of ~ 3.5 wt.% in CI carbonaceous chondrites (McDonough and Sun, 1995), which are thought to be the most primordial meteorites (e.g., Ringwood, 1966). This mismatch indicates that carbon might be lost during accretion or (and) sequestered into the core. To test a carbon-rich inner core model, it is necessary to compare the density of iron-carbon compounds, such as Fe_3C, with the observed values. The density profile of the Earth's interior can be constrained from normal mode (free-oscillation) observations. The widely-used preliminary reference Earth model (PREM) (Dziewonski and Anderson, 1981) is a self-consistent model derived from seismic travel time, normal mode data, as well as mass and moment of inertia of the Earth.

Fe_3C (cementite) contains the least amount of carbon among all stable iron-carbon compounds at ambient conditions. $(Fe,Ni)_3C$ (cohenite) has been observed in meteorites (e.g., Goodrich, 1992), as well as in inclusions of polycrystalline diamond aggregates from kimberlite (Limpopo central belt, South Africa) (Jacob *et al*., 2004). Based on thermodynamic calculation, Wood (1993) suggested that Fe_3C might be the first phase to crystallize out of a Fe-C-S liquid outer core for conceivable C/S ratios and proposed Fe_3C to be the major inner core component instead of ε-iron.

Fe_3C adopts the orthorhombic structure with space group of Pnma at ambient conditions (Fasiska and Jeffrey, 1965). No pressure-induced structural change has been reported. At ambient conditions, Fe_3C is ferromagnetic. At ambient temperature, a transition from the low-pressure ferromagnetic phase to a high-pressure non-magnetic phase has been observed, with a controversial magnetic transition pressure, i.e., ~ 6 GPa based on a synchrotron Mössbauer spectroscopy (SMS) study (Gao *et al*., 2008), ~ 9 GPa based on an X-ray magnetic circular dichroism study (Duman *et al*., 2005), and ~ 25 GPa as reported in an X-ray emission spectroscopy study (Lin *et al*., 2004a). The difference between the transition pressures reported in Lin *et al*. (2004a)'s study and in the other two studies may be partially due to data interpretation. In Lin *et al*. (2004a)'s X-ray emission spectroscopy study, the magnetic moment at 5 GPa has already decreased by ~ 50 % compared to the value at the ambient pressure.

In this study, we carried out X-ray diffraction (XRD) measurements on Fe_3C single crystals to 200 GPa, well into the Earth's core (136 GPa to 329 GPa for the outer core, and 329-364 GPa for the inner core), to study its densities and compressibility at high pressures. Compared to the powder diffraction technique, single crystal diffraction has the advantage of allowing accurate indexing of diffraction peaks hence offering more peaks usable for unit cell parameter calculation. Whereas in powder diffraction, peak broadening and peak overlapping could lead to misidentification of peaks, especially when the material has a complicated structure or when more than one phase exist along the X-ray beam. In addition, we collected SMS data between ~ 30 and ~ 90 GPa on Fe_3C. SMS probes the ^{57}Fe nuclei decay energy (energies) that is (are) coupled to the electronic environment, and is an established method to investigate the electronic configuration of iron in iron-bearing phases (e.g., Alp *et al*., 1995; Sturhahn and Jackson, 2007, and references therein).

8.2. Experimental Method

Synthetic Fe_3C from runs #090 and #094 were used in this study. Details of the #090 sample synthesis procedure were described in a previous study (Gao *et al*., 2008). The synthesis procedure for run #094 is similar to that of #093, as described by Gao *et al*. (2009). The structure and purity of the run products were confirmed using high-resolution XRD method at beamline 11-BM-B of the Advanced Photon Source (APS) and conventional Mössbauer spectroscopy method at sector 3 of the APS. Only Fe_3C phase was observed in sample #090. In sample #094, Fe_3C was confirmed to be the major phase (integrated intensity of impurity peaks is ~ 1 %).

We conducted two separate XRD runs at 300 K, the 300-μm run and the 100-μm run, with maximum achieved pressures of ~ 64 GPa and ~ 200 GPa, respectively. Prior to loadings, a few Fe_3C crystals with a size of ~ 25 μm × 20 μm × 5 μm were selected from the synthesis batch #090 based on XRD measurements at beamlines 13-BM-C and 16-BM-D of the APS. In the 300-μm run, two Fe_3C crystals c1 and c2 were loaded in a diamond anvil cell (DAC) with neon pressure medium and a ruby ball as the pressure gauge. In the 100-μm run, a piece of Fe_3C crystal was loaded in a DAC with neon pressure medium as well a NaCl powder flake and a ruby ball as pressure calibrants.

High pressures were generated using DACs with bevelled diamonds (300/100 μm culet size, 9° bevel angle, from Almax) in the 100-μm run, and flat diamonds (300 μm culet size, from Almax) in the 300-μm run. We collected XRD patterns of the Fe_3C samples at three beamlines of GSECARS at the APS: the undulator beamline 13-ID-D for the entire 100-μm run as well as 50-64 GPa data and decompression data for the 300-μm run, the bending magnet beamlines 13-BM-D for the 3-45 GPa data in the 300-μm run and 13-BM-C in the 300-μm run at ambient conditions. The monochromatic X-ray beam with a wavelength of 0.3344° was focused to a size of 5 × 5 μm^2 at beamline 13-ID-D, and to a size of 15 μm (vertical) × 5 μm (horizontal) at the beamline 13-BM-D. The wavelength of the monochromatic beam at beamline 13-BM-C was 0.8336°. To maximize the number of collected diffraction peaks, we used cubic boron nitride (cBN) seats in the upstream side (close to the incident X-ray) in the DACs, as boron and nitrogen have low *Z* numbers hence low X-ray absorption. In the downstream side, a tungsten carbide seat with an opening angle of 36° was used in the 300-μm run, matching the DAC opening. In the 100-μm run, we used a tungsten carbide seat with a smaller opening angle of 26° in order to

maximize the support for diamonds from the seat. To compensate for the reduced seat opening angle and increase collected diffraction peaks, we placed the CCD detector at three different positions and collected XRD patterns at each position. The typical X-ray exposure time in this study was 10 to 30 seconds at beamline 13-ID-D and 15 minutes at beamline 13-BM-D. We annealed the crystal c2 at ~ 30 GPa in the 300-μm run using laser heating technique at ~ 1400 K for 7 minutes. The annealing did not show any noticeable effect in the sample appearance or the diffraction patterns. The microscopic images of DAC loadings and XRD patterns are shown in Fig. 8.1.

The SMS run was conducted at beamline 3-ID-B of the APS. The SMS setup has been described previously (Gao *et al*., 2009). A piece of polycrystalline ^{57}Fe-enriched Fe_3C sample selected from the synthesis batch #094 was sandwiched between two NaCl layers in a DAC with bevelled diamonds (300/100 μm culet size, 9° bevel angle, from Almax). The purity of the sample was confirmed using X-ray diffraction method at beamline 16-ID-B of the APS (λ = 0.41416 Å) (intensity of impurity peaks account for < 0.5 %). cBN-epoxy insert was used in the Be gasket in order to enhance the sample thickness at high pressures (Lin *et al*., 2005). The NaCl pressure medium also served as the pressure calibrant (Dorogokupets and Dewaele, 2007; Fei *et al*., 2007).

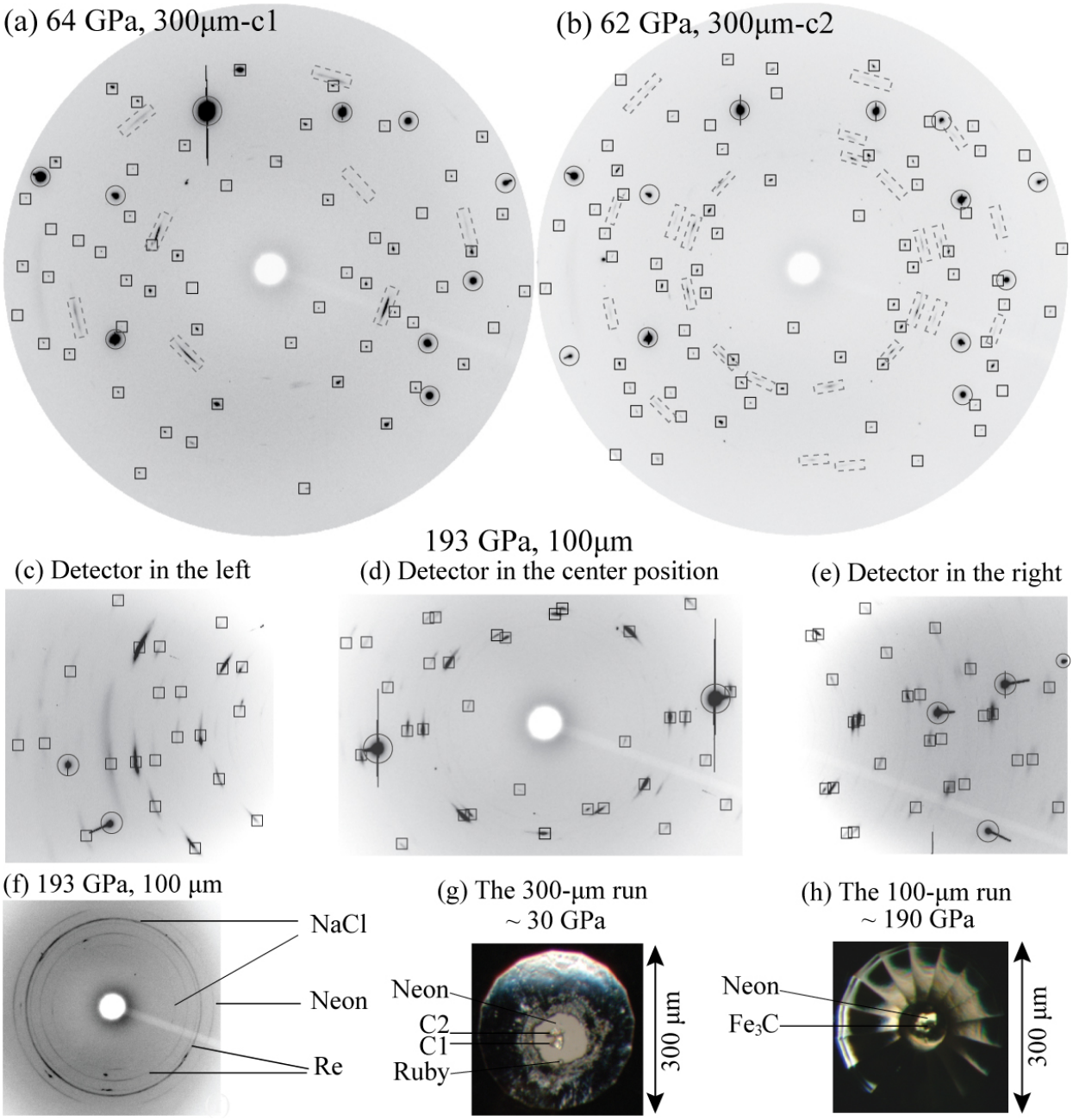

Fig. 8.1. X-ray diffraction patterns at the highest pressure in the 300-μm run on sample c1 (a), sample c2 (b) and at 193 GPa in the 100-μm run (c, d, e). The predicted reflections of Fe_3C are marked with open squares. Diffraction signals from diamonds and neon are marked with open circles and dashed rectangles, respectively. (f) X-ray diffraction pattern of NaCl, neon and Re gasket at 193 GPa in the 100-μm run. (g) An image of the 300-μm run at ~ 30 GPa after annealing. (h) An image of the 100-μm run at ~ 190 GPa..

8.3 RESULTS

8.3.1. Lattice Parameters and Equation of State

No structural phase change was observed upon compression to 200 GPa or annealing at ~ 1400 K and 30 GPa in this study. To derive unit cell parameters (Tables 8.1, 8.2; Figs. 8.2, 8.3, 8.4), we integrated the XRD patterns using *Fit2D* program (Hammersley, 1998) to intensity versus 2θ data. To avoid diffraction spots with similar 2θ to overlap in the converted data, each diffraction spot was integrated individually. We then fitted peak positions 2θ using the *CMPR* program (Toby, 2005). From peak positions, lattice parameters and unit cell volume (Tables 8.1, 8.2) were calculated using *UnitCell* program (Holland and Redfern, 1997). The diffraction spots were indexed using the GSE-ADA program (Dera, 2007). For the 300-μm run, only 21 (for sample c1) and 30 (for sample c2) peaks were available at ambient conditions, since the incident X-ray beam at beamline 13-BM-C had low energy (14.9 keV, λ = 0.8336 Å). At high pressures and upon decompression, 56 to 86 diffraction peaks were used. For the 100-μm run, 44 to 83 (68 on average) peaks were used for each pressure point to derive lattice parameters.

In the *f-F* plot, a discontinuity ~ 10 GPa is shown (Fig. 8.2). For B-M EoS, the Eulerian strain f is defined as $f = 0.5[(V_0/V)^{2/3} - 1]$, and the normalized stress F is $F = P/[3f(1+2f)^{2.5}]$ (e.g. Angel, 2000). The slope of *f-F* plot is dependent on the value of V_0. In our case, any V_0 with a value in the range of 154.1 $Å^3$ (from EoS fitting, Table 8.3) to 155.3 $Å^3$ (unit cell volume at ambient conditions based on an XRD measurement) (Scott *et al*., 2001) results in an *f-F* relationship with a discontinuity at ~ 10 GPa. The 10-GPa discontinuity in the compression data may be related to a magnetic transition from the low-pressure ferromagnetic phase to a high-pressure non-magnetic phase observed in an SMS study at ~ 6 GPa (Gao *et al*., 2008) and in an XMCD study at ~ 10 GPa (Duman *et al*., 2005). The reason why the discontinuity in the *f-F* plot is at higher pressure than the magnetic transition pressure of ~ 6 GPa in the SMS study may be the following: the 10 GPa discontinuity in the *f-F* plot marks the completion of the change, while in the SMS data 6 GPa is when the change in magnetic feature is the largest. In fact, at 6.5 GPa, small amount of magnetic residual in the SMS data still exists (Gao *et al*., 2008). On the other hand, the data points between 6 GPa and 10 GPa in the *f-F* plot do not fall on the same line as the data points below 6 GPa (Fig. 8.2).

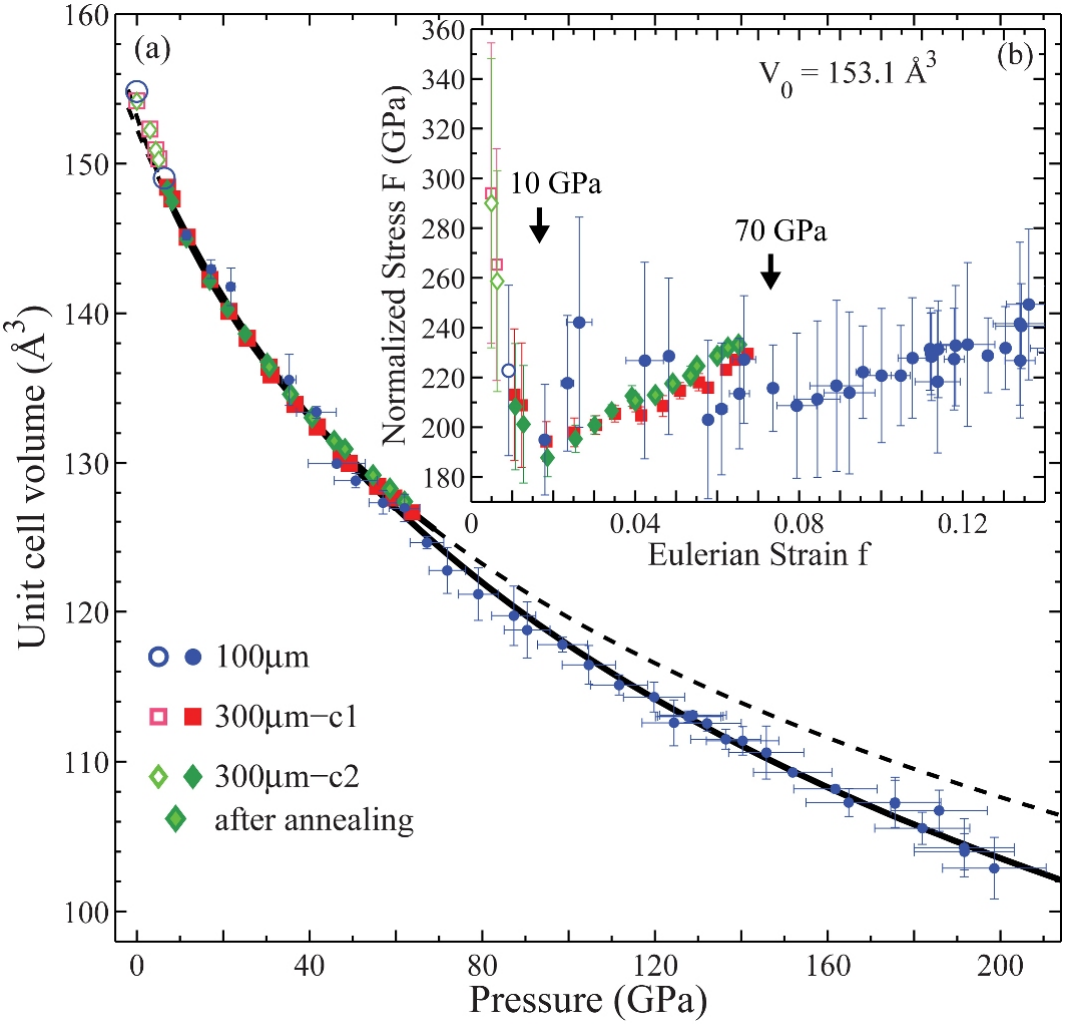

Fig. 8.2. (a) Unit cell volume of Fe_3C as a function of pressure. The low-pressure magnetic phase is represented with open symbols. The solid and dashed lines represent the Birch-Murnaghan EoS fitting results for data in the pressure range of 10-70 GPa and 10-200 GPa, respectively. (b) Normalized stress F as a function of strain f for Birch-Murnaghan EoS, revealing discontinuities at 10 GPa and ~ 70 GPa.

Table 8.1. Unit cell parameters of Fe_3C from the 300-μm run.

		Fe_3C				Neon
P_{neon}(GPa)	P_{ruby} (GPa)	*a* (Å)	*b* (Å)	*c* (Å)	*V* (Å^3)	*a* (Å)
		300 μm – crystal c1				
-	0	5.072(2)	6.729(7)	4.518(3)	154.2(2)	-
-	3.1(8)	5.052(1)	6.717(2)	4.489(1)	152.31(2)	-
-	4.4(8)	5.037(1)	6.695(2)	4.476(1)	150.93(2)	-
-	5.1(8)	5.029(1)	6.684(2)	4.472(1)	150.33(2)	-
-	7.1(8)	5.006(1)	6.657(2)	4.454(1)	148.42(2)	-
-	8.2(9)	4.998(1)	6.648(2)	4.443(1)	147.65(2)	-
11.7(4)	12.0(9)	4.970(1)	6.609(2)	4.417(1)	145.08(2)	3.521(1)
16.9(4)	17.2(9)	4.938(1)	6.567(2)	4.388(1)	142.26(2)	3.429(1)
21.2(3)	20.6(9)	4.916(1)	6.533(2)	4.363(1)	140.13(2)	3.371(1)
25.6(3)	25.2(9)	4.894(1)	6.510(2)	4.342(1)	138.33(2)	3.324(2)
30.6(4)	29.9(9)	4.872(1)	6.477(2)	4.322(1)	136.40(2)	3.278(3)
31.1(4)	30.2(9)	4.875(1)	6.469(2)	4.309(1)	135.88(2)	3.274(3)
36.6(6)	35.7(9)	4.847(1)	6.444(2)	4.287(1)	133.91(2)	3.232(3)
41.8(5)	40.7(9)	4.826(1)	6.422(2)	4.272(1)	132.40(2)	3.197(3)
47.3(6)	45.9(9)	4.809(1)	6.390(2)	4.255(1)	130.75(2)	3.165(3)
49.2(2)	--	4.808(1)	6.384(2)	4.235(1)	129.97(2)	3.155(1)
55.8(3)	53.1(9)	4.787(1)	6.358(2)	4.220(1)	128.44(2)	3.122(1)
59.5(3)	57.7(9)	4.779(1)	6.345(2)	4.210(1)	127.66(2)	3.105(1)
63.7(3)	61.4(9)	4.767(1)	6.326(2)	4.201(1)	126.67(2)	3.087(2)
		Decompression				
61.1(3)	57.2(9)	4.775(1)	6.339(2)	4.203(1)	127.21(2)	3.098(2)
51.7(4)	45.3(9)	4.798(1)	6.390(2)	4.232(1)	129.75(2)	3.142(3)
41.8(5)	36.2(9)	4.843(1)	6.447(2)	4.287(1)	133.84(2)	3.197(3)
31.7(5)	28.0(8)	4.885(1)	6.517(2)	4.328(1)	137.78(2)	3.269(1)
-	0	5.081(1)	6.741(2)	4.520(1)	154.83(2)	-
		300 μm - crystal c2				
-	0	5.069(6)	6.750(9)	4.506(1)	154.2(2)	-
-	3.1(8)	5.051(1)	6.718(1)	4.487(1)	152.25(2)	-
-	4.4(8)	5.037(1)	6.696(1)	4.475(1)	150.90(2)	-
-	5.1(8)	5.028(1)	6.689(1)	4.468(1)	150.26(2)	-
-	7.1(8)	5.005(1)	6.664(1)	4.446(1)	148.32(2)	-
-	8.2(9)	4.996(1)	6.652(1)	4.437(1)	147.46(2)	-
11.5(4)	12.0(9)	4.969(1)	6.617(1)	4.409(1)	144.96(2)	3.524(4)
16.9(4)	17.2(9)	4.938(1)	6.576(1)	4.377(1)	142.14(2)	3.429(1)
21.0(3)	20.6(9)	4.915(1)	6.548(1)	4.359(1)	140.28(2)	3.374(1)

Table 8.1 (continued)

25.1(2)	25.2(9)	4.895(1)	6.524(1)	4.341(1)	138.63(2)	3.329(1)
30.2(5)	29.9(9)	4.870(1)	6.497(1)	4.321(1)	136.74(2)	3.281(4)
			After annealing			
30.7(3)	30.2(9)	4.876(1)	6.481(1)	4.317(1)	136.42(2)	3.277(2)
35.6(3)	35.9(9)	4.849(1)	6.459(2)	4.298(1)	134.59(3)	3.239(2)
40.6(3)	40.7(9)	4.826(1)	6.438(2)	4.282(1)	133.03(3)	3.205(2)
45.7(7)	45.9(9)	4.807(1)	6.411(1)	4.266(1)	131.47(2)	3.174(4)
48.2(2)	--	4.800(1)	6.403(1)	4.260(1)	130.92(2)	3.160(1)
54.7(5)	53.1(9)	4.790(1)	6.357(1)	4.242(1)	129.18(2)	3.127(2)
58.6(3)	57.7(9)	4.779(1)	6.350(1)	4.227(1)	128.28(2)	3.109(2)
62.0(3)	61.4(9)	4.766(1)	6.335(1)	4.220(1)	127.41(2)	3.094(2)
			Decompression			
60.0(3)	57.2(9)	4.773(1)	6.345(1)	4.223(1)	127.88(2)	3.103(1)
49.9(2)	45.3(9)	4.787(1)	6.387(1)	4.272(1)	130.60(2)	3.151(1)
40.3(3)	36.2(9)	4.832(1)	6.460(1)	4.309(1)	134.52(2)	3.207(2)
30.7(2)	28.0(8)	4.874(1)	6.520(1)	4.352(1)	138.28(2)	3.277(1)
-	0	5.085(1)	6.760(1)	4.514(2)	155.17(4)	-

P_{Ruby} is pressure estimated from ruby R_1 fluorescence line (Dewaele *et al*., 2004). P_{Neon} is based on Vinet EoS of neon (Fei *et al*., 2007). "-" means that lattice parameter for liquid neon and the neon-based pressure were not available at low pressures. "--" means that pressure was not measured using ruby. Numbers in parentheses are uncertainties in the last digit(s). Uncertainty sources: P_{Neon} and P_{NaCl} – from uncertainty in lattice parameter and pressure difference between Birch-Murnaghan and Vinet EoS (Fei *et al*., 2007); lattice parameters and unit cell volumes of Fe_3C – reproducibility, which is larger than the standard deviation reported in the *UnitCell* program (Holland and Redfern, 1997) when fitting lattice parameters to multiple diffraction peaks using weighted least squares fitting method.

Table 8.2. Unit cell parameters of Fe_3C from the 100-μm run.

	Fe_3C				NaCl	Neon
P (GPa)	*a* (Å)	*b* (Å)	*c* (Å)	*V* (Å^3)	*a* (Å)	*a* (Å)
0	5.082(1)	6.737(27)	4.522(9)	154.82(33)	-	-
6.4(8)	5.013(2)	6.672(13)	4.456(4)	149.03(11)	-	-
11.5(8)	4.974(1)	6.604(13)	4.421(2)	145.23(31)	5.181(1)	3.542(5)
17.2(9)	4.938(1)	6.596(34)	4.389(4)	142.95(63)	-	3.414(5)
21.8(9)	4.917(9)	6.609(90)	4.363(15)	141.77(1.26)	-	-
35(2)	4.863(15)	6.49(12)	4.297(11)	135.56(1.71)	-	-
42(5)	4.860(15)	6.401(3)	4.289(2)	133.39(39)	-	-
46(7)	4.825(2)	6.306(15)	4.271(2)	129.96(23)	-	-
51(5)	4.808(10)	6.298(51)	4.254(11)	128.82(48)	-	-
57(3)	4.795(18)	6.267(78)	4.238(10)	127.34(82)	2.887(7)	3.116(9)
62(4)	4.782(18)	6.289(86)	4.222(11)	127.96(95)	2.868(3)	3.094(9)
67(4)	4.765(8)	6.219(42)	4.205(9)	124.61(41)	2.852(4)	3.073(9)
72(4)	4.749(12)	6.16(10)	4.196(6)	122.75(1.53)	2.834(4)	3.055(9)
79(5)	4.728(14)	6.14(11)	4.176(5)	121.17(1.75)	2.809(4)	3.030(9)
87(6)	4.713(11)	6.11(12)	4.160(3)	119.73(1.98)	2.784(3)	3.004(9)
91(6)	4.702(8)	6.09(11)	4.151(3)	118.78(1.87)	2.775(1)	2.995(9)
99(6)	4.688(6)	6.080(30)	4.133(3)	117.80(50)	2.750(3)	2.972(9)
105(7)	4.680(8)	6.040(61)	4.120(2)	116.45(1.29)	2.736(3)	2.956(9)
112(7)	4.657(5)	6.027(33)	4.101(3)	115.11(67)	2.720(3)	2.939(9)
121(8)	4.634(1)	6.055(48)	4.074(2)	114.30(99)	2.698(7)	2.920(9)
125(8)	4.629(2)	5.972(79)	4.072(3)	112.59(1.53)	2.689(7)	2.910(9)
128(8)	4.620(5)	6.010(25)	4.070(6)	113.00(38)	2.685(5)	2.903(9)
128(8)	4.617(6)	6.021(15)	4.066(3)	113.02(26)	2.683(5)	2.902(9)
129(8)	4.615(6)	6.028(16)	4.065(4)	113.10(25)	2.684(4)	2.910(9)
132(9)	4.609(6)	6.018(19)	4.057(5)	112.55(52)	2.678(3)	2.894(9)
137(9)	4.599(7)	5.981(36)	4.053(4)	111.49(66)	2.669(4)	2.885(9)
140(9)	4.586(8)	6.009(54)	4.042(8)	111.39(95)	2.660(4)	2.878(9)
146(9)	4.579(8)	6.004(96)	4.023(6)	111.60(1.77)	2.649(6)	2.868(9)
152(10)	4.571(2)	5.945(15)	4.022(9)	109.29(13)	2.640(5)	2.857(9)
162(11)	4.553(8)	5.930(27)	4.007(9)	108.18(26)	2.625(6)	2.840(9)
165(11)	4.546(12)	5.903(48)	3.998(8)	107.27(93)	2.616(8)	2.835(9)
174(12)	4.538(4)	5.91(11)	3.996(15)	107.19(1.58)	2.602(6)	2.818(9)

Table 8.2 (continued)

176(12)	4.538(14)	5.92(11)	3.994(7)	107.28(1.67)	2.601(6)	2.818(9)
182(12)	4.514(17)	5.894(54)	3.968(6)	105.56(1.07)	2.597(2)	2.809(9)
186(12)	4.504(3)	5.97(11)	3.968(23)	106.73(1.37)	2.589(6)	2.803(9)
192(13)	4.500(8)	5.86(10)	3.955(2)	104.25(1.94)	2.581(5)	2.795(9)
193(13)	4.491(11)	5.849(69)	3.959(12)	103.98(1.22)	2.581(3)	2.795(9)
199(14)	4.473(11)	5.84(13)	3.938(9)	102.89(2.06)	2.573(3)	2.785(9)

Pressure was determined from X-ray diffraction pattern of neon, which was taken near the edge of the Fe_3C crystal. "-" means that the unit cell parameter was not measured, or not available (when neon is liquid at low pressures). Numbers in the parentheses are uncertainties in the last digit(s). Uncertainty sources: *P* – based on different pressure markers (ruby, NaCl, neon) and scales (Birch-Murnaghan and Vinet EoS), including NaCl-B1 (Dorogokupets and Dewaele, 2007), NaCl-B2 (Fei *et al*., 2007), neon (Fei *et al*., 2007), and ruby (Dewaele *et al*., 2004), and pressure drift before and after X-ray diffraction on Fe_3C (< 1 %). Fe_3C – standard deviation reported in the *UnitCell* program (Holland and Redfern, 1997) when fitting lattice parameters to multiple diffraction peaks using weighted least squares fitting method and the estimated effect from non-hydrostatic stress (see text for details), with the latter being the dominant term; Lattice parameter *a* for neon and NaCl - difference based on different hkl peaks.

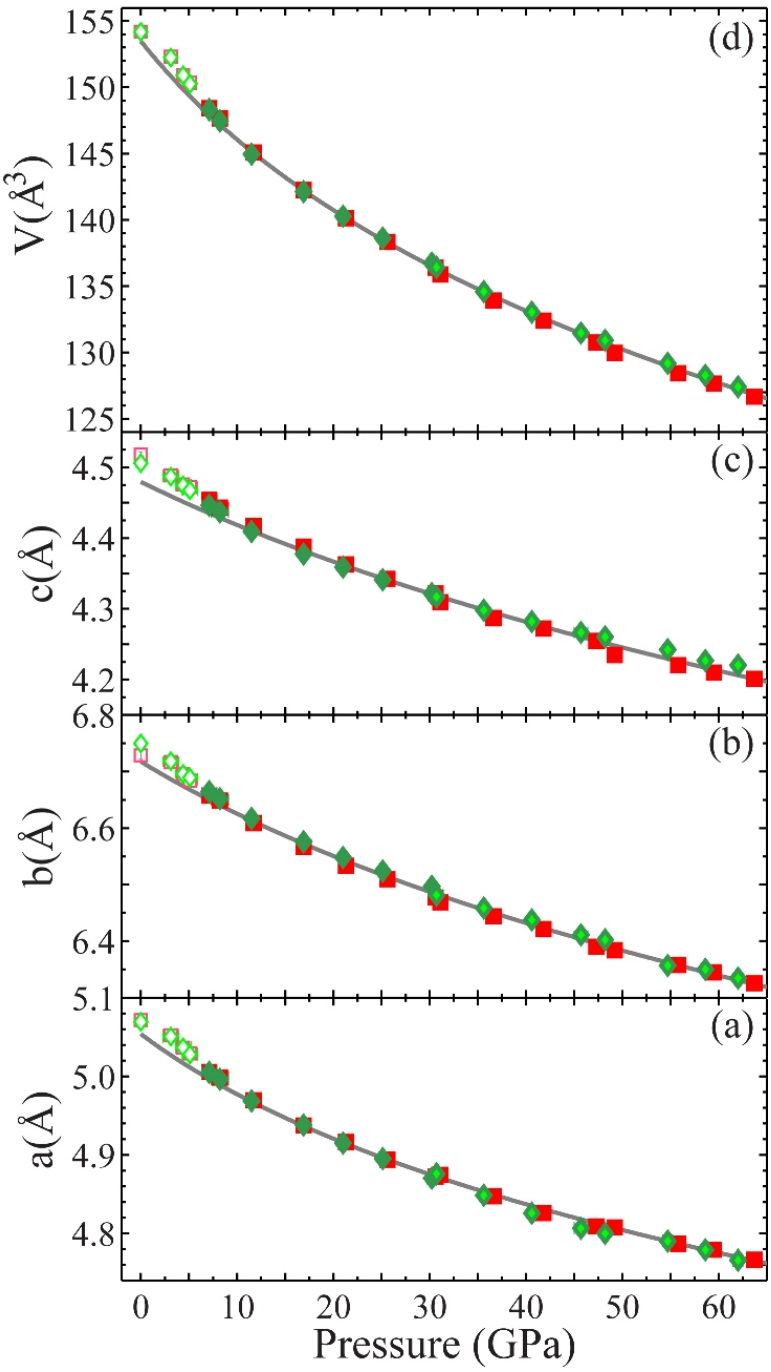

Fig. 8.3. Axial and volumetric compression curves of Fe_3C in the 300-μm run. All symbols have the same meanings as in Fig. 8.2. Solid lines are 3rd order Birch-Murnaghan fittings for the data higher than 10 GPa.

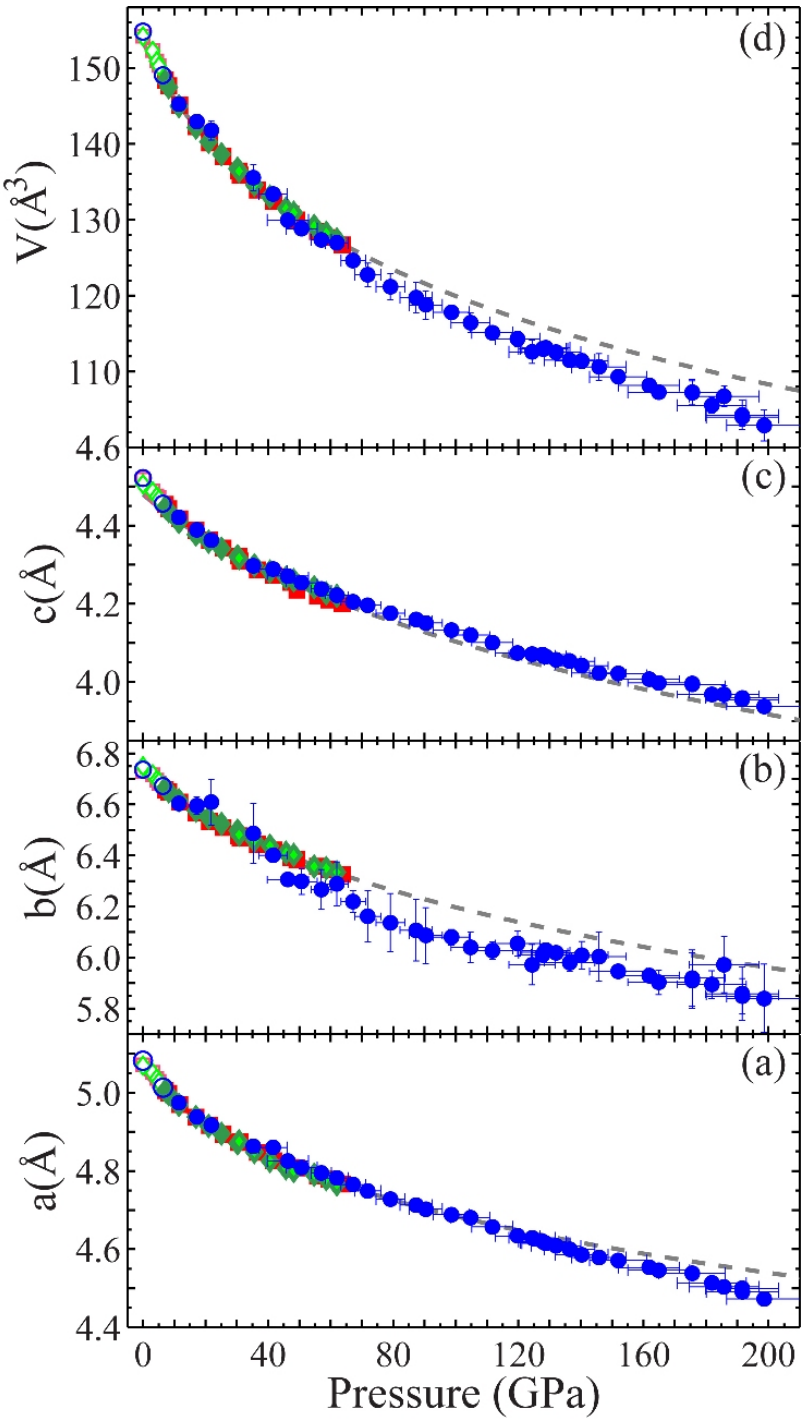

Fig. 8.4. Axial and volumetric compression curves of Fe_3C in the 100-μm run. All symbols have the same meanings as in Figs. 8.2, 8.3. Dashed lines are Birch-Murnaghan fittings of the data from the 300-μm run between 10 and 64 GPa.

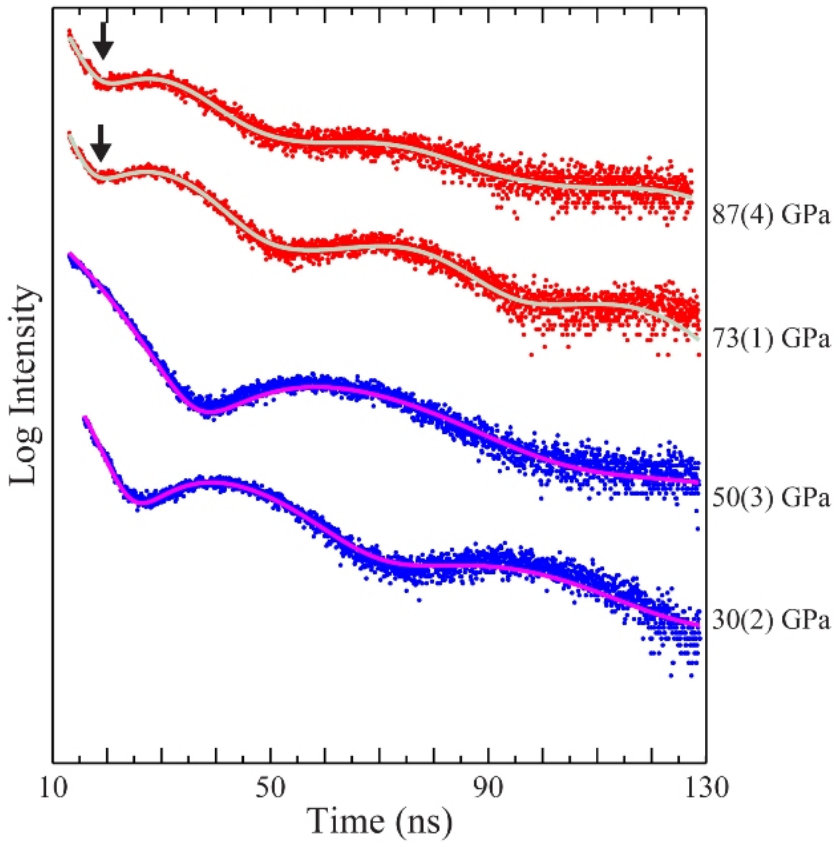

Fig. 8.5. Mössbauer spectroscopy results indicating a transition between 50 and 73 GPa. Dots and lines represent the measured data and fitting results with *CONUSS* software (Sturhahn, 2000), respectively. The two arrows emphasize the changes in the spectra. Pressures are measured using X-ray diffraction peaks of NaCl (Dorogokupets and Dewaele, 2007; Fei *et al*., 2007). The uncertainty in pressure includes pressure change during the SMS measurement and uncertainty in the NaCl lattice parameter.

Table 8.3. Equation of state parameters of Fe_3C.

V_0 ($Å^3$)	K_0 (GPa)	K'	P range (GPa)	Fitting method
Experimental, this study, B-M EoS				
152(1)	220(15)	4.4(3)	10-200	LS
146(1)	294(9)	4(fixed)	70-200	WLS
153.1 (9)	178(20)	7(1)	10-70	WLS
Experimental, this study, Vinet EoS				
153(1)	207(18)	4.9(3)	10-200	LS
145(1)	314(12)	4(fixed)	70-200	WLS
153.2(8)	178(19)	6.9(7)	10-70	WLS
Experimental, Scott et al., 2001, B-M EoS				
155.26	175(4)	5.2(3)	0-73	WLS
Experimental[*]*, B-M EoS*				
148.4	288(42)	4(fixed)	25-73	-
Experimental, Li et al., 2002, B-M EoS				
155.28	174(6)	4.8(8)	0-31	-
Calculation, Vočadlo et al., 2002, 0 K, B-M EoS				
143.49(11)	316.62(2)	4.30(2)	> 60	N/A
Calculation, Huang et al., 2006, 0 K, B-M EoS				
152.00	212	4.5	> 60	N/A
Calculation, Ono and Mibe, 2010, 0 K, B-M EoS				
-	315.5	4.37	≤ 400	N/A

BM - Birch-Murnaghan; (W)LS – (weighted) least squares fitting; N/A – not applicable; '-' -- not reported. Numbers in parentheses are uncertainties in the last digit(s). Uncertainties in this study are based on the standard deviations from (weighted) least-squares fittings.

[*] K_0 and K' are reported by Lin *et al*. (2004) and are based on the experimental data by Scott *et al*. (2001).

The abrupt reduction in lattice parameter *b* at 45 GPa reported in a previous XRD study (Ono and Mibe, 2010) is not observed in our data from the 300-μm run. In the axial compression data along *b* axis from the 100-μm run (Fig. 8.4), a discontinuity at ~ 45 GPa is observed. However, in the 100-μm run, the *b* axis of the crystal happened to be close to the DAC loading axis, resulting in less constraint on the derived lattice parameter *b*. With the presence of non-hydrostatic stress at high pressures as indicated by the elongation of diffraction peaks (Fig. 8.1), anomalies in the lattice parameter *b* are expected. On the other hand, our SMS data indicate an electronic transition between 50 GPa and 73 GPa (Fig. 8.5). As SMS data of magnetic phases

exhibit fast oscillations (e.g., Gao *et al*., 2008, and references therein), a lack of fast oscillations both below and above the transition (Fig. 8.5) indicates that both phases are non-magnetic. The cause of this transition is not yet clear, and we do not rule out the possibility of stress-induced phase stability change. The exact nature of this transition remains to be understood in future studies.

We used (weighted) least squares fitting methods implemented in the *FitEoS* program to derive equation-of-state (EoS) parameters (Table 8.3). Only the data points upon compression were used for EoS fittings. The data points upon decompression generally have higher volumes than those upon compression. The data points below the 10-GPa discontinuity (see the previous section) are not used in EoS fittings. The best Birch-Murnaghan (BM) EoS fitting results for all the data between 10 GPa and 200 GPa are V_0 = 152.3 ± 1.0 Å^3, K_0 = 220 ± 15 GPa and K' = 4.4 ± 0.3, with a rather large χ^2 of ~ 6.4. As our SMS results indicate a transition between 50 and 73 GPa, we also fitted our data below and above 70 GPa separately (Table 8.3). Fitting EoS to data sets above and below 70 GPa separately significantly improves the χ^2 values (Table 8.3). χ^2 provides an indicator of the reliability of fitting results. In our EoS fitting, χ^2 is defined as $\sum_{i=1}^{n}((P_{i,\mathrm{o}} - P_{i,c})/\sigma_i)^2/(n-m)$, where $P_{i,\mathrm{o}}$ is the observed pressure, $P_{i,\mathrm{c}}$ is the calculated pressure from the EoS, σ_i is the experimental uncertainty of pressure, n is the number of data points and m is the number of fitting parameters. Since χ^2 is the average of the ratio between fitting errors and estimated experimental errors, a model that well describes the experimental data should yield χ^2 close to 1. If the model is not sufficient enough to describe the experimental data or if the uncertainty is underestimated, χ^2 could be larger. If the experimental uncertainty is overestimated, or if the uncertainty is mainly systematic uncertainty, χ^2 would be less than 1. Strong correlations between V_0, K_0 and K' were observed in EoS fittings. The correlation coefficient between K_0 and K' (*Corr*<K_0, K'>) is between -0.98 and -0.99, similar to the values of -0.90 to -0.95 reported by Angel (2000). The correlation coefficients between V_0 and K_0 (*Corr*<V_0, K_0>) and between V_0 and K' (*Corr*<V_0, K'>) are -0.96 to -0.99 and 0.90 to 0.96, respectively. The negative sign in a correlation coefficient means that in a (weighted) least squares fitting, if one parameter increases, the other parameter will decrease. The uncertainties propagated from the correlation between EoS parameters are not negligible. More details will be discussed in section 8.4.

8.3.2 Pressure Medium and Pressure Calibration

Neon has been shown to better maintain quasi-hydrostaticity to high pressures compared to most other pressure mediums such as NaCl (e.g. Bell and Mao, 1981; Klotz *et al*., 2009). In an attempt to minimize non-hydrostatic stress, we used neon as the pressure medium in DACs in this study. We treated all neon diffraction signals as powder diffraction patterns in unit cell parameter derivation. We integrated the neon diffraction signals using *Fit2D* software (Hammersley, 2004), fitted peak positions using the *CMPR* software (Toby, 2005) and calculated lattice parameters (Tables 8.1, 8.2) from the peak positions. NaCl unit cell parameters (Table 8.1) were derived in the same way.

In both runs, neon diffraction signals were first observed at ~ 11.5 GPa. In the 300-μm run, neon crystallized into one or more quasi-single crystals, as indicated by the diffraction pattern (Fig. 8.1), while in the 100-μm run, continuous neon diffraction rings were observed. In the 300-μm run, the pressures determined from neon diffraction patterns next to crystals c1 and c2 (Vinet EoS, Fei *et al*., 2007) are almost the same up to 21.1 GPa (Table 8.2). In this loading, crystal c1 was located at the center of the sample chamber and crystal c2 was closer to the rim. At higher pressures, the neon-based pressure close to crystal c1 is larger than that of crystal c2 by 0.5 GPa at ~ 25 GPa and by 1.7 GPa at ~ 64 GPa, indicating a pressure gradient across the pressure medium. Differences as large as 2.7 GPa at 54.5 GPa between the neon-based pressures and ruby-based pressures (Dewaele *et al*., 2004) are also observed (Table 8.2), indicating pressure gradient, and/or inconsistency between neon and ruby pressure scales.

In the 100-μm run, NaCl was also used as an additional calibrant (Dorogokupets and Dewaele, 2007; Fei *et al*., 2007). Discrepancy between the pressures calculated from NaCl (B2 phase, Fei *et al*., 2007) and neon (Fei *et al*., 2007) (Fig. 8.6) are observed. The difference between the neon-based pressure using Birch-Murnaghan EoS (Fei *et al*., 2007) and NaCl-based pressure using Vinet EoS (Fei *et al*., 2007) is as large as 15 GPa at 200 GPa (8±4 %) (Fig. 8.6).

For consistency in pressure between the three data sets from sample 300 μm-c1, sample 300 μm-c2, and the sample in the 100-μm run, we used neon pressure scale (Vinet EoS, Fei *et al*., 2007) whenever available. At low pressures, when neon had not solidified yet (bellow 11.5 GPa) or neon diffraction signals were not systematically collected (below 55 GPa in the 100-μm run), ruby-based pressures (Dewaele *et al*., 2004) were used.

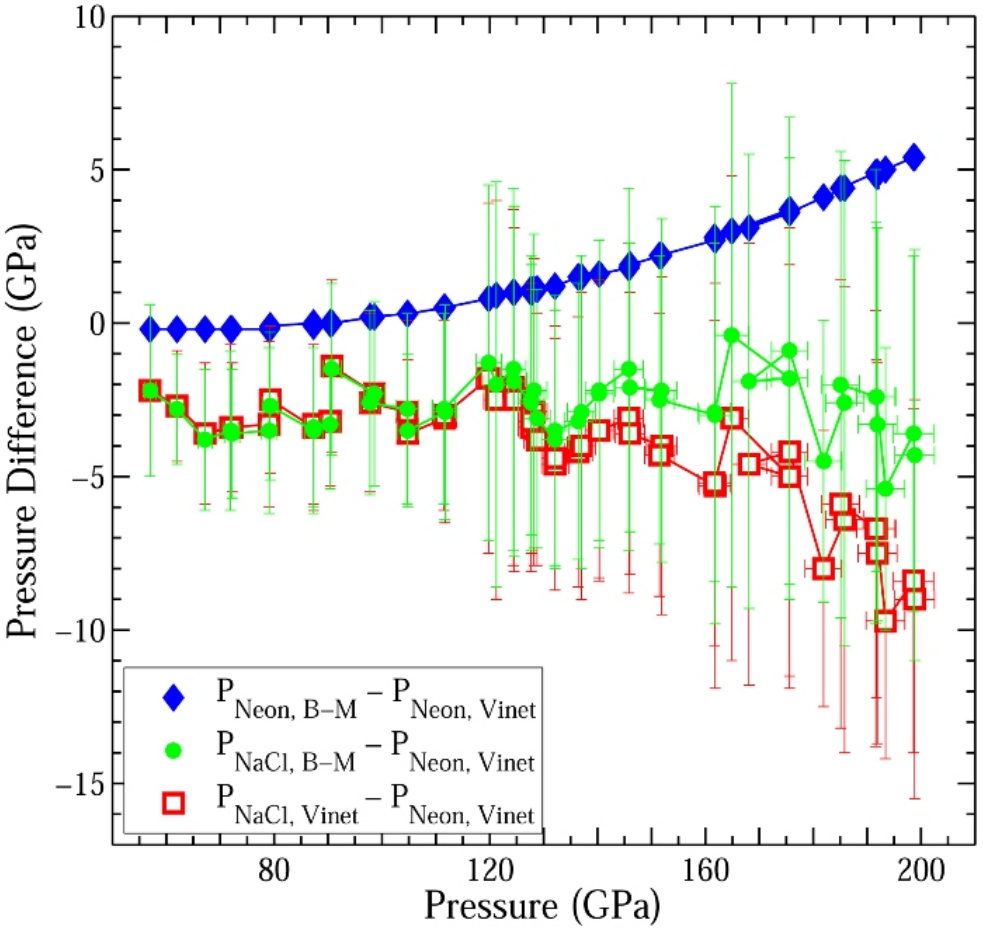

Fig. 8.6. Uncertainty in pressure determination using various equations of state (Fei *et al*., 2007). The X axis is the pressure determined using the Vinet EoS of neon. The Y axis is the difference in pressure between two pressure scales. The error bars correspond to uncertainties in the unit cell parameters.

8.3.3. Uncertainty Analysis

In the 300-μm run, none of the principal crystal axes in crystals c1 and c2 was close to the X-ray beam direction, offering good constraints on all three unit cell parameters *a*, *b* and *c*. The diffraction spots of Fe_3C remained small and round throughout the 300-μm run (up to ~ 64 GPa), indicating quasi hydrostatic condition in each sample (Fig. 8.1). Furthermore, annealing the crystal c2 at ~ 30 GPa using laser heating technique at ~ 1400 K for 7 minutes did not show any noticeable effect in the diffraction patterns. On the other hand, non-hydrostatic stress in the DAC in the 100-μm run as indicated by the elongated diffraction arcs may affect the derived lattice

parameters, especially the *b* axis, which was close to the DAC loading axis. There was a sudden increase in the length/width ratio of the elongated diffraction arcs at ~ 30 GPa – the maximum length/width ratio increased from ~ 2 at 22 GPa to ~ 5 at 30 GPa. The length/width ratio increased steadily to ~ 125 GPa (maximum length/width ratio is ~ 8 at 125 GPa), and remained the same as pressure further increased. Indeed, data scatter in the compression curves were observed around ~ 30 GPa (Figs. 8.2, 8.4) in the 100-μm rum.

In the 100-μm run in this study, the detector was placed at three different positions to collect XRD patterns. These three different sample-detector arrangements provide an insight into the estimate of non-hydrostatic stress. We calculated lattice parameters based on each of the three XRD patterns. The standard deviation between these three data sets was used as an estimate of uncertainty from non-hydrostatic stress. For the geometry of a DAC, the measured incompressibility and unit cell parameters are expected to be larger than the actual values when non-hydrostatic stress is present (Kinsland and Bassett, 1977). In compressed pure iron (Dewaele *et al*., 2006) and Fe-Si alloy (Hirao *et al*., 2004), non-hydrostatic condition has been observed to yield larger measured volumes. If we apply correction resulted from the crystal symmetry constraint in our data, the volumes of Fe_3C at high pressures in the 100-μm run may be even smaller.

8.4 IMPLICATIONS FOR CARBON IN THE EARTH'S INNER CORE

We extrapolated densities of Fe_3C to the inner core pressure and temperature (*P*-*T*) conditions (Fig. 8.7) based on the EoS (Table 8.3) from this study, an assumed inner core temperature of 5000 K, and estimated thermal expansion coefficients of 3.8×10^{-6} K^{-1} to 4.6×10^{-6} K^{-1} at 338 GPa and 550 K. The thermal expansion coefficient is estimated following the empirical relationship suggested in previous studies (Wood, 1993; Vočadlo *et al*., 2002):

$$\alpha = \alpha_0 \exp\left(\frac{6.5}{1.4}\left(\left(\frac{V}{V_0}\right)^{1.4} - 1\right)\right) \tag{8.1}$$

where V is the unit cell at the inner-core pressure (~ 338 GPa) and 300 K, V_0 and α_0 are unit cell volume and thermal expansion coefficient at ambient condition, respectively. Here we used α_0 of 4.1×10^{-5} K^{-1} at a reference temperature of 550 K and ambient pressure (Wood *et al*., 2004). We

used the value at a temperature of 550 K instead of 300 K because Fe_3C exhibits abnormally low thermal expansion coefficient at ambient conditions below the Curie temperature of ~ 480 K (invar effect) (ibid).

The extrapolated densities of Fe_3C based on the 10-200 GPa Birch-Murnaghan EoS are 12.6 – 12.9 g/cm^3, lower than the PREM values (12.8 – 13.1) (Dziewonski and Anderson, 1981) by ~ 1.2 %, comparable to the uncertainty of PREM (~ 1.5 %) referred by Dewaele *et al*. (2006). For the extrapolated density at inner core *P*-*T* conditions (~ 338 GPa and ~ 5000 K), the propagated uncertainty from our EoS parameters is ~ 0.9 %. This uncertainty (σ_ρ) includes the contribution from each EoS parameter (V_0, K_0, K') and the correlations between these parameters:

$$\begin{aligned}\sigma_\rho{}^2 = &\left(\frac{\partial P}{\partial V_0}\sigma_{V_0}\right)^2 + \left(\frac{\partial P}{\partial K_0}\sigma_{K_0}\right)^2 + \left(\frac{\partial P}{\partial K'}\sigma_{K'}\right)^2 \\ &+2Corr(V_0,K_0)\frac{\partial P}{\partial V_0}\frac{\partial P}{\partial K_0}\sigma_{V_0}\sigma_{K_0} \\ &+2Corr(V_0,K')\frac{\partial P}{\partial V_0}\frac{\partial P}{\partial K'}\sigma_{V_0}\sigma_{K'} \\ &+2Corr(K_0,K')\frac{\partial P}{\partial K_0}\frac{\partial P}{\partial K'}\sigma_{K_0}\sigma_{K'}\end{aligned} \tag{8.2}$$

where $Corr(V_0, K_0)$, $Corr(V_0, K')$ and $Corr(K_0, K')$ are the correlation coefficients between the EoS parameters V_0, K_0 and K' (see section 3.1). Using Vinet EoS and EoS derived based on data in the range of 70-200 GPa (Table 8.3) leads to similar extrapolated results (Fig. 8.7).

Based on our results, a mixture of Fe_3C and 0-20 % of iron can match the density of the inner core, for a conceivable core density deficit of 3 %. This estimate takes into account the 1.5 % uncertainty of the IC density in PREM (Dziewonski and Anderson, 1981; Dewaele *et al*., 2006), and 0.8 % propagation uncertainty from our 3rd Birch-Murnaghan EoS based on the 10-200 GPa data.

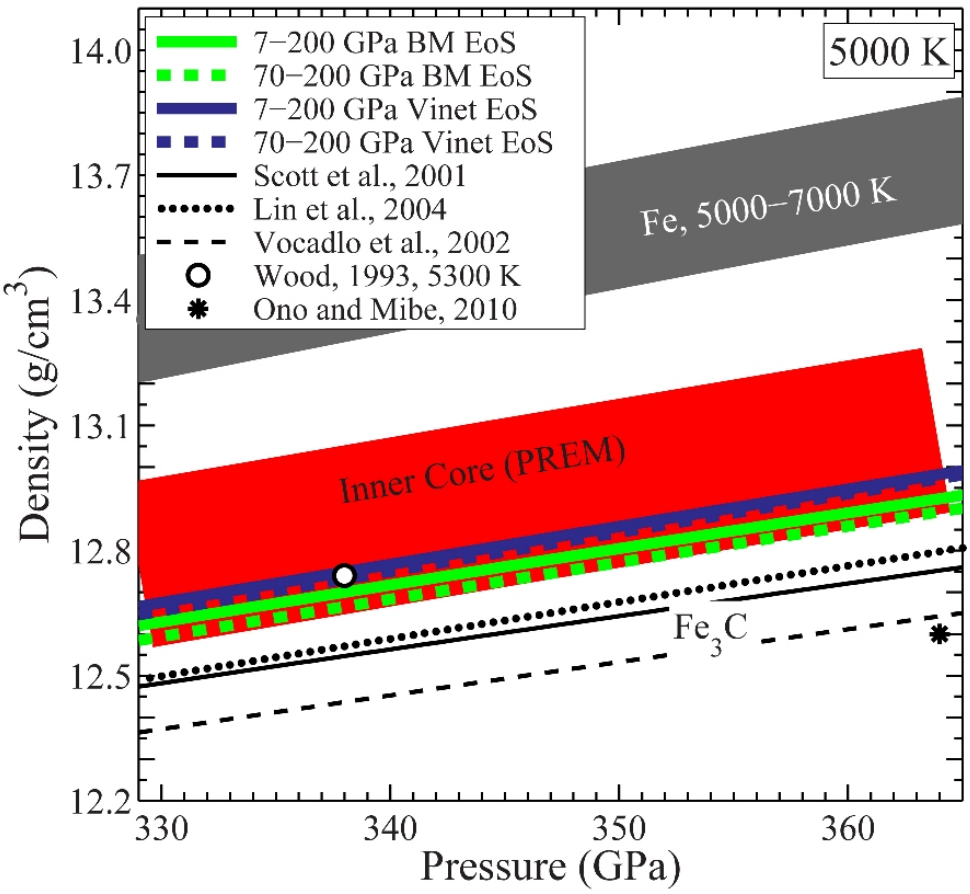

Fig. 8.7. Estimated densities of Fe_3C at the inner core pressures and 5000 K, in comparison with Fe (Dewaele *et al*., 2006) and PREM (Dziewonski and Anderson, 1981).

Accurate estimate of the Fe_3C density at the inner core *P-T* conditions require accurate pressure determination and accurate knowledge on EoS parameters and thermal expansion of Fe_3C. If we use pressures estimated using Vinet EoS of NaCl (Fei *et al*., 2007) instead of Vinet EoS of neon (ibid) in EoS fitting, the final estimated density at the inner-core *P-T* conditions would increase by ~ 1 %. A systematic decrease in the unit cell parameters of Fe_3C by 1 % (to account for possible stress effect) would result in a 2 % density increase. If the thermal expansion coefficient changes by 50 %, the estimated density of Fe_3C will change by ~ 1 %. The estimated density of Fe_3C is not significantly affected by the uncertainty in core temperature though. If the inner core temperature is assumed to be 40 % higher (7000 K instead of 5000 K), the extrapolated density is lower by only 0.8 %.

Chapter 9

Summary and Future Perspective

The advent of high-pressure devices and high brilliance synchrotron X-ray in the past few decades has enabled studies on small samples under extreme conditions, and greatly advanced our understanding of the Earth's interior. To reveal the composition of the Earth's inner core, which is a fundamental issue in the evolution of Earth and the core formation, together with collaborators, I studied the magnetic property, sound velocity, compressibility and density of Fe_3C, an inner-core candidate material, using a combination of Mössbauer spectroscopy, nuclear resonant X-ray inelastic scattering (NRIXS) and X-ray diffraction (XRD) methods integrated with laser heating, diamond anvil high-pressure cell and large volume presses.

It has been widely accepted that the Earth's core is composed of mainly iron-nickel alloy with a small addition of lighter elements (e.g., Li and Fei, 2007, and references therein). Compared to the inferred density of the inner core (e.g., Dziewonski and Anderson, 1981), the estimated density of pure iron at inner core pressure and temperature (*P*-*T*) conditions is higher by 1 – 9 wt.% (e.g., Dewaele *et al*., 2006; Li and Fei, 2007, and references therein). Carbon has been considered a possible major light element candidate, besides hydrogen, oxygen, silicon and sulphur (e.g., Li and Fei, 2007, and references therein). In particular, Fe_3C has been proposed to be the major component in the Earth's inner core in a previous thermodynamics study (Wood, 1993), although this view has been under debate recently (e.g., Scott *et al*., 2001; Vočadlo *et al*., 2002; Lin *et al*., 2004a; Gao *et al*., 2008; Fiquet *et al*., 2009; Nakajima *et al*., 2009; Lord *et al*., 2009; Ono and Mibe, 2010). This debate largely arises from our limited knowledge on the properties of Fe_3C under extreme *P*-*T* conditions. To test a carbon-rich inner core scenario, it is necessary to compare the properties of the iron-carbon compounds, such as the density and sound velocities, with the observed values (e.g., Dziewonski and Anderson, 1981). In this chapter, I summarize my results on Fe_3C, discuss how they impact our understanding about the Earth's inner core and point out directions for future work.

9.1 SUMMARY AND DISCUSSION

Seven ^{57}Fe-enriched Fe_3C samples (> 90 % enrichment) and six Fe_3C samples with natural iron isotopes were synthesized using large-volume presses. The composition and purity of the samples were confirmed using high-resolution XRD method at beamline 11-BM-B of the Advanced Photon Source (APS) at Argonne National Laboratory (ANL) and conventional Mössbauer spectroscopy (CMS) methods with ^{57}Co radioactive sources at sector 3 of the APS. The major components in all samples were confirmed to be Fe_3C with orthorhombic structure (#62, space group - Pnma). For sample #090, which was used in later high-pressure nuclear resonant scattering and XRD studies, Fe_3C was the only observed phase. In several other runs, excess iron and FeO are observed. The results from this work indicate that the run products are related to the particle size of Fe in the starting materials. Large grain size of iron in the starting material is likely to result in excess iron in the run product. In all ^{57}Fe-enriched Fe_3C samples, broad absorption lines were observed in CMS results, indicating distributions in magnetic hyperfine parameters. XRD diffraction data for the ^{57}Fe-enriched Fe_3C samples also exhibit broad diffraction lines. Even in a bulk pure batch, individual pieces with a size in the order of 10 μm in diameter still may contain large amount of impurity, as revealed in the synchrotron Mössbauer spectroscopy (SMS) measurements on pieces of sample from batch #090 (Gao *et al*., 2009; Chapter 7). Systematic differences in lattice parameters and unit cell volumes between the six Fe_3C samples with natural Fe isotopes and the seven ^{57}Fe-enriched Fe_3C samples. The unit cell volumes and lattice parameters *a* and *c* of the ^{57}Fe-enriched samples are smaller than those of the non-enriched samples, while the average lattice parameter *b* of the ^{57}Fe-enriched samples is larger than that of the non-enriched samples.

A magnetic transition in Fe_3C from the low-pressure ferromagnetic phase to a high-pressure non-magnetic phase has been reported in literature; however, the transition pressure has been controversial. An X-ray emission spectroscopy study reported a transition at ~ 25 GPa (Lin *et al*., 2004a) and an X-ray magnetic circular dichroism study reported a transition pressure at ~ 9 GPa (Duman *et al*., 2005). In this study, I carried out SMS and CMS experiments in an attempt to resolve the controversy. The results from both methods show that a magnetic transition occurs at ~ 6 GPa from a low-pressure ferromagnetically ordered phase to a high-pressure non-magnetic phase (Gao *et al*., 2008; Chapters 4, 5). The XRD data on single crystals of Fe_3C also suggest a discontinuity around this pressure (Chapter 8). The magnetic ordering of the phase above 6 GPa is not well understood.

At high pressure, the SMS data in this thesis work also suggest another transition between 50 GPa and 73 GPa (Chapter 8). This transition is very likely to be different from the 6 GPa transition, since both of the phases below and above the transition are non-magnetic, as indicated by a lack of fast oscillations. The cause of this transition is not yet clear, and it is possibly due to stress. On the other hand, a discontinuity at a similar pressure of ~ 45 GPa was indicated in the compression curves in the XRD study in this work (Chapter 8) and in a previous XRD study (Ono and Mibe, 2010).

To study the sound velocities of Fe_3C, I performed NRIXS experiments on a few-crystal sample (composed of one or a few single crystals) with *a* axis (the axis with medium length) aligned close to the direction of the X-ray beam up to 50 GPa at 300 K (Gao *et al*., 2008, Chapter 4) and on powder samples up to 45 GPa and 1450 K (Chapter 6). NRIXS method probes the lattice vibrations (phonons) of a material. From a NIRXS spectrum, phonon density of state (PDoS) was extracted using the *PHOENIX* program (Sturhahn, 2000). From the low-energy range of PDoS, Debye sound velocities V_D can be derived (e.g., Hu *et al*., 2003). Combining derived V_D and an existing equation of state, compressional wave velocity V_P and shear wave velocity V_S were derived. While V_P is largely dependent on the EoS parameters, V_S is mainly constrained by the Debye velocity V_D derived from NRIXS data (Chapter 6).

At ambient conditions, the difference in sound velocities between the few-crystal sample and a powder sample indicates anisotropy in Fe_3C (Chapters 6, 7; Gao *et al*., 2009). The anisotropy is large at ambient conditions, consistent with the recent report of extreme elastic anisotropy in cementite on the basis of first-principle calculations and XRD measurements (Nikolussi *et al*., 2008; Jiang *et al*., 2008). At high pressures, the V_P and V_S for the few-crystal sample and for power samples agree within 2 % in the explored *P*-*T* range, i.e., 0 - 50 GPa for the few-crystal data and 17-45 GPa for the powder sample data and at 300 K. The V_P and V_S for the high-pressure non-magnetic phase (> 6 GPa) follow the Birch's law – a linear dependence of sound velocity on density. The extrapolated V_P and V_S to the inner core pressures at 300 K based on each of these two data sets are higher than the inferred values for the inner core (e.g., Dziewonski and Anderson, 1981).

The effect of temperature on sound velocity is not well understood. Among the existing data, it has been controversial whether or not the high-temperature sound velocities deviate from

Birch's law. The sound velocity results from NRIXS experiments on powder Fe_3C samples up to 45 GPa and 1450 K help to shed lights on this issue (Chapter 6). The results at high temperatures suggest temperature induced shear velocity decrease, and also indicate that the temperature effect increases as temperature increases and decreases as pressure increases. The temperature needed to reconcile the sound velocity mismatch between Fe_3C and the inner core at 300 K is within the expected values for the inner core, supporting Fe_3C as a possible candidate material for the inner core.

Improved accuracy in experimentally determined sound velocities depends on improved experimental setups. A recent experimental capability of simultaneous nuclear resonant scattering and XRD measurements using synchrotron radiation has been installed at beamline 3-ID of the APS (Gao *et al*., 2009; Chapter 7). By combining the Debye velocity extracted from the NRIXS measurements and the density and elasticity data from the XRD measurements simultaneously obtained, more accurate sound velocity data can be derived. The XRD measurements also allow detection of microscale impurities, phase transitions and chemical reactions upon compression or heating. They also provide information on sample pressure, grain size distribution and unit cell volume.

To study the density and elastic properties of Fe_3C, I carried out XRD measurements on single crystals up to 200 GPa (Chapter 5). Bulk modulus and its pressure derivative were derived through equation-of-state fitting to the density versus pressure data using *FitEoS* program. Extrapolated densities to the inner core *P-T* conditions based on these EoS and estimated thermal expansion coefficients fall in the region of PREM values. These results suggest that pure Fe_3C or Fe_3C mixed with a small amount of iron could match the density of the inner core, supporting carbon as a possible major light element in the Earth's inner core.

In summary, the experimental results of density and sound velocities of Fe_3C from this work support carbon as a possible light element candidate in the inner core. The density of Fe_3C at inner-core *P-T* conditions inferred from this work suggest that pure Fe_3C or Fe_3C mixed with a small amount of iron could match the density of the inner core. The inferred compressional velocity V_P and shear velocity V_S of Fe_3C at 300 K and the inner-core pressures are higher than the observed values of the inner core. This is consistent with Fe_3C being an inner core candidate material, since the V_P and V_S of pure iron are suggested to be too low for the inner core (e.g., Lin

et al., 2005a). The measurements of V_S at high pressures and high temperatures in this work suggest temperature-induced shear velocity decrease, which may reconcile the difference between the inferred V_S of Fe_3C at 300 K at inner core pressures and that of the hot inner core.

A carbon-rich inner core with 6.7 wt. % of carbon, as in Fe_3C, is not in violation with carbon mass balance in the Earth. The inferred value of carbon concentration in the bulk silicate Earth from a pyrite model is ~ 10^2 ppm (0.01 wt. %), while the carbon concentration in CI carbonaceous chondrite, the most primordial meteorite, is ~ 3.5 wt.% (McDonough and Sun, 1995). As the Earth's core comprises nearly one third of the total mass of the Earth, and the inner core comprises about 4 % of the core, an inner core made of Fe_3C only contributes ~ 0.1 wt.% carbon to the bulk Earth, which is well within the maximum allowed value of ~ 3.5 wt. % by mass balance.

9.2 FUTURE PERSPECTIVE

The nature of the 6-GPa magnetic transition pressure is still not well understood, i.e., whether it is spin ordering change or spin state change. In a metal-like compound, the spin state can not be simply classified as high spin or low spin, but is more complicated. This issue still requires further investigation. Conducting Mössbauer spectroscopy measurements at low temperatures and high pressures above 6 GPa may help to determine whether the high pressure phase is in the paramagnetic state. It is known that Fe_3C undergoes a transition from the ferromagnetic phase to a paramagnetic phase at ~ 480 K at ambient pressure (e.g., Tsuzuki *et al*., 1984). Mössbauer spectroscopy measurements under an applied external field may shed light on whether the transition is dominated by an ordering change or spin state change.

SMS data in this study also suggest anther possible transition at higher pressure of between 50 and 73 GPa, with a mechanism that is likely to be different from the 6 GPa transition. The exact transition pressure is also not well constrained. The distribution of sample thickness and hyperfine field parameters renders the fittings to these MS spectra not unique and hinders the interpretation of the SMS spectra. SMS measurements on Fe_3C with uniform sample thickness and small distributions in hyperfine field parameters as well as better controlled hydrostatic pressure in the sample can help to reveal the nature of this observed transition. Density and compressibility measurements with XRD under better controlled hydrostatic conditions may also shed light on this issue. For such experiments, diamonds with large enough culet sizes should be used. Larger diamond culet allows larger sample chamber hence better control of the pressure

uniformity inside a DAC. Using the recently-established laser gasket drilling system at GSECARS instead of a manually-controlled EDM machine can better control the geometry of the sample chamber. This also might reduce the non-hydrostatic stress in the sample chamber. Using a sample with a small size may avoid the contact between the sample, diamonds and the gasket, although too small sample size may result in too small signal to noise ratio in diffraction signals.

Compared to the *P-T* conditions of the Earth's inner core, the *P-T* ranges in the sound velocity and density studies on Fe_3C in this thesis work are still limited, especially at high temperatures. In a 1984 article, Brett pointed out that "all discussions of the nature of the light element suffer from too few data and too many extrapolations". To date, this statement is still true. Measurements of sound velocity and density of Fe_3C at higher *P-T* conditions that are closer to the conditions of the inner core are challenging, yet they remain necessary to elucidate much of the current ambiguities. Measurements at better controlled hydrostatic conditions also will improve data accuracy and add constraints to a carbon-rich core scenario.

The role of carbon in the outer core has also been under debate. A study of iron-carbon phase diagram (Nakajima *et al*., 2009) suggests that large amount of carbon could be incorporated in the core if the Earth forming material was carbon-rich. However, an X-ray absorption image study on densities of Fe_3C melt up to 9.5 GPa and 1973 K suggests that addition of carbon lowers the bulk modulus of iron, arguing against carbon in the outer core (Terasaki *et al*., 2010). As already pointed out by Terasaki *et al*. (2010), the *P-T* range in their study is rather limited, and the constraint on the bulk modulus of Fe_3C melt is hence not strong. Further investigations on compressibility of ion-carbon melt at high *P-T* conditions are still needed.

In the past few decades, there has been cumulative evidence from seismology points to the Earth's core being anisotropic (e.g., Morelli and Dziewonski, 1986; Song and Helmberger, 1998; Sun and Song, 2008). The cause of the anisotropy is still not well understood. A number of mechanisms have been proposed in previous studies, including preferred orientation of ε–Fe (e.g. Karato, 1993; Bergman, 1997; Buffett and Wenk, 2001; Yoshida *et al.*, 1998), presence of liquid in the inner core (Singh *et al.*, 2000), and preferred orientation of bcc-iron in the inner core (Belonoshko *et al*., 2008). In Fe_3C, strong anisotropy has been suggested from first principle calculations under ambient conditions (Nikolussi *et al*., 2008; Jiang *et al*., 2008) and observed in

the NRIXS study (Gao *et al*., 2009). Whether or not Fe_3C exhibits strong anisotropy at high pressure and whether Fe_3C can help to explain the inner-core anisotropy remain to be investigated.

Besides Fe_3C, recent studies have suggested that another iron-carbon compound Fe_7C_3 might be relevant to the Earth's core. Fe_7C_3 was observed as a stable phase at above 6 GPa and 1450 K (Tsuzuki *et al*., 1984). A recent *in situ* XRD study to 29 GPa and 2300 K indicated that Fe_3C melts incongruently to Fe_7C_3 and other compounds, and suggested Fe_7C_3 to be the first phase to crystallize out an iron-carbon liquid when the carbon concentration in the liquid is no less than 6.7 wt.% (as in Fe_3C) (Nakajima *et al*., 2009). Lord *et al*. (2009) also suggested a similar idea based on X-ray radiography study on iron-carbon melting system up to 70 GPa. The density, elastic properties and sound velocities of Fe_7C_3 at high pressures and high temperatures should also be studied to constrain a carbon-rich core scenario.

One of the arguments for a Fe_3C-core in Wood (1993)'s study was the predicted shift of Fe-C eutectic melting composition towards the Fe end on a Fe-C phase diagram. However, this was not observed in a later multi-anvil and secondary electron microscopy (SEM) study by Chabot *et al*. (2008) up to 5 GPa and radiography study by Lord *et al*. (2009) up to 70 GPa. The experimental studies on phase diagrams of iron-carbon system up to 12 GPa by Hirayama *et al*. (1993) and up to 14 GPa by Nakajima *et al*. (2009) did not have enough data to constrain the eutectic point composition. To further constrain the role of carbon in the inner core, the iron-carbon system at high pressures and high temperatures remain to be investigated. The iron-carbon phase relevant to the core also depends on the mechanism of core formation. Furthermore, there is no reason to assume there is only one light element in the core. Multi light element systems also need to be further studied.

Despite extensive efforts towards a consistent pressure calibration system at high pressures and high temperatures in the past few decades, inconsistencies between different pressure scales still prevail, e.g., as observed in the mega-bar density study in this work (Chapter 5). Efforts towards consistent pressure scales are still needed.

Appendix A

FitEoS - a Java Graphical User Interface for High Pressure and High Temperature Equation of State Fitting

FitEoS is a java program that fits equation of state (EoS) parameters for a solid from experimental data of volume as a function of pressure (and temperature). An equation of state describes the relationship between volume, pressure and temperature. For a solid, EoS parameters include elastic parameters, such as bulk modulus and its pressure derivative. For high temperature EoS's, other parameters such as thermal expansion coefficient, or Mie-Grüneisen parameter are also inlvoved. In *FitEoS*, (weighted) least squares fitting method is used to extract EoS parameters from experimental data. Room-temperature EoS's included in this program are: Birch-Murnaghan EoS, Vinet EoS, natural (Hencky) strain EoS and Murnaghan EoS. High temperature EoS's that are implemented in this program are high-temperature Birch-Murnaghan EoS, Mie-Grüneisen-Debye (MGD) EoS, and a modified MGD EoS. Pressure, temperature and volume data and their uncertainties are used as input. Initial guesses of EoS parameters are also required. Outputs are fitted EoS parameters. This program is appropriate for applications in geophysics, material science or any other field where extracting EoS parameters from pressure-volume-temperature data is needed.

A.1 INTRODUCTION

Equation of state (EoS) describes the relationship between specific volume, pressure and temperature, which are essential parameters used in describing a thermodynamic state of a system.

Notations used in this article include the following:

P – pressure

σ_P – uncertainty of pressure

ε, f – strain, which describes the deformation in a material under stress

T – temperature

σ_T – uncertainty of temperature

V – unit cell volume

σ_V – uncertainty of unit cell volume

ρ – density

K – bulk modulus

K' – pressure derivative of the bulk modulus

Θ – Debye temperature

γ – Mie-Grüneisen parameter

α – thermal expansion coefficient

n – number of atoms per chemical formula

Z – number of chemical formulas per unit cell

N_{A} – Avogadro number

R – the ideal gas constant

Subscript '0' denotes a value at the reference condition, usually ambient temperature (300 K) and ambient pressure.

A.2 ISOTHERMAL EOS

A.2.1 Murnaghan's Integrated Linear EoS

Assuming a linear relationship between the bulk modulus and pressure, Murnaghan developed an EoS (e.g. Poirier, 2000; Angel 2000; and references therein), which is known as the Murnaghan's integrated linear EoS or Murnaghan's EoS. This EoS has the following form:

$$P = \frac{K_0}{K_0'}\left(\left(\frac{V_0}{V}\right)^{K_0'} - 1\right) \tag{A.1}$$

A.2.2 Birch-Murnaghan EoS

Birch-Murnaghan EoS is a widely used isothermal-temperature EoS that is based on finite strain theory (ibid). Taking Taylor expansion of Helmholtz free energy in powers of Eulerian strain, the Birch-Murnaghan EoS is derived. Pressure is related to the Helmholtz free energy by the following relationship:

$$P = -\left(\frac{\partial F}{\partial V}\right)_T \tag{A.2}$$

Eulerian strain is defined as the change in distance between two points with reference to the strained (deformed) state. It has the following form:

$$f = \frac{1}{2}\left(\left(\frac{V_0}{V}\right)^{2/3} - 1\right) \tag{A.3}$$

The 3rd-order form is expressed as:

$$\begin{aligned} P &= 3K_0 f\left(1+2f\right)^{5/2}\left(1+\frac{3}{2}\left(K'-4\right)f+\frac{3}{2}\left(K_0K''+\left(K'-4\right)\left(K'-3\right)+\frac{35}{9}\right)f^2\right) \\ &= \frac{3}{2}K_0\left(\left(\frac{V_0}{V}\right)^{7/3}-\left(\frac{V_0}{V}\right)^{5/3}\right)\left(1+\frac{3}{4}\left(K'-4\right)\left(\left(\frac{V_0}{V}\right)^{2/3}-1\right)\right) \end{aligned} \tag{A.4}$$

When K' = 4, the formula above reduces to the 2nd-order Birch-Murnaghan.

A.2.3 The Hencky (Natural)-Strain (Logarithmic) EoS

In this EoS, Hencky (natural) strain instead of Eulerian strain is used as the form of finite strain (ibid). Hencky (natural) strain does not depend upon the strained (as in Eulerian strain) or unstrained state (as in Lagrangian strain), and it has the following logarithmic form:

$$\varepsilon = \ln \frac{l}{l_0} \tag{A.5}$$

where l and l_0 are the final and initial length of the sample during deformation, respectively. It can be expressed as following if the pressure is hydrostatic (for compression case):

$$\varepsilon = \frac{1}{3} \ln \frac{V}{V_0} \tag{A.6}$$

The Taylor expansion of the Helmholtz free energy as a function of the Hencky strain leads to the following expression of the EoS (truncated to the 3rd-order):

$$P = K_0 \frac{V_0}{V} \ln \frac{V_0}{V} \left(1 + \left(\frac{K' - 4}{2} \right) \ln \frac{V_0}{V} \right) \tag{A.7}$$

The 2nd-order EoS is expresses as the following:

$$P = K_0 \frac{V_0}{V} \ln \frac{V_0}{V} \tag{A.8}$$

A.2.4 The Vinet EoS

An alternative EoS was developed based on an empirical free energy (ibid). This EoS has the following form:

$$P = 3K_0 \left(\frac{V}{V_0} \right)^{-2/3} \left(1 - \left(\frac{V}{V_0} \right)^{1/3} \right) \exp \left(\frac{3}{2} \left(K' - 1 \right) \left(1 - \left(\frac{V}{V_0} \right)^{1/3} \right) \right) \tag{A.9}$$

A.3 HIGH-TEMPERATURE EOS

A.3.1 High-temperature Birch-Murnaghan EoS

The high-temperature Birch-Murnaghan EoS is described as following:

$$P(V,T)=\frac{3}{2}K_{0,T}\left(\left(\frac{V_{0T}}{V}\right)^{7/3}-\left(\frac{V_{0T}}{V}\right)^{5/3}\right)\left(1+\frac{3}{4}\left(K'_{T}-4\right)\left(\left(\frac{V_{0T}}{V}\right)^{2/3}-1\right)\right) \tag{A.10}$$

$$V_{0,T}=V_0\exp\left(\int_{300}^{T}\left(\alpha_1+\alpha_2 T\right)\mathrm{d}T\right) \tag{A.11}$$

$$K_{0T}=K_0+\frac{\partial K_0}{\partial T}\left(T-300\right) \tag{A.12}$$

$$K_T^{'}=K^{'}+\frac{\partial K^{'}}{\partial T}\left(T-300\right) \tag{A.13}$$

Generally, $K_{0,T}$ is taken as constant, i.e., $\partial K'/\partial T = 0$ for the equation above.

If α_1 and α_2 have the units of 10^{-5} K^{-1} and $\times 10^{-9}$ K^{-2}, equation (A.11) can be rewritten as:

$$V_{0,T}=V_0\exp\left(\left(\alpha_1\cdot\left(T-300\right)+\frac{1}{2}\alpha_2\cdot\left(\left(\frac{T}{100}\right)^2-9\right)\right)\cdot 10^{-5}\right) \tag{A.14}$$

α_2 is often chosen to be zero, and in this case equation (A.11) is simplified as:

$$V_{0,T}=V_0\exp\left(\int_{300}^{T}\alpha_1\mathrm{d}T\right)=V_0\exp\left(\alpha_1\left(T-300\right)\right) \tag{A.15}$$

A.3.2 Mie-Grüneisen-Debye EoS

The Mie-Grüneisen-Debye EoS is described as (e.g. Poirier, 2000, and references therein):

$$P(V,T)=P(V,T_0)+\Delta P_{\mathrm{th}}(V,T) \tag{A.16}$$

where $P(V, T_0)$ is the isothermal pressure at the reference temperature T_0 (usually 300 K), and $\Delta P_{\mathrm{th}}(V, T)$ is the thermal pressure:

$$\Delta P_{\text{th}}(V,T) = P_{\text{th}}(V,T) - P_{\text{th}}(V,T_0) = \frac{\gamma}{V}\left(E_{\text{th}}(V,T) - E_{\text{th}}(V,T_0)\right) \tag{A.17}$$

$$E_{\text{th}}(V,T) = \frac{9nRT}{(\Theta/T)^3}\int_0^{\Theta/T}\frac{x^3}{e^x}\mathrm{d}x \tag{A.18}$$

where Θ is the Debye temperature, R is the ideal gas constant per unit cell, and n is the number of atoms per chemical formula. For MgO or NaCl, n = 2; for Au or Pt, n = 1. R is expressed as the following:

$$R = Z\frac{8.314472\ \text{J}\cdot\text{K}^{-1}\cdot\text{mol}^{-1}}{N_{\text{A}}\text{mol}^{-1}} = 0.01381\cdot Z\ \text{J}\cdot\text{K}^{-1} \tag{A.19}$$

where Z is the number of chemical formulas per unit cell

Mie-Grüneisen parameter and Debye temperature Θ are volume dependent, and they are calculated as:

$$\gamma = \gamma_0 \exp\left(\frac{V}{V_0}\right)^q \tag{A.20}$$

$$\Theta = \Theta_0 \exp\left(\frac{\gamma_0 - \gamma}{q}\right) \tag{A.21}$$

A.3.3 Modified Mie-Grüneisen-Debye EoS

When q_0 and q_1 instead of q only are used, as in the case of the MgO EoS by Speziale *et al*. (2001), q and Grüneisen parameter γ are calculated as:

$$q = q_0\left(\frac{V}{V_0}\right)^{q_1} \tag{A.22}$$

$$\gamma = \gamma_0 \exp\left(\frac{q_0}{q_1}\left(\left(\frac{V}{V_0}\right)^{q_1} - 1\right)\right) \tag{A.23}$$

With a volume dependent q, the Debye temperature does not have the simple form as in equation (A.21), but should be calculated from the definition of Mie-Grüneisen parameter (or Debye-Grüneisen parameter, see Poirier, 2000 for a list of definitions for the Grüneisen parameter):

$$\gamma = -\frac{\mathrm{d}\ln\Theta}{\mathrm{d}\ln V} \tag{A.24}$$

This leads to:

$$\Theta = \Theta_0 \exp\left(-\int_{V_0}^{V} \frac{\gamma(V)}{V}\mathrm{d}V\right) \tag{A.25}$$

A.4 WEIGHTED LEAST SQUARES FITTING METHOD

Description of least squares method can be found in a number of books (e.g. Prince, 1982). In EoS fitting, the input is experimental data of pressure P_i (i = 1, ..., n), pressure uncertainty $\sigma_{P,,i}$ (i = 1, ..., n), volume V_i (i = 1, ..., n), volume uncertainty $\sigma_{V,,i}$ (i = 1, ..., n), temperature T_i (i = 1, ..., n) and temperature uncertainty $\sigma_{T,,i}$ (i = 1, ..., n), where n is the number of data points. For a selected EoS, pressure is expressed as $y_i = f(V_i, T_i, A_1, \ldots, A_m)$, where A_j (j = 1, ..., m) are the EoS parameters we try to fit. Our goal is to find out the most reasonable EoS parameters by fitting. Assuming that the error distribution function is Gaussian, the problem is equivalent to finding the EoS parameters that lead to minimum value of S. For weighted least squares fitting, $S = \sum_{i=1}^{n} w_i \left(P_i - y_i\right)^2$, where w_i is the element in the ith row and ith column of the weight matrix W.

The weight matrix W is an $n \times n$ symmetrical matrix, with all the non-diagonal numbers equal to zero. The weight matrix W can be optionally constructed only based on the input uncertainties of pressures, or based on the input uncertainties of pressures as well as volumes and temperatures. In the latter case, a diagonal element in the ith row is defined as $w_i = C \cdot 1/(\sigma_{P,i}{}^2 + \sigma_{P\_V,i}{}^2 + \sigma_{P\_T,i}{}^2)$, where C is a normalization factor ($C = n / \sum_{i=1}^{n}\left(1/\left(\sigma_{P,i}{}^2 + \sigma_{P\_V,i}{}^2 + \sigma_{P\_T,i}{}^2\right)\right)$) to ensure that $\sum_{i=1}^{n} w_i = n$; $\sigma_{P\_V,i}$ and $\sigma_{P\_T,i}$ stand for the uncertainties of pressures propagated

from the uncertainties of volumes $\sigma_{V,i}$ and uncertainties of temperatures $\sigma_{T,i}$, respectively. This expression explicitly assumes that the input uncertainties of pressure, volume and temperature are uncorrelated.

In *FitEoS* program, we use Gaussian-Newton algorithm to find the minimum. The initial value of each EoS parameter ($A_{j,\text{init}}$, j = 1, …, m) is required as the input. We denote A_{init} as a $m\times1$ matrix composed of ($A_{j,\text{init}}$, j = 1, …, m). In an iteration, EoS parameters are updated according to $A_{\text{update}} = H^{-1}JTP$, where J is a $n \times m$ Jacobian matrix (also known as design matrix) composed of $J_{i,j} = \partial f_i/\partial A_j$, P is an $n \times 1$ matrix composed of experimental values P_i (i = 1, …, n), H is the Hessian matrix $H = J^TWJ$. Iterations will be carried out until minimum value of S is reached or until the maximum iteration number as defined by the user is reached. It should be pointed out that there is no guarantee that the minimum found using this procedure is the global minimum. It could be a local minimum or less likely a saddle point. No pure analytical method could avoid a false minimum. Reasonable initial parameters of $A_{j,\text{init}}$ (j = 1, …, m) are necessary to achieve reasonable fitting results.

The propagated error (standard deviation) for each fitted EoS parameter $\sigma_{A_j,P}$ (j = 1, …, m) is estimated as:

$$\sigma_{A_j,P}^2 = H_{j,j}s^2 \tag{A.26}$$

$$s^2 = \frac{1}{n-m}\sum_{i=1}^{n}\left(P_i - f_i\right)^2 \tag{A.27}$$

where $n - m$ is the degree of freedom. The χ^2 is calculated as $\chi^2 = P_{n,i=1}\ w_i'(P_i - y_i)^2/(n - m)$, where w_i' is the non-normalized weight (normalization factor C = 1). The $m \times m$ correlation matrix is calculated as $\rho_{kj} = H_{kj}^{-1}/(H_{kk}^{-1}\,\mathrm{H}_{jj}^{-1})^{1/2}$.

A.5 GRAPHICAL USER INERFACE

FitEoS program is written in Java, with the intention of enabling it to run on various computer operation systems. Java web start (Java SE JRE/SDK) 5.0 or up is required to run *FitEoS*. Accepted input file formats are:

- 2 column file: P (unit: GPa), V (unit: Å^3)
- 4 column file: P (unit: GPa), σ_P (unit: GPa), V (unit: Å^3), σ_V (unit: Å^3)
- 3 column file: P (unit: GPa), T (unit: K), V (unit: Å^3)
- 6 column file: P (unit: GPa), σ_P (unit: GPa), T (unit: K), σ_T (unit: K), V (unit: Å^3), σ_V (unit: Å^3)

A screenshot of *FitEoS* is shown in the following figure:

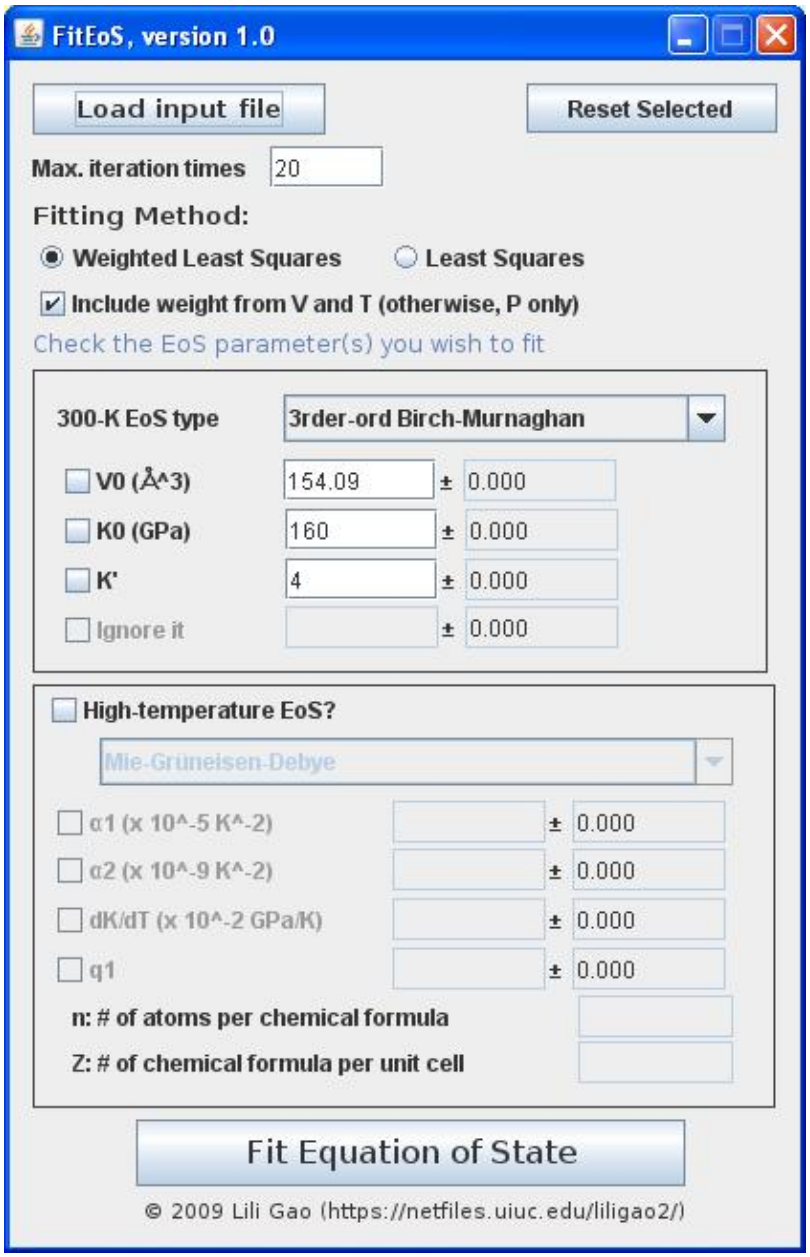

Fig. A.1. A screenshot of the *FitEoS* program (version 1.0).

Appendix B

Pressure Scale - a Java Program for Pressure Calibration

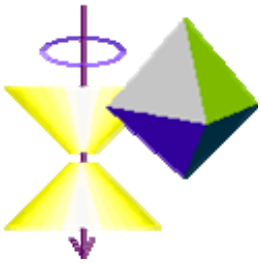

Pressure Scale is a java program used for calculating pressure and its uncertainty in high pressure studies. Users can either run the program online or download it to local computers. The inputs of the program are a known equation of state, experimentally measured volumes and temperatures. The outputs are pressure and its uncertainty. The current version implements these types of EoS: Birch-Murnaghan, Vinet, 2nd-order Hencky strain (natural strain), 3-rd order Hencky strain, Murnaghan EoS at 300 K, and Mie-Grüneisen-Debye, high-temperature Birch-Murnaghan, and modified Mie-Grüneisen-Debye EoS (Speziale *et al*., 2001) at high temperatures.

B.1 INPUT

B.1.1 Equation of State Input

Pressure Scale program reads equation of state (EoS) from a file. The default EoS file format has an extension of '.eos'. This type of EoS file can be created from the program (click the 'Create an EoS' button). JCPDS files are also accepted input files.

B.1.2 Temperature and Volume Input

Notations used in this article include the following:

P – pressure, in unit of GPa

σ_P – uncertainty of pressure, in unit of GPa

T – temperature, in unit of K

σ_T – uncertainty of temperature, in unit of K

V – unit cell volume, in unit of $Å^3$

σ_V – uncertainty of unit cell volume, in unit of $Å^3$

a, b, c– lattice parameters, in unit of Å

α, β, γ – lattice parameters, in unit of degree

$\sigma_a, \sigma_b, \sigma_c$– uncertainties of lattice parameters, in unit of Å

$\sigma_\alpha, \sigma_\beta, \sigma_\gamma$ – uncertainties of lattice parameters, in unit of degree

In *Pressure Scale* program, temperature and volume can be typed into the textboxes in the graphical user interface, or loaded from a file. The default input file format contains four columns: T (unit: K), σ_T (unit: K), V (unit: $Å^3$), σ_V (unit: $Å^3$). All accepted file formats are listed here:

- For cubic material:
  - 1 column file: V
  - 1 column file: a
  - 2 column file: T, σ_T (when '1st column is temperature' checkbox is selected)
  - 2 column file: T, a (when '1st column is temperature' checkbox is selected)
  - 2 column file: V, σ_V (when '1st column is temperature' checkbox is NOT selected)
  - 2 column file: a, σ_a (when '1st column is temperature' checkbox is NOT selected)
  - 4 column file: T, σ_T, V, σ_V (when '1st column is temperature' checkbox is selected)
  - 4 column file: T, σ_T, a, σ_a (when '1st column is temperature' checkbox is selected)
- For hexagonal and tetragonal material:

- 1 column file: V
- 2 column file: T, V (when '1st column is temperature' checkbox is selected)
- 2 column file: V, σ_V (when '1st column is temperature' checkbox is NOT selected)
- 3 column file: T, a, c (when '1st column is temperature' checkbox is selected)
- 4 column file: T, σ_T, V, σ_V (when '1st column is temperature' checkbox is selected)
- 4 column file: a, σ_a, c, σ_c (when '1st column is temperature' checkbox is NOT selected)
- 6 column file: T, σ_T, a, σ_a, c, σ_c (when '1st column is temperature' checkbox is selected)

- For orthorhombic material:
  - 1 column file: V
  - 2 column file: T, V (when '1st column is temperature' checkbox is selected)
  - 2 column file: V, σ_V (when '1st column is temperature' checkbox is NOT selected)
  - 3 column file: a, b, c (when '1st column is temperature' checkbox is NOT selected)
  - 4 column file: T, σ_T, V, σ_V (when '1st column is temperature' checkbox is selected)
  - 4 column file: T, a, b, c (when '1st column is temperature' checkbox is selected)
  - 6 column file: a, σ_a, b, σ_b, c, σ_c (when '1st column is temperature' checkbox is NOT selected)
  - 8 column file: T, σ_T, a, σ_a, b, σ_b, c, σ_c (when '1st column is temperature' checkbox is selected)
- For monoclinic material:

- 1 column file: V
- 2 column file: T, V (when '1st column is temperature' checkbox is selected)
- 2 column file: V, σ_V (when '1st column is Temperature' checkbox is NOT selected)
- 4 column file: T, σ_T, V, σ_V (when is '1st column is temperature' checkbox selected)
- 4 column file: a, b, c, α(when '1st column is temperature' checkbox is NOT selected)
- 5 column file: T, a, b, c, α (when '1st column is temperature' checkbox is selected)
- 8 column file: a, σ_a, b, σ_b, c, σ_c, α, σ_α(when '1st column is temperature' checkbox is NOT selected)
- 10 column file: T, σ_T, a, σ_a, b, σ_b, c, σ_c, α, σ_α (when '1st column is temperature' checkbox is selected)

- For triclinic material:
  - 1 column file: V
  - 2 column file: T, V (when '1st column is Temperature' checkbox is selected)
  - 2 column file: V, σ_V (when '1st column is Temperature' checkbox is NOT selected)
  - 4 column file: T, σ_T, V, σ_V (when '1st column is temperature' checkbox is selected)
  - 6 column file: a, b, c, α, β, γ (when '1st column is temperature' checkbox is NOT selected)
  - 12 column file: a, σ_a, b, σ_b, c, σ_c, α, σ_α, β, σ_β, γ, σ_γ (when '1st column is temperature' checkbox is NOT selected)
  - 12 column file: T, σ_T, a, σ_a, b, σ_b, c, σ_c, α, σ_α, β, σ_β, γ, σ_γ (when '1st column is temperature' checkbox is selected)

B.2 OUTPUT

The output of this program is pressure and its uncertainty. The formulas of EoS's included in this program are listed in Appendix A. Two types of uncertainties are available in the program: variance and absolute error.

Variance is calculated as:

$$\sigma_P = \sqrt{\left(\frac{\partial P}{\partial V_0}\sigma V_0\right)^2 + \left(\frac{\partial P}{\partial K_0}\sigma K_0\right)^2 + \ldots \left(\frac{\partial P}{\partial V}\sigma V\right)^2 + \left(\frac{\partial P}{\partial T}\sigma T\right)^2} \qquad \text{(B.1)}$$

Absolute error is calculated as:

$$\Delta_P = \left|\frac{\partial P}{\partial V_0}\right|\Delta V_0 + \left|\frac{\partial P}{\partial K_0}\right|\Delta K_0 + \ldots + \left|\frac{\partial P}{\partial V}\right|\Delta V + \left|\frac{\partial P}{\partial T}\right|\Delta T \qquad \text{(B.2)}$$

Correlations between EoS parameters are not accounted for in the uncertainty estimate in the current version of *Pressure Scale* (version 1.3).

B.3 GRAPHICAL USER INTERFACE

A screenshot of *Pressure Scale* program in the following figure:

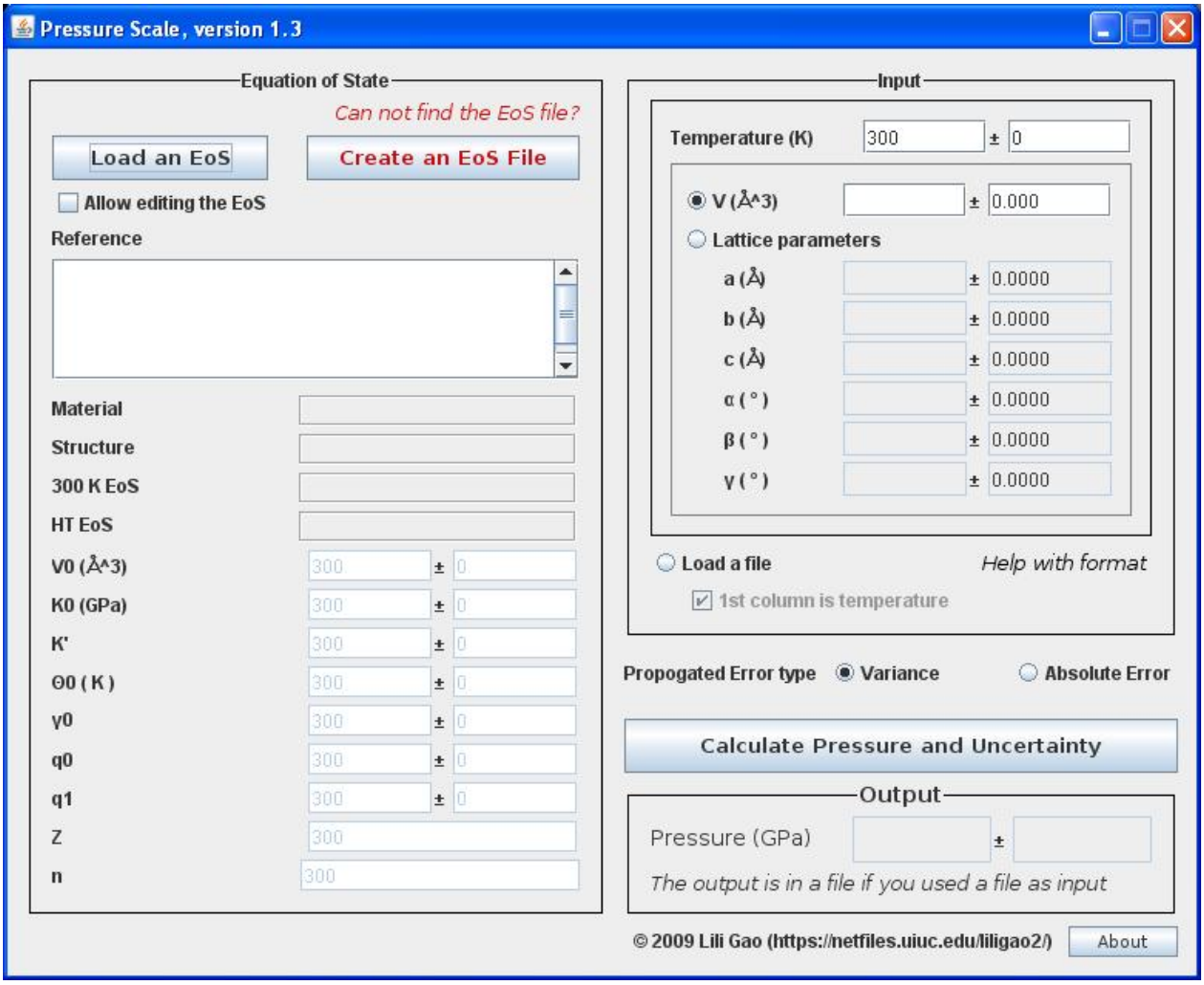

Fig. B.1. A screenshot of the *Pressure Scale* program (version 1.3).

References

Alp, E.E., Sturhahn, W. and Toellner, T. (1995) Synchrotron Mössbauer spectroscopy of powder samples. *Nucl. Instrum. Methods Phys. Res., Sect. B*, 97 (1-4), 526-529.

Anderson, O.L. (1980) The temperature profile of the upper mantle. *J. Geophys.*, 85 (B12), 7003-7010.

Angel R.J. (2000) Equations of state. In RM Hazen and RT Downs (eds.), High pressure and high-temperature crystal chemistry. *Rev. Mineral. Geochem.*, 41, 35-60.

Antonangeli, D., Occelli, F., Requardt, H., Badro, J., Fiquet, G. and Krisch, M. (2004) Elastic anisotropy in textured hcp-iron to 112 GPa from sound wave propagation measurements. *Phys. Earth Planet. Inter.*, 225, 243-251.

Andrault, D., Fiquet, G., Itié, J.P., Richet, P., Gillet, P., Hausermann, D. and Hanfland, M. (1998) Thermal pressure in the laser-heated diamond-anvil cell: an X-ray diffraction study. *Eur. J. Mineral.*, 10, 931-940.

Bancroft, G.M. (1973) Mössbauer spectroscopy: an introduction for inorganic chemists and geochemists. Wiley and Sons, New York.

Baron, A.Q.R. and Ruby, S.L. (1994) Time resolved detection of X-rays using large area avalanche photodiodes. *Nucl. Instrum. Methods Phys. Res. A*, 350, 595-626.

Bauer-Grosse, E., Le Caër, G. and Fournes, L. (1986) Mössbauer study of amorphous and crystallized $Fe_{1-x}C_x$ alloys. *Hyperfine Interact.*, 27, 297-300.

Bell, P.M. and Mao, H.K. (1981) Degree of hydrostaticity in He, Ne and Ar pressure-transmitting media. *Carnegie Inst. Washington Yb.*, 80, 404-406.

Belonoshko, A.B., Skorodumova, N.V., Rosengren A. and Johansson B. (2008) Elastic anisotropy of Earth's inner core. *Science*, 319, 797-800, DOI: 10.1126/science.1150302.

Bergman, M.I. (1997) Measurements of electric anisotropy due to solidification texturing and the implications for the Earth's inner core. *Nature*, 389, 60-63.

Bertka, C.M. and Fei, Y. (1997) Mineralogy of the Martian interior up to core-mantle boundary pressures. *J. Geophys. Res.*, 102, 5251-52643.

Bi, X.X., Ganguly, B., Huffman, G.P., Huggins, F.E., Endo, M. and Eklund, P.C. (1993) Nanocrystalline α-Fe, Fe_3C and Fe_7C_3 produced by CO_2 laser pyrolysis. *J. Mater. Res.*, 8, 1666-1674.

Birch, F. (1952) Elasticity and constitution of the Earth's interior. *J. Geophys. Res.*, 57, 227-286.

Birch, F. (1961) The velocity of compressional waves in rocks to 10 kilobars, part 2. *J. Geophys. Res.*, 66, 2199-2224.

Birch, F. (1986) Equation of state and thermodynamic parameters of NaCl to 300 kbar in the high-temperature domain. *J. Geophys. Res.*, 91(B5), 4949-4954.

Brown, J.M. and McQueen, R.G. (1986), Phase transitions, Grüneisen parameter and elasticity for shocked iron between 77 GPa and 400 GPa. *J. Geophys. Res.*, 91, 7485-7494.

Buffett, B. and Wenk, H.-R. (2001) Texturing of the inner core by Maxwell stresses. *Nature*, 413, 60-63.

Chabot, N.L., Campbell, A.J., McDonough, W.F., Draper, D.S., Agee, C.B., Humayun, M., Watson, H.C., Cottrell, E. and Saslow, S.A. (2008) The Fe–C system at 5 GPa and implications for Earth's core. *Geochimi. et Cosmochimi. Acta*, 72, 4146-4158.

Chen B., Gao, L., Funakoshi, K.-i. and Li, J. (2007) Thermal expansion of iron-rich alloys and

implications for the Earth's core. *Proc. Natl. Acad. Sci. USA*, 104 (22), 9162-9167, doi 10.1073/pnas.0610474104.

Chen, B., Li, J. and Hauck, S.A.II (2008) Non-ideal liquidus curve in the Fe-S system and Mercury's snowing core. *Geophys. Res. Lett.*, 35, L07201, doi:10.1029/2008GL033311.

Chipman, J. (1972) Thermodynamics and phase diagram of the Fe-C system. *Metal. Trans*. 3, 55-64.

Chumakov, A.I., Rüffer, R., Baron, A.Q.R., Grünsteudel, H., Grünsteudel, H.F. and Kohn, V.G. (1997) Anisotropic inelastic nuclear absorption. *Phys. Res. B*, 56, 10758-10761.

David, B., Zborilb, R., Mashlanb, M., Grygarc, T., Dumitrached F. and Schneeweiss, O. (2006) Single ferromagnetic behavior of nanopowders with Fe_3C. *J. Magn. Magn. Mater.*, 304, e787–e789.

Dera, P. (2007) GSE-ADA data analysis program for monochromatic single crystal diffraction with area detector. *GeoSoilEnviroCARS*, Argonne, IL.

Dewaele, A., Loubeyreand, P. and Mezouar, M. (2004) Equations of state of six metals above 94 GPa. *Phys. Rev. B*, 70, 094112.

Dewaele, A., Loubeyre, P., Occelli, F., Mezouar, M., Dorogokupets, P.I. and Torrent, M. (2006) Quasihydrostatic equation of state of iron above 2 Mbar. *Phys. Rev. Lett.*, 97, 215504.

Dodd, S.P., Saunders, G.A., Cankurtaran, M., James, B. and Acet, M. (2003) Ultrasonic study of the temperature and hydrostatic-pressure dependencies of the elastic properties of polycrystalline cementite. *Phys. Status Solidi A*, 198 (2), 272-281.

Dorogokupets, P.I. and Dewaele, A. (2007) Equations of state of MgO, Au, Pt, NaCl-B1 and NaCl-B2: Internally consistent high-temperature pressure scales. *High Pressure Res.*, 27 (4), 431-446.

Duman, E., Acet, M., Wassermann, E.F., Itié, J.P., Baudelet, F., Mathon, S. and Pascarelli, S. (2005) Magnetic instabilities in Fe_3C cementite particles observed with Fe K-edge X-ray circular dichroism under pressure. *Phys. Rev. Lett.*, 94, 075502, doi:10.1103/PhysRevLett.94.075502.

Dyar, M.D., Agresti, D.G., Schaefer, M.W., Grant, C.A. and Sklute, E.C. (2006) Mössbauer spectroscopy of Earth and planetary materials. *Annu. Rev. Earth Planet. Sci.*, 34, 83-125.

Dziewonski, A.M. and Anderson, D.L. (1981) Preliminary reference Earth model. *Phys. Earth Planet. Inter.*, 25, 297–356.

Eng, P.J., Newville, M., Rivers, M.L. and Sutton, S.R. (1998) Dynamically figured Kirkpatrick Baez X-ray micro-focusing optics. *Proc. SPIE*, 3449, 145-156.

Fasiska, E.J. and Jeffrey, G. A. (1965) On the cementite structure. *Acta. Cryst.*, 19, 463-471.

Fei, Y., Ricolleau, A., Frank, M., Mibe, K., Shen, G. and Prakapenka, V. (2007) Toward an internally consistent pressure scale. *Proc. Natl. Acad. Sci.*, 104 (22), 9182-9186.

Fiquet, G., Badro, J., Guyot, F., Requardt, H. and Krisch, M. (2001) Sound velocities in iron to 110 Gigapascals. *Science*, 291 (5503), 468–471.

Fiquet, G., Badro, J., Gregoryanz, E., Fei, Y. and Occelli, F. (2009) Sound velocity in iron carbide (Fe_3C) at high pressure: implications for the carbon content of the Earth's inner core. *Phys. Earth Planet. Int.*, 172, 125-129.

Frauenfelder, H. (1962) The Mössbauer effect: A review - with a collection of reprints, *Frontiers in Physics Series*, W. A. Benjamin.

Frost, D.J. (2008) The Upper Mantle and Transition Zone, *Elements*, 4, 171-176, DOI: 10.2113/GSELEMENTS.4.3.171

Fujishiro, I., Piermarini, G. J., Block, S. and Munro, R.G. (1982) Viscosities and glass transition pressures in the methanol-ethanol-water system. in *High Pressure Research in Science and Industry:*

Proceedings of the 8th AIRAPT Conference, vol. 2, edited by C.-M. Backman, T. Johannison and L. Tegner, pp. 608–611, Univ. of Uppsala, Uppsala, Sweden.

Gao, L., Chen, B., Wang, J., Alp, E.E., Zhao, J., Lerche, M., Sturhahn, W., Scott, H.P., Huang, F., Ding, Y., Sinogeikin, S.V., Lundstrom, C.C., Bass, J.D. and Li, J. (2008) Pressure-induced magnetic transition and sound velocities of Fe_3C: implications for carbon in the Earth's inner core. *Geophys. Res. Lett.*, 35, L17306, doi:10.1029/2008GL034817.

Gao, L., Chen, B., Lerche, M., Alp, E.E., Sturhahn, W., Zhao, J., Yavaş, H. and Li, J. (2009) Sound velocities of compressed Fe_3C from simultaneous synchrotron X-ray diffraction and nuclear resonant scattering measurements. *J. Synchrotron Rad.,* 16, 714722, doi:10.1107/S0909049509033731.

Gerdau, E., Rüffer, R., Winkler, H., Tolksdorf, W., Klages, C.P. and Hannon, J.P. (1985) Nuclear Bragg diffraction of synchrotron radiation in yttrium iron garnet. *Phys. Rev. Lett.*, 54, 835-838.

Goodrich C.A. (1992) Ureilites: a critical review. *Meteoritics*, 27, 327-352.

Hammersley, A. (2004) FIT2D V12.012 reference manual V6.0. European Synchrotron Radiation Facility, Grenoble, France.

Hauck, S.A.II, Aurnou, J.M. and Dombard, A.J. (2006) Sulfur's impact on core evolution and magnetic field generation on Ganymede. *J. Geophys. Res.*, 111, E09008, doi:10.1029/2005JE002557.

Hayden, L.A. and Watson, E.B. (2008) Grain boundary mobility of carbon in Earth's mantle: a possible carbon flux from the core, *Proc. Natl. Acad. Sci. US*A, 105 (25)8537–8541

Hirao, N., Ohtani, E., Kondo, T. and Kikegawa, T. (2004) Equation of state of iron silicon alloys to megabar pressure. *Phys. Chem. Miner.*, 31(6), 329-336.

Hirayama, Y, Fujii, T. and Kurita, K. (1993) The melting relation of the system, iron and carbon at high pressure and its bearing on the early stage of the Earth. *Geophys. Res. Lett.*, 20, 20952098.

Holland, T.J.B. and Redfern, S.A.T. (1997) UNITCELL: a nonlinear least-squares program for cell-parameter refinement implementing regression and deletion diagnostics. *Minera. Mag.*, 61, 65-77.

Hu, M.Y., Sturhahn, W., Toellner, T., Mannheim, P.D., Brown, D.E., Zhao, J. and Alp, E.E. (2003) Measuring velocity of sound with nuclear resonant inelastic x-ray scattering. *Phys. Rev. B*, 67(9), 094304, doi:10.1103/PhysRevB.67.094304.

Huang, L., Skorodumova, N.V., Belonoshko, A.B., Johansson, B. and Ahuja, R. (2008) Carbon in iron phases under high pressure. *Geophys. Res. Lett.*, 32, L21314, doi:10.1029/2005GL024187.

Isaak, D.G. and Anderson, O.L. (2003) Thermal expansivity of HCP iron at very high pressure and temperature. *Physica B*, 328(3-4), 345-354.

Jacob, D.E., Kronz, A. and Viljoen, K.S. (2004) Cohenite, native iron and troilite inclusions in garnets from polycrystalline diamond aggregates. *Contrib. Mineral. Petrol*., 146, 566-576.

Jiang, C., Srinivasan, S.G., Caro, A. and Maloy, S.A. (2008) Structural, elastic and electronic properties of Fe_3C from first principles. *J. Appl. Phys*., 103, 043502

Kantor, A.P., Kantor, I.Y., Kurnosov, A.V., Kuznetsov, A.Y., Dubrovinskaia, N.A., Krisch, M., Bossak, A.A., Dmitriev, V.P., Urusov, V.S. and Dubrovinsky, L.S. (2007) Sound wave velocities of fcc FeNi alloy at high pressure and temperature by mean of inelastic X-ray scattering. *Phys. Earth Planet. Inter.*, 163, 83-89.

Karato, S. (1993) Inner core anisotropy due to magnetic field-induced preferred orientation of iron. *Science*, 262, 170811.

Kavner, A. and Duffy, T.S. (2001) Pressure-volume-temperature paths in the laser-heated diamond anvil cell, *J Aplp. Phys*., 89(3): 107-1914

Kennett, B.L.N. and. Engdahl, E.R. (1991) Travel times for global earthquake location and phase identification. *Geophys. J. Int.*, 105, 429-465.

Kennett B.L.N., Engdahl, E.R. and Buland, R. (1995) Constraints on seismic velocities in the Earth from travel times. *Geophys. J. Int.*, 122, 108-124.

Kieffer, S. (1979) Thermodynamics and lattice vibrations of minerals: I. mineral heat capacities and their relationships to simple lattice vibrational models. *Rev. Geophys. and Space Phys.*, 17, 1-19.

Kinsland, G.L. and Bassett, W.A. (1977) Strength of MgO and NaCl polycrystals to confining pressures of 250 kbar at 25°C. *J. Appl. Phys.*, 48, 978-985.

Kishimoto, S. (1992) High time resolution X-ray measurements with an avalanche photodiode detector, *Rev. Sci. Instrum.*, 63, 824-827.

Kittel, C. (2005) Introduction to solid state physics. 8th ed. John Wiley and Sons, Inc. New York.

Klotz, S., Chervin, J-C., Munsch, P. and Le Marchand, G. (2009) Hydrostatic limits of 11 pressure transmitting media. *J. Phys. D: Appl. Phys.*, 42, 075413.

Larson, A.C. and Von Dreele, R.B. (2004) General structure analysis system (GSAS). *Los Alamos National Laboratory Report LAUR*, 86-748.

Lay, T., Hernlund, J. and Buffett, B.A. (2008) Core–mantle boundary heat flow. *Nature Geoscience*, 1, 25-32.

Li, J., Mao, H.K., Fei, Y., Gregoryanz, E., Eremets, M. and. Zha, C.S. (2002) Compression of Fe_3C to 30 GPa at room temperature. *Phys. Chem. Miner.*, 29(3), 166-169.

Li, J. and Fei, Y. (2007) Experimental constraints on core composition, in *Treatise on Geochemistry Update 1*, (ed. H. D. Holland and K. K. Turekian), Elsevier Ltd, Vol. 2.14, 1-31.

Liebermann, R.C. and Wang, Y. (1992) Characterization of sample environment in a uniaxial split-sphere apparatus. in: Y. Syono, M.H. Manghnani (Eds.), High-Pressure Research: Application to Earth and Planetary Sciences, American Geophysical Union, Washington, DC, 19–31.

Lin, J.F., Struzhkin, V.V., Sturhahn, W., Huang, E., Zhao, J., Hu, M.Y., Alp, E.E., Mao, H., Boctor, N. and Hemley, R.J. (2003a), Sound velocities of iron-nickel and iron-silicon alloys at high pressures. *Geophys. Res. Lett.*, 30(21), 2112, doi:10.1029/2003GL018405.

Lin, J.F., Shu, J., Mao, H.K., Hemley, R.J. and Shen, G. (2003b) Amorphous boron gasket in diamond anvil cell research. *Rev. Sci. Instrum.*, 74, 4732-4736.

Lin, J.F., Struzhkin., V.V., Mao, H.K., Hemley, R.J., Chow, P., Hu, M.Y. and Li, J. (2004a) Magnetic transition in compressed Fe_3C from X-ray emission spectroscopy. *Phys. Rev. B*, 70(21), 212405, doi:10.1103/PhysRevB. 70.212405.

Lin, J.F., Fei, Y., Sturhahn, W., Zhao, J., Mao, H.K. and Hemley, R.J. (2004b) Magnetic transition and sound velocities of Fe_3S at high pressure: Implications for Earth and planetary cores. *Earth Planet. Sci. Lett.*, 226(1-2), 33-40.

Lin, J.F., Sturhahn, W., Zhao, J., Shen, G., Mao, H.K. and Hemley, R.J. (2005a) Sound velocities of hot dense iron: Birch's Law revisited. *Science*, 308(5730), 1892-1894.

Lin, J.F., Sturhahn, W., Zhao, J., Shen, G., Mao, H.K. and Hemley, R.J. (2005b) Nuclear resonant inelastic X-ray scattering and synchrotron Mössbauer spectroscopy with laser-heated diamond anvil cells. *Advances in High-Pressure Technology for Geophysical Application*, 397-411.

Lord, O.T., Walter, M.J,. Dasgupta, R., Walker, D. and Clark, S.M. (2009) Melting in the Fe-C system to 70 GPa. *Earth Planet. Sci. Lett.*, 284, 157-167.

Lynch, F.J., Holland, R.E. and Hemeiwesh, M. (1960) Time dependence of resonantly filtered gamma rays from Fe^{57}. *Phys. Rev.*, 120, 513-520.

Mao, H.K., Bell, P.M., Shaner, J.W. and. Steinberg, D.J. (1978) Specific volume measurements of Cu, Mo, Pd and Ag and calibration of the ruby R_1 fluorescence pressure gauge from 0.06 to 1 Mbar. *J. Appl. Phys.*, 49, 3276-3283.

Mao, H. K., Y. Wu, L. C. Chen, J. F. Shu, and A. P. Jephcoat (1990), Static compression of iron to 300 GPa and $Fe_{0.8}Ni_{0.2}$ alloy to 260 GPa: Implications for composition of the core, *J. Geophys. Res.,* 95, 21737-21742.

Mao, H.K. and Hemley, R.J. (1998) New windows on the Earth's deep interior, in Ultrahigh-Pressure Mineralogy: Physics and Chemistry of the Earth's Deep Interior. *Rev. Min.*, Vol. 37 (ed. R. J. Hemley) 1-32 (Mineralogical Society of America, Washington, D.C.).

Mao, H.K., Xu, J., Struzhkin, V.V., Shu, J., Hemley, R.J., Sturhahn, W., Hu, M.Y., Alp, E.E., Vočadlo, L., Alfè, D., Price, G.D., Gillan, M.J., Schwoerer-Böhning, M., Häusermann, D., Eng, P., Shen, G., Giefers, H., Lübbers, R. and Wortmann, G. (2001) Phonon density of states of iron up to 153 Gigapascals. *Science*, 292(5518), 914-916.

Mao, W. L., Sturhahn, W., Heinz, D.L., Mao, H.-K., Shu, J. and Hemley, R.J. (2004) Nuclear resonant x-ray scattering of iron hydride at high pressure. *Geophys. Res. Lett*., 31, L15618, doi:10.1029/ 2004GL020541.

Masters, T.G. and Shearer, P.M. (1990), Summary of seismological constraints on the structure of the Earth's core. *J. Geophys. Res.*, 95, 21691–21695.

McCammon, C. (2001) Deep diamond mysteries, *Science*, 293, 813-814

McCammon, C.A. (2004) Mössbauer spectroscopy: applications. In *Spectroscopic Methods in Mineralogy (A. Beran & E. Libowitzky, eds.). EMU. Notes in Mineralogy*, vol. 6, Chapter 9, 369-398.

McDonough, W.F. and Sun, S.-S. (1995) Composition of the Earth. *Chem. Geol.*, 120, 223-253, doi: 10.1016/0009-2541(94)00140-4.

Morelli, A. and Dziewonski, A.M. (1986) Anisotropy of the inner core inferred from PKIKP travel times. *Geophys. Res. Lett.*, 13, 1545-1548.

Morelli. A. and Dziewonski, A.M. (1993) Body-wave travel times and a sph.erically symmetric P- and S-wave velocity model. *Geophys. J. Int*., 112, 178-194.

Nakajima, Y., Takahashia, E., Suzukib, T. and Funakoshic, K-i (2009) "Carbon in the core" revisited. *Phys. Earth Planet. Inter*., 174, 202-211.

Nikolussi, M., Shang, S.L., Gressmann, T., Leineweber, A., Mittemeijer, E.J., Wang, Y. and Liub, Z.K. (2008) Extreme elastic anisotropy of cementite, Fe_3C: First-principals calculations and experimental evidence. *Scr. Metall.*, 59, 814-817.

Ono, S. and Mibe, K. (2010) Magnetic transition of iron carbide at high pressures. *Phys. Earth Planet. Inter.*, 180, 1-6.

Poirier, J.P. (1994) Light-elements in the Earth's outer core-a critical-review. *Phys. Earth Planet. Inter.*, 85, 319-337.

Poirier, J.P. (2000) Introduction to the physics of the Earth's interior. Cambridge Univ. Press, New York.

Prantzos, N. (2007) Stellar nucleosynthesis. *Lectures in Astrobiology, Advances in Astrobiology and Biogeophysics*, Springer-Verlag Berlin Heidelberg, Volume 2007.

Prince, E. (1982) Mathematical techniques in crystallography and materials science. New York, Heidelberg, Berlin, Springer-Verlag.

Ringwood, A.E. (1966) Chemical evolution of terrestrial planets. *Geochim. Cosmochim. Acta*, 30, 41-104.

Ringwood, A.E. (1977) Composition of the core and implications for the origin of the Earth. *Geochem. J.*, 11, 111-135.

Ron, M. and Mathalone, Z. (1971) Hyperfine interactions of ^{57}Fe in Fe_3C, *Phys. Rev. B*, 4(3), 774–777.

Rubie, D.C., Nimmo, F. and Melosh, H.J. (2007) Formation of Earth's core. in *Treatise on Geophysics*, edited by G. Schubert and D. J. Stevenson, Elsevier, New York, 9, 51–90.

Scott, H.P., Williams, Q. and Knittle, E. (2001) Stability and equation of state of Fe_3C to 73 GPa: Implications for carbon in the Earth's core. *Geophys. Res. Lett.*, 28, 1875-1878.

Seto, M., Yoda, Y., Kikuta, S., Zhang, S.W. and Ando, M. (1995) Observation of nuclear resonant scattering accompanied by phonon excitation using synchrotron radiation. *Phys. Rev. Lett.*, 74, 3828-3831.

Shearer, P. and Masters, G. (1990) The density and shear velocity contrast at the inner core boundary. *Geophys. J. Int.*, 102, 491-498.

Shen, G., Sturhahn, W., Alp, E.E., Zhao, J., Toellner, T.S, Prakapenka, V.V., Meng, Y. and Mao, H.R. (2004) Phonon density of states in iron at high pressures and high temperatures. *Phys. Chem. Minerals.*, 31, 353359.

Shen, G., Chow, P., Xiao, Y., Sinogeikin, S., Meng, Y., Yang, W., Liermann, H.P., Shebanova, O., Rod, E., Bommannavar, A. and Mao, H.-K. (2008) HPCAT: an integrated high-pressure synchrotron facility at the Advanced Photon Source, *High Pressure Res*, 28:3, 145-162.

Shearer, P. and Masters, G. (1990) The density and shear velocity contrast at the inner core boundary, *Geophys. J. Int.*, 102, 491-498.

Signorato, R., Hignette, O. and Goulon, J. (1998) Multi-segmented piezoelectric mirrors as active/adaptive optics components, *J. Synchrotron Rad.*, 5, 797-800.

Singh, S.C., Taylor, M.A.J. and Montagner, J.P. (2000) On the presence of liquid in Earth's inner core. *Science*, 287, 2471-2474.

Song, X. and Helmberger, D.V. (1998) Seismic evidence for an inner core transition zone. *Science*, 282, 924-927.

Speziale, S., Zha, C.-S., Duffy, T.S., Hemley, R.J. and Mao, H.K. (2001) Quasi-hydrostatic compression of magnesium oxide to 52 GPa: implications for the pressure-volume-temperature equation of state. *J. Geophys. Res.*, 106, 515-528.

Steinle-Neumann, G., Stixrude, L., Cohen, R.E. and Gülseren, O. (2001) Elasticity of iron at the temperature of the Earth's inner core. *Nature*, 413, 57-60.

Stevenson, D.J. (1981) Models of the Earth's core. *Science*, 214, 611-619.

Stevenson, D.J. (2003) Planetary magnetic fields. *Earth and Planet. Science Let.*, 208(1-2), 1-11.

Sturhahn, W., Toellner, T.S., Alp, E.E., Zhang, X., Ando, M., Yoda, Y., Kikuta, S., Seto, M., Kimball, C. W. and Dabrowski, B. (1995) Phonon density of states measured by inelastic nuclear resonant scattering. *Phys. Rev. Lett.*, 74, 3832-3835.

Sturhahn, W. and Kohn, V.G. (1999) Theoretical aspects of incoherent nuclear resonant scattering. *Hyperfine Interact.*, 123/124, 367-399.

Sturhahn, W. (2000) CONUSS and PHOENIX: Evaluation of nuclear resonant scattering data. *Hyperfine Interact.*, 125, 149-172.

Sturhahn, W. (2004) Nuclear resonant spectroscopy. *J. Phys.: Condens. Matter*, 16, 5497-5530.

Sturhahn, W. and Jackson, J. (2007) Geophysical applications of nuclear resonant spectroscopy. in Advances in High-Pressure Mineralogy, edited by E. Ohtani, *Spec. Pap. Geol. Soc. Am.*, 421, 157-174.

Sun, X. and Song, X. (2008) Tomographic inversion for three-dimensional anisotropy of Earth's inner

core. *Earth Planet. Sci. Lett.,* 167, 53-70.

Terasaki, H., Nishida, K., Shibazaki, Y., Sakamaki, T., Suzuki, A., Ohtani, E. and Kikegawa, T. (2010) Density measurement of Fe_3C liquid using X-ray absorption image up to 10 GPa and effect of light elements on compressibility of liquid iron, *Geophys. Res. Lett.*, 115, B06207, doi:10.1029/ 2009JB006905.

Toby, B.H. (2001) EXPGUI, a graphical user interface for GSAS. *J. Appl. Cryst*., 34, 210-213.

Toby, B. H. (2005) CMPR - a powder diffraction toolkit. *J. Appl. Crystallogr.,* 38, 1040-1041.

Toellner, T.S., Sturhahn, W., Alp, E.E., Montano, P.A. and Ramanathan, M. (1994) Avalanche photodiodes as large dynamic range detectors for synchrotron radiation, *Nucl. Instrum. Methods Phys. Res. A*, 350, 595-600.

Toellner, T.S. (2000) Monochromatization of synchrotron radiation for nuclear resonant scattering experiments, *Hyperfine Interact.*, 125, 3-28.

Toellner, T.S., Alatas, A., Said, A., Shu, D., Sturhahn, W. and Zhao, J. (2006) A cryogenically stabilized meV-monochromator for hard X-rays, *J. Synchrotron Rad.* 13, 211-215.

Torsvik, T.K., Burke, K., Steinberger, B., Webb, S.J. and Ashwal, L.D. (2010) Diamonds sampled by plumes from the core-mantle boundary, *Nature*, 466, 253-357.

Tsuzuki, A., Sago, S., Hirano, S. and Naka, S. (1984) High temperature and pressure preparation and properties of iron-carbides Fe_7C_3 and Fe_3C, *J. Mater. Sci.*, 19, 2513-2518.

Vočadlo, L., Brodholt, J., Dobson, D.P., Knight, K.S., Marshall, W.G., Price, G.D. and Wood, I.G. (2002) The effect of ferromagnetism on the equation of state of Fe_3C studied by first-principals calculations. *Earth Planet. Sci. Lett.*, 203(1), 567-575.

Warren, B.E. (1969) X-ray diffraction, Addison-Wesley.

Wood, B. J. (1993) Carbon in the core. *Earth Planet. Sci. Lett.*, 117(3-4), 593-607.

Wood, I.G., Vočadlo, L., Knight, K. S., Dobson, D. P., Marshall, W. G., Price, G. D. and Brodholt, J. (2004) Thermal expansion and crystal structure of cementite, Fe_3C, between 4 K and 600 K determined by time-of-flight neutron powder diffraction. *J. Appl. Crystallogr.*, 37, 82–90.

Yoshida, S., Sumitaz, I. and Kumazawax, M. (1998) Models of the anisotropy of the Earth's inner core. *J. Phys.: Condens. Matter*, 10, 11215-11226.

Zhao, J., Sturhahn, W., Lin, J.F., Shen, G., Alp, E.E. and Mao, H.K. (2004) Nuclear resonant scattering at high pressure and high temperature. *High Pressure Res.*, 24, 447-457.

Author's Biography

Lili Gao was born in Yinjiayan, a village close to Xiaoyi city in Shanxi province of China in 1984, and later moved to the Xiaoyi city with family. She started her first boarding school in 1994 when she entered the middle school. She graduated from University of Science and Technology of China (USTC) in July 2004 with a Bachelor's degree in geophysics. Afterwards, she entered the Ph.D. program in Prof. Jie Li's group at University of Illinois at Urbana Champaign in the U.S.. In January 2008, she joined the sector 3 group at the Advanced Photon Source (APS) of Argonne National Laboratory, with co-advisors Dr. E. Ercan Alp and Dr. Wolfgang Sturhahn. The last year of the Ph.D. was also under the co-advisorship of Prof. Jay Bass from University of Illinois at Urbana Champaign. Following the completion of her Ph.D. in 2010, Lili will continue to work with the sector 3 group at the APS as a postdoctoral scholar.